ROBUST VIBRATION SUPPRESSION CONTROL PROFILE GENERATION

By

LI ZHOU

Bachelor of Science
Jilin University of Technology
Changchun, P. R. China
1993

Master of Science
Dalian University of Technology
Dalian, P. R. China
1996

Submitted to the Faculty of the
Graduate College of the
Oklahoma State University
in partial fulfillment of
the requirements for
the Degree of
DOCTOR OF PHILOSOPHY
May, 2005

To my wife Letong,

and my daughter Yanru

ROBUST VIBRATION SUPPRESSION CONTROL PROFILE GENERATION

Thesis Approved:

Dr. Eduardo A. Misawa

Thesis Adviser

Dr. Prabhakar R. Pagilla

Dr. Gary E. Young

Dr. Martin T. Hagan

Dr. A. Gordon Emslie

Dean of the Graduate College

TRADEMARK AND OTHER ACKNOWLEDGEMENTS

Input Shaping® is a registered trade mark of Convolve, Inc., in the United States. When this technique is referred to in this report, the terms “input shaping” or “input shaper” are used.

The details of the Input Shaping® technique can be found in the Ph.D. dissertations of Singer [71], Singhose [79], and Tuttle [98] of the Massachusetts Institute of Technology, and the United States Patents [73], [85].

Vibration Suppression Shape Filter is a technical term that is developed in this report. A comparison of the shape filter technique and Input Shaping® technique is performed in some parts of the report.

ACKNOWLEDGMENTS

I would first like to express my sincerest appreciation to my advisor, and thesis committee chairman, Dr. Eduardo A. Misawa, for his thoughts, advice, support, and patience, throughout the course of this research. Without his guidance and expertise in supervising the research, I would not have completed this work. I would like to acknowledge and thank all my thesis committee members, Dr. Prabhakar R. Pagilla, Dr. Gary E. Young, and Dr. Martin T. Hagan, for their guidance and kind help throughout my doctorate studies.

In addition, I would like to thank the National Science Foundation, and Seagate Technology LLC of Oklahoma City, Oklahoma. Without financial support from them, this work would not have been possible.

I wish to thank my former and present colleagues in the Advanced Controls Laboratory at the Oklahoma State University, Dr. Brian O'Dell, Dr. Hanz Richter, Matthew Duvall, Ban Fu Chee, Chad Stoecker, Yunfei Zou, and Neusa Maria. They are the finest people that I work with.

I would like to thank the servo engineers at Seagate Technology LLC, Clyde Goodner, Todd R. Lyle, Tim T. Walker, Nathan B. Wilson, James W. Dulaney, and Tao Zhang. From them, I know the big picture of the hard disk drive servo control problems. They are the wonderful persons I know.

To my former leaders and colleagues in H & B System Company, Masayuki Hirose, Jieping Shi, Jixin Liang, Xiaohui Ji, Ji Guo, Wanming Wei, I want to thank them for their help.

I would like to express my appreciation to my parents, Dianfu and Lianting, for giving me the encouragement to pursue the advanced academic degree. To my father-in-law,

Changxu, and my mother-in-law, Wenhong, I want to thank them for their consistent support and help.

Finally, but not least, I am extremely grateful to my wife, Letong, and my lovely daughter, Yanru. They are always my constant support. Without their love, understanding, and sacrifice, it is impossible for me to complete the work.

The research work described in this dissertation was performed at the Oklahoma State University Advanced Controls Laboratory. Li Zhou has been supported by the National Science Foundation, grant number 9978748, and Seagate Technology LLC of Oklahoma City, Oklahoma.

NOTICE

The methods described in this dissertation are patented (pending). Commercial use of these methods requires written permission from the Oklahoma State University. Li Zhou may be contacted by email <zhouli_osu@yahoo.com>.

TABLE OF CONTENTS

LIST OF TABLES

Table Page

LIST OF FIGURES

Figure Page

NOMENCLATURE

Notation, Symbols and Acronyms:

$:=$	Equal to by definition.
$\equiv$	Identically equal to.
$\Rightarrow$	Implies.
$\mathbb{R}$	The real numbers.
$\mathbb{C}$	The complex numbers.
j	Imaginary unit $\sqrt{-1}$.
$\overline{a}$	Complex conjugate of $a \in \mathbb{C}$.
$\|a\|$	Absolute value of $a \in \mathbb{C}$.
$L^2(-\infty, \infty)$	A set of square integrable functions defined on $(-\infty, \infty)$.
$\|g(t)\|_\infty^2$	Total energy of $g(t) \in L^2(-\infty, \infty)$, i.e., $\int_{-\infty}^{\infty} \|g(t)\|^2 dt$.
$L^2(-B, B)$	A set of square integrable functions defined on $[-B, B]$.
$\|g(t)\|_B^2$	The energy of $g(t)$ in the interval $[-B, B]$, i.e., $\int_{-B}^{B} \|g(t)\|^2 dt$.
A^T	The transpose of matrix A.
$A_{m,n}$	The element at the m^{th} row and n^{th} column of A matrix.
$\{h[k]\}$	A sequence indexed by k, $k = \ldots, -2, -1, 0, 1, 2, \ldots$.
$h[k]$	A single value of a sequence at index k.
$E(\infty, \infty)$	The total energy of discrete sequence $\{h[k]\}$, i.e. $E(-\infty, \infty) = \sum_{k=-\infty}^{\infty} \|h[k]\|^2$.
$E(n_1, n_2)$	The energy of the sequence $\{h[k]\}$ in the index interval $[n_1, n_2]$, i.e. $E(n_1, n_2) = \sum_{k=n_1}^{n_2} \|h[k]\|^2$.

sec	Second.
msec	Milli second, i.e. 1 msec = 10^{-3} sec.
mm	Milli meter, i.e. 1 mm = 10^{-3} meter.
μm	Micro meter, i.e. 1 μm = 10^{-6} meter.
deg	Degree.
rad	Radian.
amp or A	Ampere.
Hz	Hertz, 1 Hz = 1 cycle per second.
KHz	Kilo Hertz, 1 KHz=10^3 Hz.
GHz	Giga Hertz, 1 GHz = 10^9 Hz.
PSWF	Prolate spheroidal wave function.
DPSS	Discrete prolate spheroidal sequence.
DPSWF	Discrete prolate spheroidal wave function.
FIR	Finite impulse response.
ZV	Zero vibration.
ZVD	Zero vibration and derivative.
SISO	Single input single output.
MIMO	Multiple input multiple output.

Chapter 1

Introduction to Profile Generation

1.1 The Problem Statement

The control of flexible structures has been extensively studied in recent years. Flexible structures such as high-speed disk drive actuators require extremely precise positioning under very tight time constraints. Whenever a fast motion is commanded, residual vibration in the flexible structure is induced, which increases the settling time. One solution is to design a closed-loop control to damp out vibrations caused by the command inputs and disturbances to the plant. However, the resulting closed-loop response may still be too slow to provide an acceptable settling time. Also, the closed-loop control is not able to compensate for high frequency residual vibration which occurs beyond the closed-loop bandwidth. An alternative approach is to develop an appropriate reference trajectory that is able to minimize the excitation energy imparted to the system at its natural frequencies.

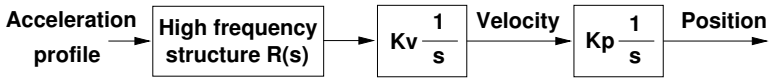

Figure 1.1: A typical flexible mechanical system.

Figure 1.1 shows a typical mechanical flexible system, where $\frac{1}{s}$ is an integrator, K_v is a velocity constant gain, and K_p is a position constant gain. The high frequency modes can be described as a transfer function $R(s)$ in which an infinite number of lightly damped

resonance modes is possible,

$$R(s) = \lim_{n\to\infty} \frac{b_n s^n + b_{n-1}s^{n-1} + \cdots + b_1 s + 1}{a_n s^n + a_{n-1}s^{n-1} + \cdots + a_1 s + 1}. \tag{1.1}$$

Figure 1.2 shows the Bode magnitude plot of a reduced order (28^{th} order) transfer function $R(s)$. This transfer function was derived from the flexible arm of an open disk drive as shown in Figure 6.4 (Chapter 6) in the Advanced Controls Laboratory at Oklahoma State University. The resonance modes change drastically due to variation of the mode parameters. On the Bode plot, the peaks of the frequency response may shift in both frequency and amplitude.

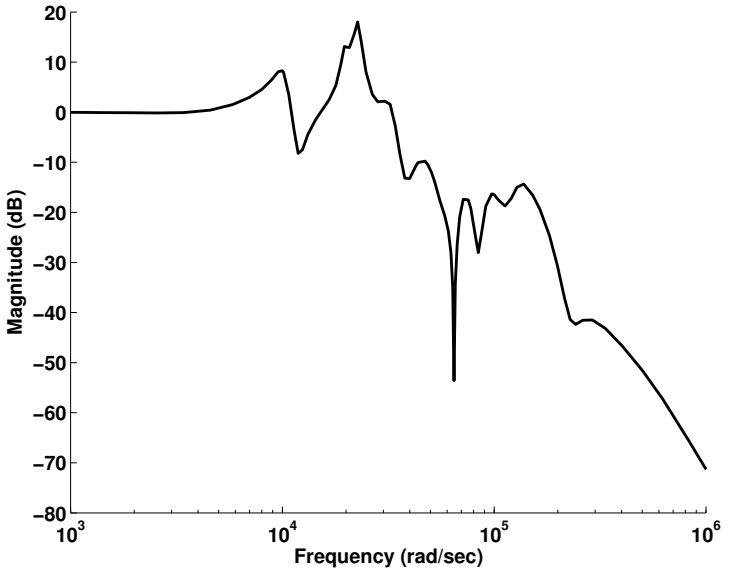

Figure 1.2: Bode magnitude plot of a reduced order transfer function $R(s)$.

The objective of robust vibration suppression trajectory generation is to find a fast input trajectory, under some physical constraint (such as motor voltage/current limit, velocity limit), with minimum possible residual vibration.

A standard approach is to consider the movement of the rigid mode described by the double integrator $\frac{1}{s^2}$, from acceleration to position. Here, the constant gains K_v and K_p are not considered. A typical trajectory for a double integrator system is shown in Figure 1.3. Notice that, to guarantee zero velocity of the rigid mode, the area of A_1 should be equal to

the area of A_2 in the acceleration profile (left plot). Physically, if the time duration of the acceleration profile is finite, the flexible beam is accelerated at the first part of move and then decelerated at the second part to move a flexible beam from one set point to another. The velocity trajectory (middle plot) starts and ends at zero to realize a rigid body move from one set point to another. Due to the possibly infinite number of resonant modes, it is unlikely that the system will be stationary after the end of acceleration, because the residual vibration settles after a long period of time. The work discussed in this report generates a robust profile which suppresses the residual vibration of a flexible dynamic system.

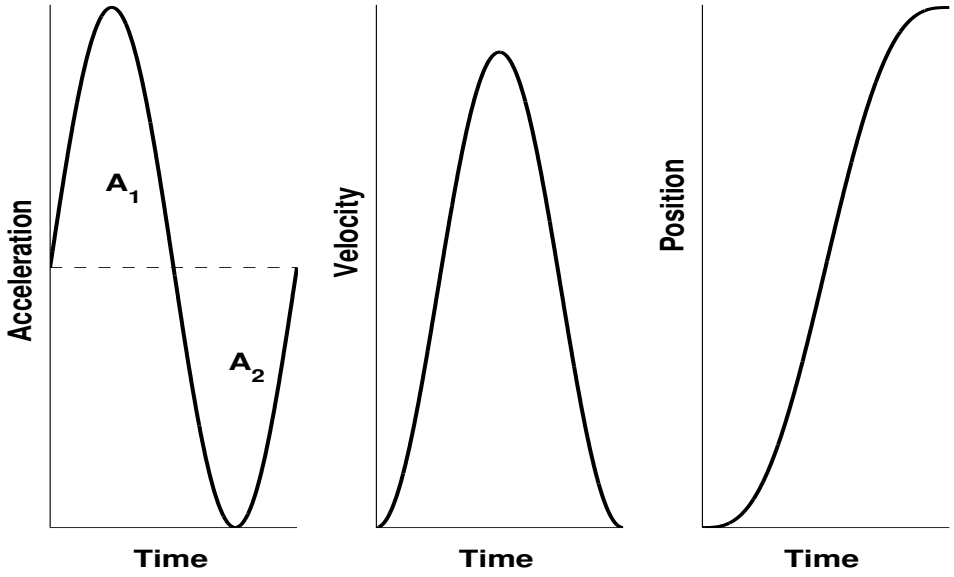

Figure 1.3: Typical trajectory for a double integrator system.

The phrase "move time" refers to the time duration of the feed forward control input, such as acceleration, current, or voltage. Settle time means the time duration after the end of move time to achieve the settle criterion, for example $\pm 5\%$ tracking error. Seek time is the sum of the move time and the settle time. These are quite standard terms in hard disk drive industry and can be easily applied to other systems without confusion. Figure 1.4 clearly shows the move time and the settle time for a hard disk drive arm movement with open-loop control. The top plot is the current input signal, the middle plot is the resultant position signal, and the bottom plot shows the position signal near the target track. In

this instance, the move time is 2.5 msec. Because of the resonant structure in the flexible system, the position signal reveals the residual vibration immediately after the move. In Figure 1.4, the settle time is about 2.5 msec with $\pm 1\%$ tracking error criterion. Note that the $\pm 1\%$ tracking error criterion means the response curve to reach and stay within 1% track of the center of the target track. This definition is different from the allowable tolerance of the transient-response specification analysis in the standard control textbooks (for example Kuo [4] and Ogata [59]). The settling time in the standard control textbooks means the time required for the response to reach and stay within a certain criterion (for example $\pm 2\%$) of the final value. The objective of the robust vibration suppression trajectory generation is to minimize the seek time.

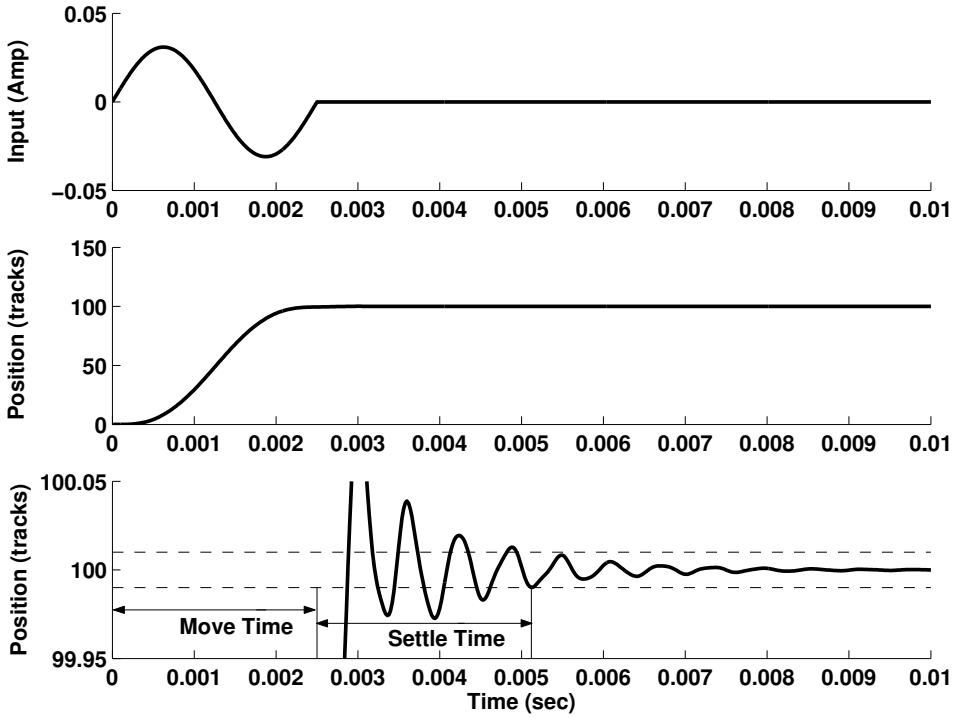

Figure 1.4: Illustration of move time and settle time of an open-loop control.

The same concepts apply to closed-loop control. Figure 1.5 clearly shows the move time and the settle time for a hard disk drive arm movement with closed-loop control. The top two plots are the reference position movement profile and the bottom two plots show

the real position signals. In this instance, the ideal reference position move time of the flexible arm is 2.5 msec. Due to the resonant structure in the flexible system, the position signal cannot settle down immediately after the move. In Figure 1.5, the settle time is about 2.5 msec with $\pm 1\%$ tracking error criterion.

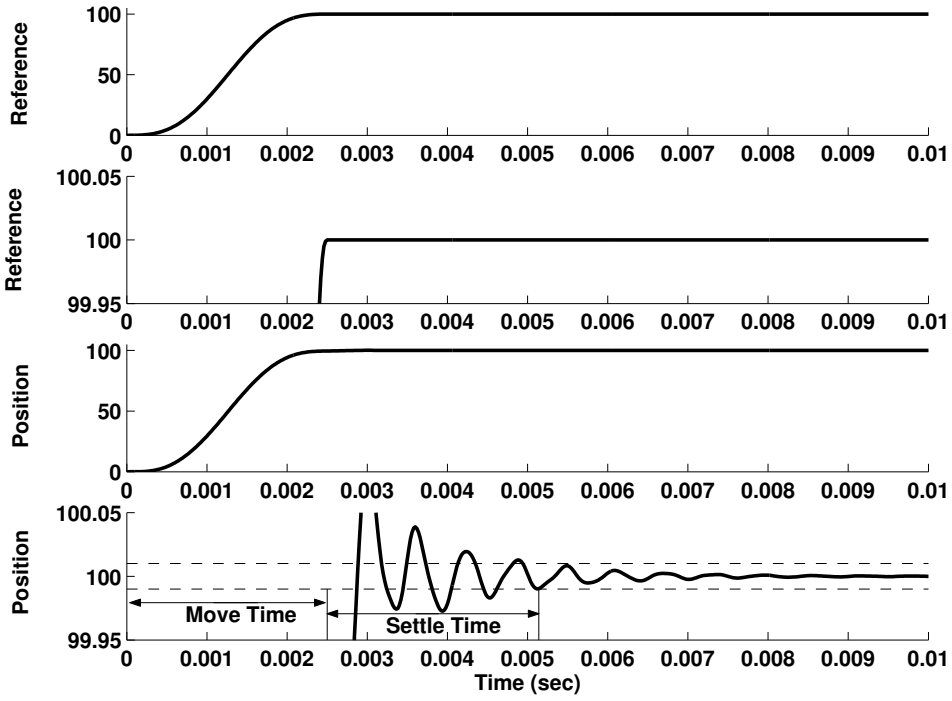

Figure 1.5: Illustration of move time and settle time of a closed-loop control.

The position reference input can be generated in two ways. First, it can be assumed as the integral of a velocity profile, as shown in Figure 1.6. In this case, since the velocity profile is a smooth trajectory starting and ending at zero, the resultant position reference is a smooth trajectory.

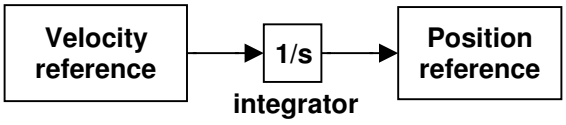

Figure 1.6: Position reference generation from a velocity profile.

Secondly, it can be generated from a step movement command through a finite support

filter, $f(t)$, $0 \leq t \leq T$, where T is the time duration of the finite support filter as shown in Figure 1.7. This finite support filter which generates a position reference is called "shape filter" in this report. From Figure 1.7, a position reference input from one set point to another can always be generated from a step movement command convolving with a shape filter. It is easy to know that the shape filter to generate the step movement command itself is a unit impulse.

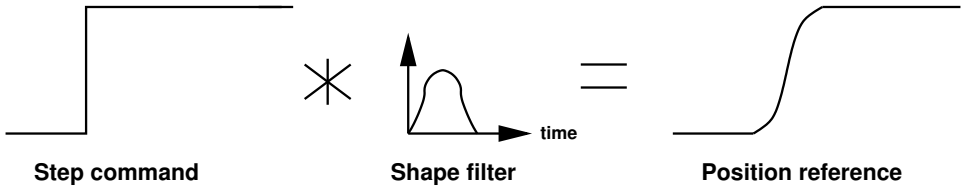

Figure 1.7: Position reference generation from a step movement command and a finite support filter.

To guarantee that the filtered command reaches the same set point as the step movement command, the integral of $f(t)$ must be imposed to 1, i.e.,

$$\int_0^T f(t)dt = 1. \tag{1.2}$$

This constraint can be simply derived: suppose that the original command signal is $s(t), t \geq 0$, and the filtered command is $q(t), t \geq 0$, then by the filter operation

$$q(t) = \int_0^t s(t-\tau)f(\tau)d\tau. \tag{1.3}$$

That the filtered command $q(t)$ reaches the same set point of original command $s(t)$ means $q(\infty) = s(\infty)$ holds. From

$$q(\infty) = \int_0^\infty s(\infty-\tau)f(\tau)d\tau, \tag{1.4}$$

$$= \int_0^T s(\infty-\tau)f(\tau)d\tau, \tag{1.5}$$

$$= s(\infty)\int_0^T f(\tau)d\tau, \tag{1.6}$$

the constraint (1.2) is derived. If the original command $s(t)$ is a step reference, say,

$$s(t) = S \cdot 1(t), \quad t \geq 0, \tag{1.7}$$

where S is step amplitude and $1(t)$ is unit step, then the filtered command $q(t)$ reaches the original command $s(t) = S \cdot 1(t)$, $t \geq 0$, immediately at the time duration T of the shape filter, i.e.,

$$q(t) = s(t), \quad t \geq T. \tag{1.8}$$

This shape filter $f(t)$, $0 \leq t \leq T$, which generates a vibration suppression position reference profile is called a "vibration suppression shape filter", or simply a shape filter, in this report.

In the discrete-time case, if the finite impulse response shape filter is $f[k]$, $0 \leq k \leq M$, the constraint (1.2) reduces to

$$\sum_{k=0}^{M} f[k] = 1. \tag{1.9}$$

A normalized robust vibration suppression velocity profile can be used as the shape filter function to generate the reference position profile. The normalization is to make the velocity profile satisfy the constraint (1.2). So if there is a robust vibration suppression velocity profile, $v(t)$, $0 \leq t \leq T$, a vibration suppression shape filter $f(t)$ can be generated by

$$f(t) = \frac{v(t)}{\int_0^T v(t)dt}. \tag{1.10}$$

The good property of this kind of shape filters is that the shape filter itself is a robust vibration suppression velocity profile, so it can generate a smooth vibration suppression position reference.

A shape filter does not necessarily start and end at zero. Figure 1.8 shows a step position command, a typical shape filter that has non-zero values at the start and end, and the filtered position reference. Although the shape filter smoothly changes from the start to the end, the initial value at time zero and the final value at time T of the shape filter are not zero.

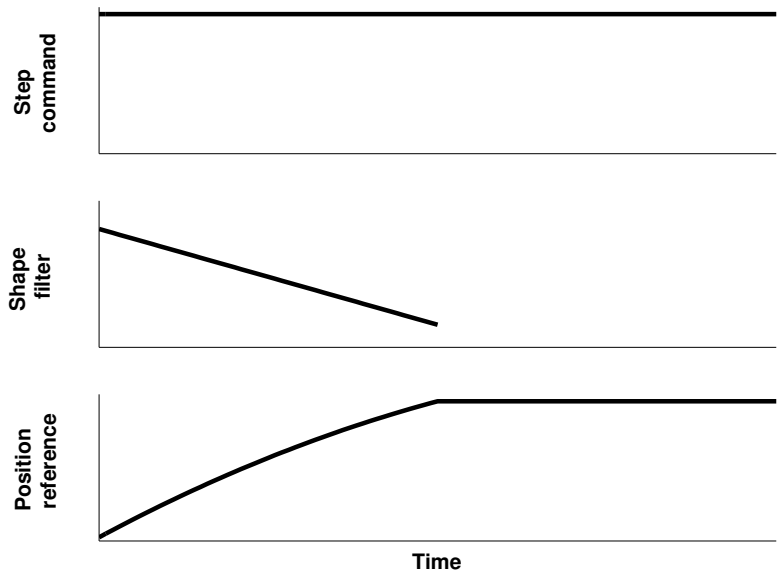

Figure 1.8: A step position command, a non-zero start and end shape filter and the filtered position reference.

Furthermore, a shape filter can also be a non-smooth function. Figure 1.9 shows a step position command, a typical non-smooth shape filter, and the filtered position reference. It shows that the shape filter function is not smooth from the start to the end.

It is easy to understand that the robust vibration suppression position reference generated from a step command $s(t) = S \cdot 1(t)$ through a shape filter, $f(t)$, $0 \leq t \leq T$, can also be generated from the integral of a scaled shape filter $S \cdot f(t)$, $0 \leq t \leq T$, since

$$s(t) * f(t) = \int_0^t s(t-\tau) f(\tau) d\tau, \tag{1.11}$$

$$= \int_0^t S \cdot 1(t-\tau) f(\tau) d\tau, \tag{1.12}$$

$$= \int_0^t S \cdot f(\tau) d\tau. \tag{1.13}$$

Here, "*" is the convolution operator. Similarly, the robust vibration suppression position reference generated from a step command $s(t) = S \cdot 1(t)$ through a discrete-time shape filter, $f[k]$, $0 \leq k \leq M$, can also be generated from the integral of a scaled shape filter $S \cdot f[k]$, $0 \leq k \leq M$.

The vibration suppression shape filters can also shape other control profiles. The control

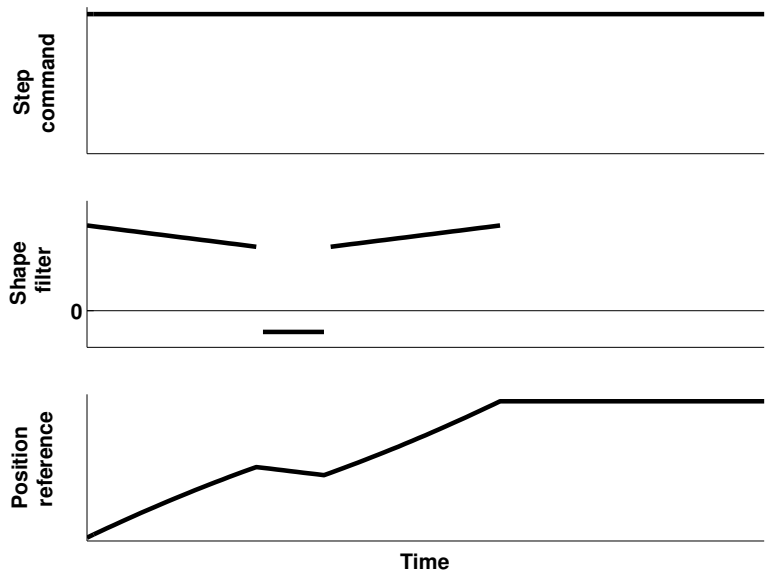

Figure 1.9: A step position command, a non-smooth shape filter and the filtered position reference.

profile here refers to the trajectories in the control system, such as acceleration, velocity, or position signals.

1.2 Background and Literature Review

Motion control of flexible structures may be tracked to 1970's when the motion control of flexible manipulator arms was studied by many researchers. Maizza-Neto [50] studied the modal analysis and closed-loop feedback control of flexible manipulator arms. Book [14, 16] studied feedback closed-loop control of flexible manipulator arms with distributed flexibility. Balas [5] developed a feedback controller for a finite number of modes in a flexible mechanical system. This research has been further extensively studied since 1970's. A full survey on this research prior to 1990's was done by Book [15] in the paper entitled "Controlled Motion in an Elastic World". Book [15] stated in the survey paper that "The technique for (space) manipulators was, and continuous to be, to move the joints slowly and wait for the tip of the arm to settle to equilibrium." With the requirement of

light weight and fast response, flexibility becomes a formidable problem in motion control of flexible structures. Not only the closed-loop feedback control methods were studied, but also the feedforward control methods (known as "input command shaping") were developed. "Input command shaping and closed-loop feedback for vibration control are two distinct approaches toward vibration reduction of flexible systems (Singer and Seering [72])." Input command shaping involves the appropriately choosing the shape of the input command for either open-loop system or closed-loop system so that the system vibrations are reduced. Generally, these techniques include shaped function synthesis, open-loop optimal control, impulse shaping filters, and system-inversion-based motion planning.

One of the pioneering works of the shaped function synthesis was introduced by Aspinwall [2], who used a finite Fourier series expansion to construct forcing functions to attenuate the residual dynamic response for slewing a flexible beam. The response spectrum envelope is made small only in a limited region. Also the forcing functions are sensitive to the control system. Another pioneering work was introduced by Swigert [94], who used a performance index which reflects the concern for the accuracy of the terminal boundary conditions to the changes in mode eigen-frequencies. However, the control inputs are difficult to calculate, and only a few modes are considered. Junkins et al. [96] developed a near minimum-time open-loop control input for single-axis maneuvers of a flexible structure by shaping the control profiles with two independent parameters. Bhat and Miu [10, 11, 12] have shown that control waveforms can be optimized using the Laplace domain synthesis technique. But the control inputs need to be assumed through a judicious choice.

None of the previous methods consider all the resonance modes, which in reality may be infinite in number. Also, the modes' responses change drastically due to resonance modeling uncertainty. To overcome the resonance frequency variation, Yamamura and Ono [107] have developed a robust vibrationless control solution derived for an enlarged multi-degree-of-freedom system that has some virtual frequencies within the range of the varying natural frequencies. Meckl and Roberto [53] followed the same approach and developed a forcing

function using a series of ramped sinusoids for one nominal resonance model. The spectrum magnitude of the forcing function becomes small at the nominal resonance frequency and the four additional frequencies surrounding the nominal frequency. But the spectrum magnitude of the forcing function increases significantly at frequencies beyond these.

In the more recent work of Yamamura and Ono [104, 105, 106], the authors described a frequency-shaped cost functional whose weighting function was represented by a first-order and second-order high-pass filter in the design of vibrationless access control forces. The control forces have small frequency components in the high frequency region. But the decay rate in the frequency domain depends on the shape of the weighting function. Mizoshita et al. [54] developed an access control called SMART (Structural Vibration Minimized Acceleration Trajectory) for hard disk drives. The access formula is derived from the minimum-jerk cost function where the SMART state values (position, velocity, and acceleration) are expressed using time polynomials. But the jerk cost function has no direct relationship to the residual vibration.

Optimal control approaches have been studied to generate an input command for a flexible dynamic system. Typically, an objective function is selected to be minimized. For example, the famous Bang-Bang Principle was explained by Hermes [32] as: "It had been an intuitive assumption for some time that if the control for a system is operating from a limited source of power and if it is desired to have the system change from one state to another in minimum time, then it is necessary at all times to utilize all the power available; that is, to use bang-bang control." With the Bang-Bang Principle, the time-optimal commands must be piecewise constant functions of time and the constants are solely determined by the actuator maximum and minimum input limits. That means the time-optimal control must always saturate the actuators. Although the analytical results do exist for systems with order greater than two in special cases [3, 37, 43, 70], it is not easy to analytically derive the time-optimal command for a system in which the order is greater than two. Workman [103] studied an adaptive proximate time-optimal servomechanisms

for a second-order system. Pao [61] studied the proximate time-optimal control of third-order servomechanisms. Tuttle and Seering [98, 100, 101, 102] developed a numerical method to create time-optimal commands for linear systems. Other types of optimal control select different objective functions, for example, integral squared error plus some control penalty. Generally, these objective functions do not explicitly include a direct measure of both the move time and the unwanted resonant dynamics. These profiles are therefore very sensitive to unmodeled flexible dynamics.

The posicast control developed by Smith [91, 92, 95] uses a kind of set point shaping. This method breaks a step input into two smaller steps, one of which is delayed in time. The delayed input results in a vibration cancellation for a precisely known resonance, therefore reducing the settling time for a point-to-point motion command. A method incorporating robustness was later developed and patented [71, 73, 79, 85] by Singer et al. Instead of using two impulses to generate the delayed input, input shapers use three or more impulses to generate a delayed input. Robustness is improved by increasing the number of impulses. Input shaping technique has been extensively studied in both linear systems by Singer [72, 69], Singhose [76, 78, 80, 81, 82, 83, 84], Jones [33], Tuttle [99] and some special nonlinear systems by Gorinevsky [28], Magee [47], Kozak [38], Park [64], Kenison [34], Kinceler [36], Smith [90]. The relationship between input shaping technique and time-optimal control has been studied by Pao and Singhose [63, 77], Lau and Pao [41, 42], Baumgart and Pao [7]. One of the disadvantages of this technique is that the input shapers induce delays that increase in number of pulses. Another disadvantage is that it is impossible to design an input shaper to accommodate all the resonant modes in a flexible structure. Since the input shapers are generated from non-continuous impulse functions, they cannot be used as the velocity profiles in open-loop control. Generally, the input shapers are used to shape the step reference command into several small steps in closed-loop control.

Singh and Vadali [74, 75] developed two or three-impulse time-delay filter by canceling the complex poles of a flexible system to attenuate the residual vibration. Magee and

Book [46, 48, 49] also developed the two or three-impulse optimal arbitrary time-delay filter technique by choosing a cost function involving both the error signal and the time rate of change in the error signal. The cost function is expressed as an explicit function of the unknown filter coefficients, and the function can be minimized with respect to the unknown filter terms. Magee [46] showed that the two or three-impulse optimal arbitrary time-delay filter reduced to input shaping technique by choosing the time-delay value to be a special number.

Moulin and Bayo [55] addressed the problem of open-loop control of the end-point trajectory of a single-link flexible arm by an inverse dynamic solution. Rastegar et al. [97] used a number of basic sinusoidal time functions and their harmonics to trajectory synthesis. Piazzi and Visioli [66] determined the command function of the system by means of a non-causal system inversion with a continuous derivative of an arbitrary order. One disadvantage of these techniques is that a precise model of the system is generally required. Another disadvantage of these system-inversion-based motion planning techniques is that the smooth motion and robustness is achieved at the expense of long move time.

1.3 Closed-Loop Control Schemes Using Robust Vibration Suppression Profiles

In this section, closed-loop control schemes using the robust vibration suppression profiles are described.

In general, there are two closed-loop control schemes in the motion control of a flexible system. Figure 1.10 shows a standard closed-loop control scheme. The position reference is the reference input to the closed-loop system. The robust position reference can be generated from the robust velocity reference or a step movement command through a vibration suppression shape filter.

Another kind of closed-loop control scheme is the model reference control, as shown

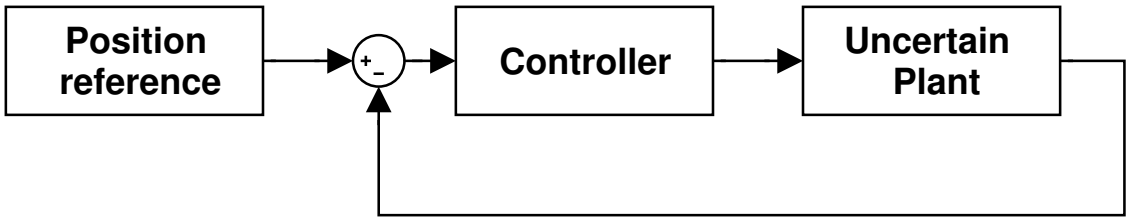

Figure 1.10: Standard closed-loop control scheme.

in Figure 1.11. In this control scheme, the forcing function signal is directly sent to both the uncertain plant and a reference model of the plant. The controller takes as its input the tracking error, which is the difference of the real position and the position reference generated by the reference model. The robust forcing function can be generated from a robust velocity profile through the physical system dynamics as shown in Figure 1.12.

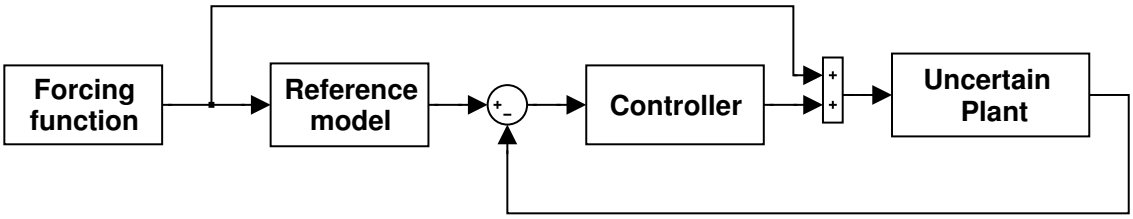

Figure 1.11: Model reference closed-loop control scheme.

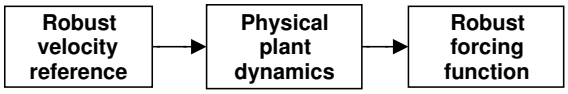

Figure 1.12: Robust forcing function generation from velocity reference.

In practice, the position reference from the reference model may be saved in a table and directly used as a reference input as shown in Figure 1.13.

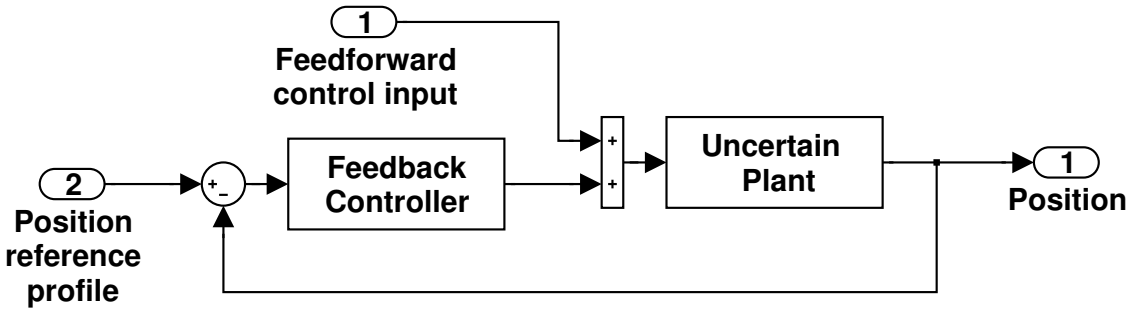

Figure 1.13: Implementation of model reference closed-loop control with robust vibration suppression control profiles.

1.4 Development and Philosophy of the Design Method

In this section, the development and philosophy of the robust vibration suppression control profile generation method studied in this thesis are outlined.

1.4.1 Robust Vibration Profile Generation from Filter Point of View

If the acceleration signal is denoted by $u(t)$, the flexible system unit impulse response denoted by $h(t)$, and the position movement including residual vibrations denoted by $y(t)$, then the following relationship holds

$$\underbrace{y(t)}_{\text{residual vibration signal}} = \underbrace{h(t)}_{\substack{\text{flexible system unit} \\ \text{impulse response}}} * \underbrace{u(t)}_{\text{acceleration profile}} \tag{1.14}$$

in the time domain, and the the following relationship holds

$$\underbrace{Y(\omega)}_{\text{signal}} = \underbrace{H(\omega)}_{\text{filter}} \cdot \underbrace{U(\omega)}_{\text{signal}} \tag{1.15}$$

in the frequency domain. Here $U(\omega) = \int_0^\infty u(t)e^{-j\omega t}dt$ is the continuous-time Fourier transform (see Appendix A) of the acceleration signal $u(t)$. Similarly, $Y(\omega)$ is the Fourier transform of the function $f(t)$ and $H(\omega)$ is the Fourier transform of the function $h(t)$.

If residual vibrations occur, all the residual vibrations will appear in $Y(\omega)$ in the frequency domain. Remember that $H(\omega)$ cannot be changed, but $U(\omega)$ is to be designed.

Now consider the relationship $y(t) = h(t) * u(t)$ again. Since $h(t)$ which includes the resonance modes cannot be changed, the relationship may be written in a different way as

$$\underbrace{y(t)}_{\substack{\text{residual vibration signal}}} = \underbrace{u(t)}_{\substack{\text{filter unit impulse response to suppress high frequency resonance modes}}} * \underbrace{h(t)}_{\substack{\text{signal composing of the unit impulse response of the flexible system}}} \tag{1.16}$$

in the time domain, and the relationship

$$\underbrace{Y(\omega)}_{\text{signal}} = \underbrace{U(\omega)}_{\text{filter}} \cdot \underbrace{H(\omega)}_{\text{signal}} \tag{1.17}$$

in the frequency domain.

If $u(t)$ is considered as a filter impulse response, the good properties filter $u(t)$ should possess are

1. The duration of filter $u(t)$, say, T, should be as short as possible;

2. The filter $u(t)$ should cut off all the high frequency components (greater than or equal to the first resonance frequency) of $h(t)$ as much as possible. However, since $\int_0^T u(t)dt = 0$ or $U(0) = 0$ is required for the rigid body movement, filter $u(t)$ also filters out the DC part of $h(t)$. The resultant velocity $v(t) = \int_0^t u(t)dt$ should behave like a low pass filter.

First, the ideal case of property 1 is the time-optimal "bang-bang" command. The "bang-bang" form control input has been studied extensively for pure rigid mode and a

rigid mode plus one or two resonance modes. Since the energy of the "bang-bang" forcing function almost spreads all over the frequency domain, it is not a good candidate for robust residual vibration suppression. The detail of this concept is studied in Chapter 2.

Then property 2 is considered here. Can an ideal low-pass filter impulse response be used as a velocity profile? The question sounds extremely exciting and a little silly. It is exciting because, if it is possible then all the resonance modes of $h(t)$ can be canceled out. It is silly, because nobody has ever tried it before. What does the ideal low-pass filter velocity profile look like? To answer this question, a typical ideal low-pass filter function is shown in Figure 1.14.

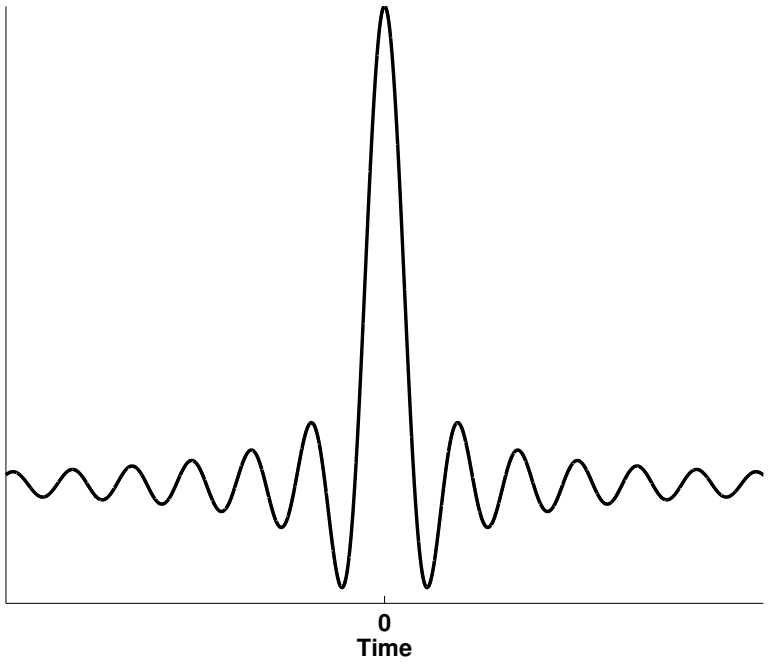

Figure 1.14: Ideal low-pass filter impulse function.

The ideal low-pass filter function spreads all over the time domain from $-\infty$ to ∞. From mathematical theory, it is known that the band-limited signal is an entire function (that is further discussed in Chapter 3) in t. To use the ideal low-pass filter function as a velocity profile, the signal needs to be shifted forward to make the start time be zero and the end time be ∞. The price of infinite time duration is too expensive that it is impossible

for it to be realized. This result is worse than the "bang-bang" forcing function. So the idea is really impractical. How about the truncated versions of the ideal low-pass filter function? Figure 1.15 shows two possible shifted truncated versions of the ideal low-pass filter function corresponding different truncation intervals. The shifted truncated versions of the ideal low-pass filter can be used as velocity profiles for a rigid body from one set point to another set point.

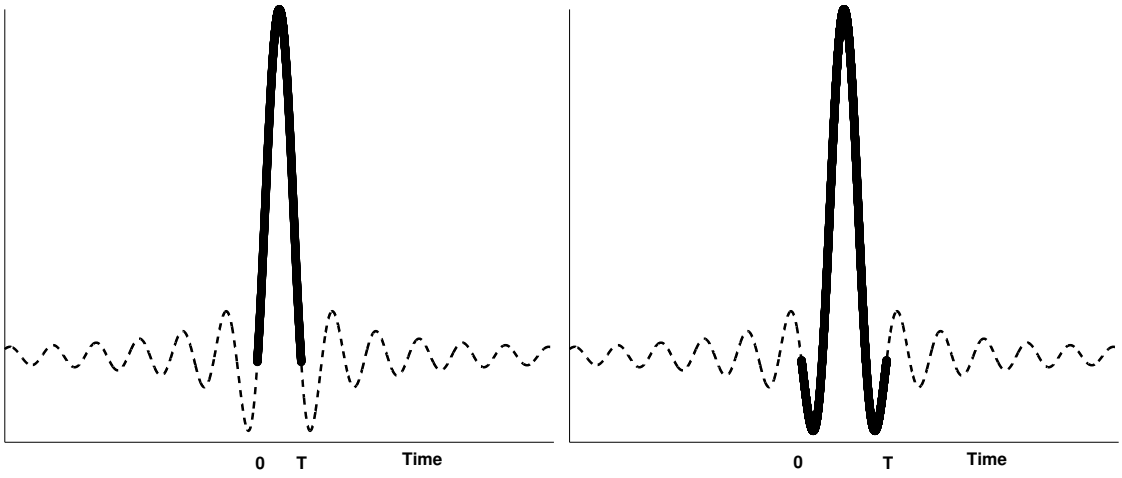

Figure 1.15: Two possible shifted truncated ideal low-pass filter functions.

Unfortunately, the shifted truncated versions of the ideal low-pass filter loss too much energy compared to the ideal low-pass filter. So the spectrum of truncated versions of the ideal low-pass filter never behaves like the ideal low-pass filter. It is an unwise idea again.

Although it is unsuccessful in trying to find a perfect profile to satisfy both property 1 and property 2, it is understood that it is not easy to find a function that simultaneously concentrates its energy both at time domain and frequency domain. In Chapter 2 and Chapter 3, some variables are defined to evaluate the concentration or localization of a signal both in the time domain and the frequency domain. Functions in mathematics that achieve these qualities are studied. The generation of robust vibration suppression control profile and vibration suppression shape filter based on these functions are investigated.

1.4.2 Robustness to Modeling Uncertainty

The robust vibration suppression control profiles in Chapter 2 and Chapter 3 that are originated from the thought in last subsection are robust to the variation of the resonance frequencies since the energy components after a certain frequency Ω_0 can be made negligibly small. If a control profile has little energy after a certain frequency Ω_0, i.e. to say that the control profile behaves like a band-limited signal, the high frequency energy components embedded in a flexible system will be definitely suppressed.

The Chapter 4 discusses the robust vibration suppression control profile generation for a specific resonance mode. In this case, the robustness of the shape filter is examined with respect to variation of the natural frequency and the damping ratio. Since all the shape filters in this thesis are generated from continuous functions, the smoothness of the shape filters simultaneously suppresses the high frequency resonance modes. The robustness of the shape filter to suppress high frequence resonance modes is examined in Chapter 4.

1.5 Thesis Outline and Main Contributions

Chapter 2 presents the robust vibration suppression profile generation and the robust vibration shape filter generation based on time-frequency uncertainty. Simulation results of hard disk drive open-loop control and experimental results of flexible beam position control show the effectiveness of the method. Chapter 3 presents the robust vibration suppression profile generation and the robust vibration shape filter generation based on optimal energy concentrated functions. Again, simulation results of hard disk drive open-loop control and experimental results of flexible beam position control show the effectiveness of the method. The robust vibration suppression profiles generated in Chapter 2 and Chapter 3 suppress all the resonance modes whose resonance frequencies are located beyond a certain frequency Ω_0. Chapter 4 discusses the robust vibration suppression shape filter generation or robust vibration suppression control profile generation for a specific resonance mode in a

flexible system. Chapter 6 presents experimental results for the hard disk drive position control using the techniques developed in this report. Finally, Chapter 7 presents the concluding remarks. A number of conclusions and recommendations for future research are highlighted.

This thesis makes several contributions to the field of robust vibration suppression control profile generation for flexible systems. The main contributions of this research are as following:

- Generation of a control profile, such as velocity or acceleration, which can suppress all the resonance modes whose resonance frequencies are located beyond a certain frequency Ω_0.
- Generation of a robust vibration suppression shape filter which can suppress all the resonance modes whose resonance frequencies are located beyond a certain frequency Ω_0.
- Generation of a control profile, such as velocity or acceleration, which can suppress a specific resonance mode in a flexible system.
- Generation of a robust vibration suppression shape filter which can suppress a specific resonance mode in a flexible system.
- Generation of a control profile, such as velocity or acceleration, which can suppress all the resonance modes in a flexible system.
- Generation of a robust vibration suppression shape filter which can suppress all the resonance modes in a flexible system.
- Generation of a robust vibration suppression control profile with multiple constraints, such as velocity constraint, drive current constraint or drive voltage constraint.

Chapter 2

Robust Vibration Suppression Profile Generation Based on Time-Frequency Uncertainty

2.1 Time-Frequency Localization

In theory, the most efficient way to reduce the move time is to use the time-optimal control input which has the bang-bang form. In practice, to suppress the high frequency residual vibration, the control input must have a small energy distribution at high frequencies (i.e. the control input should behave like an ideal low-pass filter.) However a signal cannot be found using existing techniques which simultaneously achieves the two properties. The following analysis clearly shows this phenomenon.

Figure 2.1 shows the typical time-optimal command and its spectrum magnitude. The time-optimal command has a sharp decay in the time domain but a very slow decay in the frequency domain. From the top plot in Figure 2.1, the time-optimal command suddenly changes from zero to maximum at time zero and suddenly changes from minimum to zero at the end of the command. From the bottom plot in Figure 2.1, the magnitude spectrum of the time-optimal command slowly changes its amplitudes from 0 rad/sec to the extremely

high frequency. The total energy of the time-optimal command concentrates in the time domain but spreads over all in the frequency domain. Figure 2.2 shows the typical ideal low-pass filter function and its spectrum. Similarly, the ideal low-pass filter function has a sharp decay in the frequency domain but a very slow decay in the time domain. So both bang-bang form forcing function and ideal low-pass filter function are not suitable for robust vibration suppression profile generation.

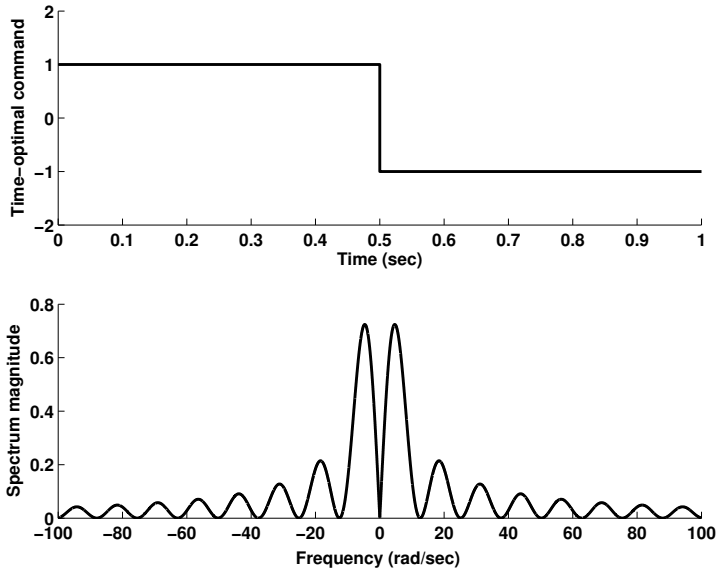

Figure 2.1: Time-optimal command input and its spectrum magnitude.

In the communication field, it is known that one cannot simultaneously confine a function $h(t)$ and its Fourier transform $H(\omega)$ too strictly. This phenomenon is clearly stated by the Heisenberg Uncertainty Principle: if the time-spread $\Delta_{h(t)}$ of $h(t)$ is measured by

$$\Delta_{h(t)}^2 = \frac{\int_{-\infty}^{\infty}(t-t^*)^2|h(t)|^2dt}{\int_{-\infty}^{\infty}|h(t)|^2dt}, \tag{2.1}$$

and the frequency-spread $\Delta_{H(\omega)}$ of $H(\omega)$ is measured by

$$\Delta_{H(\omega)}^2 = \frac{\int_{-\infty}^{\infty}(\omega-\omega^*)^2|H(\omega)|^2d\omega}{\int_{-\infty}^{\infty}|H(\omega)|^2d\omega}, \tag{2.2}$$

where t^* is defined as center of $h(t)$ and ω^* is defined as center of $H(\omega)$ by

$$t^* = \frac{\int_{-\infty}^{\infty}t|h(t)|^2dt}{\int_{-\infty}^{\infty}|h(t)|^2dt} \tag{2.3}$$

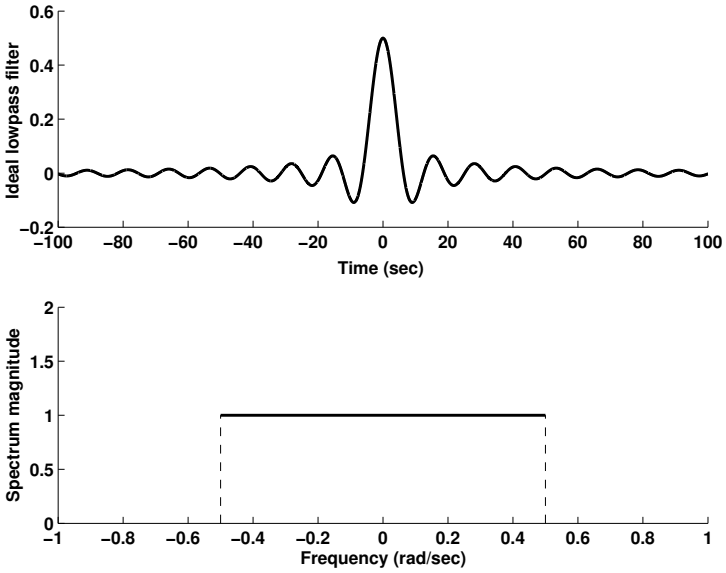

Figure 2.2: Ideal low-pass filter function and its Fourier transform.

and

$$\omega^* = \frac{\int_{-\infty}^{\infty} \omega |H(\omega)|^2 d\omega}{\int_{-\infty}^{\infty} |H(\omega)|^2 d\omega}. \tag{2.4}$$

Then the function $h(t)$ must satisfy the inequality

$$\Delta_{h(t)} \Delta_{H(\omega)} \geq \frac{1}{2}. \tag{2.5}$$

Thus, both $\Delta_{h(t)}$ and $\Delta_{H(\omega)}$ cannot, for any Fourier transform pair, be small. Furthermore, the equality in (2.5) will hold if and only if $h(t)$ (and hence $H(\omega)$) are Gaussian [18, 19]

$$h(t) = ce^{jat} e^{\frac{-(t-b)^2}{4\alpha}} \tag{2.6}$$

for some real constants a, b, c, and α with $a > 0$ and $c \neq 0$.

In the engineering field, $2\Delta_{h(t)}$ is called the root mean square (RMS) duration of $h(t)$, and $2\Delta_{H(\omega)}$ is called the RMS bandwidth of the function $h(t)$. Let $a = 0$ make (2.6) a real function and let $c = 1, b = 0$ and $\alpha = \frac{1}{2}$ reduce (2.6) to a simple form

$$h(t) = e^{\frac{-t^2}{2}}. \tag{2.7}$$

The derivative of $h(t)$ in (2.7) is given by

$$\phi(t) = -te^{\frac{-t^2}{2}}. \tag{2.8}$$

The derivative of $\phi(t)$ in (2.8) is given by

$$\frac{d}{dt}\phi(t) = -(1-t^2)e^{(-\frac{1}{2}t^2)}, \tag{2.9}$$

which is the equation for the so-called "Mexican hat" wavelet.

Figure 2.3 shows the waveform of $\phi(t)$. It is clear that $\phi(t)$ decays very quickly such that the value of $\phi(t)$ at some t is negligible. It also demonstrates that the total energy of $\phi(t)$ concentrates locally near zero. Figure 2.4 shows the waveform of the derivative of $\phi(t)$. It shows that the derivative of $\phi(t)$ also has the same rapid decay and energy concentration properties as those of $\phi(t)$. By computing the higher order derivatives of $\phi(t)$, it can be known that all the derivatives of $\phi(t)$ have these two properties.

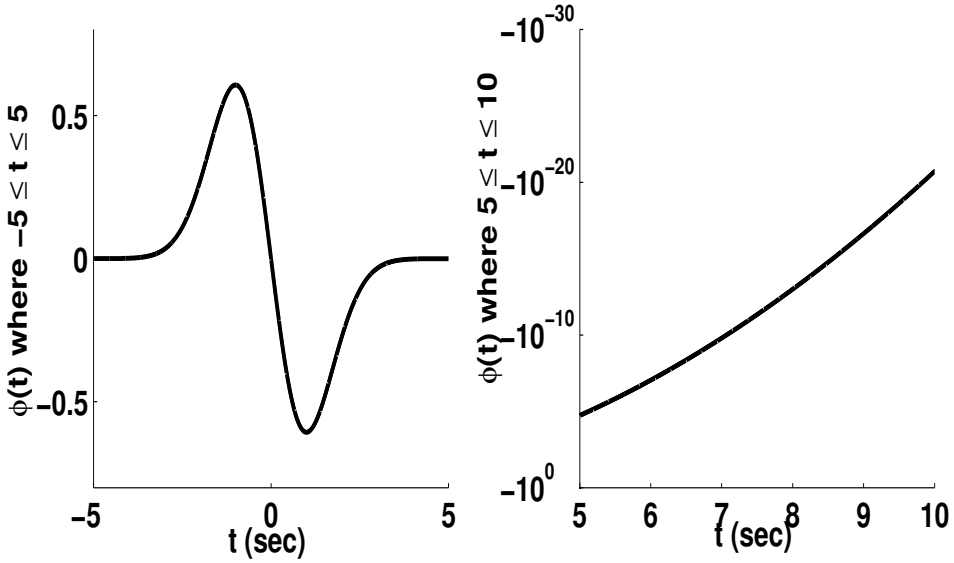

Figure 2.3: Waveform of $\phi(t)$.

Now the waveform of $\phi(t)$ is considered from the spectrum point of view. The Fourier transform $\Phi(\omega) = \int_{-\infty}^{\infty} \phi(t)e^{-j\omega t}dt$ is given as

$$\Phi(\omega) = j\sqrt{2\pi}\omega e^{(-\frac{1}{2}\omega^2)}. \tag{2.10}$$

Figure 2.5 shows the spectrum of $\phi(t)$. It is clear that $\Phi(\omega)$ decays very quickly such that the value of $\Phi(\omega)$ at some ω is negligible. It also demonstrates that the total energy of

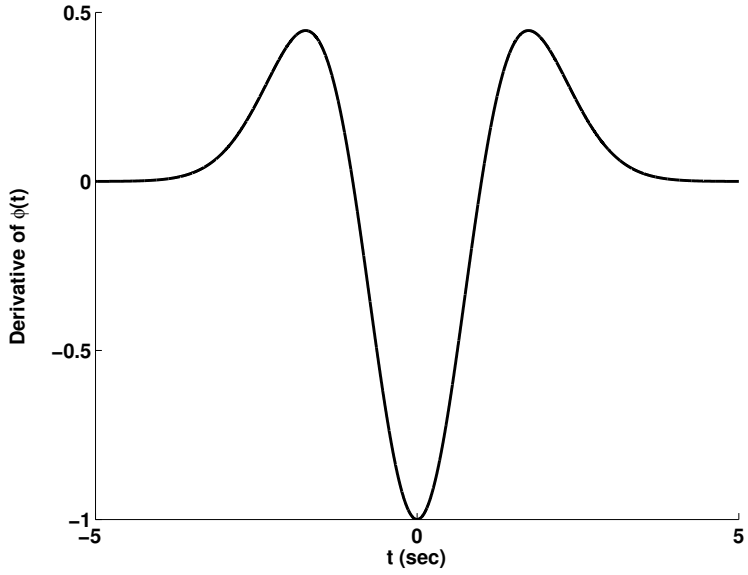

Figure 2.4: Waveform of the derivative of $\phi(t)$.

$\Phi(\omega)$ concentrates locally near zero.

Since the value of $\phi(t)$ is negligibly small as $|t|$ becomes large, $\phi(t)$ may be truncated at the range of $-D \leq t \leq D$ to obtain a time-limited version of $\phi(t)$, then shifted forward to make the start time equal to zero and end time equal to $2D$ as in (2.11).

$$g_\phi(t) = \begin{cases} \phi(t-D), & \text{if } 0 \leq t \leq 2D; \\ 0, & \text{otherwise.} \end{cases} \tag{2.11}$$

Figure 2.6 shows the $g_\phi(t)$ and $\phi(t)$ waveforms for $D = 5$. Referring to Figure 1.3, $g_\phi(t)$ can be used as an acceleration candidate for a double integrator system. To guarantee the position constraint, a constant gain K must be multiplied by the waveform of $g_\phi(t)$. Since $\phi(t)$ decays rapidly as t increases, the energy distribution of $g_\phi(t)$, which is the shifted time-limited version of $\phi(t)$, approaches the energy distribution of $\phi(t)$. So, if the resonance frequencies of the flexible structure are located at the region where the spectrum of $g_\phi(t)$ is negligibly small, $g_\phi(t)$ can suppress residual vibrations of the flexible system. In this case, most of the energy of $g_\phi(t)$ concentrates before the first resonance frequency, so it can suppress the residual vibration caused by all the resonance modes.

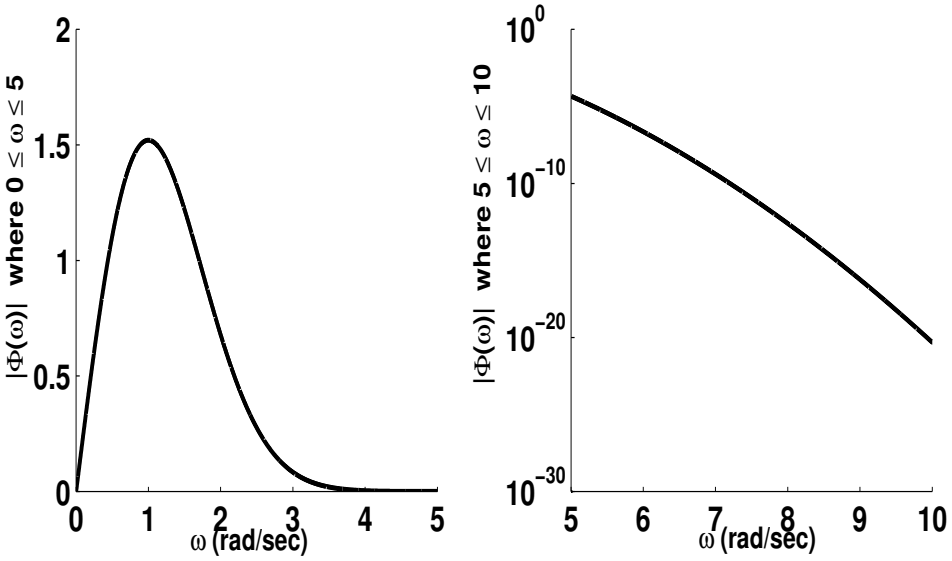

Figure 2.5: Spectrum magnitude of $\phi(t)$.

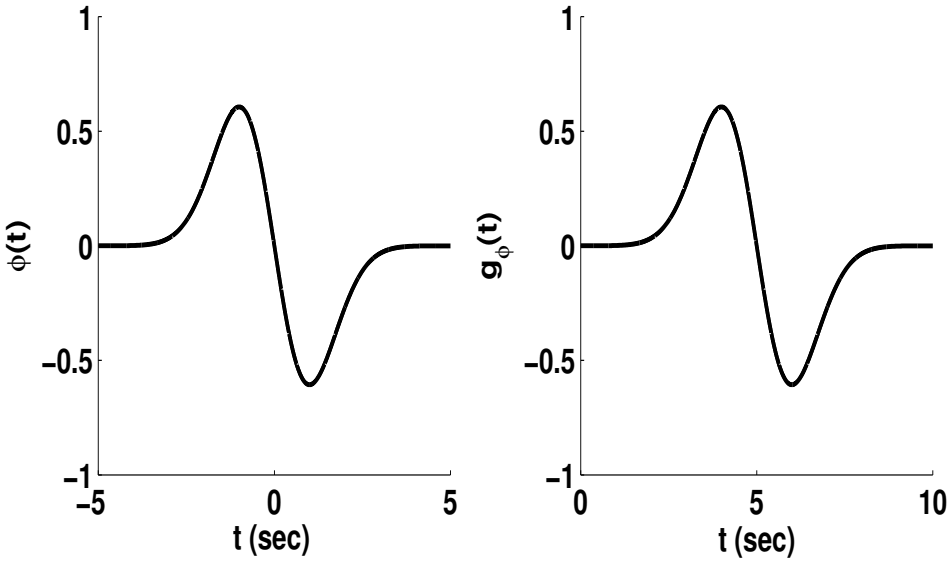

Figure 2.6: $\phi(t)$ and $g_\phi(t)$ (shifted time-limited version of $\phi(t)$).

2.2 Robust Vibration Suppression Control Profile Design

Considering the similar waveforms of $\phi(t)$ but with a different time localization and frequency localization, a scaled version of (2.8) may be introduced as

$$\phi_n(t) = -te^{(-\frac{1}{2}2^{(2n)}t^2)}, \tag{2.12}$$

where n is a real number. When $n = 0$, (2.12) reduces to (2.8).

Note the following properties of $\phi_n(t)$: the maximum of $\phi_n(t)$ is $\frac{e^{-1/2}}{2^n}$, which is achieved at time $-\frac{1}{2^n}$; the minimum of $\phi_n(t)$ is $-\frac{e^{-1/2}}{2^n}$, which is achieved at $t_m = \frac{1}{2^n}$. So, as n increases, the waveform of $\phi_n(t)$ narrows down to near zero, and the absolute value of $\phi_n(t)$ decreases. As n decreases, the waveform of $\phi_n(t)$ becomes wide and the absolute value of peak of $\phi_n(t)$ increases.

The Fourier transform $\Phi_n(\omega) = \int_{-\infty}^{\infty} \phi_n(t)e^{-j\omega t}dt$ is given as

$$\Phi_n(\omega) = \frac{j\sqrt{2\pi}\omega e^{(-\frac{1}{2}\frac{\omega^2}{2^{(2n)}})}}{2^{(3n)}}. \tag{2.13}$$

Note the following properties of $\Phi_n(\omega)$: the maximum of $|\Phi_n(\omega)|$ is $\frac{\sqrt{2\pi}e^{-1/2}}{2^{(2n)}}$, which is achieved at $\omega_m = 2^n$. As n increases, the waveform of $\Phi_n(\omega)$ becomes wide and the maximum of $|\Phi_n(\omega)|$ decreases. As n decreases, the waveform of $\Phi_n(\omega)$ becomes narrow and the maximum of $|\Phi_n(\omega)|$ increases.

Since $t_m\omega_m = 1$ holds, t_m and ω_m cannot be decreased or increased simultaneously. To demonstrate this characteristic and see how the waveforms of $\phi_n(t)$ and $\Phi_n(\omega)$ change with n, the waveforms of $\phi_5(t)$ and $|\Phi_5(\omega)|$ are plotted in Figure 2.7, and the waveforms of $\phi_{-5}(t)$ and $|\Phi_{-5}(\omega)|$ are plotted in Figure 2.8.

Since the value of $\phi_n(t)$ become negligibly small as $|t|$ becomes large, $\phi_n(t)$ may be truncated at the range of $-D \leq t \leq D$ to obtain a time-limited version of $\phi_n(t)$, then shifted forward the waveform to make the start time equal to zero and end time equal to

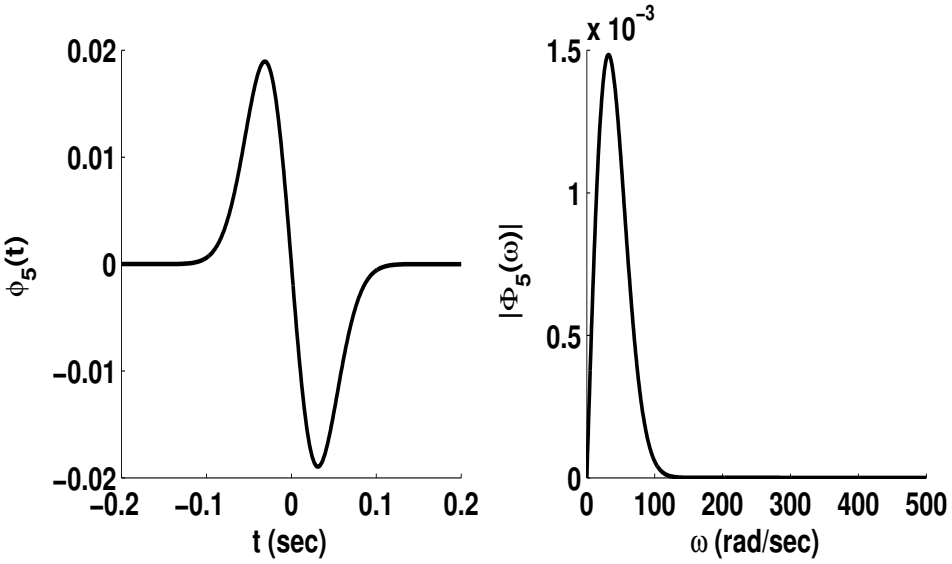

Figure 2.7: Waveforms of $\phi_5(t)$ and its spectrum magnitude.

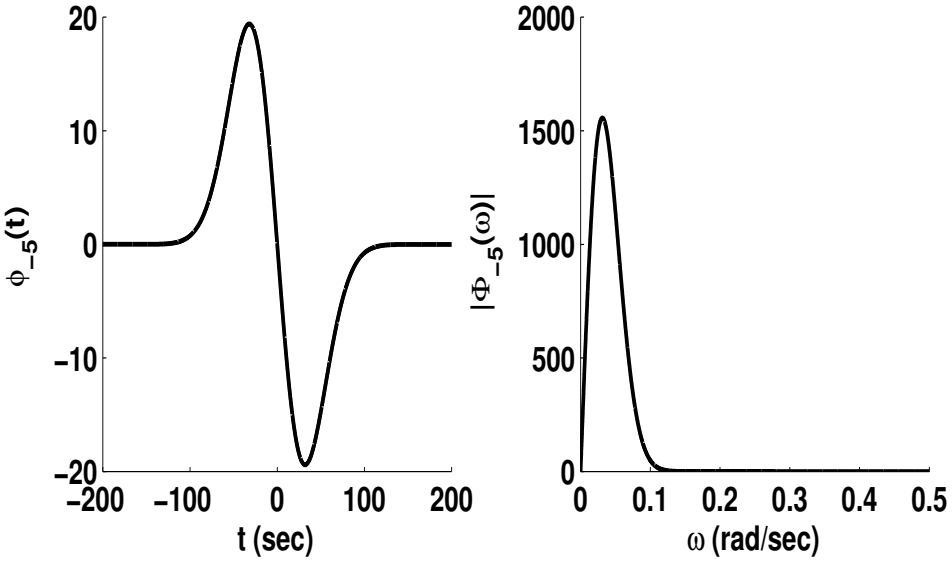

Figure 2.8: Waveforms of $\phi_{-5}(t)$ and its spectrum magnitude.

$2D$ as in (2.14).

$$g_{\phi,n}(t) = \begin{cases} \phi_n(t-D), & \text{if } 0 \le t \le 2D; \\ 0, & \text{otherwise.} \end{cases} \tag{2.14}$$

So, $g_{\phi,n}(t)$ can be used as an acceleration profile candidate for a double integrator system. To guarantee the position constraint, a constant gain K must be multiplied by the waveform $g_{\phi,n}(t)$. Since $\phi_n(t)$ decays rapidly as t increases, the energy distribution of $g_{\phi,n}(t)$, which is the shifted, time-limited version of $\phi_n(t)$ nears the energy distribution of $\phi_n(t)$. So, if the resonance frequencies of the flexible structure are located in the region where the spectrum of $g_{\phi,n}(t)$ is negligibly small, then $g_{\phi,n}(t)$ cannot induce the residual vibration of the flexible system. In this case, most of the energy of $g_{\phi,n}(t)$ concentrates before the first resonance frequency, so it can minimize the residual vibration caused by all the resonance modes.

The Fourier transform of the truncated version of $\phi_n(t)$ is very hard to calculate even though $\Phi_n(\omega)$ is very easy to calculate. Continuous-time Fourier transform $G_{\phi,n}(\omega)$ involves the complex error function, which though is not elaborated on here. In the following analysis, the discrete-time Fourier transform (see Appendix A) may be used instead of the continuous-time Fourier transform.

Now the discrete-time version of (2.14) is derived. If the sampling period is T_s sec and the total discrete-time sequence has $M+1$ impulses,

$$g_{\phi,n}[k] = \begin{cases} \phi_n((k-\frac{M}{2})T_s), & \text{if } 0 \le k \le M; \\ 0, & \text{otherwise.} \end{cases} \tag{2.15}$$

So the discrete-time sequence $g_{\phi,n}[k], 0 \le k \le M$, is antisymmetric, and $\frac{M}{2}$ is the center of symmetry. Figure 2.9 shows the waveform of $g_{\phi,0}[k], 0 \le k \le M$ with $T_s = 0.5$ and $M = 20$. Figure 2.10 shows the waveform of $g_{\phi,0}[k], 0 \le k \le M$ with $T_s = 0.5$ and $M = 21$.

When M is even, the discrete-time Fourier transform $G_{\phi,n}(\omega) = \sum_{k=-\infty}^{\infty} g_{\phi,n}[k]e^{-j\omega k}$

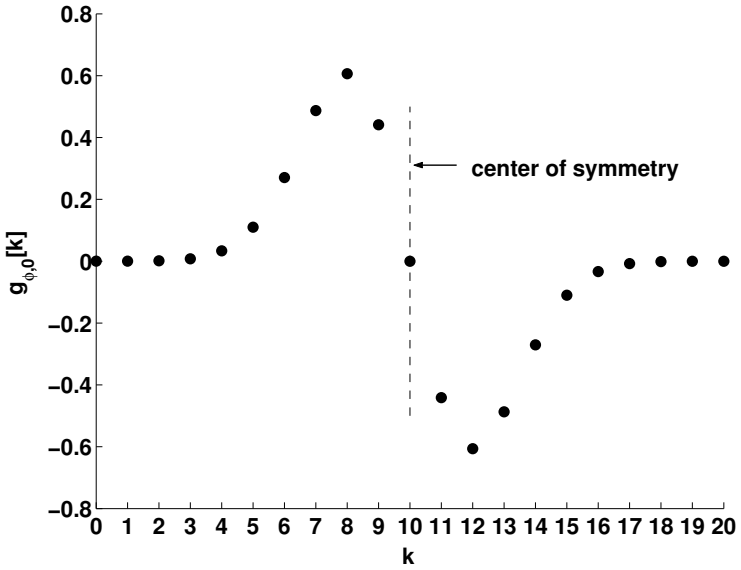

Figure 2.9: Waveform of $g_{\phi,0}[k]$ with $T_s = 0.5$ and $M = 20$.

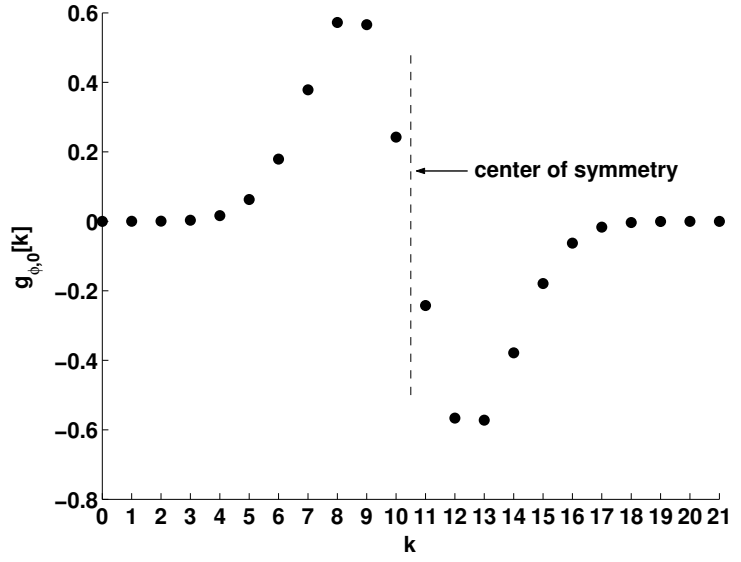

Figure 2.10: Waveform of $g_{\phi,0}[k]$ with $T_s = 0.5$ and $M = 21$.

$= \sum_{k=0}^{M} g_{\phi,n}[k]e^{-j\omega k}$ can be computed as [60]

$$G_{\phi,n}(\omega) = je^{-j\omega M/2}\left[\sum_{k=1}^{M/2} 2g_{\phi,n}[M/2-k]\sin(\omega k)\right], \tag{2.16}$$

$$= je^{-j\omega M/2}\left[2\sum_{k=1}^{M/2} \phi_n(-kT_s)\sin(\omega k)\right]. \tag{2.17}$$

The magnitude of $G_{\phi,n}(\omega)$ for even M is

$$|G_{\phi,n}(\omega)| = \left|2\sum_{k=1}^{M/2} \phi_n(-kT_s)\sin(\omega k)\right|. \tag{2.18}$$

When M is odd, the discrete-time Fourier transform $G_{\phi,n}(\omega) = \sum_{k=-\infty}^{\infty} g_{\phi,n}[k]e^{-j\omega k}$ $= \sum_{k=0}^{M} g_{\phi,n}[k]e^{-j\omega k}$ can be computed as [60]

$$G_{\phi,n}(\omega) = je^{-j\omega M/2}\left[\sum_{k=1}^{(M+1)/2} 2g_{\phi,n}[(M+1)/2-k]\sin(\omega(k-1/2))\right], \tag{2.19}$$

$$= je^{-j\omega M/2}\left[2\sum_{k=1}^{(M+1)/2} \phi_n((\frac{1}{2}-k)T_s)\sin(\omega(k-1/2))\right]. \tag{2.20}$$

The magnitude of $G_{\phi,n}(\omega)$ for odd M is

$$|G_{\phi,n}(\omega)| = \left|2\sum_{k=1}^{(M+1)/2} \phi_n((\frac{1}{2}-k)T_s)\sin(\omega(k-1/2))\right|. \tag{2.21}$$

In contrast to the continuous-time Fourier transform of $g_{\phi,n}(t)$, the discrete-time Fourier transform of $g_{\phi,n}[k]$ can be easily calculated.

Given a fixed move time, the acceleration profile can be determined after choosing the scaling parameter n. The value of n can be optimized from the characteristics of the uncertain resonance structure. From the Bode magnitude plot of the resonance structure, the first resonance frequency can be located to be Ω_0 rad/sec. The following objective can be defined in terms of $\omega_0 = \Omega_0 T_s$, where T_s is the sampling period in seconds.

$$J = \frac{\int_0^{\omega_0} |G_{\phi,n}(\omega)|^2 d\omega}{\int_0^{\pi} |G_{\phi,n}(\omega)|^2 d\omega} \tag{2.22}$$

or

$$1 - J = \frac{\int_0^{\pi} |G_{\phi,n}(\omega)|^2 d\omega - \int_0^{\omega_0} |G_{\phi,n}(\omega)|^2 d\omega}{\int_0^{\pi} |G_{\phi,n}(\omega)|^2 d\omega}. \tag{2.23}$$

The following optimization problem can be used to determine the optimal value of n.

$$\max_n J \text{ or } \min_n (1 - J) \tag{2.24}$$

Physically, the objectives imply that the best waveform of $g_{\phi,n}[k]$ maximizes the proportion of its energy before the first resonance frequency, or minimizes the proportion of its energy after the first resonance frequency, according to an arbitrary move time. For engineering applications, the integral in (2.24) can be easily approximated by the cumulative summation of the element $|G_{\phi,n}(\omega)|^2$. So without any optimization algorithm, the optimal n can be approximated from the plot of J or $1 - J$ (2.24) in terms of n.

Bayo [9, 8] and Singer [71] have studied Gaussian function to generate a continuous-time open-loop driving function for a flexible manipulator. However, in their studies, the Gaussian function profile or the derivative of the Gaussian function are simply made to start at a small number in the time domain. The tradeoff between the move time and energy concentration of the control profile in the frequency domain is not studied in their work. Furthermore, robust vibration suppression shape filter and closed-loop control using Gaussian functions are also studied in this chapter.

2.3 Simulation Results for Hard Disk Drive Seek Control

Consider the following flexible system which is embedded in a hard disk assembly, where the input is the current signal in amps and the output is the position signal in tracks.

$$H(s) = K_c \cdot K_v \cdot K_p \cdot R(s) \frac{1}{s^2}, \tag{2.25}$$

here $K_c = 1.3 \ \frac{\text{tracks/sample}^2}{\text{amp}}$ is a constant gain from current to acceleration, $K_v = 5 \times 10^4 \ \frac{\text{samples}}{\text{sec}}$ is the velocity gain, $K_p = 5 \times 10^4 \ \frac{\text{samples}}{\text{sec}}$ is the position gain, and $R(s)$ is a 28^{th} order resonance structure. The Bode magnitude plot of $R(s)$ is shown in Figure 1.2.

Figure 2.11 shows the change of the objective $1-J$ with n for $\Omega_0 = 9.68 \times 10^3$ rad/sec, $T_s = 2 \times 10^{-5}$ sec and the move time is 5×10^{-3} sec. It is observed that the objective is very insensitive to the optimal n. Figure 2.12 shows the same information as Figure 2.11 with a log scale of the Y axis. In this case, optimal n was found to be about 10.93.

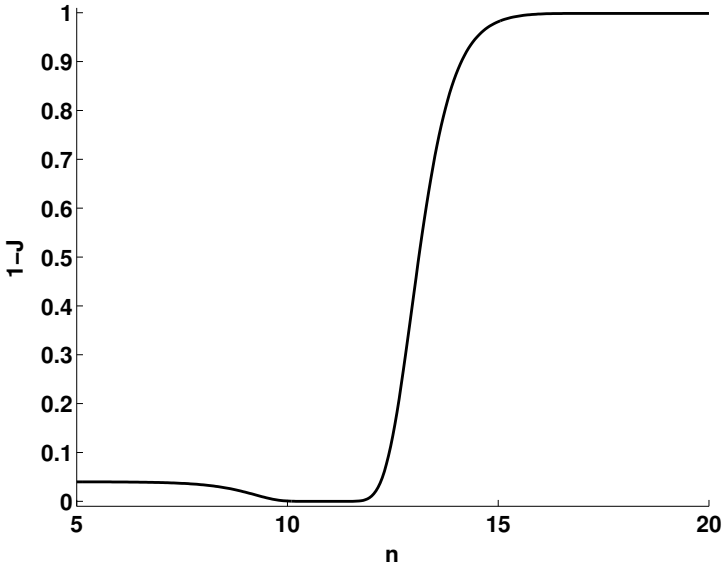

Figure 2.11: The change of $1 - J$ (linear scale) with n.

With the optimal value of n computed, the current signal for a 100 tracks seek can then be calculated. Figure 2.13 shows the current signal. Figure 2.14 shows the jerk signal which is the derivative of the current signal. Figure 2.15 shows the position signal. Figure 2.16 shows the position signal near the target track. To see the residual vibration, the position error signal, which is defined as the position output difference between $H(s)$ in (5.26) and the reference model $H_{ref}(s)$ can be plotted, where $H_{ref}(s)$ is defined as

$$H_{ref}(s) = K_c \cdot K_v \cdot K_p \frac{1}{s^2}. \tag{2.26}$$

Figure 2.17 shows that the position signal settles within $\pm\frac{1}{1000}$ track before the move time of 5×10^{-3} sec. So, the current signal suppresses the residual vibration induced by all the resonance modes.

Next, the current signal will be analyzed from the filter point of view. Figure 2.18

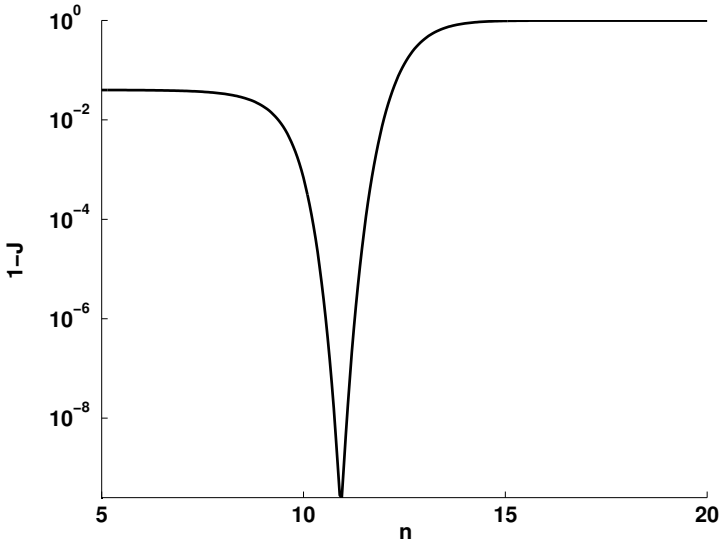

Figure 2.12: The change of $1 - J$ (log scale) with n.

shows the reference velocity signal which is the integral of the acceleration signal. This signal is considered as the impulse response of a Finite Impulse Response (FIR) filter. The magnitude of the frequency response of this FIR filter is shown in Figure 2.19. It is clear that this FIR filter has a very good cutoff of high frequency signals.

Finally, the move time is reduced to 2.5×10^{-3} sec and the control input signal is designed again. The optimal value of n is calculated approximately to be 11.41. Figure 2.20 shows the current signal. Figure 2.21 shows the jerk signal which is the derivative of the current signal. Figure 2.22 shows the position signal. Figure 2.23 shows the position error signal. Figure 2.24 shows the position signal near the target track. It shows that the position signal settles within $\pm\frac{5}{100}$ track immediately after the move time which is 2.5×10^{-3} sec. So, the current signal suppresses the residual vibration induced by all the resonance modes. Figure 2.25 shows the reference velocity signal. As before this signal is considered as the impulse response of an FIR filter. The magnitude of the frequency response of this FIR filter is shown in Figure 2.26. Again this FIR filter has a very good cutoff of high frequency signals, although the magnitudes at high frequencies are somewhat larger than those of Figure 2.19.

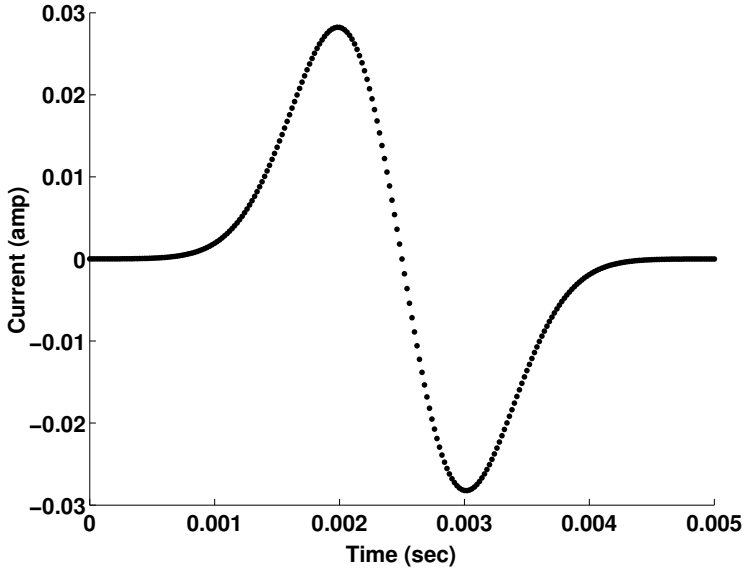

Figure 2.13: Current control input signal for 5 msec move.

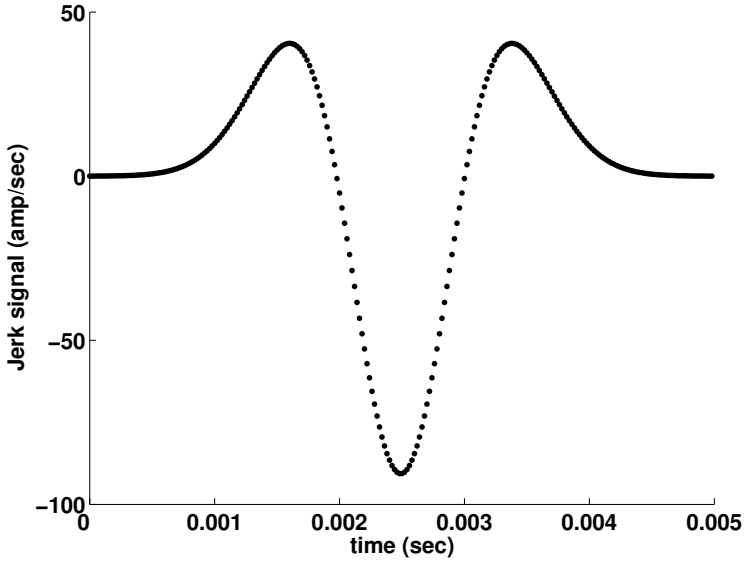

Figure 2.14: Jerk signal for 5 msec move.

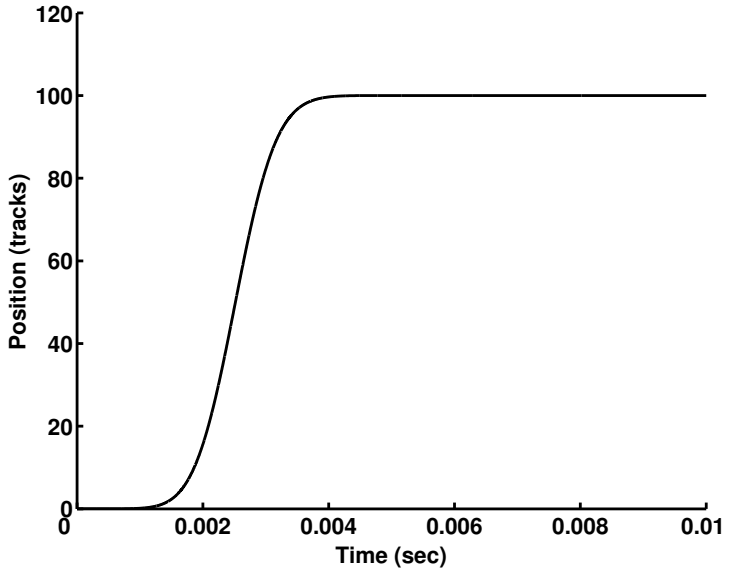

Figure 2.15: Position signal for 5 msec move.

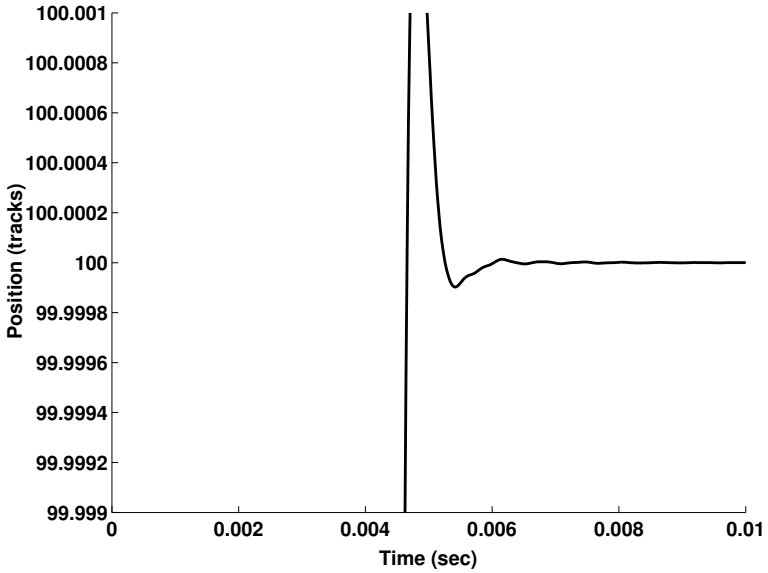

Figure 2.16: Position signal near the target for 5 msec move.

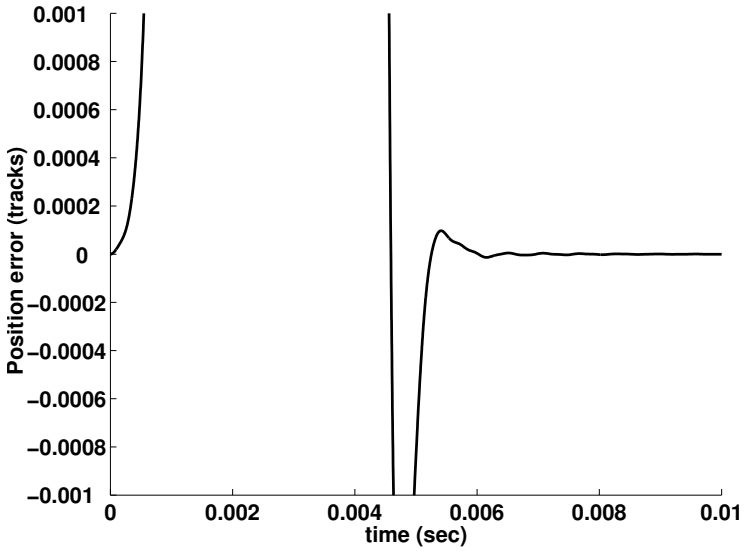

Figure 2.17: Position error signal for 5 msec move.

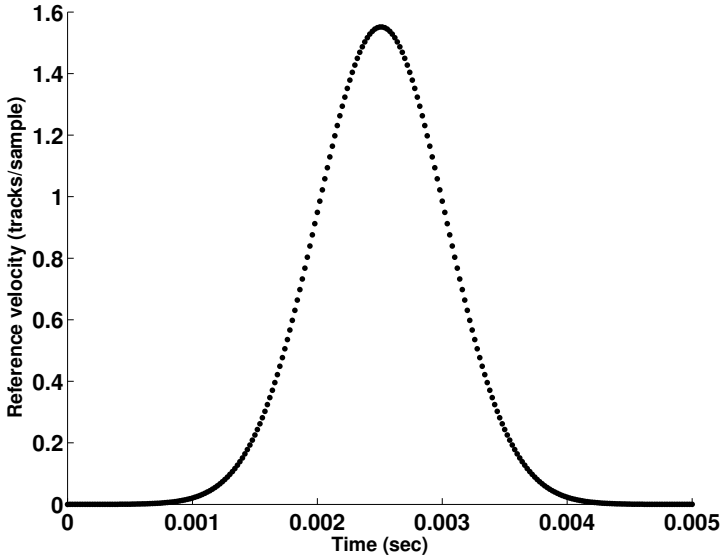

Figure 2.18: Reference velocity signal for 5 msec move.

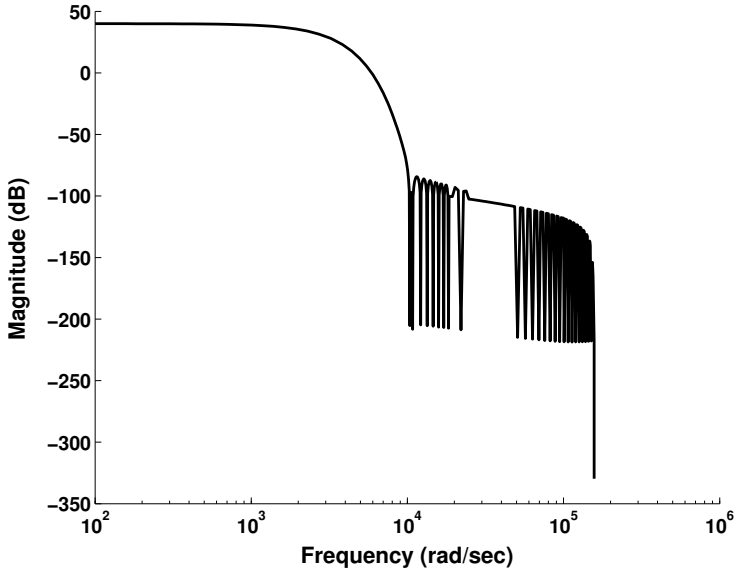

Figure 2.19: Frequency response of the FIR filter for 5 msec move.

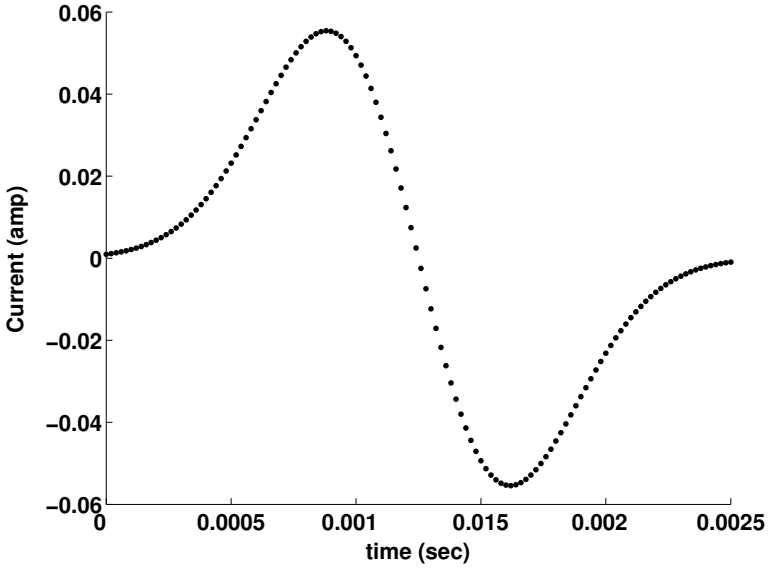

Figure 2.20: Current control input signal for 2.5 msec move.

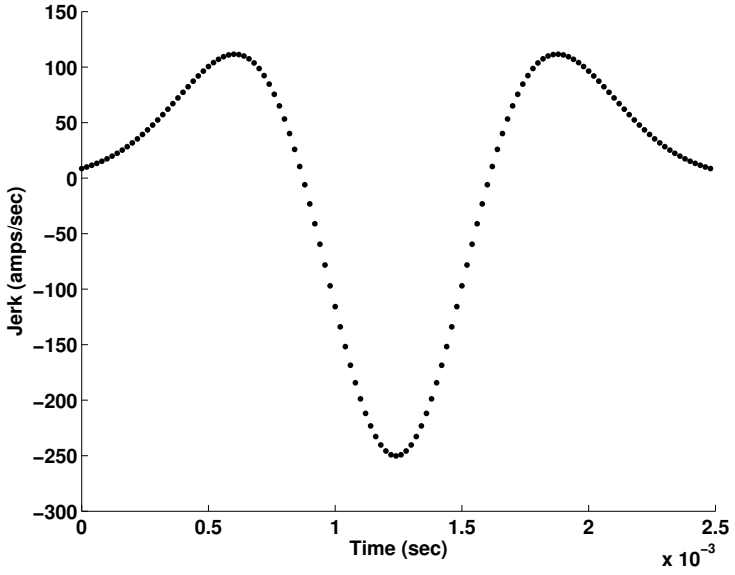

Figure 2.21: Jerk signal for 2.5 msec move.

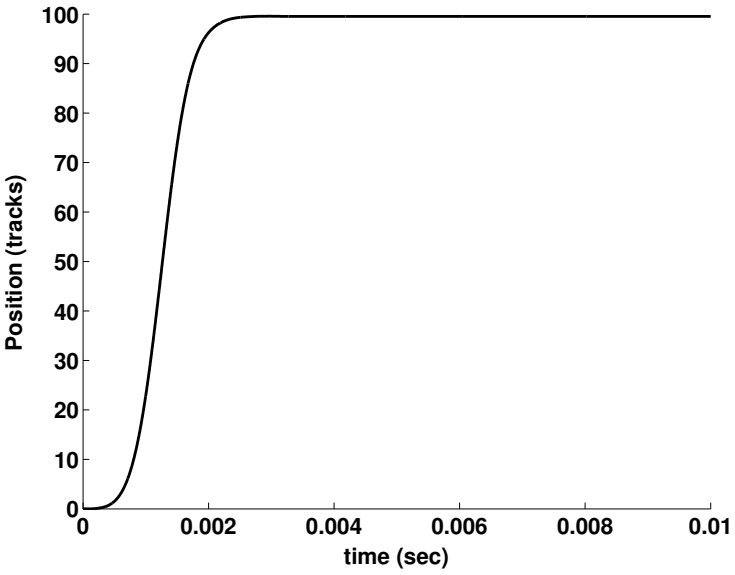

Figure 2.22: Position signal for 2.5 msec move.

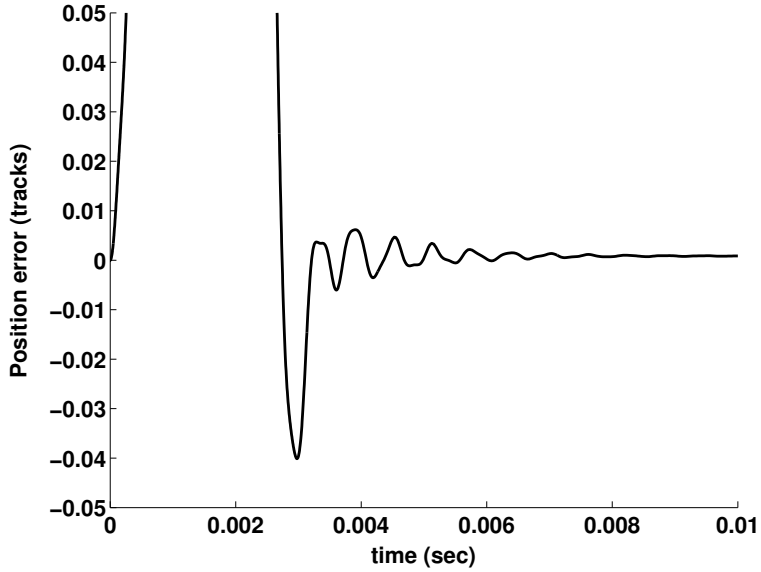

Figure 2.23: Position error signal for 2.5 msec move.

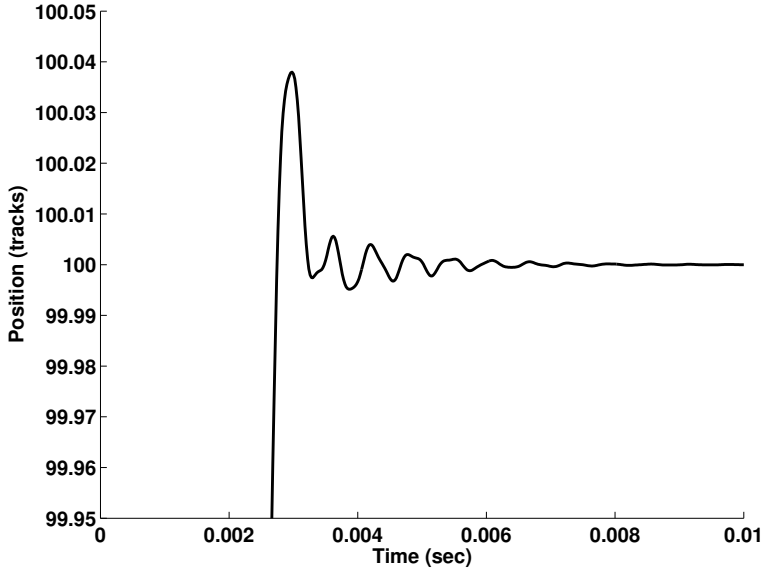

Figure 2.24: Position signal near the target track for 2.5 msec move.

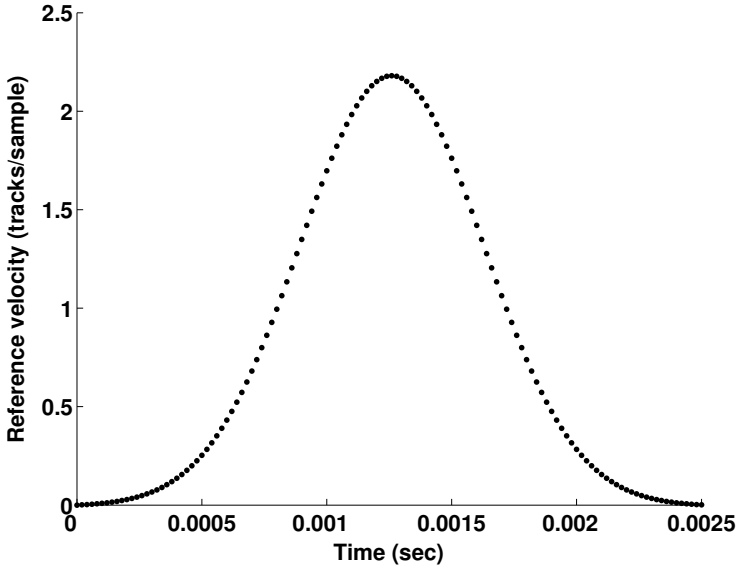

Figure 2.25: Reference velocity signal for 2.5 msec move.

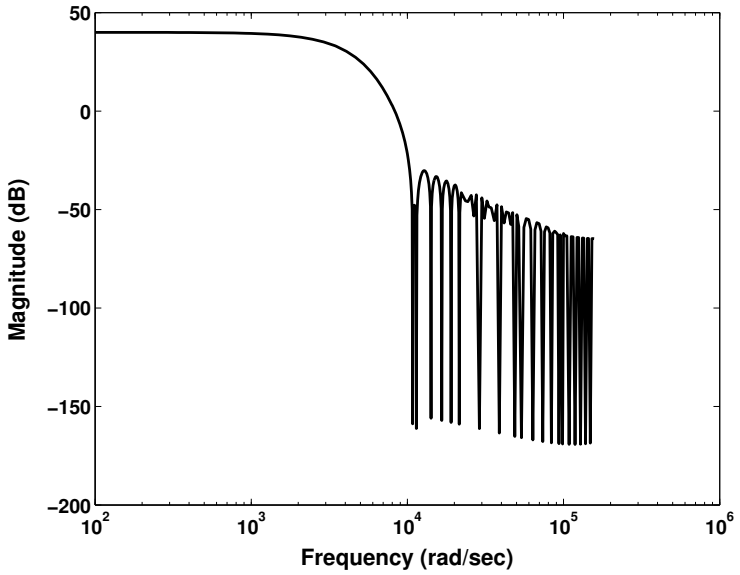

Figure 2.26: Frequency response of the FIR filter for 2.5 msec move.

It must be pointed out that the control input move time cannot be arbitrarily reduced if a certain settling time is required. It depends on the resonance characteristics. As shown before, a signal cannot arbitrarily achieve both time and frequency localization. Reducing move time will result a poor frequency concentration. Figure 2.27 shows the concentration $1 - J$ defined in (2.23) with different move time for the same sampling period and first resonance frequency given before. From Figure 2.27, if the move time of the control input is chosen to be 0.5 msec, the minimal proportion of its energy after the first resonance is about 0.45 which is very poor. There is a tradeoff between the move time of a control input and its concentration in the frequency domain as shown in Figure 2.27.

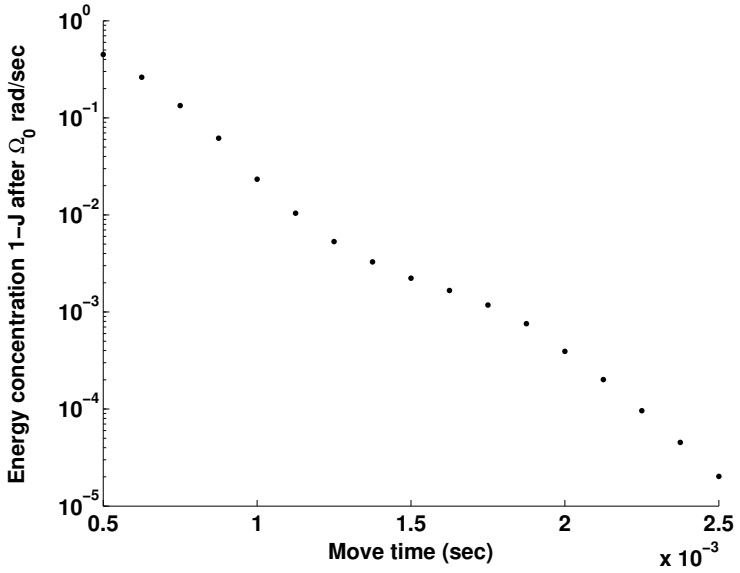

Figure 2.27: Concentration $1 - J$ with different move time.

2.4 Robust Vibration Suppression Shape Filter Generation Based on Time-Frequency Uncertainty

From the previous section, a robust acceleration profile is generated. A robust velocity profile with initial value of zero can be generated from the robust acceleration profile.

The resultant velocity profile starts and ends at zero values. As shown in Chapter 1, the normalized velocity profile function can be used as a shape filter. In this section, a vibration suppression shape filter is directly generated from Gaussian functions that can optimally achieve the time-frequency localization in the sense of Heisenberg uncertainty.

A scaled version of the simple Gaussian function in (2.7) may be introduced as

$$h_n(t) = e^{-\frac{1}{2}2^{2n}t^2}. \tag{2.27}$$

Since the value of $h_n(t)$ is negligibly small as $|t|$ becomes large, $h_n(t)$ may be truncated at the range of $-D \leq t \leq D$ to obtain a time-limited version of $h_n(t)$ then shifted forward to make the start time equal to zero and the end time equal to $2D$ as in (2.28),

$$g_{h,n}(t) = \begin{cases} h_n(t-D), & \text{if } 0 \leq t \leq 2D; \\ 0, & \text{otherwise.} \end{cases} \tag{2.28}$$

The discrete-time version of (2.28) is derived. If the sampling period is T_s sec and the total discrete-time sequence has $M+1$ impulses,

$$g_{h,n}[k] = \begin{cases} h_n((k-\frac{M}{2})T_s), & \text{if } 0 \leq k \leq M; \\ 0, & \text{otherwise.} \end{cases} \tag{2.29}$$

So the discrete-time sequence $g_{h,n}[k]$, $k = 0, 1, \ldots, M$, is symmetric and $\frac{M}{2}$ is the center of symmetry.

When M is an even integer, the discrete-time Fourier transform $G_{h,n}(\omega) = \sum_{k=-\infty}^{\infty} g_{h,n}[k]e^{-j\omega k}$ $= \sum_{k=0}^{M} g_{h,n}[k]e^{-j\omega k}$ can be computed as [60]

$$G_{h,n}(\omega) = e^{-j\omega M/2}\left[\sum_{k=0}^{M/2} a[k]\cos(\omega k)\right], \tag{2.30}$$

where

$$a[0] = g_{h,n}[M/2], \tag{2.31}$$

$$a[k] = 2g_{h,n}[M/2-k], \quad k = 1, 2, \cdots, M/2. \tag{2.32}$$

The magnitude of $G_{h,n}(\omega)$ for even M is

$$|G_{h,n}(\omega)| = \left| \sum_{k=0}^{M/2} a[k] \cos(\omega k) \right|. \tag{2.33}$$

When M is odd, the discrete-time Fourier transform $G_{h,n}(\omega) = \sum_{k=-\infty}^{\infty} g_{h,n}[k] e^{-j\omega k}$ $= \sum_{k=0}^{M} g_{h,n}[k] e^{-j\omega k}$ can be computed as [60]

$$G_{h,n}(\omega) = e^{-j\omega M/2} \left[\sum_{k=1}^{(M+1)/2} b[k] \cos(\omega(k - \frac{1}{2})) \right], \tag{2.34}$$

where

$$b[k] = 2g_{h,n}[(M+1)/2 - k], \quad k = 1, 2, \cdots, \frac{M+1}{2}. \tag{2.35}$$

The magnitude of $G_{h,n}(\omega)$ for odd M is

$$|G_{h,n}(\omega)| = \left| \sum_{k=1}^{(M+1)/2} b[k] \cos(\omega(k - \frac{1}{2})) \right|. \tag{2.36}$$

Given a fixed time duration of the vibration suppression shape filter profile in (2.29), the shape filter profile can be determined after choosing the scaling parameter n. The value of n can be computed from the characteristics of the uncertain resonance structure. From the Bode magnitude plot of the resonance structure, the first resonance frequency can be located to be Ω_0 rad/sec. The following objective can be defined in terms of $\omega_0 = \Omega_0 T_s$, where T_s is the sampling period in seconds.

$$J = \frac{\int_0^{\omega_0} |G_{h,n}(\omega)|^2 d\omega}{\int_0^{\pi} |G_{h,n}(\omega)|^2 d\omega} \tag{2.37}$$

or

$$1 - J = \frac{\int_0^{\pi} |G_{h,n}(\omega)|^2 d\omega - \int_0^{\omega_0} |G_{h,n}(\omega)|^2 d\omega}{\int_0^{\pi} |G_{h,n}(\omega)|^2 d\omega}. \tag{2.38}$$

The following optimization problem can be used to determine the optimal value of n.

$$\max_n J \text{ or } \min_n (1 - J) \tag{2.39}$$

Physically, the objectives imply that the best waveform of $g_{h,n}[k]$ maximizes the proportion of its energy before the first resonance frequency Ω_0, or minimizes the proportion of its energy after the first resonance frequency Ω_0, according to an arbitrary move time. For engineering applications, the integral in (2.39) can be easily approximated by the cumulative summation of the element $|G_{h,n}(\omega)|^2$. So without any optimization algorithm, the optimal n can be approximated from the plot of J or $1-J$ of (2.39) in terms of n. After the optimal profile $g_{h,n}[k]$, $0 \leq k \leq M$, is derived, the following normalization can be processed to make the sum of the $M+1$ impulses of a vibration suppression shape filter to be 1.

$$f[k] = \begin{cases} \frac{g_{h,n}[k]}{\sum_{m=0}^{M} g_{h,n}[m]}, & \text{if } 0 \leq k \leq M; \\ 0, & \text{otherwise.} \end{cases} \tag{2.40}$$

Notice that the initial and final values of the sequence $g_{h,n}[k], 0 \leq k \leq M$, are not zero, so it cannot be directly used as a robust vibration suppression velocity profile to realize a rigid body movement from one set point to another. Since the sequence $g_{h,n}[k]$ decays sharply at the start and end points, it can be vertically shifted down to make the start and end values to be zero as in (2.41),

$$vel[k] = g_{h,n}[k] - g_{h,n}[0], \quad 0 \leq k \leq M. \tag{2.41}$$

Notice that $g_{h,n}[0] = g_{h,n}[M]$ because the sequence is a symmetric function. The sequence $vel[k], 0 \leq k \leq M$, can be used as a velocity profile. Depending on the rigid body position movement, the velocity must be multiplied with a constant. The discrete-time sequence of the acceleration profile $acc[k]$ can be generated from the discrete-time sequence of the velocity profile $vel[k]$ by

$$acc[k] = \frac{vel[k+1] - vel[k]}{T_s}, \tag{2.42}$$

where T_s is the sampling period. Depending on the rigid body position movement, the acceleration profile must be multiplied with a constant.

Remark 2.1 *The method to generate the robust vibration suppression acceleration profile in (2.42) is different from the method to generate the robust vibration suppression acceleration profile in Section 2.2. In Section 2.2, the acceleration profile is generated from the shifted time-limited discrete-time sequence of the derivative of Gaussian function. In this section, a shifted time-limited discrete-time sequence of the Gaussian function is firstly generated. This discrete-time sequence $g_{h,n}[k]$ in (2.29) is used to generate a robust vibration suppression shape filter or a robust vibration suppression velocity profile. The time differencing of the velocity profile in (2.41) is exactly a robust vibration suppression acceleration profile. From numerical computation, it is known that the two acceleration profiles are almost the same because the optimal scale parameters are approximately the same in both cases.*

2.5 Optimal Scale Parameter n Computation from a Scalar Bounded Nonlinear Function Miminization Problem

The calculation of the optimal scale parameter n in Section 2.2 and Section 2.4 can also be reduced to a scalar bounded nonlinear function minimization problem. So the Matlab routine *fminbnd* in the Optimization Toolbox can be used to find the optimal scale parameter n very quickly.

Consider again the objective and the optimization problem in Section 2.2 and Section 2.4,

$$J = \frac{\int_0^{\omega_0} |G_n(\omega)|^2 d\omega}{\int_0^{\pi} |G_n(\omega)|^2 d\omega} \tag{2.43}$$

and

$$\min_n (1 - J), \tag{2.44}$$

where $G_n(\omega)$ is the discrete-time Fourier transform of the sequence $g_n[k]$. $g_n[k] = g_{\phi,n}[k]$ is the shifted time-limited discrete-time sequence of the derivative of Gaussian function in Section 2.2 or $g_n[k] = g_{h,n}[k]$ is the shifted time-limited discrete-time sequence of the Gaussian function in Section 2.4.

First, the energy of the discrete-time sequence $g_n[k]$, $k = 0, 1, \ldots, M$, in the frequency interval $[0, \omega_0]$, i.e. $\frac{1}{2\pi}\int_0^{\omega_0} |G_n(\omega)|^2 d\omega$, can be approximated from the cumulative summation of the element $|G_n(\omega)|^2$, where $G_n(\omega)$ is a continuous function of n and ω. The interval $[0, \omega_0]$ can be divided into m subintervals, $[x_0, x_1], [x_1, x_2], \ldots, [x_{m-1}, x_m]$, each of length $\Delta\omega = \omega_0/m$. So $x_i = 0 + i\Delta\omega$, $i = 0, 1, \ldots, m-1$. The energy of $G_n(\omega)$ in the frequency interval $[0, \omega_0]$ can be written as

$$\frac{1}{2\pi}\int_0^{\omega_0} |G_n(\omega)|^2 d\omega \approx \frac{1}{2\pi}\left[|G_n(x_1^*)|^2\Delta\omega + |G_n(x_2^*)|^2\Delta\omega \cdots + |G_n(x_m^*)|^2\Delta\omega\right], \quad (2.45)$$

$$\approx \frac{1}{2\pi}\sum_{i=1}^{m} |G_n(x_i^*)|^2\Delta\omega, \quad (2.46)$$

where x_i^* is a sample point in the interval $[x_i, x_{i+1}]$. For example, x_i^* can be chosen to be x_i, or x_{i+1}, or the middle point of the interval $\frac{x_i + x_{i+1}}{2}$.

The energy of the discrete-time sequence $g_n[k]$ in the frequency interval $[0, \pi]$, i.e. $\frac{1}{2\pi}\int_0^{\pi} |G_n(\omega)|^2 d\omega$, can also be approximated in a similar way.

Another simple way to calculate $\frac{1}{2\pi}\int_0^{\pi} |G_n(\omega)|^2 d\omega$ is discussed here. Since $\frac{1}{2\pi}\int_{-\pi}^{\pi} |G_n(\omega)|^2 d\omega$ is the total energy of the discrete-time sequence $g_n[k]$, from Parseval's theorem

$$\frac{1}{2\pi}\int_{-\pi}^{\pi} |G_n(\omega)|^2 d\omega = \sum_{k=0}^{M} |g_n[k]|^2, \quad (2.47)$$

the following equation holds

$$\frac{1}{2\pi}\int_{0}^{\pi} |G_n(\omega)|^2 d\omega = \frac{1}{2}\sum_{k=0}^{M} |g_n[k]|^2. \quad (2.48)$$

The above equation is derived from the fact that $|G_n(\omega)|$ is an even function of ω for the real sequence $g_n[k]$.

So the energy concentration $1 - J$ is reduced to a function of one variable n. The calculation of optimal n is to find a minimum of a function of one variable on a fixed

interval

$$\min_{n}(1 - J(n)) \quad \text{such that } n_1 < n < n_2, \tag{2.49}$$

where n_1 and n_2 are scalars. The fixed numbers of n_1 and n_2 can be chosen from the plot of $(1-J)$ in terms of n. As n increases, $(1-J)$ approaches to 1 since the exponential term $e^{-\frac{1}{2}2^{2n}t^2}$ approaches to 0. As n decreases, $(1-J)$ approaches to a non zero constant since the exponential term $e^{-\frac{1}{2}2^{2n}t^2}$ approaches to 1.

Remark 2.2 *The algorithm fminbnd in Matlab is based on Golden Section search and parabolic interpolation. The detail of the algorithm can be found in [26].*

Remark 2.3 *The objective function J in (2.43) is the energy concentration of the sequence $g_n[k]$ in the frequency interval $[0, \omega_0]$ with respect to the energy in the frequency interval $[0, \pi]$. Since the Fourier transform of a real signal has conjugate symmetry, J can also be written as*

$$J = \frac{\int_0^{\omega_0} |G_n(\omega)|^2 d\omega}{\int_0^{\pi} |G_n(\omega)|^2 d\omega} = \frac{\int_{-\omega_0}^{\omega_0} |G_n(\omega)|^2 d\omega}{\int_{-\pi}^{\pi} |G_n(\omega)|^2 d\omega}, \tag{2.50}$$

i.e. the fraction of the energy in the frequency interval $[-\omega_0, \omega_0]$ with respect to the total energy. The direct calculation of the objective function J rather than evaluating the Fourier spectrum for arbitrary signal sequences is studied in Chapter 3.

2.6 Experimental Results on Flexible Link with Strain Gauge

2.6.1 Description

The photo [1] in Figure 2.28 shows the modular flexible link apparatus manufactured by Quanser Consulting, Inc. A strain gauge mounted at the base is calibrated to measure the

[1] The photo is adopted from Quanser Consulting, Inc.

deflection of the tip. The purpose of the experiment is to design a feedback system which reduces the oscillations of the tip while moving the tip to a desired position [68].

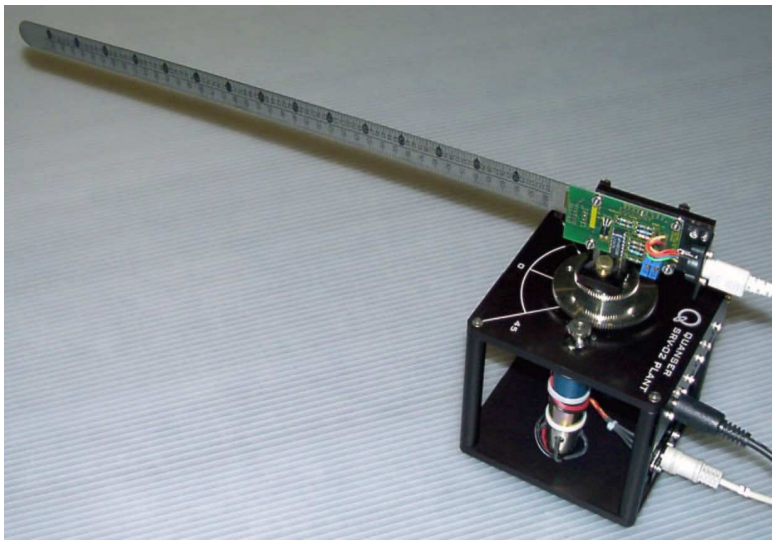

Figure 2.28: Quanser SRV02 plant with flexible link module.

2.6.2 Mathematical Model

The DC servo motor dynamics are shown in Figure 2.29. The input is the applied voltage V_a and the output is the link slew angle θ.

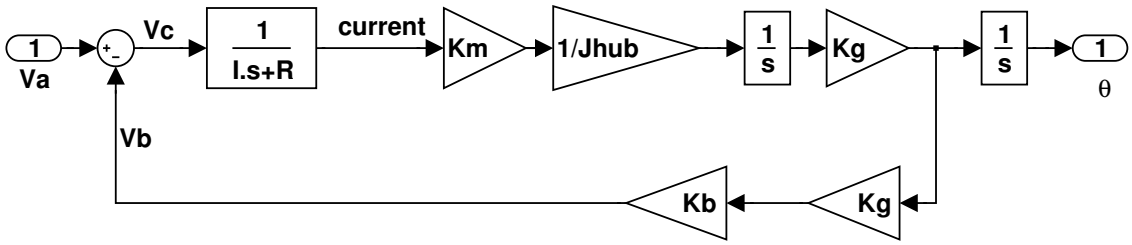

Figure 2.29: The DC servo motor dynamics.

The applied voltage is the sum of the control voltage V_c and the back-emf voltage V_b

$$V_a = V_c + V_b. \tag{2.51}$$

The control voltage in terms of motor current i is

$$V_c = Ri + I\frac{di}{dt}, \tag{2.52}$$

where I is the armature inductance and R is the armature resistance. The back-emf voltage in terms of the link slew angle velocity $\dot{\theta}$ is

$$V_b = K_g K_b \dot{\theta}, \tag{2.53}$$

where K_g is the gear ratio, and K_b is the back-emf constant.

A simplified model of the flexible link including the deflection of the tip is shown in Figure 2.30 [68]. A lumped parameter model for the system can be derived using the following simple method:

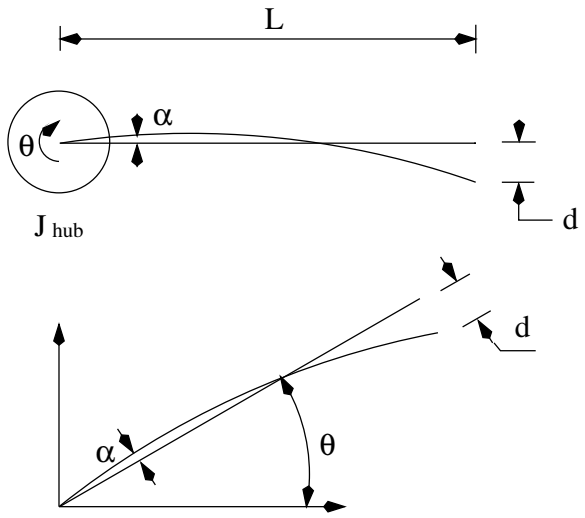

Figure 2.30: Simplified model of flexible link.

1) Obtain the natural frequency of the link with the base clamped. This is obtained experimentally to be $f_n \approx 3 - 4$ Hz. Then, the angular deflection of the tip with respect to the clamped frame is given by

$$\ddot{\alpha} = -\omega_n^2 \alpha, \tag{2.54}$$

where $\omega_n = 2\pi f_n$.

2) Estimate the stiffness of the clamped joint since the following equation holds

$$\omega_n = \sqrt{\frac{K_{stiff}}{J_{load}}} \quad \text{then} \quad K_{stiff} = (2\pi f_n)^2 J_{load}, \tag{2.55}$$

where J_{load} is the inertia of the link assuming a rigid body

$$J_{load} = \frac{1}{3} m_L L^2. \tag{2.56}$$

From Figure 2.30, the governing equation of the simplified model is given by

$$\ddot{\theta} = \frac{K_{stiff}}{J_{hub}}\alpha - \frac{K_m^2 K_g^2}{R J_{hub}}\dot{\theta} + \frac{K_m K_g}{R J_{hub}} V_a. \tag{2.57}$$

If the approximation $\ddot{\theta} + \ddot{\alpha} = -\frac{K_{stiff}}{J_{load}}\alpha$ holds, then

$$\ddot{\alpha} = -\frac{K_{stiff}}{J_{hub} J_{load}}(J_{hub} + J_{load})\alpha + \frac{K_m^2 K_g^2}{R J_{hub}}\dot{\theta} - \frac{K_m K_g}{R J_{hub}} V_a. \tag{2.58}$$

A feedback controller is designed based on the state space model of (2.57) and (2.58) in [68]. The same feedback controller is used in the following different feed forward schemes. The parameters in the governing equations are shown in Table 2.1.

Parameter	**Symbol**	**Value**	**Unit**
Total hub inertia	J_{hub}	0.0021	Kg-m^2
Motor torque constant	K_m	0.00767	N-m/A
Gear ratio	K_g	14.1×5	
Back-emf constant	K_b	0.804×10^{-3}	volts/rpm
Link length	L	0.6	m
Link mass	m_L	0.06	Kg
Motor terminal resistance	R	2.6	Ohm
Motor armature inductance	I	0.18	mH

Table 2.1: System parameters.

2.6.3 Standard Closed-Loop Control

The standard closed-loop control scheme developed in Section 1.3 is used to reduce the residual vibration of the flexible link. The discrete-time scaled Gaussian functions are used to generate the robust vibration suppression position references.

Figure 2.31 shows the discrete Gaussian function profiles with $\Omega_0 = 9$ rad/sec, $T_s = 0.002$ sec, and the slew angle $\theta = 50$ deg, where Ω_0 is the approximate first resonance frequency of the closed-loop system. Figure 2.32 shows the robust position reference profiles during the move time. After the move time, the position reference holds its final value. Figure 2.33 shows the proportion of the energy after the frequency Ω_0, i.e. $1 - J$ in (2.23). Here, the discrete-time sequences to generate the discrete-time Fourier transform in (2.22) and (2.23) are the discrete Gaussian function sequences as shown in Figure 2.31.

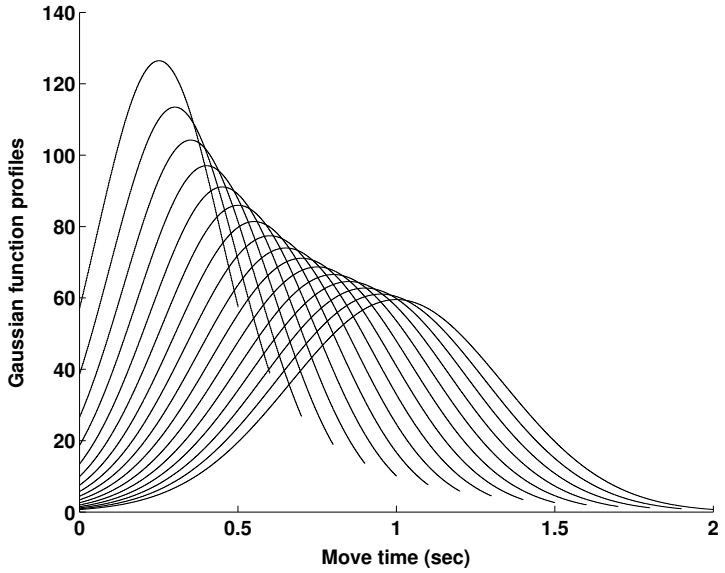

Figure 2.31: Gaussian function profiles.

Figure 2.34 shows the experimental results with the robust position reference profile with the move time of 1 sec. It shows the tip vibration (at the left bottom plot) almost stops at the end of the move time. Figure 2.35 shows the experimental results with the step reference input. Clearly the tip vibration (at the left bottom plot) is very large during the

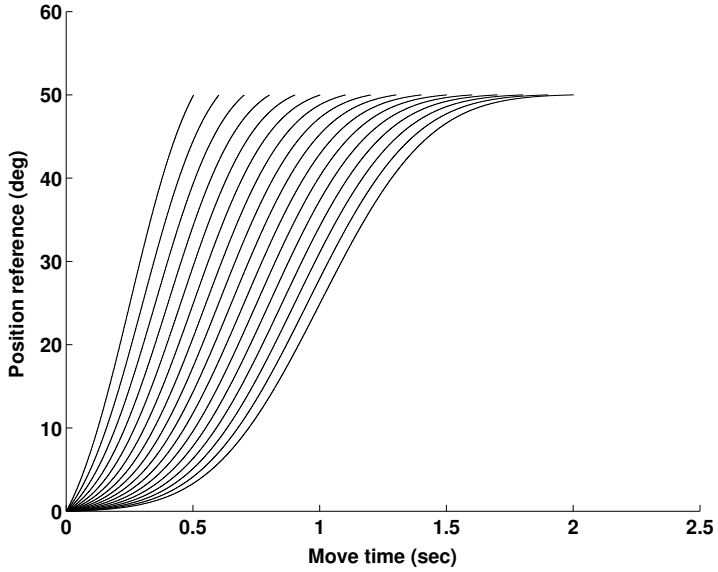

Figure 2.32: Position reference profiles.

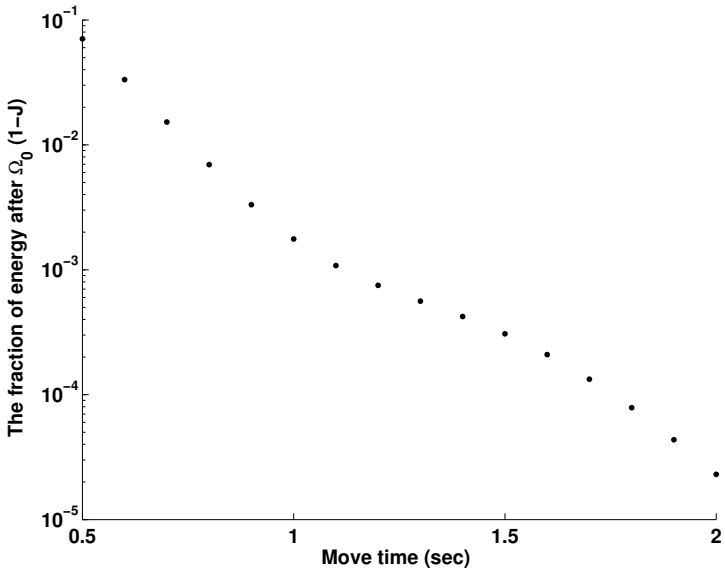

Figure 2.33: The proportion of the energy after Ω_0.

move time and decays very slowly after the move time. In testing, the vibration of the tip of the flexible link was clearly visible.

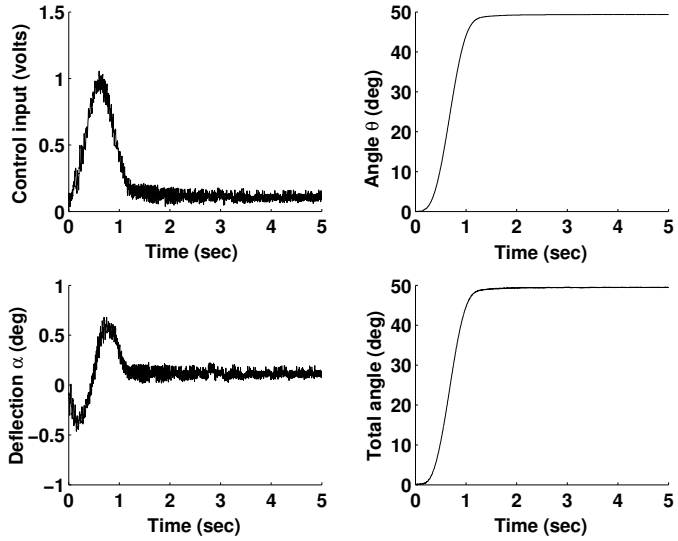

Figure 2.34: Experimental results of a flexible link closed-loop control with robust position reference.

From Fig. 2.31, it is known the initial and final values of the discrete-time Gaussian functions are not zero. The Gaussian function profiles $g_{h,n}[k]$ may be vertically shifted down to force it to start and end at zero,

$$vel[k] = g_{h,n}[k] - g_{h,n}[0], \quad k = 0, 1, \cdots, M. \tag{2.59}$$

Notice that $g_{h,n}[0] = g_{h,n}[M]$ because the sequence $g_{h,n}[k]$ is a symmetric function. The sequence $vel[k]$, $0 \leq k \leq M$, can be used as a velocity profile. The resultant $vel[k]$ from Fig. 2.31 is shown in Fig. 2.36. Although the energy concentration property is impaired for short move time, the velocity reference becomes smooth at the start and the end of the movement. Fig. 2.37 shows the robust position reference profiles with zero initial and final velocities. Fig. 2.38 shows the experimental results with this robust position reference and the move time of 1 sec. It shows the results are almost the same as the results of the nonzero initial and final Gaussian profile.

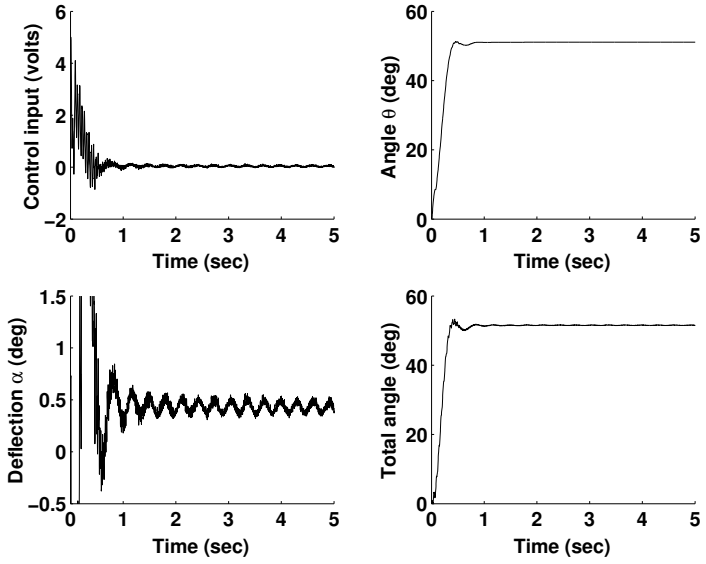

Figure 2.35: Experimental results of a flexible link closed-loop control with step reference.

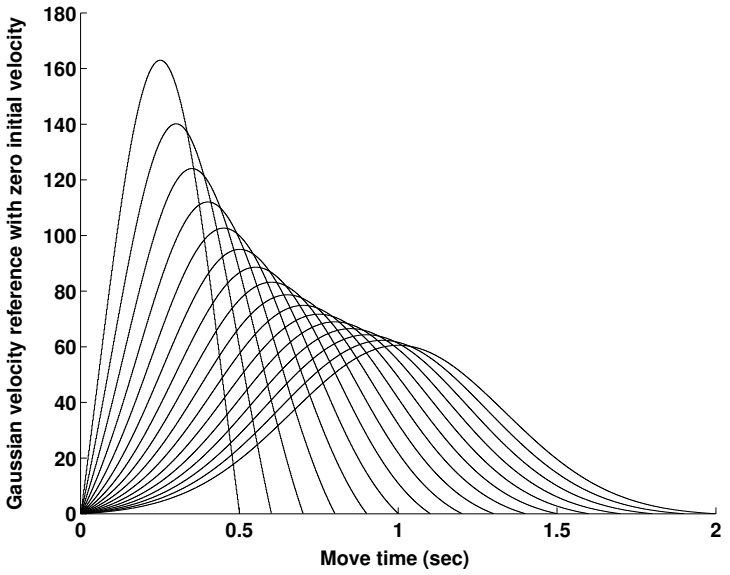

Figure 2.36: Vertically shifted Gaussian velocity profiles.

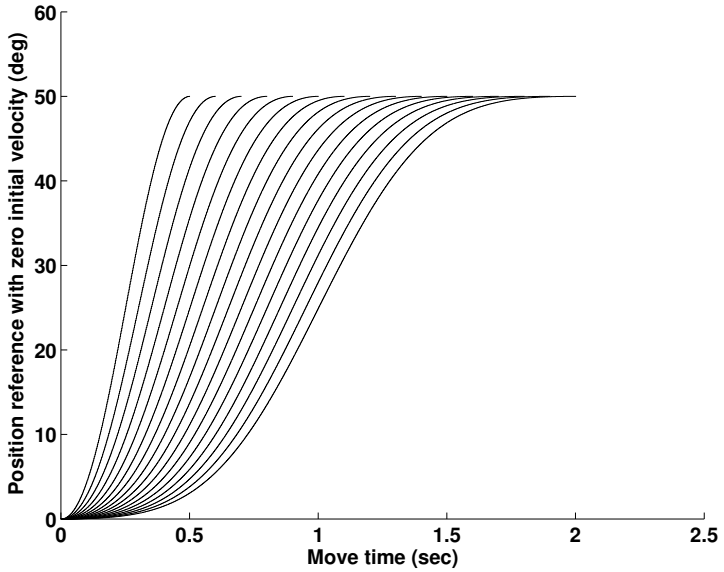

Figure 2.37: Position reference profiles with zero initial and final velocities.

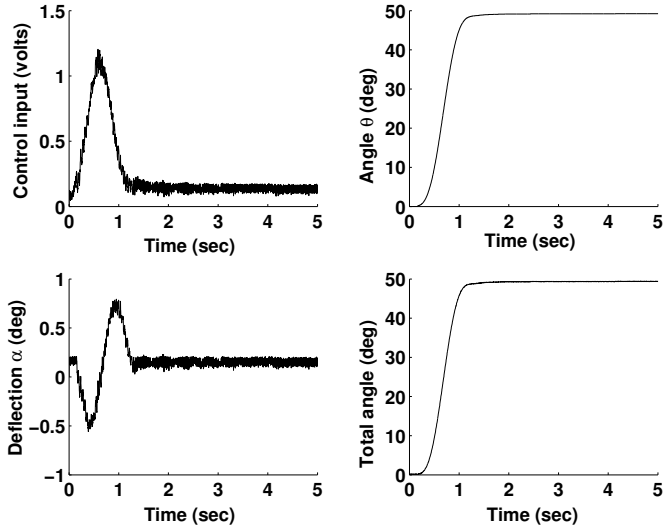

Figure 2.38: Experimental results of a flexible link closed-loop control.

2.6.4 Model Reference Closed-Loop Control

The model reference closed-loop control scheme developed in Section 1.3 is here to reduce the residual vibration of the flexible link. Again, the Gaussian functions are used to generate the robust velocity references. The robust forcing function can be derived as shown in Figure 1.12. From the DC motor servo dynamic model in Figure 2.29, the applied motor voltage is

$$\begin{aligned} V_a &= V_c + V_b \\ &= Ri + I\frac{di}{dt} + K_g K_b \dot{\theta}. \end{aligned} \tag{2.60}$$

The armature current i has a relationship with the acceleration signal $\ddot{\theta}$ as

$$i = \frac{J_{hub}}{K_g K_m}\ddot{\theta}. \tag{2.61}$$

So both i and $\frac{di}{dt}$ can be derived from the velocity signal $\dot{\theta}$. Finally, the motor applied voltage is a function of the velocity signal $\dot{\theta}$.

In the above derivations, all the signals are assumed to be continuous signals. The discrete-time signal of the applied motor voltage can be approximated from the discrete-time signal of the link velocity. In the model reference closed-loop control scheme, the velocity reference can be designed from $vel[k]$ in (2.59). If the discrete-time sequence of the velocity signal is $vel[k]$, $0 \leq k \leq M$, the discrete-time signal of the acceleration, $acc[k]$, can be approximated as

$$acc[k] = \frac{vel[k+1] - vel[k]}{T_s}, \quad 0 \leq k \leq M-1, \tag{2.62}$$

$$acc[M] = 0, \tag{2.63}$$

where T_s is the sampling period. The discrete-time signal of di/dt can be generated in a similar way.

Figure 2.39 shows the model reference control profiles generated from the move time of 1 sec and $\Omega_0 = 9$ rad/sec. Figure 2.40 shows the experimental results with the robust

forcing function. It shows the tip vibration (at the left bottom plot) almost stops at the end of the move time. In many industry applications, the plant is actuated by a current source supply as shown in Section 2.3. In the current source power supply, the generation of the current profile is the same as that of Section 2.3.

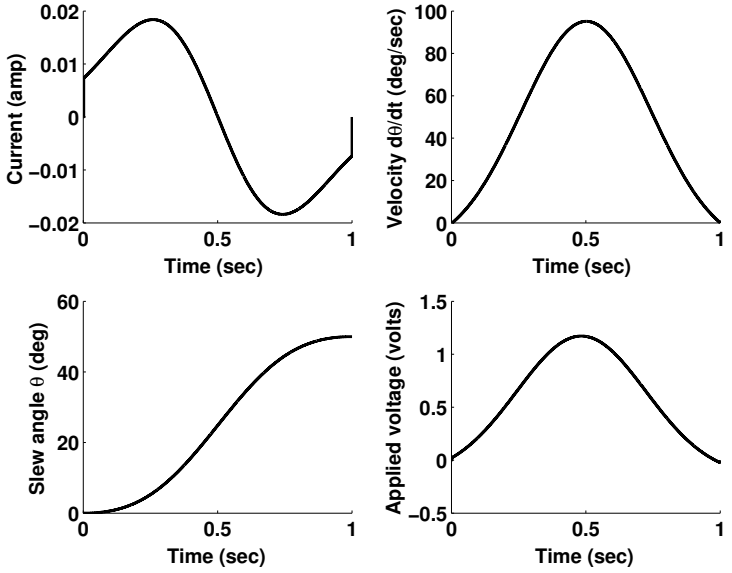

Figure 2.39: Model reference control profiles.

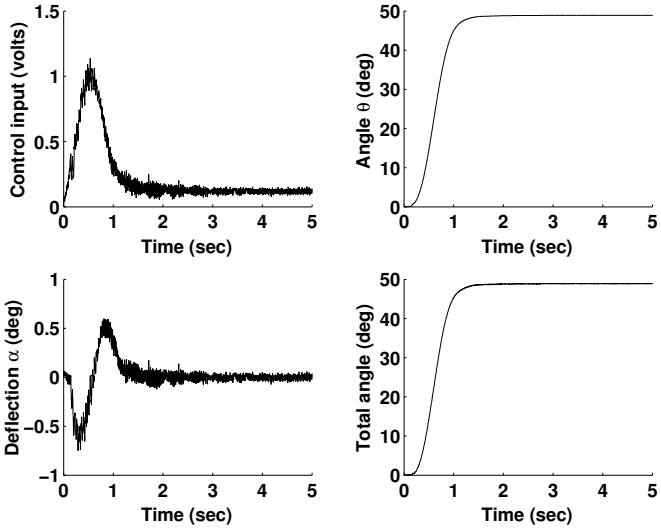

Figure 2.40: Experimental results of a flexible link model reference control.

Chapter 3

Robust Vibration Suppression Profile Generation Based on Optimal Energy Concentration Functions

In Chapter 2, the following objective functions are defined in terms of the $\omega_0 = \Omega_0 T_s$ to compute the optimal scale parameter $n \in \mathbb{R}$ for the discrete-time scaled Gaussian function $g_n[k]$,

$$J = \frac{\int_0^{\omega_0} |G_n(\omega)|^2 d\omega}{\int_0^{\pi} |G_n(\omega)|^2 d\omega} \tag{3.1}$$

or

$$1 - J = \frac{\int_0^{\pi} |G_n(\omega)|^2 d\omega - \int_0^{\omega_0} |G_n(\omega)|^2 d\omega}{\int_0^{\pi} |G_n(\omega)|^2 d\omega}, \tag{3.2}$$

where T_s is the sampling period in second and Ω_0 is a frequency in rad/sec so that all the resonances occur beyond this Ω_0. The following optimal problem can be used to determine the value of n,

$$\max_n J \text{ or } \min_n (1 - J). \tag{3.3}$$

Physically, the objectives are to find the best waveform of the $g_n[k]$ such that the proportion of its energy before the first resonance frequency is maximized, or the proportion of its

energy after the first resonance frequency is minimized, according to an arbitrary fixed move time.

Consider the objective (3.1) again and suppose a continuous-time filter $f(t)$ is to have a finite support impulse response defined only on $0 \leq t \leq T$. Also, as much of the impulse response energy as possible is contained in $|\omega| \leq \Omega$, i.e.,

$$\max_{f(t)} \frac{\int_{-\Omega}^{\Omega} |F(\omega)|^2 d\omega}{\int_{-\infty}^{\infty} |F(\omega)|^2 d\omega}, \tag{3.4}$$

where $F(\omega) = \int_0^T f(t) e^{-i\omega t} dt$ is the Fourier transform of $f(t)$. Here, the detail on the function $f(t)$ is not known and it can be an arbitrary energy bounded signal.

The answer to this problem is the shifted prolate spheroidal wave functions. This problem was accidentally solved by Slepian and his colleagues at Bell Labs in 1961 when studying communication theory [89, 39, 40, 86]. In this chapter, robust vibration suppression profile generation using prolate spheroidal wave functions will be examined.

Instead of using concentration in the sense of Heisenberg uncertainty, Slepian et al. introduced a more meaningful measure of a signal for the communication engineer

$$\alpha^2(T) := \frac{\int_{-T/2}^{T/2} |f(t)|^2 dt}{\int_{-\infty}^{\infty} |f(t)|^2 dt}, \tag{3.5}$$

i.e., the fraction of the signal's energy that lies in the time interval $[-T/2, T/2]$. Similarly,

$$\beta^2(\Omega) := \frac{\int_{-\Omega}^{\Omega} |F(\omega)|^2 d\omega}{\int_{-\infty}^{\infty} |F(\omega)|^2 d\omega} \tag{3.6}$$

is a measure of concentration of the amplitude spectrum of $f(t)$.

Slepian's original question was to determine how large $\alpha^2(T)$ can be for $f(t)$ in the space of band-limited signals. The group accidentally found the prolate spheroidal wave functions were exactly the solutions to the original problem. In short, given any $T > 0$ and any $\Omega > 0$, the original problem has a countably infinite set of functions $\psi_0(t), \psi_1(t), \psi_2(t), \ldots$ and a set of corresponding $\lambda_i = \alpha^2(T), i = 0, 1, 2, \ldots$, such that

$$\lambda_0 > \lambda_1 > \lambda_2 > \cdots . \tag{3.7}$$

The best choice of $f(t)$ satisfying (3.4) is the first shifted spheroidal wave function

$$f(t) = \psi_0(t + T/2, c), \tag{3.8}$$

where $c = \Omega T/2$.

The unexpected quality of the waveform of ψ_0 is that it can be used to generate a shape filter or a reference velocity candidate to suppress all the high frequency resonance vibrations with the energy concentration objective (3.3). The base functions in (3.3) in this chapter are the prolate spheroidal wave functions. Since the waveform of the reference velocity is known, the acceleration, jerk, position and other profiles can be derived to synthesize the control input signals to suppress the residual vibration in a flexible system.

3.1 Band-Limited and Time-Limited Signals

$L^2(-\infty, \infty)$ is denoted as the class of all complex valued functions $f(t)$ defined on the whole real line $(-\infty, \infty)$ and integrable in absolute square, such that

$$\|f(t)\|_\infty^2 := \int_{-\infty}^{\infty} |f(t)|^2 dt \tag{3.9}$$

is referred to as the total energy of $f(t)$. Similarly, $L^2(-A, A)$ is denoted the set of all complex valued functions $f(t)$ defined on the real line $[-A, A]$ and integrable in absolute square in the interval $[-A, A]$, such that

$$\|f(t)\|_A^2 := \int_{-A}^{A} |f(t)|^2 dt \tag{3.10}$$

is referred to as the energy of $f(t)$ in the interval $[-A, A]$. $Df(t)$ is a time-limited version of $f(t)$ obtained by the following rule

$$Df(t) = \begin{cases} f(t), & \text{if } |t| \leq T/2, \\ 0, & \text{otherwise}, \end{cases} \tag{3.11}$$

where T is a positive number.

The finite energy signal $f(t)$ is said to be band-limited to the band $[-\Omega, \Omega]$, if the Fourier transform of $f(t)$, i.e., $F(\omega)$ vanishes if $\omega > \Omega$. In this case, the signal has the following finite Fourier integral representation

$$f(t) = \frac{1}{2\pi} \int_{-\Omega}^{\Omega} F(\omega) e^{j\omega t} d\omega. \tag{3.12}$$

Slepian et al. [89] notes that members of band-limited signals are entire functions of the variable t. A complex function is said to be entire if it is analytic at all finite points of the complex plane. Landau et al. [39] shows that the only $L^2(-\infty, \infty)$ signal $f(t)$ with both time-limited and band-limited properties is zero for all t, i.e., $f(t) \equiv 0$.

3.2 Energy Concentration Problem In Continuous-Time Case

As shown, Slepian's original problem was to determine how large $\alpha^2(T)$ can be for signals $f(t)$ that are band-limited to the band $[-\Omega, \Omega]$. The following steps are outlined to solve this problem by following Slepian et al. [89, 39, 88].

First, $f(t)$ in (3.5) is expressed in terms of its amplitude spectrum $F(\omega)$.

$$\alpha^2(T) = \frac{\int_{-T/2}^{T/2} f(t)\overline{f(t)} dt}{\frac{1}{2\pi}\int_{-\Omega}^{\Omega} |F(\omega)|^2 d\omega}, \tag{3.13}$$

$$= \frac{\int_{-T/2}^{T/2} \frac{1}{2\pi}\int_{-\Omega}^{\Omega} e^{j\omega t} F(\omega) d\omega \frac{1}{2\pi}\int_{-\Omega}^{\Omega} e^{-j\omega' t}\overline{F(\omega')} d\omega' dt}{\frac{1}{2\pi}\int_{-\Omega}^{\Omega} |F(\omega)|^2 d\omega}, \tag{3.14}$$

$$= \frac{\frac{1}{2\pi}\int_{-\Omega}^{\Omega}\int_{-\Omega}^{\Omega}\int_{-T/2}^{T/2} e^{j\omega t} e^{-j\omega' t} F(\omega)\overline{F(\omega')} dt d\omega d\omega'}{\int_{-\Omega}^{\Omega} |F(\omega)|^2 d\omega}, \tag{3.15}$$

$$= \frac{\frac{1}{2\pi}\int_{-\Omega}^{\Omega}\int_{-\Omega}^{\Omega}\int_{-T/2}^{T/2} e^{j(\omega-\omega')t} dt F(\omega)\overline{F(\omega')} d\omega d\omega'}{\int_{-\Omega}^{\Omega} |F(\omega)|^2 d\omega}. \tag{3.16}$$

Since

$$\frac{\sin\left(\frac{T}{2}(\omega - \omega')\right)}{\pi(\omega - \omega')} = \frac{1}{2\pi}\int_{-T/2}^{T/2} e^{j(\omega-\omega')t} dt, \tag{3.17}$$

$$\alpha^2(T) = \frac{\int_{-\Omega}^{\Omega}\int_{-\Omega}^{\Omega} \frac{\sin\left(\frac{T}{2}(\omega-\omega')\right)}{\pi(\omega-\omega')} F(\omega)\overline{F(\omega')}d\omega d\omega'}{\int_{-\Omega}^{\Omega} F(\omega)\overline{F(\omega)}d\omega}. \tag{3.18}$$

Here, $F(\omega)$ is an arbitrary function in $L^2(-\Omega,\Omega)$, and the problem of maximizing $\alpha^2(T)$ has been reduced to a homogeneous linear integral equation with a symmetric kernel in Courant and Hilbert's *Methods of Mathematical Physics* [20]. All functions $F(\omega)$ that maximizes $\alpha^2(T)$ must satisfy the following integral equation

$$\int_{-\Omega}^{\Omega} \frac{\sin\left(\frac{T}{2}(\omega-\omega')\right)}{\pi(\omega-\omega')} F(\omega')d\omega' = \alpha^2(T)F(\omega), \quad |\omega \leq \Omega|. \tag{3.19}$$

An integral equation of the above form is known as a homogeneous Fredholm equation of the second kind. To further simplify the equation, the following substitutions and definitions are made

$$\omega' = \Omega y, \quad \omega = \Omega x, \quad \psi(y) := F(\Omega y), \quad \lambda := \alpha^2(T), \quad c := \frac{T\Omega}{2}.$$

With the above substitutions and definitions, (3.19) is reduced to

$$\int_{-1}^{1} \frac{\sin\left(c(x-y)\right)}{\pi(x-y)} \psi(y)dy = \lambda\psi(x), \quad |x| \leq 1. \tag{3.20}$$

It can be shown that the symmetric kernel $\frac{\sin(c(x-y))}{\pi(x-y)}$ is positive definite (see Appendix B). From the Fredholm equation theory [20], (3.20) has solutions in $L^2(-1,1)$ only for a set of discrete real positive values of λ, such that $\lambda_0 \geq \lambda_1 \geq \lambda_2 \geq \ldots$ and that $\lim_{n\to\infty}\lambda_n = 0$. The corresponding eigenfunctions, $\psi_0(x), \psi_1(x), \psi_2(x), \ldots$ can be chosen to be real and orthogonal on $[-1,1]$. They are complete in $L^2(-1,1)$. Here, eigenfunctions which differ only by an arbitrary multiplicative constant is considered as a single solution.

Equation (3.20) only defines $\psi(x)$ for $|x| \leq 1$. The left side of (3.20), however, is well defined for all x. The following definition, extends x in (3.20) to the whole real line $(-\infty,\infty)$.

$$\psi_n(x) = \frac{1}{\lambda_n}\int_{-1}^{1} \frac{\sin\left(c(x-y)\right)}{\pi(x-y)} \psi_n(y)dy, \quad |x| > 1. \tag{3.21}$$

The eigenfunction $\psi_n(x)$ are now defined on $(-\infty,\infty)$ and it can be shown that they are orthogonal on $(-\infty,\infty)$ as well as on $[-1,1]$. It is very hard to directly solve (3.20).

Slepian et al. found that the solutions (eigenfunctions) of (3.20) are also solutions of the following second-order differential equation eigenvalue problem (see Appendix C),

$$\frac{d}{dx}(1-x^2)\frac{d\psi}{dx} + (\chi - c^2x^2)\psi = 0. \tag{3.22}$$

Equation (3.22) is known as the equation of prolate spheroidal wave functions. The detail of prolate spheroidal wave functions can be found in [93, 24]. It is known that (3.22) has solutions bounded everywhere only for discrete real positive values of χ, such that $0 < \chi_0 < \chi_1 < \chi_2 \ldots$. The corresponding solutions $\psi_0, \psi_1, \psi_2, \ldots$ are called prolate spheroidal wave functions (pswf's).

Now the problem to maximize (3.6) in the space of time-limited functions is considered. Let $f(t) \in L^2(-\infty, \infty)$ have total energy $E = \|f\|_\infty^2$. The time-limited version of $f(t)$ has total energy $E_D = \|Df\|_\infty^2 \leq E$. Since $Df(t)$ cannot be a band-limited signal, the energy of $Df(t)$ spreads over $(-\infty, \infty)$ in frequency domain. Now an optimal time-limited function $Df(t)$ is to be determined to maximize $\beta^2(\Omega)$ in (3.6). Slepian et al. notes that the answer to this question is uniquely $D\psi_0(t)$ except for a multiplicative constant. To show this, $F(\omega)$ in (3.6) is expressed in terms of its time domain function $Df(t)$.

$$\beta^2(\Omega) = \frac{\frac{1}{2\pi}\int_{-\Omega}^{\Omega} |DF(\omega)|^2 d\omega}{\frac{1}{2\pi}\int_{-\infty}^{\infty} |DF(\omega)|^2 d\omega}, \tag{3.23}$$

where $DF(\omega)$ is the Fourier transform of $Df(t)$

$$DF(\omega) = \int_{-T/2}^{T/2} f(t) e^{-j\omega t} dt. \tag{3.24}$$

$$\beta^2(\Omega) = \frac{\frac{1}{2\pi}\int_{-\Omega}^{\Omega} DF(\omega)\overline{DF(\omega)}d\omega}{\int_{-T/2}^{T/2}|f(t)|^2dt}, \tag{3.25}$$

$$= \frac{\frac{1}{2\pi}\int_{-\Omega}^{\Omega}\int_{-T/2}^{T/2} f(s)e^{-j\omega s}ds\int_{-T/2}^{T/2}\overline{f(t)}e^{j\omega t}dtd\omega}{\int_{-T/2}^{T/2}|f(t)|^2dt}, \tag{3.26}$$

$$= \frac{\int_{-T/2}^{T/2}\int_{-T/2}^{T/2}\frac{1}{2\pi}\int_{-\Omega}^{\Omega} e^{j\omega(t-s)}d\omega f(s)\overline{f(t)}dsdt}{\int_{-T/2}^{T/2}|f(t)|^2dt}, \tag{3.27}$$

$$= \frac{\int_{-T/2}^{T/2}\int_{-T/2}^{T/2}\frac{\sin(\Omega(t-s))}{\pi(t-s)} f(s)\overline{f(t)}dsdt}{\int_{-T/2}^{T/2}|f(t)|^2dt}, \tag{3.28}$$

$$= \frac{\int_{-T/2}^{T/2}\int_{-T/2}^{T/2}\frac{\sin(\Omega(s-t))}{\pi(s-t)} f(s)\overline{f(t)}dsdt}{\int_{-T/2}^{T/2}|f(t)|^2dt} \tag{3.29}$$

It is known from [20] that the solution to this problem is $\beta^2(\Omega) = \lambda_0$, where λ_0 is the largest eigenvalue of the integral equation

$$\lambda f(s) = \int_{-T/2}^{T/2}\frac{\sin(\Omega(s-t))}{\pi(s-t)}f(t)dt, \quad |t| \le \frac{T}{2}. \tag{3.30}$$

$D\psi_0(t)$ is the corresponding eigenfunction in $L^2(-T/2, T/2)$ for which λ attains the maximum value λ_0.

Although the general theory of prolate spheroidal wave functions has been known for a long time [93, 24] in the field of physics and mathematics, the complexity of the theory still makes them difficult to compute. Previous computation methods are generally based on the extensive tables of numerical values [93, 24]. Recently, Falloon et al. [22, 23] have developed a package, written in Mathematica computer algebra system to compute the spheroidal wave functions to arbitrary precision.

Since the discrete-time version of the prolate spheroidal wave functions will be examined in the subsequent sections. The detail of the computation of the continuous-time prolate spheroidal wave functions is not elaborated on here.

3.3 Energy Concentration Problem In Discrete-Time Case

In this section, the energy concentration problem in the discrete-time case is studied. The results for this case were originally derived by Slepian [87]. Let $\{h[k]\} = \ldots, h[-1], h[0], h[1], \ldots$ be a real or complex valued sequence with finite energy and a unitless sampling period $T_s = 1$. The discrete-time Fourier transform (see Appendix A) of $h[k]$ is

$$H(f) = \sum_{k=-\infty}^{\infty} h[k] e^{-j2\pi fk}, \tag{3.31}$$

$H(f)$ is a periodic function in f with period 1. The discrete-time sequence $\{h[k]\}$ has the following representation

$$h[k] = \int_{-1/2}^{1/2} H(f) e^{j2\pi fk} df. \tag{3.32}$$

The energy of the sequence $\{h[k]\}$ in the index interval $[n_1, n_2]$ is denoted as

$$E(n_1, n_2) := \sum_{k=n_1}^{n_2} |h[k]|^2, \tag{3.33}$$

and the total energy is denoted as

$$E := E(-\infty, \infty) = \sum_{k=-\infty}^{\infty} |h[k]|^2. \tag{3.34}$$

As like the continuous-time case, it is natural to ask how large the fraction of the energy in the index range from 0 to $N-1$ can be for a band-limited sequence, i.e., to determine the maximum value of

$$\alpha^2(N) := \frac{E(0, N-1)}{E(-\infty, \infty)} = \frac{\sum_{k=0}^{N-1} |h[k]|^2}{\sum_{k=-\infty}^{\infty} |h[k]|^2} \tag{3.35}$$

for all band-limited sequences with bandwidth $W < 1/2$.

Similarly, an optimal sequence is to be determined to maximize the fraction of the energy in the frequency range $|f| \leq W < 1/2$, i.e., to determine the maximum value of

$$\beta^2(W) := \frac{\int_{-W}^{W} |H(f)|^2 df}{\int_{-1/2}^{1/2} |H(f)|^2 df} \tag{3.36}$$

for all sequence $\{h[k]\}$ index-limited to $[0, N-1]$. A sequence is index-limited to the interval $[n_1, n_2]$ if $h[k] = 0$ for $k < n_1$ and $k > n_2$.

For the problem of (3.35), the concentration measure $\alpha^2(N)$ can be written as

$$\alpha^2(N) = \frac{\sum_{k=0}^{N-1} |h[k]|^2}{\sum_{k=-\infty}^{\infty} |h[k]|^2}, \tag{3.37}$$

$$= \frac{\sum_{k=0}^{N-1} h[k]\overline{h[k]}}{\sum_{k=-\infty}^{\infty} |h[k]|^2}, \tag{3.38}$$

$$= \frac{\sum_{k=0}^{N-1} \int_{-W}^{W} H(f) e^{j2\pi fk} df \int_{-W}^{W} \overline{H(f')} e^{-j2\pi f'k} df'}{\int_{-W}^{W} |H(f)|^2 df}, \tag{3.39}$$

$$= \frac{\int_{-W}^{W} H(f) df \int_{-W}^{W} \overline{H(f')} df' \sum_{k=0}^{N-1} e^{j2\pi(f-f')k}}{\int_{-W}^{W} |H(f)|^2 df}. \tag{3.40}$$

By defining

$$H(f) := G(f) e^{-j\pi f(N-1)}, \tag{3.41}$$

$$\alpha^2(N) = \frac{\int_{-W}^{W} G(f) e^{-j\pi f(N-1)} df \int_{-W}^{W} \overline{G(f')} e^{j\pi f'(N-1)} df' \sum_{k=0}^{N-1} e^{j2\pi(f-f')k}}{\int_{-W}^{W} |G(f)|^2 df}, \tag{3.42}$$

$$= \frac{\int_{-W}^{W} G(f) df \int_{-W}^{W} \overline{G(f')} df' e^{-j\pi(f-f')(N-1)} \sum_{k=0}^{N-1} e^{j2\pi(f-f')k}}{\int_{-W}^{W} |G(f)|^2 df}. \tag{3.43}$$

Since

$$e^{-j\pi(f-f')(N-1)} \sum_{k=0}^{N-1} e^{j2\pi(f-f')k} = e^{-j\pi(f-f')(N-1)} \frac{1 - e^{j2\pi(f-f')N}}{1 - e^{j2\pi(f-f')}}, \tag{3.44}$$

$$= \frac{e^{-j\pi(f-f')N}}{e^{-j\pi(f-f')}} \frac{1 - e^{i2\pi(f-f')N}}{1 - e^{i2\pi(f-f')}}, \tag{3.45}$$

$$= \frac{e^{-j\pi(f-f')N} - e^{j\pi(f-f')N}}{e^{-j\pi(f-f')} - e^{j\pi(f-f')}}, \tag{3.46}$$

$$= \frac{2\sin(\pi N(f-f'))}{2\sin(\pi(f-f'))}, \tag{3.47}$$

$$= \frac{\sin(\pi N(f-f'))}{\sin(\pi(f-f'))}, \tag{3.48}$$

$\alpha^2(N)$ is reduced to the following form

$$\alpha^2(N) = \frac{\int_{-W}^{W} \int_{-W}^{W} \frac{\sin(\pi N(f-f'))}{\sin(\pi(f-f'))} G(f) \overline{G(f')} df df'}{\int_{-W}^{W} |G(f)|^2 df}. \tag{3.49}$$

Here, $G(f)$ is an arbitrary function in $L^2(-W, W)$, and all functions $G(f)$ that maximizes $\alpha^2(N)$ must satisfy the following integral equation

$$\int_{-W}^{W} \frac{\sin(\pi N(f-f'))}{\sin(\pi(f-f'))}\psi(f')df' = \lambda\psi(f), \quad |f| \leq W. \tag{3.50}$$

Since the kernel in the above homogeneous Fredholm equation of the second kind is degenerate (see Appendix D). It has only N non-zero distinct, real and positive eigenvalues and they can be ordered such that

$$1 > \lambda_0(N,W) > \lambda_1(N,W) > \cdots > \lambda_{N-1}(N,W) > 0. \tag{3.51}$$

There are N linearly independent real eigenfunctions of (3.50) corresponding to these eigenvalues and they are denoted as $U_0(N,W;f), U_1(N,W;f), \ldots, U_{N-1}(N,W;f)$. Again, eigenfunctions that differ only by an arbitrary non-zero multiplicative constant is considered as one eigenfunction. They are called the discrete prolate spheroidal wave functions (DPSWF's). $U_k(N,W;f)$ can be extended to $[-1/2, 1/2]$ from (3.50), so the DPSWF's $U_k(N,W;f)$ and their corresponding eigenvalues $\lambda_k(N,W)$ are defined by

$$\begin{aligned}\int_{-W}^{W} \frac{\sin(\pi N(f-f'))}{\sin(\pi(f-f'))}U_k(N,W;f')df' &= \lambda_k(N,W)U_k(N,W;f) \\ k &= 0, 1, \cdots, N-1.\end{aligned} \tag{3.52}$$

The DPSWF $U_k(N,W;f)$ has exactly k zeros in $[-W, W]$ and $N-1$ zeros in $[-1/2, 1/2]$. It is even function if k is even and odd function if k is odd. The band-limited sequence that maximizes $\alpha^2(N)$ in (3.35) is

$$h[k] = \int_{-W}^{W} U_0(N,W;f)e^{j2\pi fk}e^{j\pi f(N-1)}df, \quad k = \cdots, -1, 0, 1, \cdots. \tag{3.53}$$

With a normalization factor $1/\lambda_0(N,W)$, the following discrete sequence is generated

$$v_0[k](N,W) = \frac{1}{\lambda_0(N,W)}\int_{-W}^{W} U_0(N,W;f)e^{j2\pi fk}e^{j\pi f(N-1)}df, \quad k = \cdots, -1, 0, 1, \cdots. \tag{3.54}$$

The normalization factor $\frac{1}{\lambda_0(N,W)}$ follows Slepian's notation [87] and can be replaced by an arbitrary constant. $v_0[k]$ is called zeroth order discrete prolate spheroidal sequence (DPSS).

The n^{th} order DPSS following Slepian's notation [87] can be generated by

$$v_n[k](N,W) = \frac{1}{\epsilon_n \lambda_n(N,W)} \int_{-W}^{W} U_n(N,W;f) e^{j2\pi fk} e^{j\pi f(N-1)} df, \quad n = 0, 1, \cdots, N-1, \tag{3.55}$$

where

$$\epsilon_n = \begin{cases} 1, & n \text{ even;} \\ \sqrt{-1}, & n \text{ odd.} \end{cases} \tag{3.56}$$

Slepian [87] notes the DPSS's also satisfy the following system of equations

$$\sum_{k'=0}^{N-1} \frac{\sin\left(2\pi W(k-k')\right)}{\pi(k-k')} v_n[k'](N,W) = \lambda_n(N,W) v_n[k](N,W), \quad n, k = 0, 1, \cdots, N-1. \tag{3.57}$$

This is to say that $\lambda_n(N,W)$, $n = 0, 1, \ldots, N-1$ are the eigenvalues of the $N \times N$ matrix A, where the $(k,k')^{th}$ element of A matrix is given by

$$A_{k,k'} := \frac{\sin\left(2\pi W(k-k')\right)}{\pi(k-k')}, \quad k, k' = 0, 1, \cdots, N-1. \tag{3.58}$$

The eigenvector of matrix A corresponding to the n^{th} eigenvalue $\lambda_n(N,W)$ is exactly the DPSS $v_n[k](N,W)$ with indices from $k = 0$ to $k = N-1$, namely

$$v_n[0](N,W), v_n[1](N,W), \cdots, v_n[N-1](N,W).$$

Now with the results of the first concentration problem (3.35) available, the concentration problem (3.36) for index-limited sequences is studied. If a sequence $h[k]$ is index-limited to the interval $[0, N-1]$, the discrete-time Fourier transform of the index-limited sequence is

$$H(f) = \sum_{k=-\infty}^{\infty} h[k] e^{-j2\pi fk} = \sum_{k=0}^{N-1} h[k] e^{-j2\pi fk}. \tag{3.59}$$

The concentration measure in (3.36) can be computed as

$$\beta^2(W) = \frac{\int_{-W}^{W} H(f)\overline{H(f)}df}{\sum_{k=0}^{N-1}|h[k]|^2}, \tag{3.60}$$

$$= \frac{\int_{-W}^{W}\sum_{k=0}^{N-1} h[k]e^{-j2\pi fk}\sum_{k'=0}^{N-1}\overline{h[k']}e^{j2\pi fk'}df}{\sum_{k=0}^{N-1}|h[k]|^2}, \tag{3.61}$$

$$= \frac{\sum_{k=0}^{N-1}\sum_{k'=0}^{N-1} h[k]\overline{h[k']}\int_{-W}^{W} e^{j2\pi f(k'-k)}df}{\sum_{k=0}^{N-1}|h[k]|^2}, \tag{3.62}$$

$$= \frac{\sum_{k=0}^{N-1}\sum_{k'=0}^{N-1} h[k]\overline{h[k']}\frac{\sin(2\pi W(k'-k))}{\pi(k'-k)}}{\sum_{k=0}^{N-1}|h[k]|^2}, \tag{3.63}$$

$$= \frac{\sum_{k=0}^{N-1}\sum_{k'=0}^{N-1} h[k]\frac{\sin(2\pi W(k-k'))}{\pi(k-k')}\overline{h[k']}}{\sum_{k=0}^{N-1}|h[k]|^2}. \tag{3.64}$$

For a real valued sequence $h[k]$, $\beta^2(W)$ can be written as (Percival [65], page 122)

$$\beta^2(W) = \frac{\mathbf{h}^T A\mathbf{h}}{\mathbf{h}^T\mathbf{h}}, \tag{3.65}$$

or

$$\mathbf{h}^T A\mathbf{h} = \beta^2(W)\mathbf{h}^T\mathbf{h}, \tag{3.66}$$

where $\mathbf{h}^T := \begin{bmatrix} h[0] & h[1] & \cdots & h[N-1] \end{bmatrix}$ and A is a $N \times N$ matrix defined in (3.58). Differentiate both sides of (3.66), and the sequence $h[k], k = 0, 1, \ldots, N-1$, that maximizes $\beta^2(W)$ must satisfy

$$A\mathbf{h} = \lambda(N, W)\mathbf{h} \tag{3.67}$$

or

$$\sum_{k'=0}^{N-1}\frac{\sin(2\pi W(k-k'))}{\pi(k-k')}h[k'] = \lambda(N, W)h[k]. \tag{3.68}$$

The above equation is exactly equivalent to (3.57) that describes the zeroth order to $(N-1)^{th}$ order DPSS with indices from 0 to $N-1$. The index-limited sequence that maximizes $\beta^2(W)$ is exactly the zeroth order DPSS, $v_0[k]$, $k = 0, 1, \ldots, N-1$.

3.4 Computation of Discrete-Time Prolate Spheroidal Sequences (DPSS's)

3.4.1 Discrete-Time Prolate Spheroidal Sequences with Sampling Period of 1

In the previous section, the sampling interval is assumed to be unit-less 1. So the Nyquist frequency (defined as $\frac{1}{2T_s}$) is unit-less $\frac{1}{2}$. In this case, the signal bandwidth W in the energy concentration problem must satisfy $0 \leq W < \frac{1}{2}$.

Since a DPSS that differs only by a non-zero multiplicative constant is considered as one DPSS, normalization and parity conventions need to be imposed. Following Slepian's notation [87], first the energy of n^{th} order DPSS, $v_n[k]$, $k = 0, 1, \ldots, N-1$ is normalized to be 1.

$$\sum_{k=0}^{N-1} (v_n[k](N, W))^2 = 1. \tag{3.69}$$

Secondly, the following constraints are imposed.

$$\sum_{k=0}^{N-1} v_n[k](N, W) \geq 0, \tag{3.70}$$

$$\sum_{k=0}^{N-1} (N - 1 - 2k) v_n[k](N, W) \geq 0. \tag{3.71}$$

Constraint (3.70) means the sum of each DPSS is made non-negative and constraint (3.71) means that each DPSS is made to start with a positive lobe.

It is already known that DPSS and its concentration measure can be computed from the eigenvectors and eigenvalues of a $N \times N$ symmetric matrix whose element is described in Equation (3.58).

Slepian [87] showed that n^{th} order DPSS also satisfies the following difference equation

$$\begin{aligned}\frac{1}{2}k(N-k)v_n[k-1](N,W)+\left[\cos(2\pi W)\left(\frac{N-1}{2}-n\right)^2-\theta_n(N,W)\right]v_n[k](N,W)\\ +\frac{1}{2}(k+1)[N-1-k]v_n[k+1](N,W)=0,\\ n,k=0,1,\cdots,N-1.\end{aligned} \tag{3.72}$$

So the n^{th} order DPSS can be generated from the following eigenvector problem

$$\sigma(N,W)\mathbf{v}_n(N,W)=\theta_n(N,W)\mathbf{v}_n(N,W), \tag{3.73}$$

where $\sigma(N,W)$ denotes the $N\times N$ tri-diagonal matrix whose element in the i^{th} row and j^{th} column is given by

$$\sigma(N,W)_{i,j}=\begin{cases}\frac{1}{2}i(N-i), & j=i-1;\\ \left(\frac{N-1}{2}-i\right)^2\cos(2\pi W), & j=i;\\ \frac{1}{2}(i+1)(N-1-i), & j=i+1;\\ 0, & |j-i|>1,\end{cases} \tag{3.74}$$

and $\mathbf{v}_n(N,W)=\begin{bmatrix}v_n[0](N,W) & v_n[1](N,W) & \cdots & v_n[N-1](N,W)\end{bmatrix}^T$. The N eigenvalues of $\sigma(N,W)$ are real and distinct. They can be denoted such that

$$\theta_0(N,W)>\theta_1(N,W)>\cdots>\theta_{N-1}(N,W). \tag{3.75}$$

Since the DPSS $v_n[k](N,W)$, $k=0,1,\ldots,N-1$, can be generated from matrix $\sigma(N,W)$, the concentration measure $\lambda_n(N,W)$ can be calculated from (3.65).

Percival and Walden [65] compared other computation methods of DPSS's when studying multi-taper spectra analysis. They proposed ([65], page 390, Exercise [8.1]) an efficient way in (3.76) to compute the eigenvalue $\lambda_n(N,W)$ in (3.57) given the n^{th} order DPSS $v_n[k]$, $k=0,1,\ldots,N-1$, is given.

$$\lambda_n(N,W)=2\left(Wq_0+2\sum_{\tau=1}^{N-1}\frac{\sin(2\pi W\tau)}{\pi\tau}q_\tau\right), \tag{3.76}$$

where

$$q_\tau := \sum_{k=0}^{N-\tau-1} v_n[k](N,W)v_n[k+\tau](N,W). \tag{3.77}$$

The above method to calculate eigenvalue $\lambda_n(N,W)$ can be easily derived from (3.57). Let

$$\rho(\tau) := \frac{\sin(2\pi W\tau)}{\pi\tau}, \tag{3.78}$$

(3.57) is reduced to

$$\sum_{k'=0}^{N-1} \rho(k-k')v_n[k'] = \lambda_n v_n[k], \quad n,k = 0,1,\cdots,N-1. \tag{3.79}$$

Here, $\lambda_n(N,W)$ and $v_n[k](N,W)$ are simply denoted as λ_n and $v_n[k]$ for derivation. For each n, $n = 0,1,\ldots,N-1$, there are N equations corresponding to k, $k = 0,1,\ldots,N-1$.

$$\begin{aligned}
&\rho(0-0)v_n[0]+\rho(0-1)v_n[1]+\rho(0-2)v_n[2]+\cdots+\rho(0-(N-1))v_n[N-1]=\lambda_n v_n[0],\\
&\rho(1-0)v_n[0]+\rho(1-1)v_n[1]+\rho(1-2)v_n[2]+\cdots+\rho(1-(N-1))v_n[N-1]=\lambda_n v_n[1],\\
&\rho(2-0)v_n[0]+\rho(2-1)v_n[1]+\rho(2-2)v_n[2]+\cdots+\rho(2-(N-1))v_n[N-1]=\lambda_n v_n[2],\\
&\qquad\qquad\qquad\qquad\qquad\qquad\qquad\qquad\cdots=\cdots,\\
&\rho(N-1-0)v_n[0]+\rho(N-1-1)v_n[1]+\rho(N-1-2)v_n[2]+\cdots+\rho(N-1-(N-1))v_n[N-1]=\lambda_n v_n[N-1]
\end{aligned}\tag{3.80}$$

For the system of above N equations, multiply the both sides of the i^{th} equation with $v_n[i-1]$, $i=1,2,\ldots,N$, and consider $\rho(0)=2W$, another system of equations is obtained.

$$\begin{aligned}
&2Wv_n[0]^2+\rho(-1)v_n[1]v_n[0]+\rho(-2)v_n[2]v_n[0]+\cdots+\rho(-(N-1))v_n[N-1]v_n[0]=\lambda_n v_n[0]^2,\\
&\rho(1)v_n[0]v_n[1]+2Wv_n[1]^2+\rho(-1)v_n[2]v_n[1]+\cdots+\rho(1-(N-1))v_n[N-1]v_n[1]=\lambda_n v_n[1]^2,\\
&\rho(2)v_n[0]v_n[2]+\rho(1)v_n[1]v_n[2]+2Wv_n[2]^2+\cdots+\rho(2-(N-1))v_n[N-1]v_n[2]=\lambda_n v_n[2]^2,\\
&\qquad\qquad\qquad\qquad\qquad\qquad\qquad\qquad\cdots=\cdots,\\
&\rho(N-1)v_n[0]v_n[N-1]+\rho(N-2)v_n[1]v_n[N-1]+\rho(N-3)v_n[2]v_n[N-1]+\cdots+2Wv_n[N-1]^2=\lambda_n v_n[N-1]^2
\end{aligned}\tag{3.81}$$

Sum the above equations together along the diagonal directions, and consider $\rho(\tau)=\rho(-\tau)$, obtain the following equation

$$2W\sum_{k=0}^{N-1}v_n[k]^2+4\rho_1\sum_{k=0}^{N-1-1}v_n[k]v_n[k+1]+4\rho_2\sum_{k=0}^{N-1-2}v_n[k]v_n[k+2]+\cdots+4\rho_{N-1}\sum_{k=0}^{N-1-(N-1)}v_n[k]v_n[k+N-1]=\lambda_n\sum_{k=0}^{N-1}v_n[k]^2. \tag{3.82}$$

Consider the normalization constraint $\sum_{k=0}^{N-1} v_n[k]^2 = 1$,

$$\lambda_n = 2W \sum_{k=0}^{N-1} v_n[k]v_n[k] + 4 \sum_{\tau=1}^{N-1} \rho(\tau) \sum_{k=0}^{N-\tau-1} v_n[k]v_n[k+\tau], \tag{3.83}$$

$$= 2 \left(Wq_0 + 2 \sum_{\tau=1}^{N-1} \frac{\sin(2\pi W\tau)}{\pi\tau} q_\tau \right). \tag{3.84}$$

Percival and Walden [65] note that (3.76) is an efficient way to compute the eigenvalues since q_τ, $\tau = 0, 1, \ldots, N-1$, has the form of an auto-covariance sequence and can be computed using fast algorithms, such as FFTs.

In the Matlab Signal Processing Toolbox [52], there is a Matlab routine *[v, e] = dpss(n, n * W)* to generate the DPSS's of length n in the columns of v, and their corresponding concentrations in vector e, W is the normalized half-bandwidth, $0 \leq W < 1/2$. Although the routine *dpss* is used for multi-taper spectral analysis in Matlab, it can be directly used here to generate a robust vibration suppression profile based on the idea described in this chapter.

3.4.2 Discrete-Time Prolate Spheroidal Sequences with an Arbitrary Sampling Period

If the sampling interval is T_s sec/sample, the resultant Nyquist frequency is $\frac{1}{2T_s}$ Hz or $\frac{\pi}{T_s}$ rad/sec. If the energy of DPSS's is concentrated to the bandwidth at Ω rad/sec, the normalized bandwidth W is

$$W = \frac{\Omega T_s}{2\pi}. \tag{3.85}$$

So the Matlab routine *[v, e] = dpss(n, n * W)* can be used again to generate the DPSS's.

3.5 Robust Vibration Suppression Shape Filter and Control Profile Design

In this section, robust vibration suppression shape filter and control profile generation based on discrete prolate spheroidal sequences are studied.

Assume that the frequency bandwidth to be $\Omega_0 = 9.68 \times 10^3$ rad/sec, the time duration of the DPSS is chosen to be 1.5×10^{-3} sec, and the sampling period of the discrete sequence is $T_s = 5 \times 10^{-5}$ sec. The first four discrete prolate spheroidal sequences are generated and shown in Figure 3.1. Their corresponding energy concentration is $\lambda_0 = 0.999\ 995$, $\lambda_1 = 0.999\ 730$, $\lambda_2 = 0.993\ 707$, and $\lambda_3 = 0.926\ 472$. So the zeroth order discrete prolate spheroidal sequence $v_0[k]$ achieves the optimal energy concentration in the frequency band $[-\Omega_0, \Omega_0]$. A robust vibration suppression shape filter can be generated from the zeroth order discrete prolate spheroidal sequence $v_0[k]$ by

$$f[k] = \frac{v_0[k]}{\sum_{k=0}^{N-1} v_0[k]}, \quad k = 0, 1, \cdots, N-1, \tag{3.86}$$

where N is the total data number of the sequence $v_0[k]$.

Since the initial and final values of the sequence $v_0[k]$ are not zero, the sequence $v_0[k]$ cannot be directly used as a robust vibration velocity profile. From the waveform of $v_0[k]$,

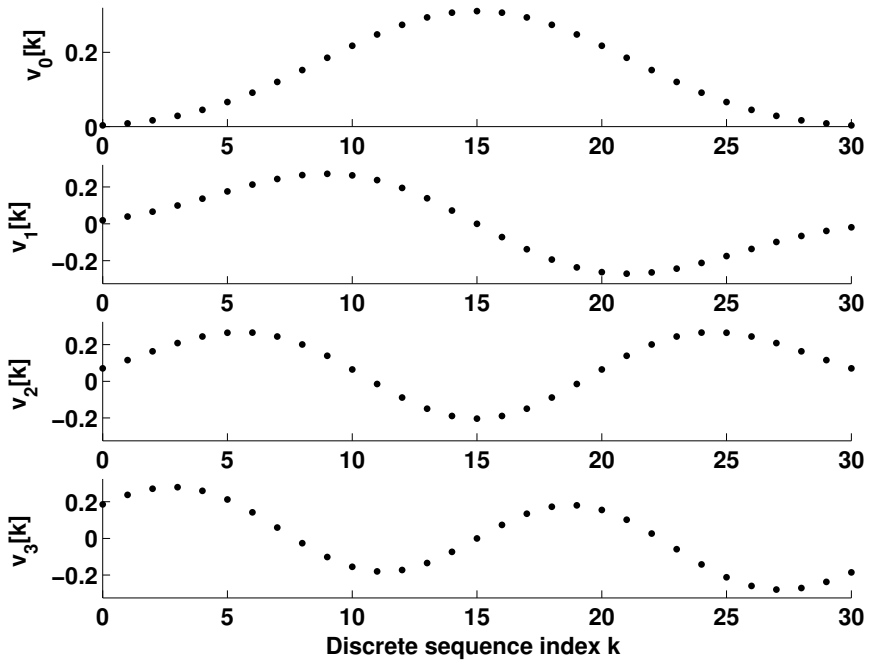

Figure 3.1: Discrete prolate spheroidal sequences for the time duration 1.5×10^{-3} sec.

it is clear that the $v_0[k]$ behaves like Gaussian functions such that the values decay sharply at the start and end points. So the sequence $v_0[k]$ can be vertically shifted down to make the start and end values to be zero,

$$vel[k] = v_0[k] - v_0[0], \quad k = 0, 1, \cdots, N-1. \tag{3.87}$$

Notice that $v_0[0] = v_0[N-1]$ because the sequence is a symmetric function. The sequence $vel[k]$, $k = 0, 1, \ldots, N-1$, can be used as a velocity profile. The resultant robust vibration suppression velocity profile is shown in Figure 3.2. Depending on the rigid body position movement, the velocity profile must be multiplied with a constant.

The discrete-time sequence of the acceleration profile $acc[k]$ can be generated from the discrete-time sequence of the velocity profile $vel[k]$ by

$$acc[k] = \frac{vel[k+1] - vel[k]}{Ts}, \tag{3.88}$$

where T_s is the sampling period. Depending on the rigid body position movement, the acceleration profile must be multiplied with a constant.

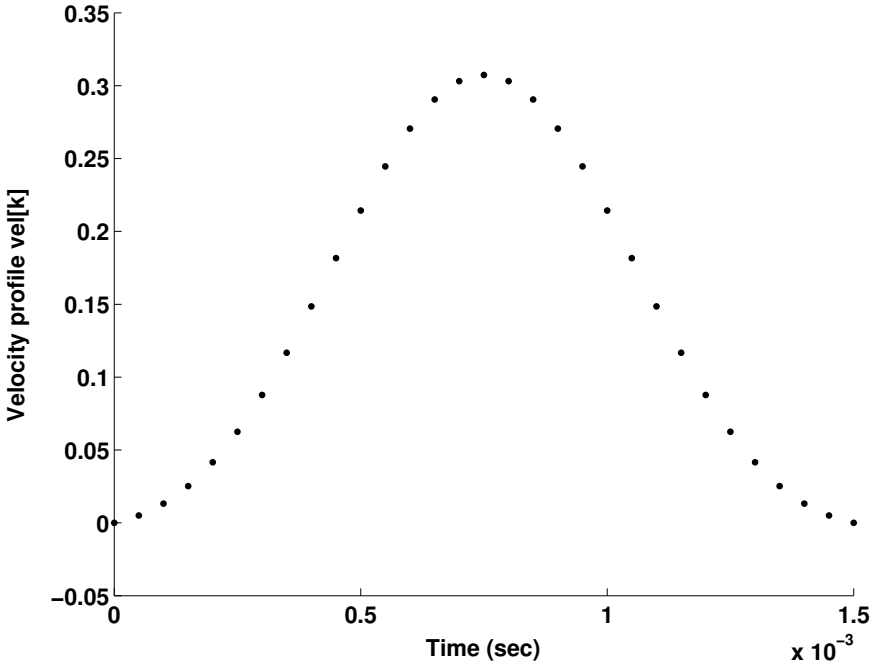

Figure 3.2: A robust vibration suppression velocity profile from discrete prolate spheroidal sequence $v_0[k]$ with the move time 1.5×10^{-3} sec.

The vertically shifted discrete prolate spheroidal sequence $vel[k]$ slightly impairs its energy concentration. For the above example, the energy concentration measure $\beta^2(W)$ of $vel[k]$ is approximately $0.999\ 979$. Compared with the optimal energy concentration value $\lambda_0 = 0.999\ 995$, the vertically shifted version of $v_0[k]$, i.e., $vel[k]$ only loses a little energy concentration. With the decrease of the move time, the difference of the energy concentration measure between $v_0[k]$ and $vel[k] = v_0[k] - v_0[0]$ will increase. Figure 3.3 shows the difference of the energy concentration measure $\beta^2(W)$ between $v_0[k]$ and $vel[k] = v_0[k] - v_0[0]$ from the move time 0.5×10^{-3} sec to move time 1.5×10^{-3} sec. It shows that at the time duration of 0.5×10^{-3} sec, the difference of the energy concentration measure between $v_0[k]$ and $vel[k] = v_0[k] - v_0[0]$ is about $0.958 - 0.888 = 0.070$. The big difference is caused because the initial and final values of the optimal energy concentrated DPSS $v_0[k]$ are very large. For the time duration of 0.5×10^{-3} sec, the resultant $v_0[k]$ with the same frequency band Ω_0 is shown in Figure 3.4. It clearly shows that the initial and final

values of the discrete sequence $v_0[k]$ decay slowly, so the choose of time duration of the discrete sequence as 0.5×10^{-3} sec is not suitable to suppress all the resonance frequency ($\geq \Omega_0 = 9.68 \times 10^3$ rad/sec) modes in a flexible system. The plot of energy concentration measure with respect to the time duration gives a tradeoff between energy concentration measure and time duration when the first resonance frequency Ω_0 and the sampling period T_s are determined.

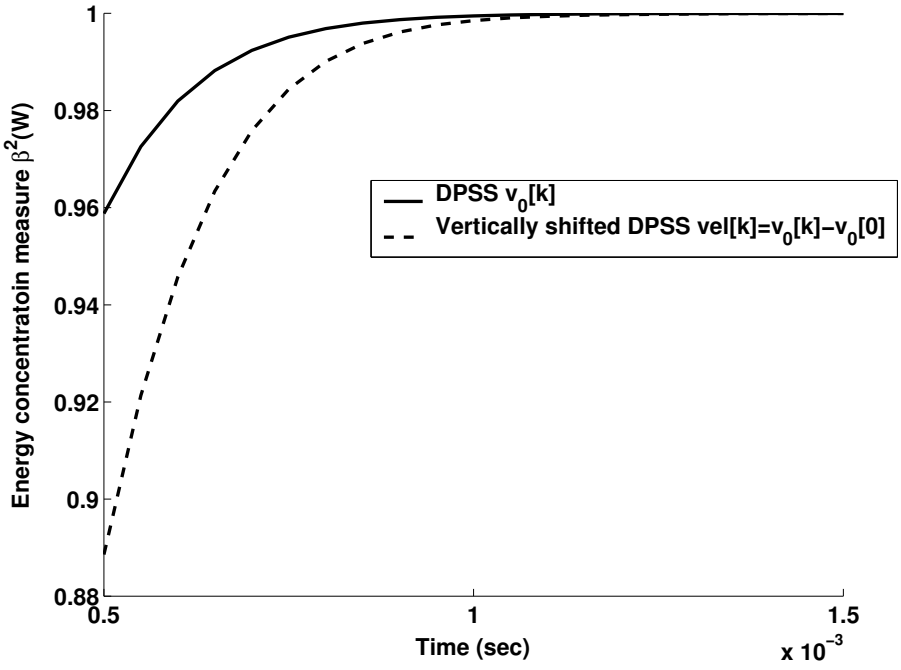

Figure 3.3: The difference of the energy concentration measure $\beta^2(W)$ between $v_0[k]$ and $vel[k] = v_0[k] - v_0[0]$.

Notice the first order optimal energy concentrated discrete prolate spheroidal sequence $v_1[k]$ in Figure 3.1 can be directly used as an acceleration profile. From computation, the resultant velocity profile is almost the same as $vel[k]$ in the sense of energy concentration in the frequency band $\omega \leq |\Omega_0|$.

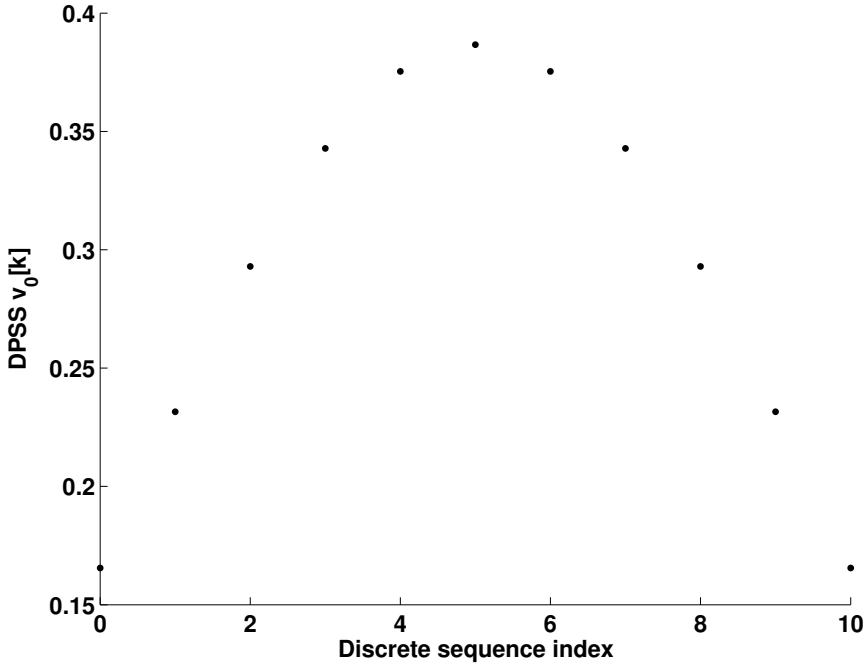

Figure 3.4: DPSS $v_0[k]$ with the time duration 0.5×10^{-3} sec.

3.6 Simulation Results for Hard Disk Drive Seek Control

In this section, the discrete prolate spheroidal sequence is used to design a robust acceleration profile to suppress all the resonance modes in a hard disk model. Consider the following flexible system which is embedded in a hard disk assembly, where the input is the current signal in amps and the output is the position signal in tracks.

$$H(s) = K_c \cdot K_v \cdot K_p \cdot R(s)\frac{1}{s^2}, \tag{3.89}$$

where $K_c = 8.125 \, \frac{\text{tracks/sample}^2}{\text{amp}}$ is a constant gain from current to acceleration, $K_v = 1/T_s = 2 \times 10^4 \, \frac{\text{samples}}{\text{sec}}$ is the velocity gain, $K_p = 1/T_s = 2 \times 10^4 \, \frac{\text{samples}}{\text{sec}}$ is the position gain, and $R(s)$ is a 28^{th} order resonance structure. The Bode magnitude plot of $R(s)$ is shown in Figure 1.2.

With parameters settings $\Omega_0 = 9.68 \times 10^3$ rad/sec, a move time of 2.5×10^{-3} sec, and a sampling period of $T_s = 5 \times 10^{-5}$ sec, the first two discrete prolate spheroidal sequences are shown in Figure 3.5. Their corresponding concentrations (3.1) in the frequency band

$|\omega| \leq \Omega_0$ are approximately $0.999\ 999\ 999$ and $0.999\ 999\ 937$. Here, the discrete-time sequences to generate the discrete-time Fourier transform in (3.1) are the first two discrete prolate spheroidal sequences as shown in Figure 3.5. So the waveform $v_0[k]$ gives the best concentration to cut off the high frequency resonance components. The acceleration profile $acc[k]$ can be derived from $v_0[k]$ through (3.87) and (3.88). Alternatively, $v_1[k]$ can be directly used as the acceleration profile candidate. From computation, the resultant velocity profile is almost the same as $vel[k]$ in the sense of energy concentration in the frequency band $\omega \leq |\Omega_0|$.

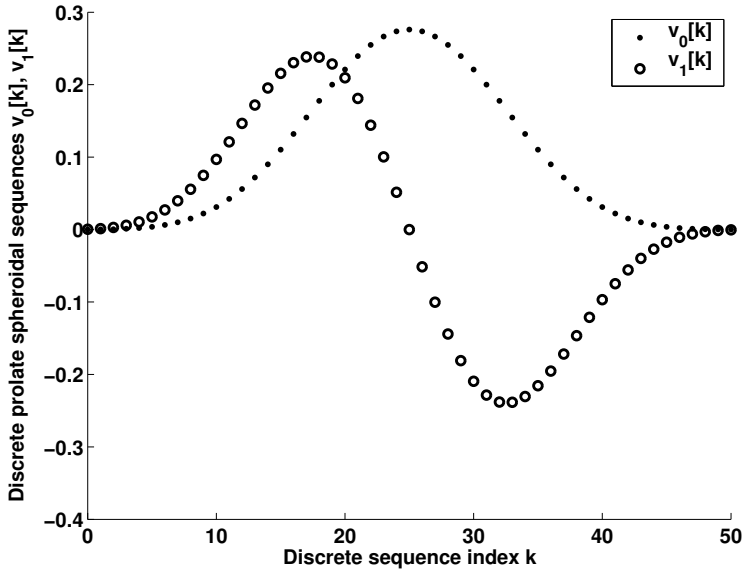

Figure 3.5: Discrete prolate spheroidal sequences for the move time 2.5×10^{-3} sec.

Next, $v_0[k]$ is used to design the control input signal. Figure 3.6 shows the current signal. Figure 3.7 shows the jerk signal, which is the derivative of the current signal. Figure 3.8 shows the position signal. Figure 3.9 shows the position signal near the target track. It shows that the position signal settles within $\pm\frac{5}{100}$ track immediately after the move time of 2.5×10^{-3} sec. So the current signal suppresses the residual vibration induced by all the resonance modes. Now, the current signal is analyzed from the filter point of view. Figure 3.10 shows the reference velocity signal. This signal is treated as the impulse response of a Finite Response Filter. The magnitude of the frequency response of this Finite

Response Filter is shown in Figure 3.11. It is clear that this Finite Response Filter has very good cutoff of high frequency signals.

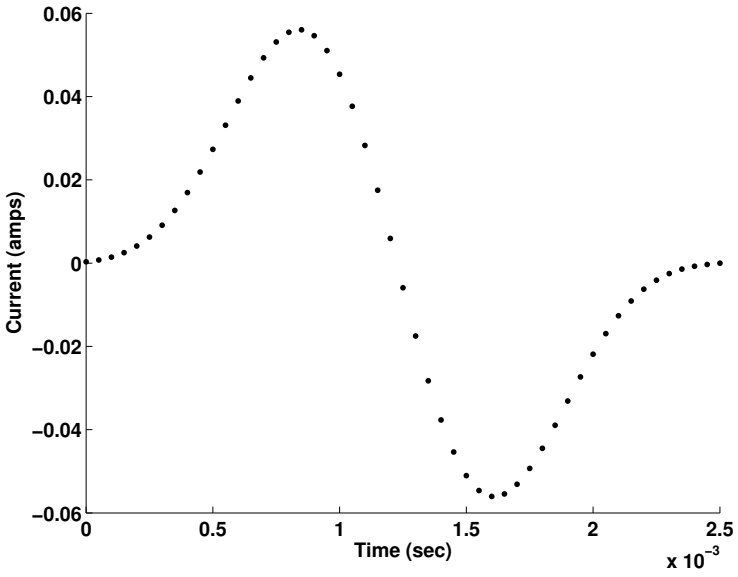

Figure 3.6: Current control input signal.

It must be noted that the control input move time cannot be arbitrarily reduced if a certain seek time is required. It depends on the resonance characteristics. As shown in Chapter 2, a signal cannot arbitrarily achieve both time and frequency localization. Reducing move time will result a poor frequency concentration. Figure 3.12 shows the concentration $1 - J$ defined in (3.2) of the current control input with different move time for the same sampling period and first resonance frequency given before. From Figure 3.12, if the move time of the control input is chosen to be 0.5 msec, the minimal proportion of its energy after the first resonance is about 0.4 which is very poor. There is a tradeoff between the move time of a control input and its concentration in the frequency domain as shown in Figure 3.12.

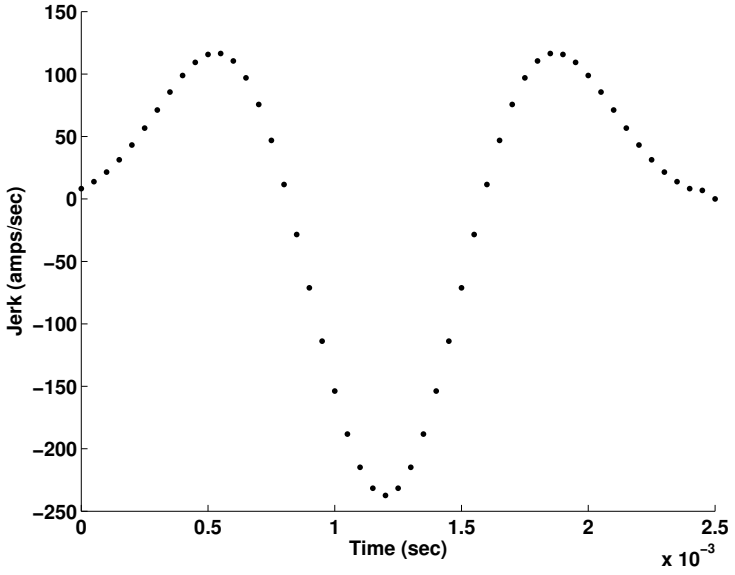

Figure 3.7: Jerk signal.

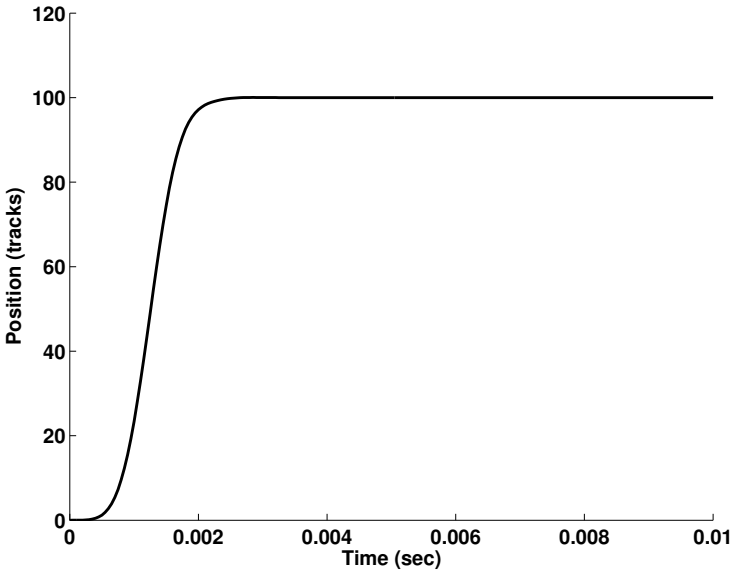

Figure 3.8: Position signal.

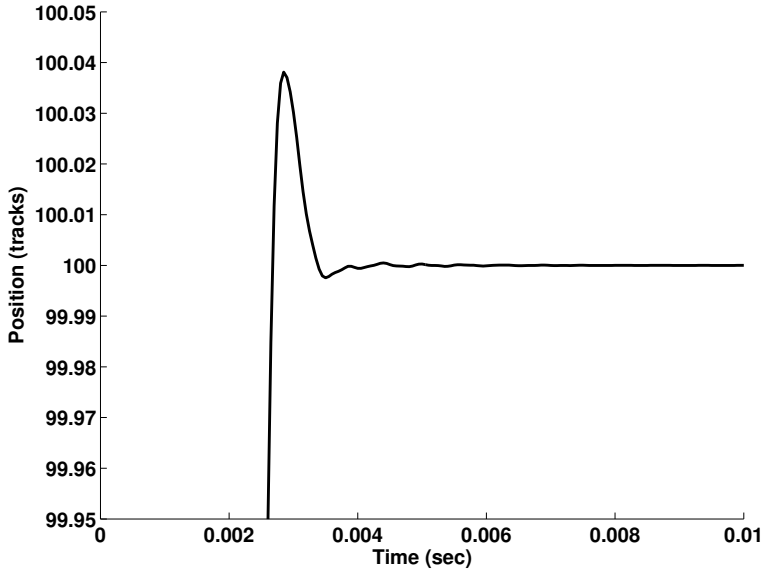

Figure 3.9: Position signal near the target track.

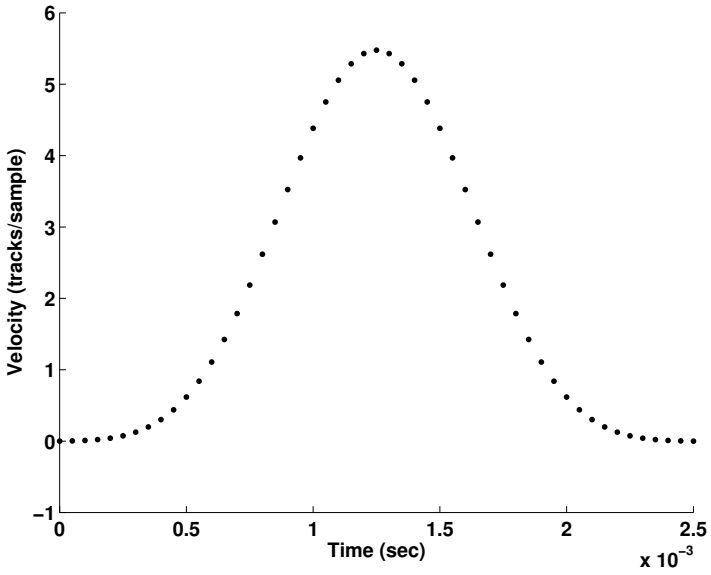

Figure 3.10: Reference velocity signal.

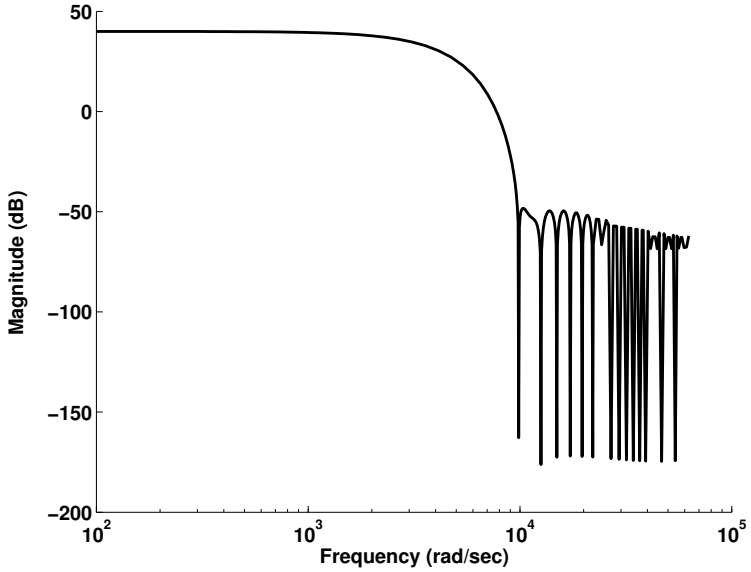

Figure 3.11: Frequency response of the Finite Response Filter.

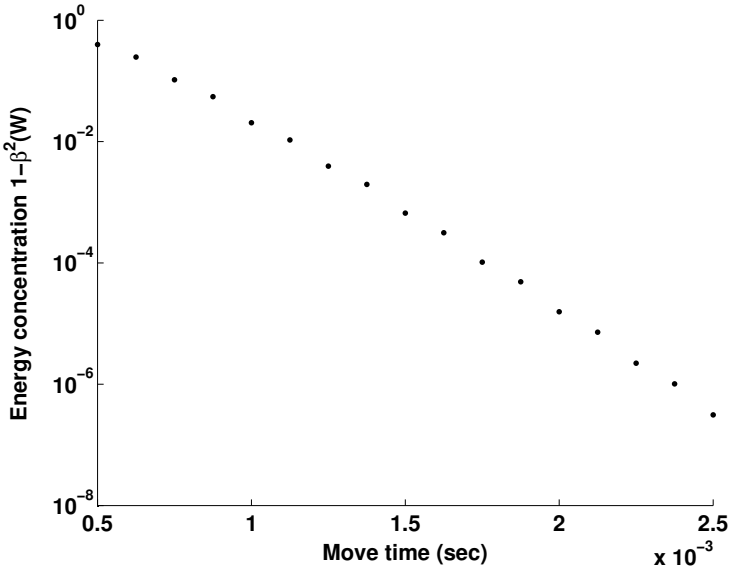

Figure 3.12: Concentration $1 - \beta^2(W)$ of current control input with different move time.

3.7 Experimental Results on Flexible Link with Strain Gauge

3.7.1 Open-Loop Control

First, the time-optimal control algorithm will be implemented based on the simplified model. The time-optimal command of 50 deg slew angle θ and experimental results of the corresponding total angle are shown in Figure 3.13. Residual vibrations is clearly visible after the end of the time-optimal command. The maximal range of the deflection is over 20 deg. This is caused by the uncertainties of the plant. From the analysis of the Chapter 2, the optimal-control is very sensitive to model uncertainty.

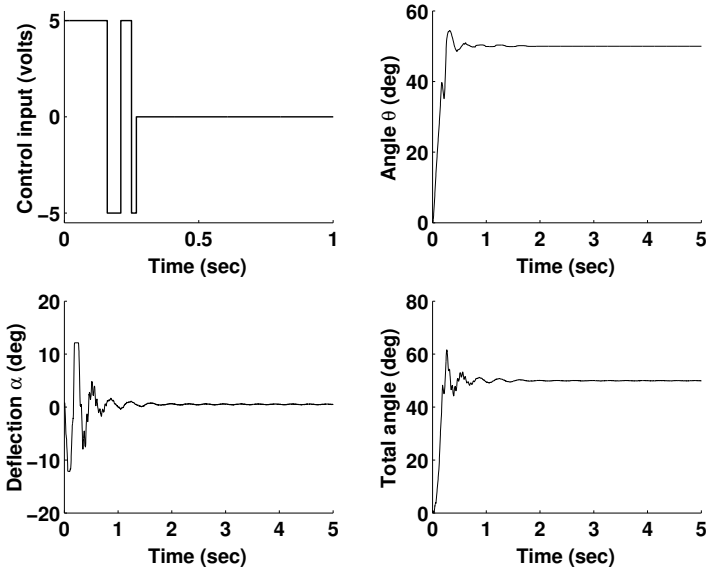

Figure 3.13: Time-optimal command input and output total angle.

Next, the discrete prolate spheroidal sequence function is used to generate the robust open-loop control input forcing function. The robust forcing function can be derived as shown in Figure 1.12. Consider the DC motor servo dynamic model in Figure 2.29, the

applied motor voltage is

$$\begin{aligned} V_a &= V_c + V_b \\ &= Ri + I\frac{di}{dt} + K_g K_b \dot{\theta}. \end{aligned} \tag{3.90}$$

The armature current i has a relationship with the acceleration signal $\ddot{\theta}$ as

$$i = \frac{J_{hub}}{K_g K_m}\ddot{\theta}. \tag{3.91}$$

So both i and $\frac{di}{dt}$ can be derived from the velocity signal $\dot{\theta}$. Finally the motor applied voltage is a function of the velocity signal $\dot{\theta}$.

In the above derivations, all the signals are assumed to be continuous signals. The discrete-time signal of the applied motor voltage can be approximated from the discrete-time signal of the link velocity. If the discrete-time sequence of the velocity signal is $vel[k]$, $0 \leq k \leq M$, the discrete-time signal of the acceleration, $acc[k]$, can be approximated as

$$acc[k] = \frac{vel[k+1] - vel[k]}{T_s}, \quad 0 \leq k \leq M-1, \tag{3.92}$$

$$acc[M] = 0, \tag{3.93}$$

where T_s is the sampling period. The discrete-time signal of di/dt can be generated in a similar way.

The link is slewed 50 deg using the prolate spheroidal wave function profile based on $\Omega_0 = 2\pi \times 3$ rad/sec (the natural frequency of the flexible link) and a move time of 1 sec. Figure 3.14 shows the current, slew velocity, slew angle, and the motor applied voltage profiles. Figure 3.15 shows the experimental results with the derived motor applied voltage. Compared with the time-optimal control, the tip deflection is greatly reduced.

From Figure 3.15, there is a very large oscillation which occurs during the move time. This may be caused by the transient interaction between the flexible link and the connected parts. It includes the nonlinearity of the high transmission ratio gear and the flexible cable mounted at the clamped end of the link. This transient vibration has a frequency component

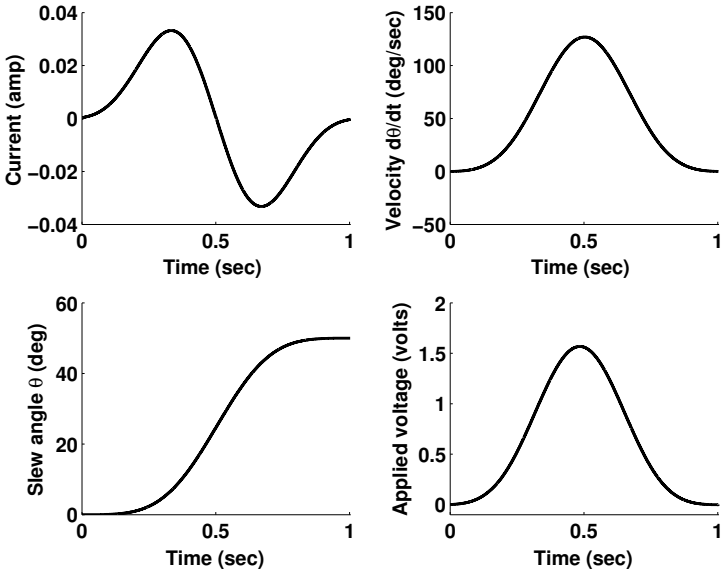

Figure 3.14: Open-loop control profiles for $\Omega_0 = 2\pi \times 3$ rad/sec and move time of 1 sec.

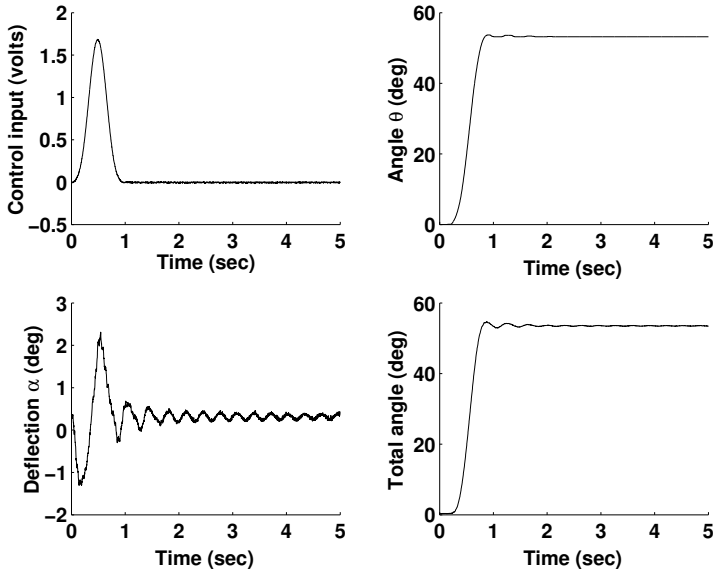

Figure 3.15: Experimental results of a flexible link open-loop control with prolate spheroidal wave-based control input ($\Omega_0 = 2\pi \times 3$ rad/sec and move time of 1 sec).

of about 1 Hz. To reduce the transient vibration, the prolate spheroidal wave function is redesigned based on $\Omega_0 = 2\pi \times 1$ rad/sec and the move time of 1 sec. Figure 3.16 shows the current, slew velocity, slew angle, and the motor applied voltage profiles for the redesigned prolate spheroidal wave. Figure 3.17 shows the experimental results with the derived motor applied voltage. Compared with Figure 3.15, both the transient vibration and the tip deflection are reduced.

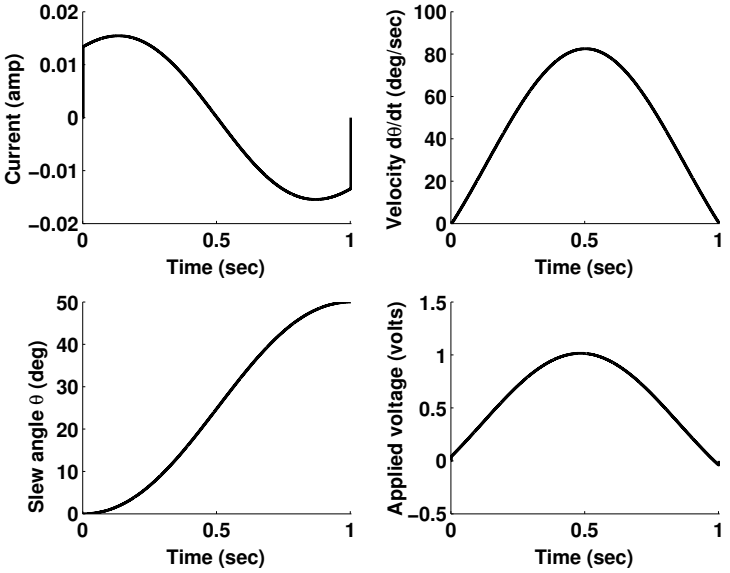

Figure 3.16: Open-loop control profiles for $\Omega_0 = 2\pi \times 1$ rad/sec and move time of 1 sec.

3.7.2 Standard Closed-Loop Control

The standard closed-loop control scheme developed in Section 1.3 is used to reduce the residual vibration of the flexible link. The discrete prolate spheroidal sequences are used to generate the robust vibration suppression position references.

Figure 3.18 shows the discrete prolate spheroidal sequence profiles with $\Omega_0 = 9$ rad/sec, $T_s = 0.002$ sec, and the slew angle $\theta = 50$ deg, where Ω_0 is the approximate first resonance frequency of the closed-loop system. Figure 3.19 shows the robust position reference profiles during the move time. After the move time, the position reference holds its final value.

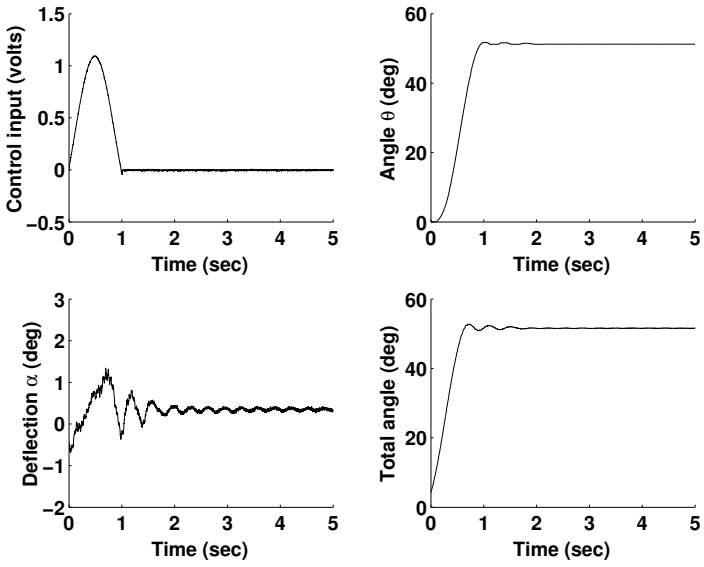

Figure 3.17: Experimental results of a flexible link open-loop control with prolate spheroidal wave-based input ($\Omega_0 = 2\pi \times 1$ rad/sec and move time of 1 sec).

Figure 3.20 shows the proportion of the energy after the frequency Ω_0, i.e. $1 - J$ in (3.2). Here the discrete-time sequences to generate the discrete-time Fourier transform in (3.2) are the discrete prolate spheroidal sequences as shown in Figure 3.18. Figure 3.21 shows the real energy distribution of each robust velocity reference signal sequence.

Figure 3.22 shows the experimental results with the robust position reference profile with the move time of 1 sec. It shows the tip vibration (at the left bottom plot) almost stops at the end of the move time. Figure 3.23 shows the experimental results with the step reference input. Clearly the tip vibration (at the left bottom plot) is very large during the move time and decays very slowly after the move time. In testing, the vibration of the tip of the flexible link was clearly visible.

From Figure 3.18, it is known the initial and final values of the discrete prolate spheroidal sequences are not zero. The discrete prolate spheroidal sequence may be vertically shifted down to force it to start at zero and end at zero. The resultant sequence $vel[k] = v_0[k] - v_0[0]$ as shown in Figure 3.24 can be used as a velocity profile. Although the optimality of the best concentration property is impaired for short move time, the velocity reference becomes

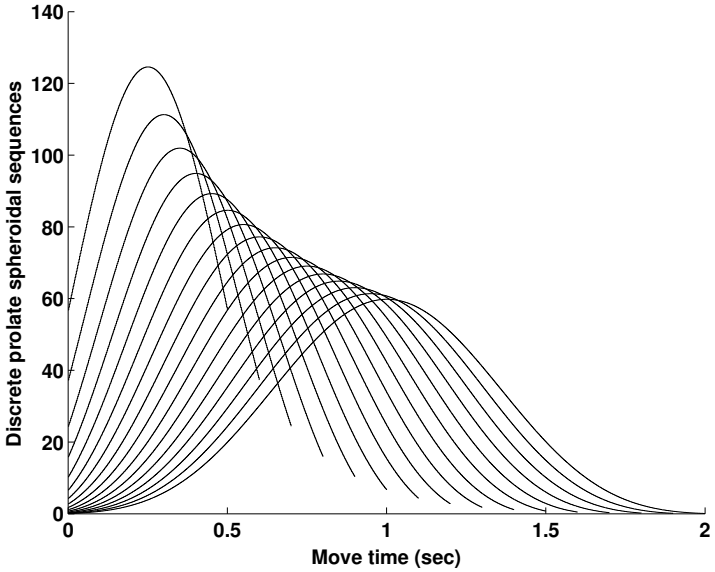

Figure 3.18: Discrete prolate spheroidal sequences.

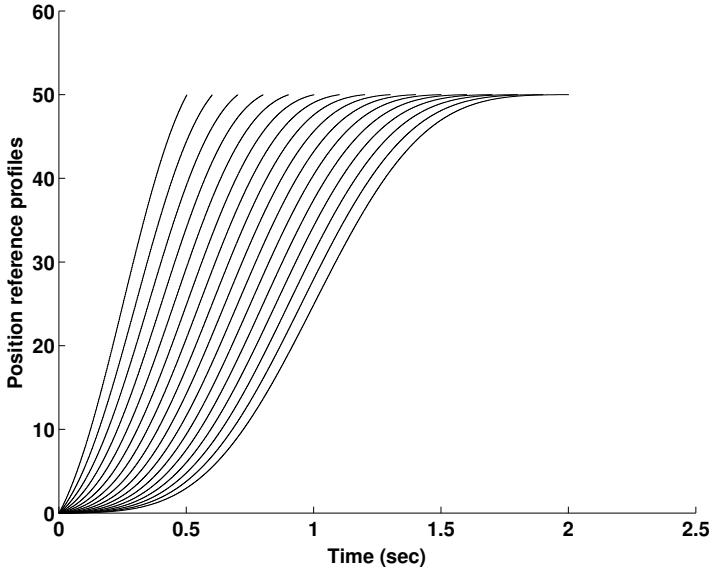

Figure 3.19: Position reference profiles.

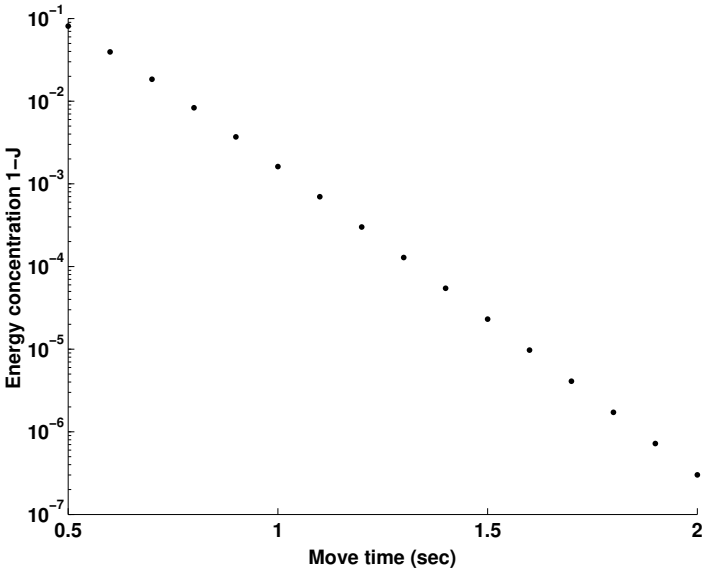

Figure 3.20: The proportion of the energy after Ω_0.

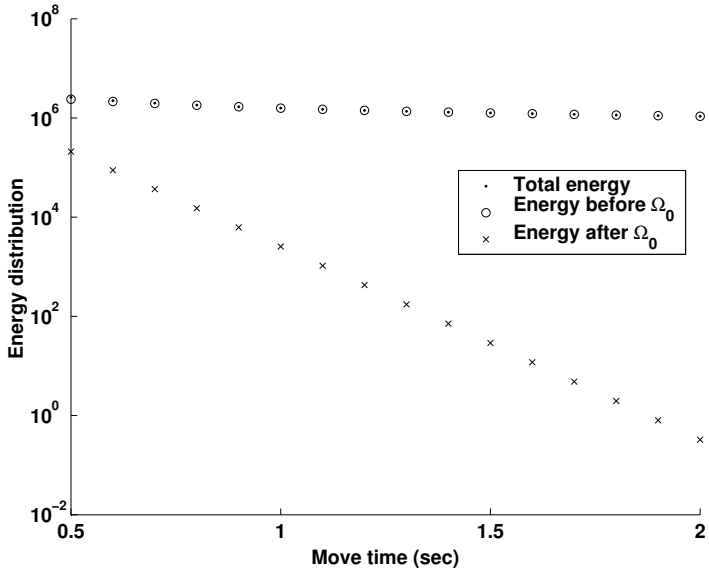

Figure 3.21: The energy distribution of the robust velocity reference profiles.

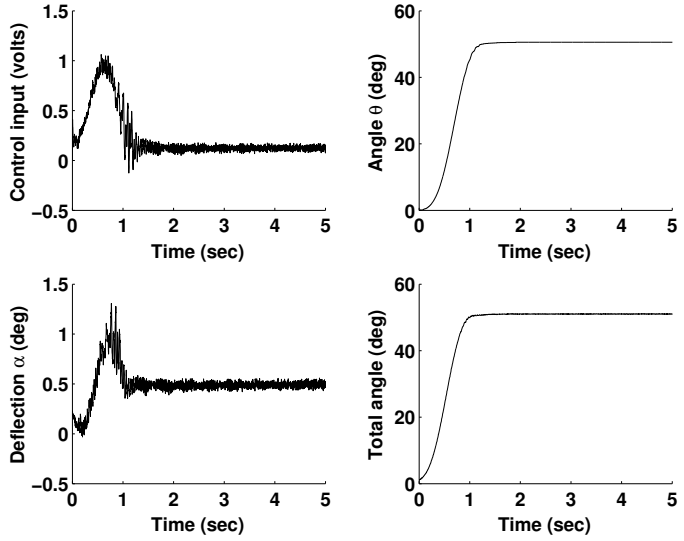

Figure 3.22: Experimental results of a flexible link closed-loop control with robust position reference.

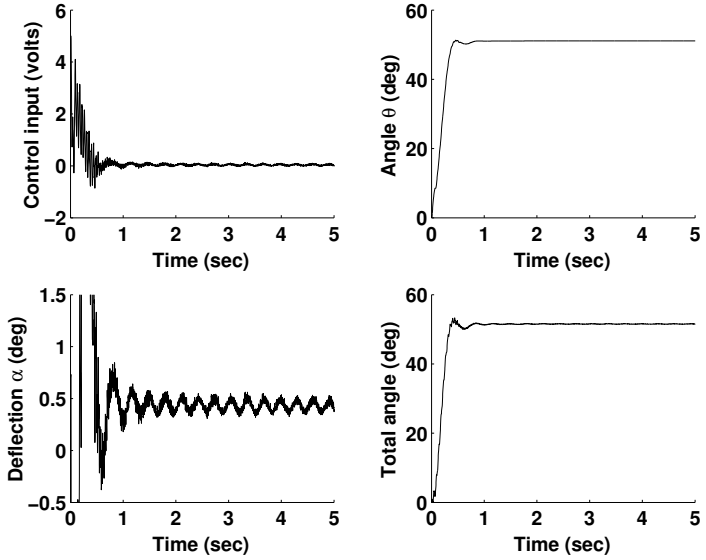

Figure 3.23: Experimental results of a flexible link closed-loop control with step reference.

smooth at the start and the end of the movement. Figure 3.25 shows the robust position reference profiles with zero initial and final velocities. Figure 3.26 shows the experimental results with this robust position reference and the move time of 1 sec. It shows the results are almost the same as the results of the nonzero initial and final DPSS profile.

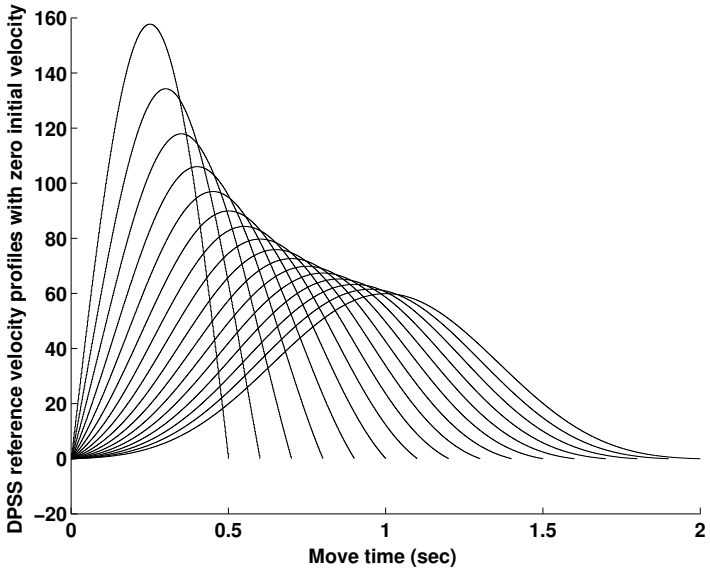

Figure 3.24: Vertically shifted prolate spheroidal waves.

3.7.3 Model Reference Closed-Loop Control

The model reference closed-loop control scheme developed in Section 1.3 is here to reduce the residual vibration of the flexible link. Again, the prolate spheroidal wave functions are used to generate the robust velocity references. The robust forcing function can be derived as shown in Figure 1.12. From the DC motor servo dynamic model in Figure 2.29, the applied motor voltage is

$$\begin{aligned} V_a &= V_c + V_b \\ &= Ri + I\frac{di}{dt} + K_g K_b \dot{\theta}. \end{aligned} \tag{3.94}$$

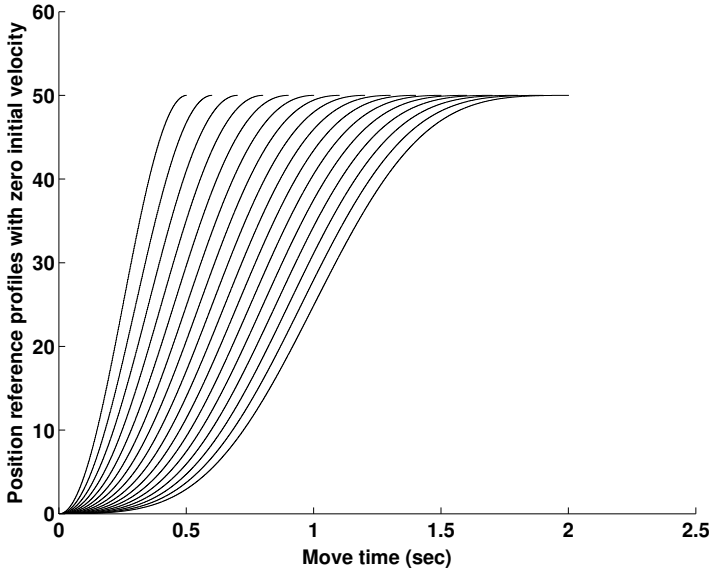

Figure 3.25: Position reference profiles with zero initial and final velocities.

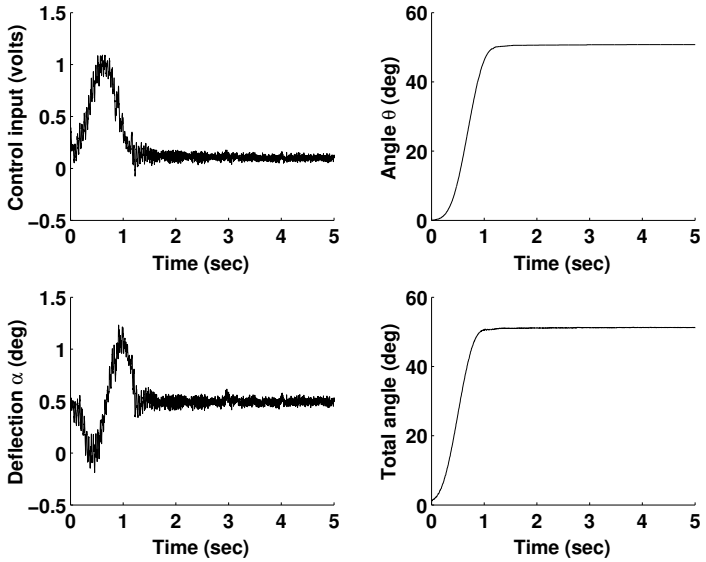

Figure 3.26: Experimental results of a flexible link closed-loop control.

The armature current i has a relationship with the acceleration signal $\ddot{\theta}$ as

$$i = \frac{J_{hub}}{K_g K_m}\ddot{\theta}. \tag{3.95}$$

So both i and $\frac{di}{dt}$ can be derived from the velocity signal $\dot{\theta}$. Finally, the motor applied voltage is a function of the velocity signal $\dot{\theta}$. In the model reference closed-loop control scheme, the velocity reference should be designed to start and end at zero to move the flexible beam from one set point to another. So in the flexible link model reference closed-loop control, the forcing function of the motor is the applied voltage, and it is generated in the same way as in open-loop control. The only difference is that Ω_0 should be chosen corresponding to the first resonance frequency of the closed-loop system.

In the above derivations, all the signals are assumed to be continuous signals. The discrete-time signal of the applied motor voltage can be approximated from the discrete-time signal of the link velocity. If the discrete-time sequence of the velocity signal is $vel[k]$ from (3.87), the discrete-time signal of the acceleration, $acc[k]$, can be approximated from (3.88). The discrete-time signal of di/dt can be generated in a similar way.

Figure 3.27 shows the model reference control profiles generated from the move time of 1 sec and $\Omega_0 = 9$ rad/sec. Figure 3.28 shows the experimental results with the robust forcing function. It shows the tip vibration (at the left bottom plot) almost stops at the end of the move time. In many industry applications, the plant is actuated by a current source supply as shown in Section 4.13. In the current source power supply, the generation of the current profile is the same as that of Section 4.13.

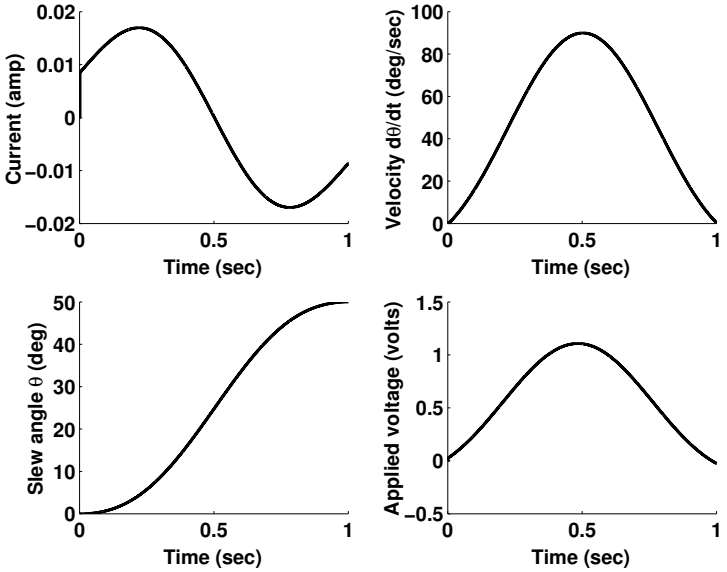

Figure 3.27: Model reference control profiles.

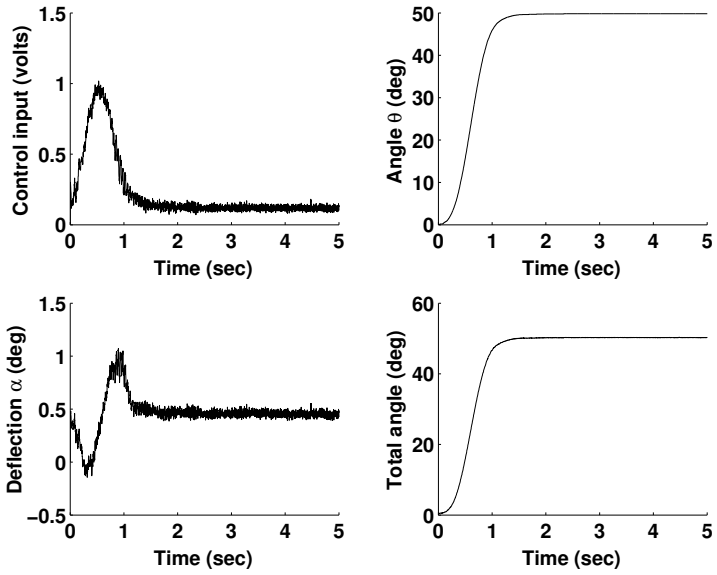

Figure 3.28: Experimental results of a flexible link model reference control.

Chapter 4

Robust Vibration Suppression Shape Filter Generation for a Specific Resonance Mode

4.1 Philosophy Development

In the previous chapters, a robust vibration suppression profile is generated based on the time-frequency uncertainty and prolate spheroidal wave functions. The robust control profile suppresses all the high frequency ($\geq \Omega_0$) resonance modes. In practical system, a lower resonance frequency mode may exist which is located far from the high frequency resonance modes as shown in Figure 4.1. The lower frequency resonant modes may come from several factors. For example, the lower frequency resonant modes of the flexible arm in a hard disk drive include the transient interaction between the flexible arm and the connected parts, such as the flexible cable.

If the low frequency Ω_1 in Figure 4.1 is chosen to be a bandwidth in the generation of prolate spheroidal wave functions, the time duration of the shape filter is inefficiently increased. The research discussed in this chapter generates a robust vibration suppression profile for a given specific resonant mode.

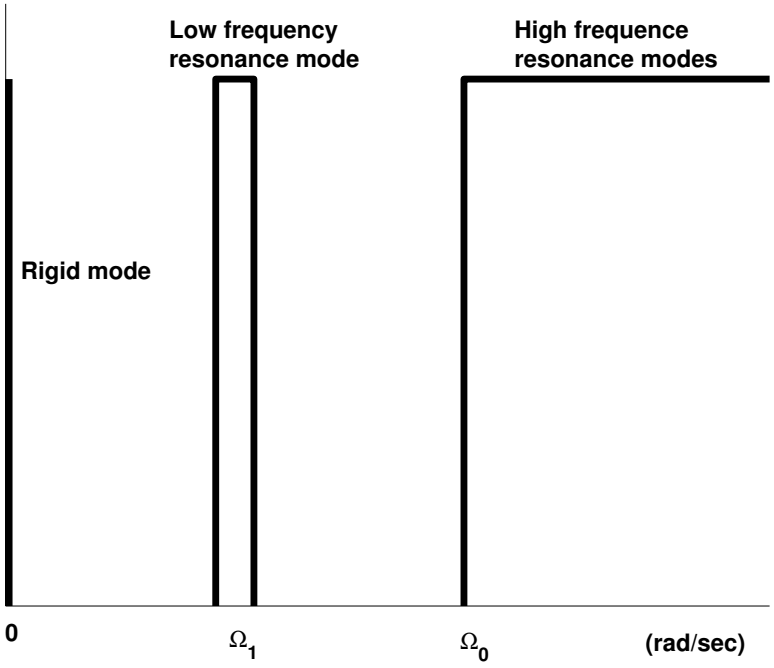

Figure 4.1: Illustration of existence of a low resonance frequency mode located far from the high frequency modes in a flexible system.

The key point here is to find the relationship between the finite control forcing function and the amplitude spectrum of the residual vibration in the modal description of a flexible system.

4.2 Relationship Between Control Input and Residual Vibration

The relationship between the Fourier transform of the control forcing function and the residual vibrations in time domain is derived.

4.2.1 Undamped Case

Consider a unidirectional flexible mechanical system in the modal equation description

$$\ddot{x}_0(t) = z_0 u(t), \tag{4.1}$$

$$\ddot{x}_i(t) + \omega_i^2 x_i(t) = z_i u(t), \quad i = 1, 2, 3, \cdots, \tag{4.2}$$

where x_0 is the rigid mode displacement and x_i, $i \geq 1$, are the resonant mode displacements. The variable $u(t)$ is a control forcing function, z_i is coefficient corresponding to the i^{th} mode ($0 \leq \zeta_i < 1$) and ω_i is the natural angular frequency of the i^{th} mode.

Assume the mechanical system is stationary initially, the displacement and velocity of the i^{th} natural mode of vibration due to the forcing function $u(t)$ are given as:

$$x_i(t) = \frac{z_i}{\omega_i} \int_0^t \sin\left(\omega_i(t-\tau)\right) u(\tau) d\tau, \quad i \geq 1, \tag{4.3}$$

$$\dot{x}_i(t) = z_i \int_0^t \cos\left(\omega_i(t-\tau)\right) u(\tau) d\tau, \quad i \geq 1. \tag{4.4}$$

If the time duration of the forcing function is T_0, i.e., $u(t) = 0, t > T_0$, the Fourier transform of the forcing function is

$$U(\omega) = \int_0^\infty u(t) e^{-j\omega t} dt = \int_0^{T_0} u(t) e^{-j\omega t} dt. \tag{4.5}$$

The displacement and velocity of a resonant mode at the end of the move time T_0 are given by:

$$x_i(T_0) = \frac{z_i}{\omega_i} \int_0^{T_0} \sin\left(\omega_i(T_0-\tau)\right) u(\tau) d\tau, \quad i \geq 1, \tag{4.6}$$

$$\dot{x}_i(T_0) = z_i \int_0^{T_0} \cos\left(\omega_i(T_0-\tau)\right) u(\tau) d\tau, \quad i \geq 1. \tag{4.7}$$

A relationship between the end conditions of the resonant modes at $t = T_0$ and the Fourier transform of the forcing function can be derived as

$$\frac{\dot{x}_i(T_0)}{\omega_i} + j x_i(T_0) = \frac{z_i}{\omega_i} \int_0^{T_0} u(\tau) e^{j\omega_i(T_0-\tau)} d\tau, \tag{4.8}$$

$$= \frac{z_i}{\omega_i} e^{j\omega_i T_0} \int_0^{T_0} u(\tau) e^{-j\omega_i \tau} d\tau, \tag{4.9}$$

$$= \frac{z_i}{\omega_i} e^{j\omega_i T_0} U(\omega_i). \tag{4.10}$$

After the move time T_0, the forcing function is zero, i.e., $u(t) = 0, t > T_0$, so the system becomes a free vibration. For each resonant mode, the displacement condition $x_i(T_0)$ and velocity condition $\dot{x}_i(T_0)$ determine the subsequent oscillation completely. And the residual vibration amplitude is given by the following equation [30]:

$$C_i(T_0) = \sqrt{\frac{\dot{x}_i^2(T_0)}{\omega_i^2} + x_i^2(T_0)}. \tag{4.11}$$

From (4.10), the residual vibration amplitude can be described in terms of the Fourier transform of the forcing function as in (4.12)

$$C_i(T_0) = \sqrt{\frac{\dot{x}_i^2(T_0)}{\omega_i^2} + x_i^2(T_0)} = \frac{|z_i|}{\omega_i}|U(\omega_i)|. \tag{4.12}$$

So a conclusion may be drawn on the relationship between the residual vibration and the control input.

Conclusion 4.2.1 *Given a forcing function $u(t)$, $0 \leq t \leq T_0$, the residual vibration of the i^{th} mode immediately after the move time T_0 is eliminated, i.e., $C_i(T_0) = 0$, if and only if the magnitude spectrum of the forcing function has zero value at the natural frequency ω_i, i.e., $U(\omega_i) = 0$.*

Proof. Obviously, $C_i(T_0) = 0 \Rightarrow x_i(T_0) = \dot{x}_i(T_0) = 0 \Rightarrow U(\omega_i) = 0$. Similarly, $U(\omega_i) = 0 \Rightarrow x_i(T_0) = \dot{x}_i(T_0) = 0 \Rightarrow C_i(T_0) = 0$. ■

Robustness can be improved if higher order derivatives of $U(\omega)$ with respect to ω at $\omega = \omega_i$ are set to zero, i.e.,

$$\left.\frac{d^k U(\omega)}{d\omega^k}\right|_{\omega=\omega_i} = 0, \quad k = 1, \cdots, n. \tag{4.13}$$

In addition to $U(\omega_i) = 0$, the n (≥ 1) constraints in (4.13) flatten the spectrum of $U(\omega)$ at $\omega = \omega_i$. So the additional constraints in (4.13) make the values of $|U(\omega)|$ around $\omega = \omega_i$ be close to the value of $|U(\omega_i)|$ which is zero.

The relationship in (4.12) is also studied by Yamamura and Ono [107].

4.2.2 Damped Case

Consider a unidirection flexible mechanical system with damping in the modal equation description

$$\ddot{x}_0(t) = z_0 u(t), \tag{4.14}$$

$$\ddot{x}_i(t) + 2\zeta_i\omega_i\dot{x}_i(t) + \omega_i^2 x_i(t) = z_i u(t), \quad i = 1, 2, 3, \cdots, \tag{4.15}$$

where x_0 is the rigid mode displacement and x_i, $i \geq 1$, are the resonant mode displacements. $u(t)$ is a control forcing function, ζ_i is damping ratio of the i^{th} mode, $0 \leq \zeta_i < 1$, and ω_i is the natural angular frequency of the i^{th} mode. The damped natural frequency is $\omega_{di} = \sqrt{1-\zeta_i^2}\omega_i$. Here both ω_i and ω_{di} have units of rad/sec.

Assume the mechanical system is stationary initially, the displacement and velocity of the i^{th} natural mode of vibration due to the forcing function $u(t)$ are given as:

$$x_i(t) = \frac{z_i}{\omega_{di}} \int_0^t e^{-\zeta_i\omega_i(t-\tau)} \sin\left(\omega_{di}(t-\tau)\right) u(\tau) d\tau, \quad i \geq 1, \tag{4.16}$$

$$\dot{x}_i(t) = \frac{z_i}{\sqrt{1-\zeta_i^2}} \int_0^t e^{-\zeta_i\omega_i(t-\tau)} \Big(\sqrt{1-\zeta_i^2} \cos\left(\omega_{di}(t-\tau)\right) - \zeta_i \sin\left(\omega_{di}(t-\tau)\right) \Big)$$
$$u(\tau) d\tau, \quad i \geq 1. \tag{4.17}$$

If the time duration of the forcing function is T_0, i.e., $u(t) = 0, t > T_0$, the Fourier transform of the forcing function is

$$U(\omega) = \int_0^\infty u(t) e^{-j\omega t} dt = \int_0^{T_0} u(t) e^{-j\omega t} dt. \tag{4.18}$$

The displacement and velocity of a resonant mode at the end of the move time T_0 are given by:

$$x_i(T_0) = \frac{z_i}{\omega_{di}} \int_0^{T_0} e^{-\zeta_i\omega_i(T_0-\tau)} \sin\left(\omega_{di}(T_0-\tau)\right) u(\tau) d\tau, \quad i \geq 1, \tag{4.19}$$

$$\dot{x}_i(T_0) = \frac{z_i}{\sqrt{1-\zeta_i^2}} \int_0^{T_0} e^{-\zeta_i\omega_i(T_0-\tau)} \Big(\sqrt{1-\zeta_i^2} \cos\left(\omega_{di}(T_0-\tau)\right) - \zeta_i \sin\left(\omega_{di}(T_0-\tau)\right) \Big)$$
$$u(\tau) d\tau, \quad i \geq 1. \tag{4.20}$$

To derive the relationship between the end condition of the resonant modes and the Fourier transform of the forcing function, a manipulation is needed to handle (4.19) and (4.20). From (4.20), the following equation holds

$$\frac{\dot{x}_i(T_0)}{\omega_i} = \frac{z_i e^{-\zeta_i\omega_i T_0}}{\sqrt{1-\zeta_i^2}\omega_i}\int_0^{T_0} e^{\zeta_i\omega_i\tau}\Big(\sqrt{1-\zeta_i^2}\cos\left(\omega_{di}(T_0-\tau)\right)-\zeta_i\sin\left(\omega_{di}(T_0-\tau)\right)\Big)u(\tau)d\tau. \tag{4.21}$$

From (4.19), the following equations hold

$$\zeta_i x_i(T_0) = \frac{z_i e^{-\zeta_i\omega_i T_0}}{\sqrt{1-\zeta_i^2}\omega_i}\int_0^{T_0} e^{\zeta_i\omega_i\tau}\zeta_i\sin\left(\omega_{di}(T_0-\tau)\right)u(\tau)d\tau \tag{4.22}$$

and

$$j\sqrt{1-\zeta_i^2}x_i(T_0) = \frac{z_i e^{-\zeta_i\omega_i T_0}}{\sqrt{1-\zeta_i^2}\omega_i}\int_0^{T_0} e^{\zeta_i\omega_i\tau}j\sqrt{1-\zeta_i^2}\sin\left(\omega_{di}(T_0-\tau)\right)u(\tau)d\tau. \tag{4.23}$$

Summation of (4.21), (4.22) and (4.23) results the following relationship between the end condition of the resonant modes and the Fourier transform of the forcing function.

$$\frac{\dot{x}_i(T_0)}{\omega_i} + \zeta_i x_i(T_0) + j\sqrt{1-\zeta_i^2}x_i(T_0) = \frac{z_i e^{-\zeta_i\omega_i T_0}}{\sqrt{1-\zeta_i^2}\omega_i}\int_0^{T_0} e^{\zeta_i\omega_i\tau}\sqrt{1-\zeta_i^2}e^{j\omega_{di}(T_0-\tau)}$$

$$u(\tau)d\tau \tag{4.24}$$

$$= \frac{z_i e^{-\zeta_i\omega_i T_0}e^{j\omega_{di}T_0}}{\omega_i}\int_0^{T_0} e^{\zeta_i\omega_i\tau}u(\tau)e^{-j\omega_{di}\tau}d\tau \tag{4.25}$$

$$= \frac{z_i e^{-\zeta_i\omega_i T_0}e^{j\omega_{di}T_0}}{\omega_i}U_e(\omega_{di}), \tag{4.26}$$

where $U_e(\omega_{di}) = \int_0^\infty u_e(t)e^{-j\omega_{di}t}dt = \int_0^{T_0} u_e(t)e^{-j\omega_{di}t}dt$ and $u_e(t) := e^{\zeta_i\omega_i t}u(t)$, $0 \le t \le T_0$.

A relationship between the end conditions of the resonant modes at $t = T_0$ and the Fourier transform of $u_e(t) = e^{\zeta_i\omega_i t}u(t)$, $0 \le t \le T_0$, can be derived as

$$\sqrt{\left[\frac{\dot{x}_i(T_0)}{\omega_i} + \zeta_i x_i(T_0)\right]^2 + (1-\zeta_i^2)x_i^2(T_0)} = \frac{|z_i|e^{-\zeta_i\omega_i T_0}}{\omega_i}|U_e(\omega_{di})|. \tag{4.27}$$

Consider the initial amplitude of the free vibration which starts at $t = T_0$,

$$C_i(T_0) = \sqrt{\frac{\dot{x}_i^2(T_0)}{\omega_i^2} + x_i^2(T_0)}. \tag{4.28}$$

The conclusion may be drawn on the relationship between the residual vibration and the control input.

Conclusion 4.2.2 *Given a forcing function $u(t)$, $0 \leq t \leq T_0$, the residual vibration of the i^{th} mode immediately after the move time T_0 is eliminated, i.e., $C_i(T_0) = 0$, if and only if the magnitude spectrum of $u_e(t) = e^{\zeta_i \omega_i t} u(t)$, $0 \leq t \leq T_0$, has zero value at the damped natural frequency ω_{di}, i.e., $U_e(\omega_{di}) = U_e(\sqrt{1-\zeta_i^2}\omega_i) = 0$.*

Proof. Obviously, $C_i(T_0) = 0 \Rightarrow x_i(T_0) = \dot{x}_i(T_0) = 0 \Rightarrow U_e(\omega_{di}) = 0$. Similarly, $U_e(\omega_{di}) = 0 \Rightarrow x_i(T_0) = \dot{x}_i(T_0) = 0 \Rightarrow C_i(T_0) = 0$. ■

The important discovery of Conclusion (4.2.2) shows that the spectrum of the forcing function $u(t)$, has zero value at the damped natural frequency $\omega = \omega_{di} = \sqrt{1-\zeta_i^2}\omega_i$, i.e., $U(\omega_{di}) = 0$, is not able to guarantee eliminating the residual vibration caused by the undamped natural frequency ω_i and damping ratio ζ_i.

Robustness can be improved if higher order derivatives of $U_e(\omega)$ with respect to ω at $\omega = \omega_{di}$ are set to zero, i.e.,

$$\left.\frac{d^k U_e(\omega)}{d\omega^k}\right|_{\omega=\omega_{di}} = 0, \quad k = 1, \cdots, n. \tag{4.29}$$

In addition to $U_e(\omega_{di}) = 0$, the n (≥ 1) constraints in (4.29) flatten the spectrum of $U_e(\omega)$ at $\omega = \omega_{di}$. So the additional constraints in (4.29) make the values of $|U_e(\omega)|$ around $\omega = \omega_{di}$ be close to the value of $|U_e(\omega_{di})|$ which is zero.

4.3 Philosophy Different from Previous Techniques

From the analysis of the relationship between control input and residual vibration of a damped resonant mode, the following conclusions are drawn.

Conclusion 4.3.1 *If there exists a finite support base function $h(t)$, $0 \leq t \leq T_0$, such that $H(\omega_{di}) = H(\sqrt{1-\zeta_i^2}\omega_i) = 0$, then, $h(t)$ may have two possible properties such that*

1. *Function $\frac{h(t)}{e^{\zeta_i\omega_i t}}$ is a robust control profile candidate to eliminate the residual vibration caused by the resonant mode with the natural frequency ω_i and the damping ratio ζ_i.*

2. *Function $\frac{h(t)}{e^{\zeta_i\omega_i t}}$ with a constraint $\int_0^{T_0}\frac{h(t)}{e^{\zeta_i\omega_i t}}dt = 1$, is a vibration suppression shape filter that can be used to filter out an arbitrary control profile, and the shaped control profile eliminates the residual vibration caused by the resonant mode with the natural frequency ω_i and the damping ratio ζ_i.*

Proof. First property: Let $u(t) = \frac{h(t)}{e^{\zeta_i\omega_i t}}$ and $H(\omega_{di}) = 0$. Obviously $u_e(t) = u(t)e^{\zeta_i\omega_i t} = \frac{h(t)}{e^{\zeta_i\omega_i t}}e^{\zeta_i\omega_i t} = h(t)$ and $U_e(\omega_{di}) = H(\omega_{di}) = 0$. From Conclusion 4.2.2, $u(t)$ is a control profile candidate that eliminates the residual vibration caused by the resonant mode with the natural angular frequency ω_i and the damping ratio ζ_i.

Second property: Assume the original control profile is given by $g(t)$, then the output shaped through a filter $\frac{h(t)}{e^{\zeta_i\omega_i t}}$ is $u(t) = \int_0^t g(t-\tau)\frac{h(\tau)}{e^{\zeta_i\omega_i \tau}}d\tau$. If the control profile $u(t)$ is to eliminate the residual vibration, the magnitude spectrum of $u_e(t) = u(t)e^{\zeta_i\omega_i t}$ must have zero value at ω_{di}. Since $u_e(t) = u(t)e^{\zeta_i\omega_i t} = \int_0^t g(t-\tau)\frac{h(\tau)}{e^{\zeta_i\omega_i \tau}}d\tau e^{\zeta_i\omega_i t} = \int_0^t g(t-\tau)e^{\zeta_i\omega_i(t-\tau)}h(\tau)d\tau$, the Fourier spectrum of $u_e(t)$ is the multiplication of the spectrum of $g(t)e^{\zeta_i\omega_i t}$ and the spectrum of $h(t)$. Furthermore, $H(\omega_{di}) = 0$ implies that $U_e(\omega_{di}) = 0$ for any arbitrary original control profile. The additional constraint $\int_0^{T_0}\frac{h(t)}{e^{\zeta_i\omega_i t}}dt = 1$ is imposed to ensure that the integral of the shape filter is normalized to be 1. Physically, if the shaped command is to reach the same set point as the un-shaped command, the integral of the shape filter should be exactly 1. ■

Conclusion 4.3.2 *If there exists a finite support base function $h(t)$, $0 \le t \le T_0$, such that $H(\omega_{di}) = 0$, then robustness of the vibration suppression shape filter in Conclusion 4.3.1 can be improved by the following filter operation,*

$$f_n(t) = \int_0^t f_{n-1}(t-\tau)f_1(\tau)d\tau, \quad n \ge 2, \tag{4.30}$$

where $f_1(t) = \frac{h(t)/e^{\zeta_i\omega_i t}}{\int_0^{T_0} h(t)/e^{\zeta_i\omega_i t}dt}$ *and the resultant spectrum of* $f_n(t)$ *is* $F_n(\omega) = F_1^n(\omega)$.

Proof. Without loss of generality, $\int_0^{T_0} h(t)/e^{\zeta_i\omega_i t}dt = 1$ is assumed, which means the function $f_1(t) = h(t)/e^{\zeta_i\omega_i t}$ has been already normalized.

First, if $f_1(t) = \frac{h(t)}{e^{\zeta_i\omega_i t}}$ is a robust vibration suppression shape filter, then $f_{1e}(t) = f_1(t)e^{\zeta_i\omega_i t} = h(t)$ and $F_{1e}(\omega_{di}) = H(\omega_{di}) = 0$. From the above operation, $f_2(t) = \int_0^t f_1(t-\tau)f_1(\tau)d\tau$, so $f_{2e}(t) = f_2(t)e^{\zeta_i\omega_i t} = \int_0^t f_1(t-\tau)f_1(\tau)d\tau \cdot e^{\zeta_i\omega_i t} = \int_0^t \frac{h(t-\tau)}{e^{\zeta_i\omega_i(t-\tau)}}\frac{h(\tau)}{e^{\zeta_i\omega_i\tau}}d\tau \cdot e^{\zeta_i\omega_i t} = \int_0^t h(t-\tau)h(\tau)d\tau$. Hence $F_{2e}(\omega) = H(\omega)H(\omega) = H^2(\omega)$. So $F_{2e}(\omega_{di}) = H^2(\omega_{di}) = 0$ and $\frac{dF_{2e}(\omega)}{d\omega}|_{\omega=\omega_{di}} = 2H(\omega_{di}) = 0$ hold. The case of $n > 2$ is obviously proven in a similar way.

Secondly, the above proof procedure applies to the case that $f_1(t) = \frac{h(t)}{e^{\zeta_i\omega_i t}}$ is a vibration suppression velocity profile. ■

Here, the robust control profile or shape filter $f_1(t)$ in (4.30) is said to have the robustness order 1. The robust control profile or shape filter $f_n(t)$ generated from the filter operation in (4.30) is said to have the robustness order n.

Conclusion 4.3.3 *The shape filter* $f_n(t)$ *in (4.30) can also be generated from the following operation*

$$f_n(t) = \frac{h_n(t)/e^{\zeta_i\omega_i t}}{\int_0^\infty h_n(t)/e^{\zeta_i\omega_i t}dt} = \frac{h_n(t)/e^{\zeta_i\omega_i t}}{\left[\int_0^{T_0} h_1(t)/e^{\zeta_i\omega_i t}dt\right]^n}, \tag{4.31}$$

where $h_1(t) = h(t), 0 \le t \le T_0$, *and* $h_n(t) = \int_0^t h_{n-1}(t-\tau)h_1(\tau)d\tau$ $(n \ge 2)$ *is called the base function with robustness order* n.

Proof. For any finite support functions $a(t)$ and $b(t)$,

$$\int_{-\infty}^{\infty} a(t) * b(t)dt = \int_{-\infty}^{\infty}\left[\int_{-\infty}^{\infty} a(t-\tau)b(\tau)d\tau\right]dt, \tag{4.32}$$

$$= \int_{-\infty}^{\infty} b(\tau)\left[\int_{-\infty}^{\infty} a(t-\tau)dt\right]d\tau, \tag{4.33}$$

$$= \left[\int_{-\infty}^{\infty} a(t)dt\right]\left[\int_{-\infty}^{\infty} b(\tau)d\tau\right]. \tag{4.34}$$

So the area under a convolution of two finite support functions is the product of areas under the factors. It is easy to show that the denominators of (4.31) hold since

$$\int_0^\infty h_n(t)/e^{\zeta_i\omega_i t}dt = \int_0^{nT_0} h_n(t)/e^{\zeta_i\omega_i t}dt, \tag{4.35}$$

$$= \int_0^{nT_0}\int_0^t h_{n-1}(t-\tau)h_1(\tau)d\tau/e^{\zeta_i\omega_i t}dt, \tag{4.36}$$

$$= \int_0^{nT_0}\int_0^t \frac{h_{n-1}(t-\tau)}{e^{\zeta_i\omega_i(t-\tau)}}\frac{h_1(\tau)}{e^{\zeta_i\omega_i\tau}}d\tau dt, \tag{4.37}$$

$$= \int_0^{nT_0}\int_0^{nT_0} \frac{h_{n-1}(t-\tau)}{e^{\zeta_i\omega_i(t-\tau)}}\frac{h_1(\tau)}{e^{\zeta_i\omega_i\tau}}d\tau dt, \tag{4.38}$$

$$= \int_0^{(n-1)T_0} \frac{h_{n-1}(t)}{e^{\zeta_i\omega_i t}}dt \int_0^{T_0} \frac{h_1(\tau)}{e^{\zeta_i\omega_i\tau}}d\tau, \tag{4.39}$$

$$= \cdots\cdots, \tag{4.40}$$

$$= \left[\int_0^{T_0} h_1(t)/e^{\zeta_i\omega_i t}dt\right]^n \tag{4.41}$$

To show (4.31) is true, mathematical induction is used. When $n = 1$, it is simply true. It can be shown that (4.31) is true when $n = 2$ since

$$f_2(t) = \int_0^t f_1(t-\tau)f_1(\tau)d\tau, \tag{4.42}$$

$$= \frac{\int_0^t \frac{h_1(t-\tau)}{e^{\zeta_i\omega_i(t-\tau)}}\frac{h_1(\tau)}{e^{\zeta_i\omega_i\tau}}d\tau}{\int_0^{T_0}\frac{h_1(t)}{e^{\zeta_i\omega_i t}}dt\int_0^{T_0}\frac{h_1(\tau)}{e^{\zeta_i\omega_i\tau}}d\tau}, \tag{4.43}$$

$$= \frac{\int_0^t h_1(t-\tau)h_1(\tau)d\tau/e^{\zeta_i\omega_i t}}{\int_0^{\infty}\frac{h_1(t-\tau)}{e^{\zeta_i\omega_i(t-\tau)}}dt\int_0^{\infty}\frac{h_1(\tau)}{e^{\zeta_i\omega_i\tau}}d\tau}, \tag{4.44}$$

$$= \frac{h_2(t)/e^{\zeta_i\omega_i t}}{\int_0^\infty\int_0^\infty \frac{h_1(t-\tau)}{e^{\zeta_i\omega_i(t-\tau)}}\frac{h_1(\tau)}{e^{\zeta_i\omega_i\tau}}d\tau dt}, \tag{4.45}$$

$$= \frac{h_2(t)/e^{\zeta_i\omega_i t}}{\int_0^\infty h_2(t)/e^{\zeta_i\omega_i t}dt}. \tag{4.46}$$

Assume (4.31) is true for $n = 1, 2, \ldots, k-1$, then when $n = k$,

$$f_k(t) = \int_0^t f_{k-1}(t-\tau) f_1(\tau) d\tau, \tag{4.47}$$

$$= \frac{\int_0^t \frac{h_{k-1}(t-\tau)}{e^{\zeta_i \omega_i (t-\tau)}} \frac{h_1(\tau)}{e^{\zeta_i \omega_i \tau}} d\tau}{\int_0^{(k-1)T_0} \frac{h_{k-1}(t)}{e^{\zeta_i \omega_i t}} dt \int_0^{T_0} \frac{h_1(\tau)}{e^{\zeta_i \omega_i \tau}} d\tau}, \tag{4.48}$$

$$= \frac{\int_0^t h_{k-1}(t-\tau) h_1(\tau) d\tau / e^{\zeta_i \omega_i t}}{\int_0^\infty \frac{h_{k-1}(t-\tau)}{e^{\zeta_i \omega_i (t-\tau)}} dt \int_0^\infty \frac{h_1(\tau)}{e^{\zeta_i \omega_i \tau}} d\tau}, \tag{4.49}$$

$$= \frac{h_n(t)/e^{\zeta_i \omega_i t}}{\int_0^\infty \int_0^\infty \frac{h_{k-1}(t-\tau)}{e^{\zeta_i \omega_i (t-\tau)}} \frac{h_1(\tau)}{e^{\zeta_i \omega_i \tau}} d\tau dt}, \tag{4.50}$$

$$= \frac{h_n(t)/e^{\zeta_i \omega_i t}}{\int_0^\infty h_n(t)/e^{\zeta_i \omega_i t} dt}. \tag{4.51}$$

So the statement of (4.31) is true for all $n \geq 2$. ■

The following analysis shows that all the input shapers from the input shaping technique are special vibration suppression shape filters possessing the second property of Conclusion 4.3.1. Some disadvantages of the input shaping technique are also demonstrated. The robust profile generation technique described in this report simultaneously achieves the two properties in Conclusion 4.3.1. Also the robust profile generation technique can suppress all the high frequency unknown resonant vibrations. However, the input shaping technique does not have this property, which means that the input shaping technique has potential disadvantages if high frequency resonance modes exist in a flexible system. These potential disadvantages are the price of non-smoothness of the input shaping functions.

4.4 A Special Case (Input Shaping Technique)

In this section, the input shaping technique is proved to be a special case of the functions which only possesses the second property of Conclusion 4.3.1. Also, potential disadvantages of using the input shaping technique are made clear.

The input shaping technique [71, 73, 79, 85] was derived using the response of a linear, time-invariant second order system to a sequence of impulses. By setting the amplitude of

vibration for a multi-impulse input to be zero, the impulse amplitudes and corresponding impulse starting times can be solved. However, the input shaping technique can be derived to be a special case of vibration suppression shape filter possessing the second property of Conclusion 4.3.1. In Section 4.12, it is shown that input shaping technique constructs a small portion of the impulse function based shape filter.

4.4.1 A Special Case of Property 2 of Conclusion 4.3.1

Let $f(t) = \frac{h(t)}{e^{\zeta_i \omega_i t}}$ and $f(t)$ is assumed to be an impulse function. First, $f(t)$ is assumed to be a two-impulse function, i.e.,

$$f(t) = \begin{cases} A_1 & \text{if } t = t_1, \\ A_2 & \text{if } t = t_2, \\ 0 & \text{otherwise.} \end{cases} \tag{4.52}$$

Since $h(t) = f(t)e^{\zeta_i \omega_i t}$, then to guarantee $H(\omega_{di}) = H(\sqrt{1-\zeta_i^2}\omega_i) = 0$, the following equations must hold.

$$A_1 + A_2 e^{\zeta_i \omega_i t_2} \cos(\omega_{di} t_2) = 0, \tag{4.53}$$

$$A_2 e^{\zeta_i \omega_i t_2} \sin(\omega_{di} t_2) = 0. \tag{4.54}$$

Here t_1 is always assumed to be zero to reduce the time duration of the shape filter. With the additional constraint of a shape filter, $A_1 + A_2 = 1$, the resultant function $f(t)$ is given by

$$f(t) = \begin{cases} \frac{1}{1+K} & \text{if } t = 0, \\ \frac{K}{1+K} & \text{if } t = \Delta T, \\ 0 & \text{otherwise,} \end{cases} \tag{4.55}$$

where $K = e^{-\frac{\zeta_i \pi}{\sqrt{1-\zeta_i^2}}}$ and $\Delta T = \frac{\pi}{\omega_{di}} = \frac{\pi}{\omega_i \sqrt{1-\zeta_i^2}}$. This derived vibration suppression shape filter is exactly the input shaping Zero Vibration (ZV) impulse filter. The base function of

this shape filter (4.55) is

$$h(t) = \begin{cases} 1 & \text{if } t = 0, \\ 1 & \text{if } t = \Delta T, \\ 0 & \text{otherwise}, \end{cases} \tag{4.56}$$

where $\Delta T = \frac{\pi}{\omega_{di}} = \frac{\pi}{\omega_i \sqrt{1-\zeta_i^2}}$.

To improve robustness, the filter operation of Conclusion 4.3.2 is performed. Let $f_1(t) = f(t)$, then $f_2(t) = \int_0^t f_1(t-\tau) f_1(\tau) d\tau$, and the resultant shape filter with robustness order $n = 2$ is given by

$$f_2(t) = \begin{cases} \frac{1}{1+2K+K^2} & \text{if } t = 0, \\ \frac{2K}{1+2K+K^2} & \text{if } t = \Delta T, \\ \frac{K^2}{1+2K+K^2} & \text{if } t = 2\Delta T, \\ 0 & \text{otherwise.} \end{cases} \tag{4.57}$$

This derived shape filter is exactly the input shaping Zero Vibration Derivative (ZVD) impulse filter. The base function of this shape filter (4.57) is

$$h(t) = \begin{cases} 1 & \text{if } t = 0, \\ 2 & \text{if } t = \Delta T, \\ 1 & \text{if } t = 2\Delta T, \\ 0 & \text{otherwise.} \end{cases} \tag{4.58}$$

If $n = 3$, then $f_3(t) = \int_0^t f_2(t-\tau) f_1(\tau) d\tau$, and the resultant shape filter with robustness

order $n = 3$ is given by

$$f_3(t) = \begin{cases} \frac{1}{1+3K+3K^2+K^3} & \text{if } t = 0, \\ \frac{3K}{1+3K+3K^2+K^3} & \text{if } t = \Delta T, \\ \frac{3K^2}{1+3K+3K^2+K^3} & \text{if } t = 2\Delta T, \\ \frac{K^3}{1+3K+3K^2+K^3} & \text{if } t = 3\Delta T, \\ 0 & \text{otherwise.} \end{cases} \tag{4.59}$$

This derived shape filter is exactly the input shaping ZVDD impulse filter. The base function of this shape filter (4.59)is

$$h(t) = \begin{cases} 1 & \text{if } t = 0, \\ 3 & \text{if } t = \Delta T, \\ 3 & \text{if } t = 2\Delta T, \\ 1 & \text{if } t = 3\Delta T, \\ 0 & \text{otherwise.} \end{cases} \tag{4.60}$$

Robustness can also be further improved by the filter operation of Conclusion 4.3.2. The price of the robustness improvement is that the time duration of the shape filter is increased.

The above impulse filter derivation assumes all the impulses are positive. Negative impulses can also be assumed. The resultant negative shape filter may be shorter than the positive shape filter. However, Singhose [79] has pointed out that negative input shapers can cause large unmodeled high frequency vibration.

Since the shape filter function in this section is assumed to be an impulse function, it is not a smooth function. So the two-impulse or three-impulse functions cannot be used as a velocity profile. The non-smooth shape filter is very sensitive to unmodeled high frequency resonant modes. This detail will be analyzed in the next section.

It must be noted that the input shaping technique is only a special case of the impulse functions which possesses the second property of Conclusion 4.3.1. There are a number of impulse functions that possess the second property of Conclusion 4.3.1. Since a smooth function will be generated to simultaneously achieve the two properties of Conclusion 4.3.1, further investigation of the impulse shape filter is not described here.

4.4.2 Potential Disadvantages of Using Input Shaping Technique

Input shaping technique is shown to be a special case of the functions which only possess the second property of Conclusion 4.3.1. In this section, potential disadvantages of using the input shaping technique are demonstrated. Since the input shaping impulse filters are not smooth, so it has a potential to amplify the unmodeled high frequency vibration in a flexible system. The resultant high frequency residual vibration is extremely large.

For a second-order harmonic oscillator of the natural frequency ω_i rad/sec and the damping ratio ζ_i,

$$\frac{\omega_i^2}{s^2 + 2\zeta_i\omega_i s + \omega_i^2}, \tag{4.61}$$

the magnitude of the total response immediately after the N^{th} impulse is given by [71, 72]

$$V_{amp}(\omega_i, \zeta_i) = e^{-\zeta_i\omega_i t_N} \frac{\omega_i}{\sqrt{1-\zeta_i^2}} \sqrt{(AC(\omega_i, \zeta_i))^2 + (AS(\omega_i, \zeta_i))^2}, \tag{4.62}$$

where

$$AC(\omega_i, \zeta_i) = \sum_{k=1}^{N} A_k e^{\zeta_i\omega_i t_k} \cos\left(\omega_i\sqrt{1-\zeta_i^2}t_k\right), \tag{4.63}$$

$$AS(\omega_i, \zeta_i) = \sum_{k=1}^{N} A_k e^{\zeta_i\omega_i t_k} \sin\left(\omega_i\sqrt{1-\zeta_i^2}t_k\right). \tag{4.64}$$

A_k and t_k are the amplitude and time location at which the impulse occurs, N is the total number of impulses, t_N is the time of the last impulse, and $\omega_{di} = \omega_i\sqrt{1-\zeta_i^2}$ is the damped natural frequency.

The sensitivity of the impulse shape filter can be displayed graphically by a sensitivity curve: a plot of residual vibration amplitude versus frequency error. Let $q = \omega_{actual}/\omega_{model}$,

(4.62) becomes

$$V_{amp}(q\omega_i, \zeta_i) = e^{-\zeta_i q\omega_i t_N} \frac{q\omega_i}{\sqrt{1-\zeta_i^2}} \times \sqrt{\left(AC(q\omega_i, \zeta_i)\right)^2 + \left(AS(q\omega_i, \zeta_i)\right)^2}, \tag{4.65}$$

where $\omega_i = \omega_{model}$, $\omega_{actual} = q\omega_i$, and

$$AC(q\omega_i, \zeta_i) = \sum_{k=1}^{N} A_k e^{\zeta_i q\omega_i t_k} \cos\left(q\omega_i \sqrt{1-\zeta_i^2} t_k\right), \tag{4.66}$$

$$AS(q\omega_i, \zeta_i) = \sum_{k=1}^{N} A_k e^{\zeta_i q\omega_i t_k} \sin\left(q\omega_i \sqrt{1-\zeta_i^2} t_k\right). \tag{4.67}$$

Since for any finite impulse shape filter $f(t), 0 \le t \le T_0$, the integral of $f(t)$ is $\int_0^{T_0} f(t)dt = 1$, the rigid body movement amplitude can be assumed as $\int_0^{T_0} f(t)dt = 1$. So the residual vibration level can be defined as a percentage of the rigid body motion amplitude as in (4.68)

$$\frac{V_{amp}(q\omega_i, \zeta_i)}{\int_0^{T_0} f(t)dt}. \tag{4.68}$$

For the impulse shape filter case, $\int_0^{T_0} f(t)dt = \sum_{k=1}^{N} A_k = 1$. Figure 4.2 shows the sensitivity curve of the input shaping ZVD impulse filter with $\omega_{model} = 1$ rad/sec and different damping $\zeta_i = 0, 0.05, 0.2$. The sensitivity curve shows that the residual vibration is amplified at the unmodeled high frequency. For example, if $\omega_{actual} = 2$ rad/sec and the damping ratio $\zeta_i = 0$, then the ZVD input shaping impulse filter based on $\omega_{model} = 1$ rad/sec and $\zeta_i = 0$ will result a residual vibration amplitude of $200\% = 2$ for the second-order oscillator described by (4.61). The residual vibration amplitude is extremely large compared with the rigid body motion amplitude of 1.

A sensitivity curve plot of residual vibration amplitude versus damping error can be calculated in a similar way. Figure 4.3 shows the sensitivity curve of the input shaping ZVD impulse filter with $\omega_i = 1$ rad/sec and actual damping ratio. The model damping ratio is assumed to be 0.1. From Figure 4.3, a large variation in the damping ratio is tolerated.

Since the impulse shape filter is not smooth, it has the potential to amplify the unmodeled high frequency vibration in a flexible system. Moreover, it cannot be used as a velocity

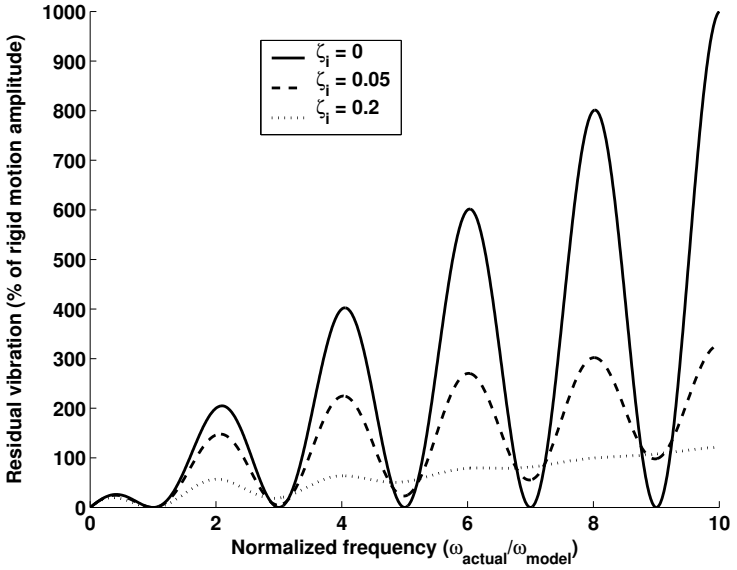

Figure 4.2: ZVD input shaping residual vibration level versus actual natural frequency.

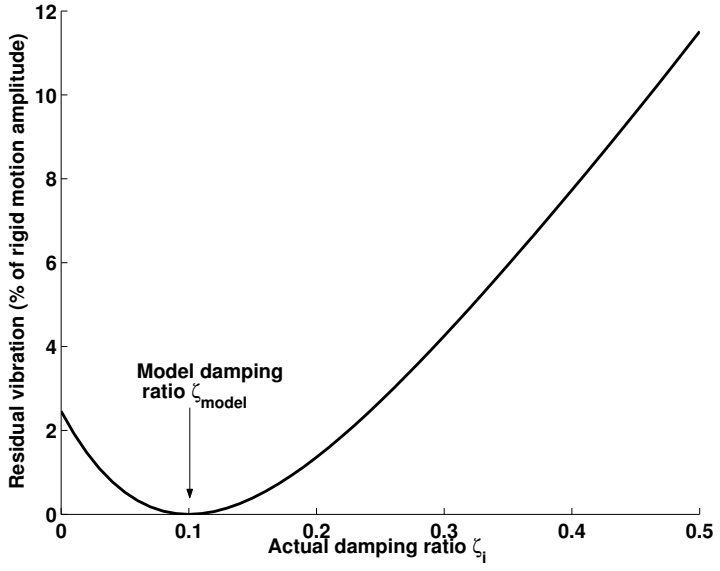

Figure 4.3: ZVD input shaping residual vibration level versus actual damping ratio.

profile. In the following analysis, a smooth shape filter will be developed. The smoothness of the shape filter suppresses the high frequency vibration.

Remark 4.1 *The definition in (4.65) is different from the sensitivity concept of Singer [71, 72] and Singhose [79]. In their definition, the sensitivity curve is expressed as the magnitude of the total response immediately after the N^{th} impulse divided by the magnitude of the response with unit impulse occurring at time 0. Since the magnitude of the response with unit impulse occurring at time 0 is given by*

$$\frac{\omega_i}{\sqrt{1-\zeta_i^2}}, \tag{4.69}$$

their definition of residual vibration level is

$$\frac{V_{amp}(q\omega_i, \zeta_i)}{\frac{\omega_i}{\sqrt{1-\zeta_i^2}} \sum_{k=1}^{N} A_k} \tag{4.70}$$

or simply

$$e^{-\zeta_i q\omega_i t_N} \sqrt{\left(AC(q\omega_i, \zeta_i)\right)^2 + \left(AS(q\omega_i, \zeta_i)\right)^2}, \tag{4.71}$$

because $V_{amp}(q\omega_i, \zeta_i)$ exactly has the term $\frac{\omega_i}{\sqrt{1-\zeta_i^2}}$ and $\sum_{k=1}^{N} A_k = 1$.

It is known from (4.69) that the magnitude of the response with unit impulse occurring at time 0 linearly increases with respect to actual undamped natural frequency ω_i if ζ_i is assumed to be a constant. Therefore, their definition does not consider the true residual vibration magnitude. For example, the definition (4.71) shows that the residual vibration level is 100% when the actual undamped natural frequency is 0. However, the true magnitude of the residual vibration given in (4.65) is 0 when the actual undamped natural frequency is 0.

4.5 Another Special Case (Optimal Arbitrary Time-Delay Filter (OATF))

In this section, the optimal arbitrary time-delay filter (OATF) developed by Magee and Book [46, 48, 49] is proved to be a special case of the functions which only possesses the second property of Conclusion 4.3.1.

OATF technique chooses a cost function involving both the error signal and the time rate of change in the error signal. The cost function is expressed as an explicit function of the unknown filter coefficients, and the function can be minimized with respect to the unknown filter terms. Magee and Book [46, 48] showed that the ZV and ZVD input shapers can be derived from the OATF algorithm if an appropriate time-delay value was chosen. In Section 4.12, it is shown that OATF technique, like input shaping technique, only constructs a small portion of the impulse function based shape filter.

4.5.1 Another Special Case of Property 2 of Conclusion 4.3.1

The OATF that minimizes the elastic response of a single mode of vibration is given by [46, 48]

$$f(t) = \begin{cases} 1 & \text{if } t = 0, \\ -2\cos(\omega_{di}T_1)e^{-\zeta_i\omega_i T_1} & \text{if } t = T_1, \\ e^{-2\zeta_i\omega_i T_1} & \text{if } t = 2T_1, \\ 0 & \text{otherwise}, \end{cases} \tag{4.72}$$

where T_1 is an arbitrary time-delay value, ω_i rad/sec is the undamped natural frequency and ζ_i is the damping ratio, $\omega_{di} = \sqrt{1-\zeta_i^2}\omega_i$ is the damped natural frequency.

It is very simple to know that the function $h(t) = f(t)e^{\zeta_i\omega_i t}$ from the three-impulse function $f(t)$ in (4.72) is a base function such that the Fourier transform of $h(t)$, $H(\omega)$ is

zero at $\omega = \omega_{di}$, i.e., $H(\omega_{di}) = 0$. First, $h(t) = f(t)e^{\zeta_i \omega_i t}$ is given by

$$h(t) = \begin{cases} 1 & \text{if } t = 0, \\ -2\cos(\omega_{di} T_1) & \text{if } t = T_1, \\ 1 & \text{if } t = 2T_1, \\ 0 & \text{otherwise}, \end{cases} \tag{4.73}$$

and the Fourier transform of three-impulse function $h(t)$, $H(\omega)$ at $\omega = \omega_{di}$ is given by

$$H(\omega_{di}) = 1 - 2\cos(\omega_{di} T_1) e^{-j\omega_{di} T_1} + e^{-2j\omega_{di} T_1}, \tag{4.74}$$

$$= 1 - (e^{j\omega_{di} T_1} + e^{-j\omega_{di} T_1}) e^{-j\omega_{di} T_1} + e^{-2j\omega_{di} T_1}, \tag{4.75}$$

$$= 1 - (1 + e^{-2j\omega_{di} T_1}) + e^{-2j\omega_{di} T_1}, \tag{4.76}$$

$$= 0. \tag{4.77}$$

So the OATF $f(t)$ in (4.72) can be generated from the above three-impulse base function $h(t)$ in (4.73) by the following operation from the second property of Conclusion 4.3.1.

$$f(t) = \frac{h(t)}{e^{\zeta_i \omega_i t}}. \tag{4.78}$$

An interesting property of this shape filter is that the time duration T_1 of two sequential impulses can be chosen to be any positive number.

4.5.2 Relationship Between OATF and Input Shaping Technique

Magee [46] showed that the OATF $f(t)$ reduced to ZV input shaper or ZVD input shaper by choosing the time-delay value T_1 to be a special number. For example, by choosing $T_1 = \frac{\pi}{2\omega_{di}}$, the OATF $f(t)$ in (4.72) becomes a two-impulse function

$$f(t) = \begin{cases} 1 & \text{if } t = 0, \\ e^{\frac{-\zeta_i \pi}{\sqrt{1-\zeta_i^2}}} & \text{if } t = \frac{\pi}{\omega_{di}}, \\ 0 & \text{otherwise.} \end{cases} \tag{4.79}$$

The normalized $f(t)$ is exactly the two-impulse ZV input shaper function as given by

$$f(t) = \begin{cases} \frac{1}{1+K} & \text{if } t = 0, \\ \frac{K}{1+K} & \text{if } t = \frac{\pi}{\omega_{di}}, \\ 0 & \text{otherwise,} \end{cases} \tag{4.80}$$

where $K = e^{\frac{-\zeta_i \pi}{\sqrt{1-\zeta_i^2}}}$.

By choosing $T_1 = \frac{\pi}{\omega_{di}}$, the three-impulse function OATF $f(t)$ in (4.72) becomes

$$f(t) = \begin{cases} 1 & \text{if } t = 0, \\ 2e^{\frac{-\zeta_i \pi}{\sqrt{1-\zeta_i^2}}} & \text{if } t = \frac{\pi}{\omega_{di}}, \\ e^{\frac{-2\zeta_i \pi}{\sqrt{1-\zeta_i^2}}} & \text{if } t = \frac{2\pi}{\omega_{di}}, \\ 0 & \text{otherwise.} \end{cases} \tag{4.81}$$

The normalized $f(t)$ is exactly the three-impulse ZVD input shaper function as given by

$$f(t) = \begin{cases} \frac{1}{1+K+K^2} & \text{if } t = 0, \\ \frac{2K}{1+K+K^2} & \text{if } t = \frac{\pi}{\omega_{di}}, \\ \frac{K^2}{1+K+K^2} & \text{if } t = \frac{2\pi}{\omega_{di}}, \\ 0 & \text{otherwise,} \end{cases} \tag{4.82}$$

where $K = e^{\frac{-\zeta_i \pi}{\sqrt{1-\zeta_i^2}}}$.

Like input shaping technique, OATF algorithm is based on non-continuous impulse functions, so it is not a smooth function. Since the impulse shape filter is not smooth, it has the potential to amplify the unmodeled high frequency vibration in a flexible system. Moreover, the three-impulse function cannot be used as a velocity profile. In the following analysis, a smooth shape filter will be developed. The smoothness of the shape filter suppresses the high frequency vibration.

4.6 Robust Shape Filter Generation Using Rectangle Window

4.6.1 Continuous-Time Rectangle Based Shape Filter Generation

Assume the robust shape filter is generated from a rectangle window given by

$$h(t) = \begin{cases} \frac{1}{T}, & \text{if } 0 \le t \le T, \\ 0, & \text{otherwise.} \end{cases} \tag{4.83}$$

The Fourier transform of $h(t)$ is given by

$$H(\omega) = \int_0^T \frac{1}{T} e^{-j\omega t} dt, \tag{4.84}$$

$$= \frac{1 - e^{-j\omega T}}{j\omega T}, \tag{4.85}$$

and the magnitude spectrum is given by

$$|H(\omega)| = \left| \frac{1 - e^{-j\omega T}}{j\omega T} \right|, \tag{4.86}$$

$$= \left| \frac{\sin(\omega T/2)}{(\omega T)/2} \right|. \tag{4.87}$$

If $H(\omega_{di}) = H(\sqrt{1-\zeta_i^2}\omega_i) = 0$, then $T = \frac{2\pi}{\omega_{di}}$, which is the same time duration as the input shaping ZVD impulse filter. So a smooth shape filter can be generated as

$$f(t) = \frac{h(t)/e^{\zeta_i \omega_i t}}{\int_0^\infty h(t)/e^{\zeta_i \omega_i t} dt}, \tag{4.88}$$

$$= \frac{h(t)/e^{\zeta_i \omega_i t}}{(1 - e^{-\zeta_i \omega_i T})/(\zeta_i \omega_i T)}, \tag{4.89}$$

$$= \begin{cases} \frac{\zeta_i \omega_i}{1 - e^{-\zeta_i \omega_i T}} e^{-\zeta_i \omega_i t} & \text{if } 0 \le t \le T, \\ 0 & \text{otherwise.} \end{cases} \tag{4.90}$$

When $\zeta_i = 0$, the shape filter $f(t)$ is simply equal to $h(t)$ in (4.83). To improve robustness, the filter operation of Conclusion 4.3.2 is performed. Let $f_1(t) = f(t)$, then $f_2(t) =$

$\int_0^t f_1(t-\tau)f_1(\tau)d\tau$, and the resultant shape filter with robustness order $n = 2$ is given by

$$f_2(t) = \begin{cases} \left(\frac{\zeta_i\omega_i}{1-e^{-\zeta_i\omega_i T}}\right)^2 e^{-\zeta_i\omega_i t}t & \text{if } 0 \le t < T, \\ \left(\frac{\zeta_i\omega_i}{1-e^{-\zeta_i\omega_i T}}\right)^2 e^{-\zeta_i\omega_i t}(2T-t) & \text{if } T \le t \le 2T, \\ 0 & \text{otherwise.} \end{cases} \tag{4.91}$$

When $\zeta_i = 0$, the resultant shape filter with robustness order $n = 2$ is simply given by

$$f_2(t) = \begin{cases} \frac{1}{T^2}t & \text{if } 0 \le t < T, \\ \frac{1}{T^2}(2T-t) & \text{if } T \le t \le 2T, \\ 0 & \text{otherwise.} \end{cases} \tag{4.92}$$

If $n = 3$, then $f_3(t) = \int_0^t f_2(t-\tau)f_1(\tau)d\tau$, and the resultant shape filter with robustness order $n = 3$ is given by

$$f_3(t) = \begin{cases} \left(\frac{\zeta_i\omega_i}{1-e^{-\zeta_i\omega_i T}}\right)^3 e^{-\zeta_i\omega_i t}(\frac{t^2}{2}) & \text{if } 0 \le t < T, \\ \left(\frac{\zeta_i\omega_i}{1-e^{-\zeta_i\omega_i T}}\right)^3 e^{-\zeta_i\omega_i t}(-t^2+3Tt-\frac{3}{2}T^2) & \text{if } T \le t < 2T, \\ \left(\frac{\zeta_i\omega_i}{1-e^{-\zeta_i\omega_i T}}\right)^3 e^{-\zeta_i\omega_i t}\frac{(t-3T)^2}{2} & \text{if } 2T \le t \le 3T, \\ 0 & \text{otherwise.} \end{cases} \tag{4.93}$$

Robustness can also be further improved by the filter operation of Conclusion 4.3.2. The price of the robustness improvement is that the time duration of the shape filter is increased.

Figure 4.4 shows the resultant shape filter function $f_1(t)$ in the time domain and the magnitude spectrum $|F_1(\omega)|$ in the frequency domain, with $\omega_i = 1$ rad/sec and $\zeta_i = 0$. Figure 4.5 shows the resultant shape filter function $f_2(t)$ and the magnitude spectrum $|F_2(\omega)|$, with $\omega_i = 1$ rad/sec and $\zeta_i = 0$. Figure 4.6 shows the resultant shape filter function $f_3(t)$ and the magnitude spectrum $|F_3(\omega)|$, with $\omega_i = 1$ rad/sec and $\zeta_i = 0$.

For the damped case, Figure 4.7 shows the resultant shape filter function $f_1(t)$ in the time domain and the magnitude spectrum $|F_1(\omega)|$ in the frequency domain, with $\omega_i = 1$

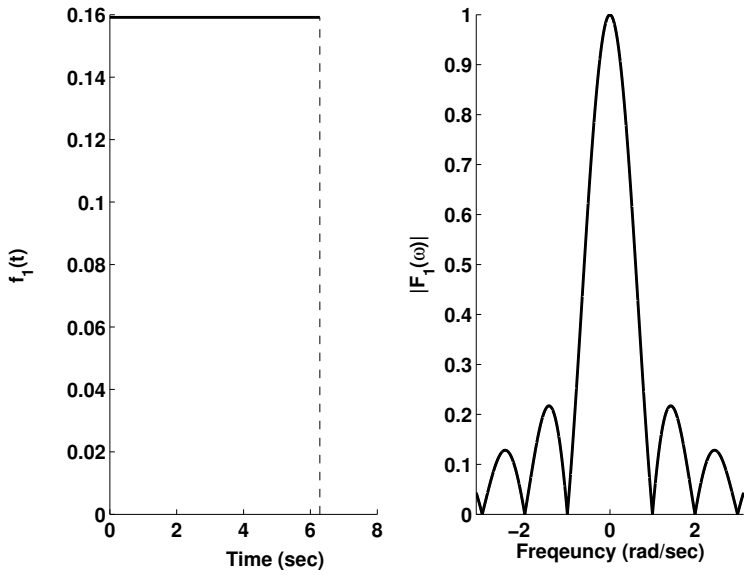

Figure 4.4: Rectangle based shape filter with $\omega_i = 1, \zeta_i = 0$, and the robustness order $n = 1$.

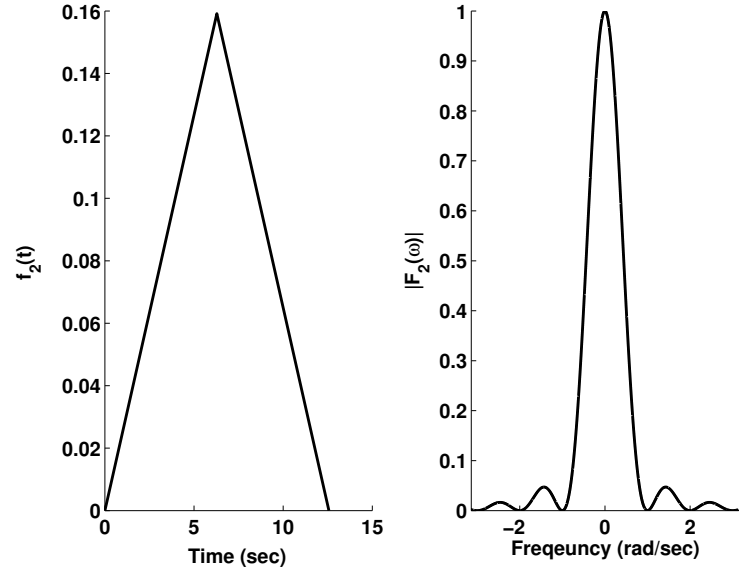

Figure 4.5: Rectangle based shape filter with $\omega_i = 1, \zeta_i = 0$, and the robustness order $n = 2$.

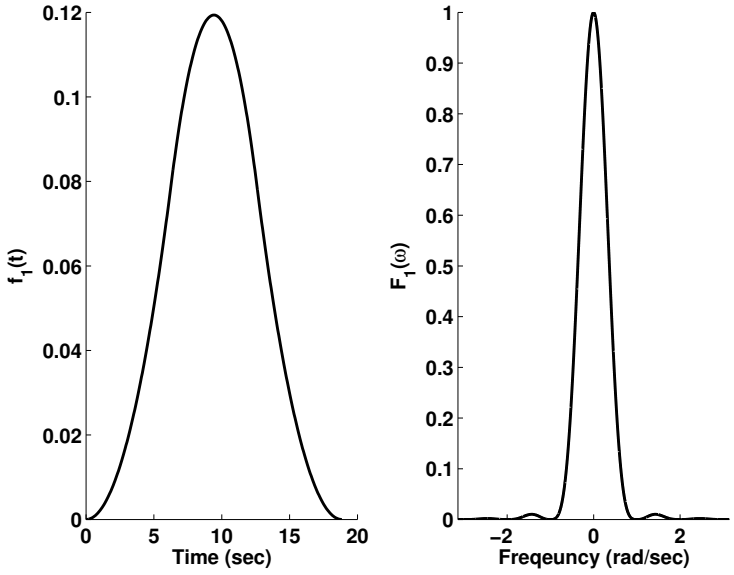

Figure 4.6: Rectangle based shape filter with $\omega_i = 1, \zeta_i = 0$, and the robustness order $n = 3$.

rad/sec and $\zeta_i = 0.05$. Figure 4.8 shows the resultant shape filter function $f_2(t)$ and the magnitude spectrum $|F_2(\omega)|$, with $\omega_i = 1$ rad/sec and $\zeta_i = 0.05$. Figure 4.9 shows the resultant shape filter function $f_3(t)$ and the magnitude spectrum $|F_3(\omega)|$, with $\omega_i = 1$ rad/sec and $\zeta_i = 0.05$.

4.6.2 Discrete-Time Rectangle Based Shape Filter Generation

Now the discrete-time rectangle based shape filter is derived. If the sampling period is T_s sec and the total discrete-time sequence has $M + 1$ impulses, the rectangle function is

$$h[k] = \begin{cases} 1, & \text{if } 0 \leq k \leq M, \\ 0, & \text{otherwise.} \end{cases} \tag{4.94}$$

The discrete-time Fourier transform of $h[k]$ is given by

$$H(\omega) = \sum_{k=0}^{M} h[k] e^{-j\omega k}, \tag{4.95}$$

$$= e^{-j\omega M} \frac{\sin\left[\omega(M+1)/2\right]}{\sin\left(\omega/2\right)}, \tag{4.96}$$

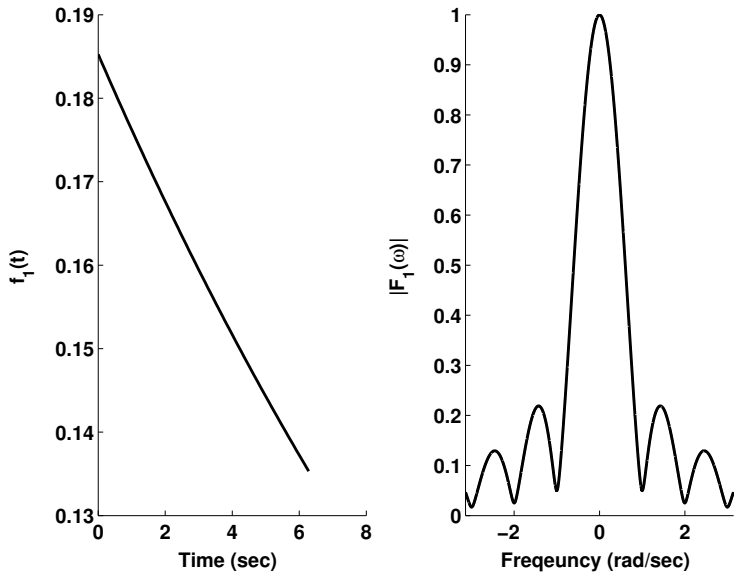

Figure 4.7: Rectangle based shape filter with $\omega_i = 1, \zeta_i = 0.05$, and the robustness order $n = 1$.

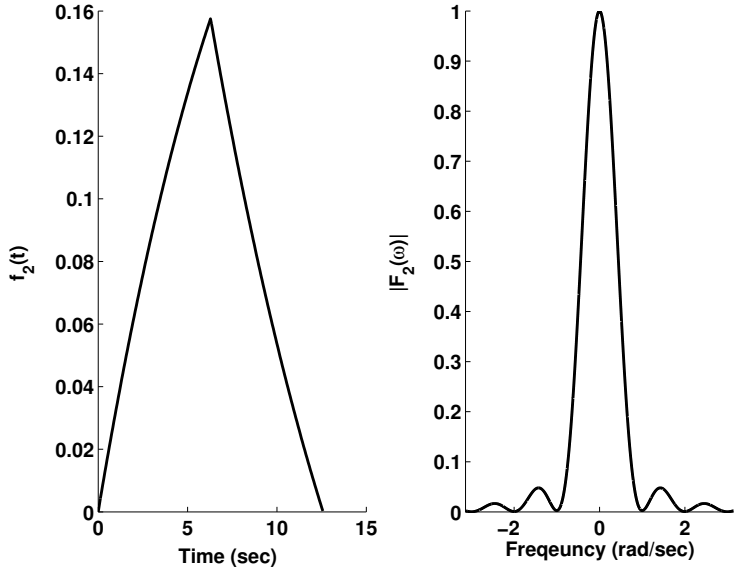

Figure 4.8: Rectangle based shape filter with $\omega_i = 1, \zeta_i = 0.05$, and the robustness order $n = 2$.

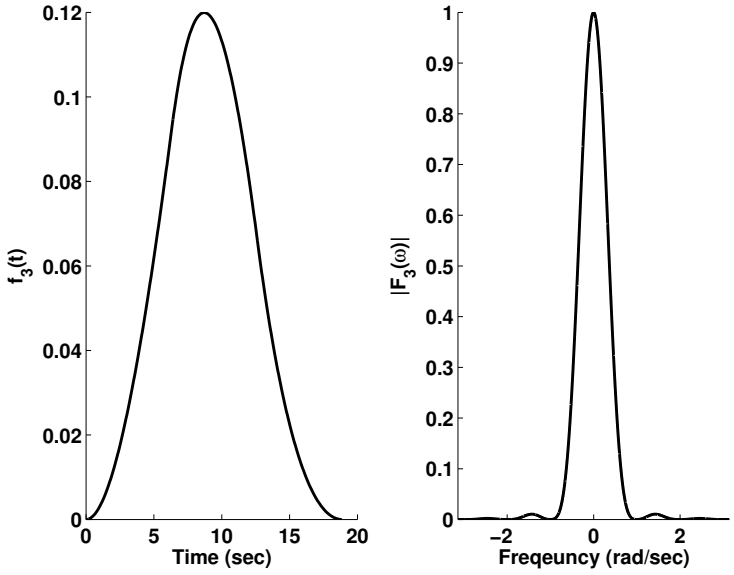

Figure 4.9: Rectangle based shape filter with $\omega_i = 1, \zeta_i = 0.05$, and the robustness order $n = 3$.

and the magnitude spectrum of $h[k]$ is given by

$$|H(\omega)| = \left| \frac{\sin\left[\omega(M+1)/2\right]}{\sin\left(\omega/2\right)} \right|. \tag{4.97}$$

Here the unit of ω in the discrete-time Fourier transform is radians. If $H(\omega_{di}T_s) = H(\sqrt{1-\zeta_i^2}\,\omega_i T_s) = 0$, then $\omega_{di}T_s = \frac{2\pi}{M+1}$ and $M = \frac{2\pi}{\omega_{di}T_s} - 1$. If M is a positive integer, a smooth shape filter can be generated as

$$f[k] = \frac{h[k]/e^{\zeta_i\omega_i kT_s}}{\sum_{m=0}^{M} h[m]/e^{\zeta_i\omega_i mT_s}}, \tag{4.98}$$

$$= \frac{h[k]/e^{\zeta_i\omega_i kT_s}}{(1-e^{-\zeta_i\omega_i(M+1)T_s})/(1-e^{-\zeta_i\omega_i T_s})}, \tag{4.99}$$

$$= \begin{cases} \frac{1-e^{-\zeta_i\omega_i T_s}}{1-e^{-\zeta_i\omega_i(M+1)T_s}} e^{-\zeta_i\omega_i kT_s} & \text{if } 0 \le k \le M, \\ 0 & \text{otherwise.} \end{cases} \tag{4.100}$$

When $\zeta_i = 0$, the shape filter $f[k]$ is simply equal to $h[k]/(M+1)$. To improve robustness, the filter operation of Conclusion 4.3.2 is performed. Let $f_1[k] = f[k]$, then $f_2[k] = \sum_{m=0}^{k} f_1[k-m]f_1[m]$, and the resultant shape filter with robustness order $n = 2$ is given

by

$$f_2[k] = \begin{cases} \left(\frac{1-e^{-\zeta_i\omega_i T_s}}{1-e^{-\zeta_i\omega_i(M+1)T_s}}\right)^2 e^{-\zeta_i\omega_i kT_s}(k+1) & \text{if } 0 \le k \le M, \\ \left(\frac{1-e^{-\zeta_i\omega_i T_s}}{1-e^{-\zeta_i\omega_i(M+1)T_s}}\right)^2 e^{-\zeta_i\omega_i kT_s}(2M+1-k) & \text{if } M+1 \le k \le 2M, \\ 0 & \text{otherwise.} \end{cases} \tag{4.101}$$

When $\zeta_i = 0$, the resultant shape filter with robustness order $n = 2$ is simply given by

$$f_2[k] = \begin{cases} \frac{1}{(M+1)^2}(k+1) & \text{if } 0 \le k \le M, \\ \frac{1}{(M+1)^2}(2M+1-k) & \text{if } M+1 \le k \le 2M, \\ 0 & \text{otherwise.} \end{cases} \tag{4.102}$$

If $n = 3$, then $f_3[k] = \sum_{m=0}^{k} f_2[k-m]f_1[m]$, and the resultant shape filter with robustness order $n = 3$ is given by

$$f_3[k] = \begin{cases} \left(\frac{1-e^{-\zeta_i\omega_i T_s}}{1-e^{-\zeta_i\omega_i(M+1)T_s}}\right)^3 e^{-\zeta_i\omega_i kT_s}(k+1)(\frac{k}{2}+1) & \text{if } 0 \le k \le M, \\ \left(\frac{1-e^{-\zeta_i\omega_i T_s}}{1-e^{-\zeta_i\omega_i(M+1)T_s}}\right)^3 e^{-\zeta_i\omega_i kT_s}(-\frac{3}{2}M^2+3Mk+\frac{3}{2}M+1-k^2) & \text{if } M+1 \le k \le 2M, \\ \left(\frac{1-e^{-\zeta_i\omega_i T_s}}{1-e^{-\zeta_i\omega_i(M+1)T_s}}\right)^3 e^{-\zeta_i\omega_i kT_s}(3M+1-k)\frac{(3M+2-k)}{2} & \text{if } 2M+1 \le k \le 3M, \\ 0 & \text{otherwise.} \end{cases} \tag{4.103}$$

Robustness can also be further improved by the filter operation of Conclusion 4.3.2. The price of the robustness improvement is that the time duration of the shape filter is increased.

4.6.3 Comparison of Rectangle Based Shape Filter and ZVD Input Shaping Technique

In this section, a comparison between the discrete-time rectangle based shape filter $f_1[k]$ and the ZVD input shaping is performed. The sampling period T_s is chosen to be $\frac{\pi}{100\omega_{di}}$. First, the continuous-time rectangle based shape filter $f_1(t)$ in (4.90) has the same time

duration as the ZVD input shaper which is $\frac{2\pi}{\omega_{di}}$. In the discrete-time case, the time duration of the rectangle based shape filter $f_1[k] = f[k]$ in (4.100) is

$$MT_s = \left(\frac{2\pi}{\omega_{di}T_s} - 1\right) T_s = \frac{2\pi}{\omega_{di}} - T_s. \tag{4.104}$$

This results that the time duration of discrete-time rectangle based shape filter $f_1[k]$ is always less one sample period T_s than the time duration of the ZVD input shaper. Figure 4.10 shows the ZVD input shaper (left) and the rectangle based shape filter (right) with $\omega_i = 1$ rad/sec and $\zeta_i = 0.05$. It clearly shows the amplitude of the ZVD input shaper suddenly changes. However, the rectangle based shape filter smoothly changes from the start to the end.

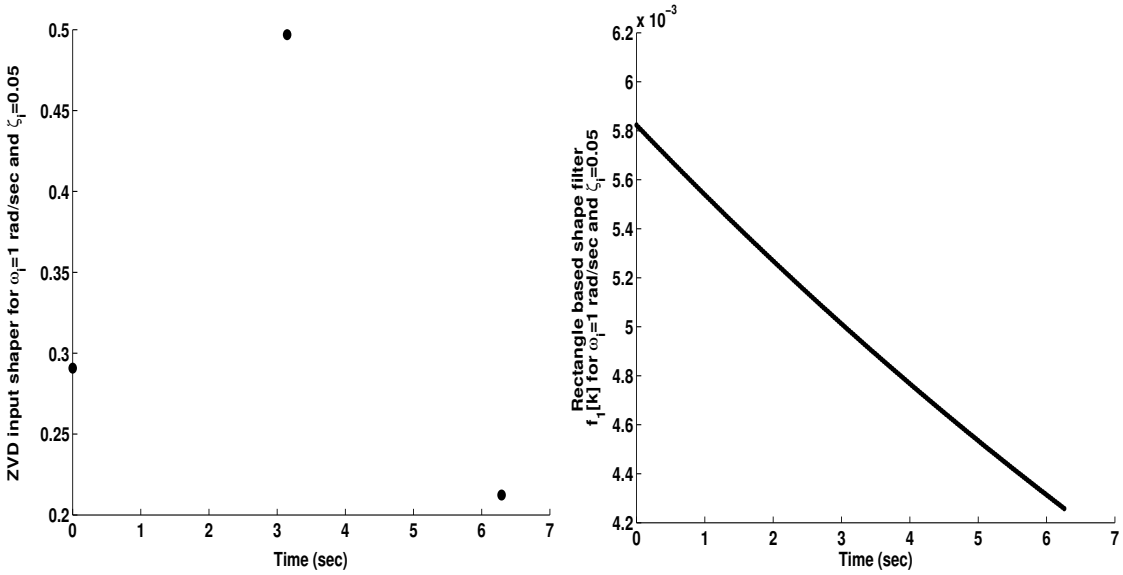

Figure 4.10: Left: ZVD input shaper with $\omega_i = 1$ and $\zeta_i = 0.05$; Right: Rectangle based shape filter $f_1[k]$ with $\omega_i = 1$ and $\zeta_i = 0.05$

The residual vibration level (4.68) can be plotted for ZVD input shaping and rectangle based shape filter $f_1[k]$. In Figure 4.11, the left part shows the sensitivity curve of the ZVD input shaper with $\omega_{model} = 1$ rad/sec and different damping $\zeta_i = 0, 0.05, 0.2$, and the right part shows the sensitivity curve of the rectangle based shape filter $f_1[k]$ with $\omega_{model} = 1$ rad/sec and different damping $\zeta_i = 0, 0.05, 0.2$. Although the sensitivity curve

of the rectangle based shape filter at the model natural frequency $\omega = \omega_{model} = 1$ rad/sec is not as flat as that of the ZVD input shaper, the high frequency unmodeled dynamics are suppressed by the smoothness of the rectangle based shape filter.

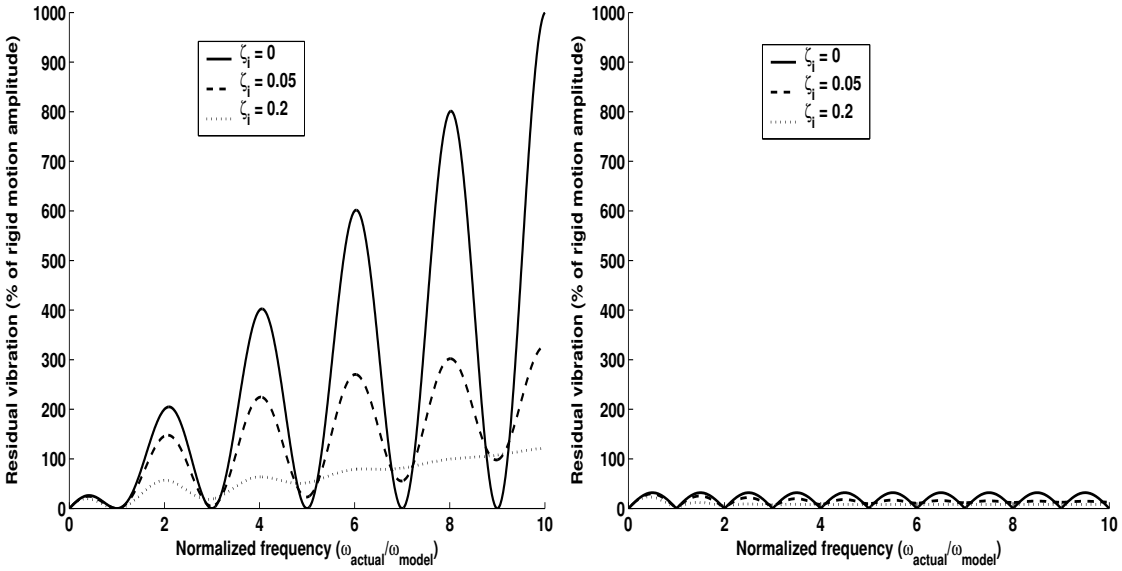

Figure 4.11: Left: ZVD input shaping sensitivity plot versus actual natural frequency; Right: Rectangle based shape filter $f_1[k]$ sensitivity plot versus actual natural frequency.

A sensitivity of vibration amplitude versus damping error is also compared. In Figure 4.12, the left part shows the sensitivity curve of the ZVD input shaper with $\omega_i = 1$ rad/sec and the actual damping ratio, the right part shows the sensitivity curve of the rectangle based shape filter $\omega_i = 1$ rad/sec and the actual damping ratio. Although the sensitivity curve of the rectangle based shape filter at the expected model damping ratio is not as flat as that of the ZVD input shaper, still a large variation in the damping ratio is tolerated.

The outputs of a step command through the ZVD input shaper and rectangle based shape filter $f_1[k]$ are compared in Figure 4.13. The sudden change of the shaped command in the left plot is caused by the non-smoothness of the ZVD input shaper, however, in the right plot, the shaped command smoothly changes from the start set point to the end set point. Besides the potential disadvantages of inducing the high frequency unmodeled dynamics, the non-smooth shaped command is difficult to be followed in the model refer-

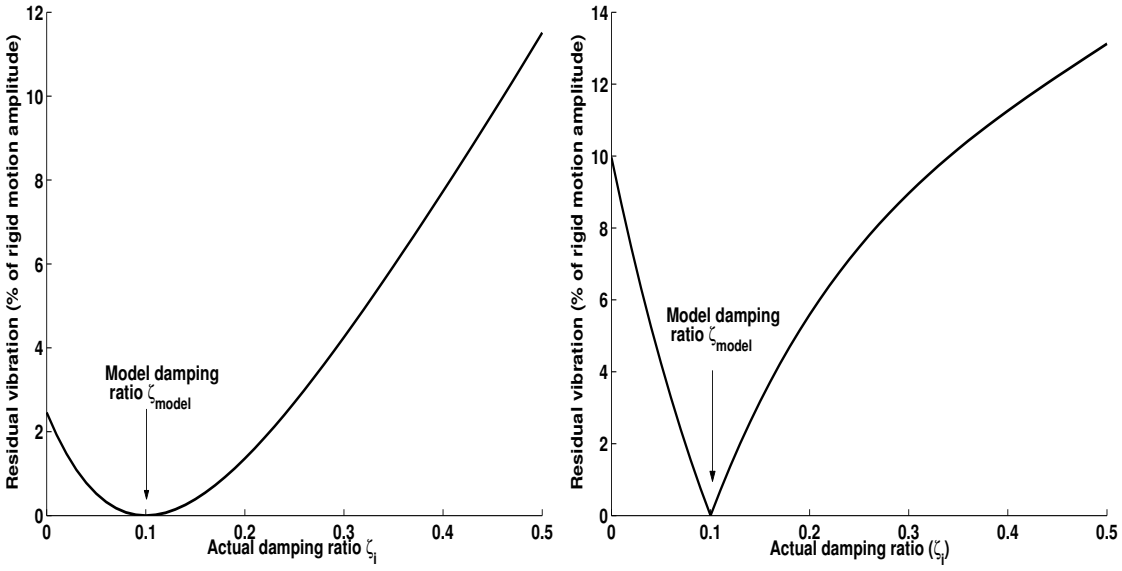

Figure 4.12: Left: ZVD input shaping sensitivity plot versus actual damping ratio; Right: Rectangle based shape filter $f_1[k]$ sensitivity plot versus actual damping ratio.

ence closed-control scheme. The smoother command with more robustness of the rectangle based shape filter can be generated through the filter operation in Conclusion 4.3.2.

Next, simulation results of the position outputs of a second-order harmonic oscillator in (4.61) with a step reference input are compared. Figure 4.14 shows the simulation model of using ZVD input shaper. Figure 4.15 shows the simulation model of using rectangle based shape filter. In both cases, the step reference inputs are sent to ZVD input shaper or rectangle based shape filter. Both ZVD input shaper and rectangle based shape filter are designed by the model undamped natural frequency $\omega_i = 1$ rad/sec and model damping ratio $\zeta_i = 0.05$. Figure 4.16 shows the position outputs with the actual undamped natural frequency $\omega_{actual} = 1$ rad/sec. In this case, residual vibrations are canceled immediately after the time duration of the shape filter. Figure 4.17 shows the position outputs with the actual undamped natural frequency $\omega_{actual} = 1.5$ rad/sec. In this case, ZVD input shaper induces a bigger residual vibration than the rectangle based shape filter since the input shapers have no property to suppress the high frequency unmodeled resonant dynamics. The situation becomes more obvious when the actual undamped natural frequency increases. Figure 4.18

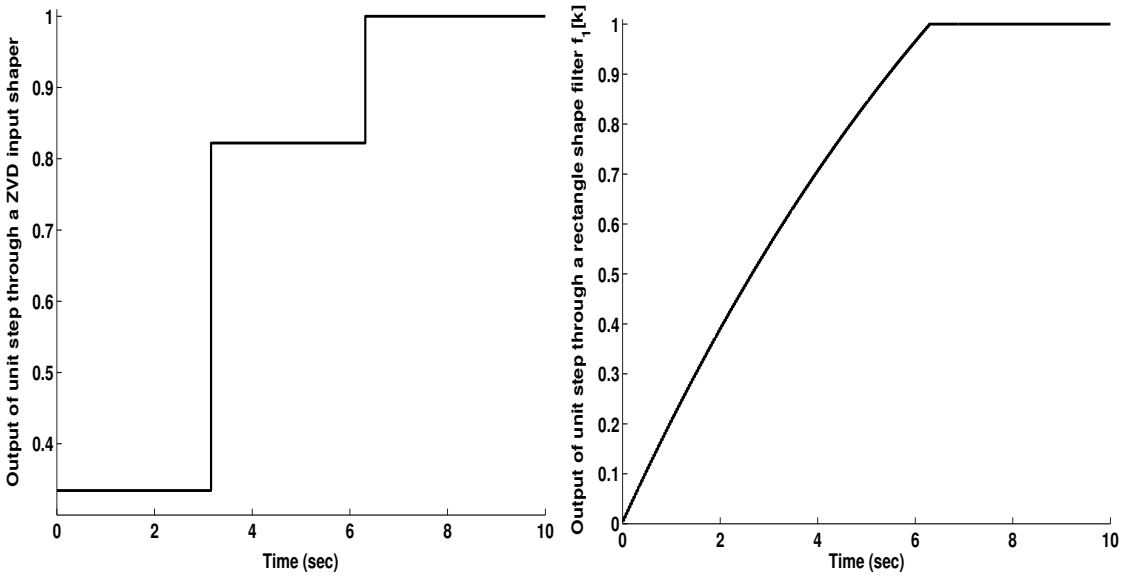

Figure 4.13: Left: Output of a unit step through a ZVD input shaping; Right: Output of a unit step through a rectangle based shape filter $f_1[k]$.

shows the position outputs with the actual undamped natural frequency $\omega_{actual} = 2$ rad/sec. It clearly shows that the residual vibration amplitude caused by the ZVD input shaper is larger than that of the rectangle based shape filter.

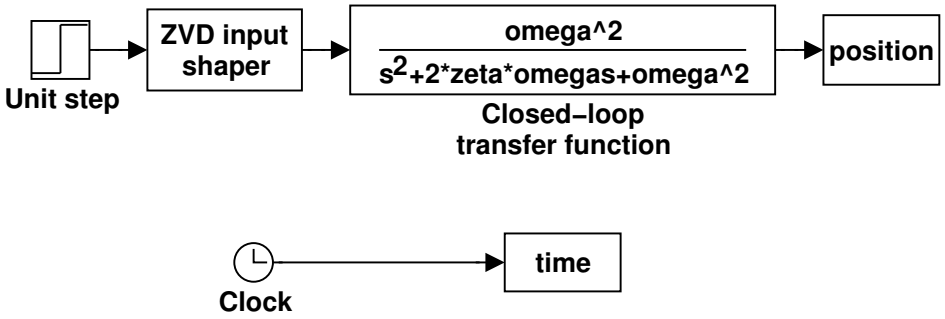

Figure 4.14: A simulation block of regular closed-loop using ZVD input shaper.

Although the rectangle based shape filter function $f_1[k]$ is a velocity candidate, it is not suitable to be used in practice since its initial and final values are too large. With the filter operation in Conclusion 4.3.2, a smoother shape filter with more robustness can be generated. Meanwhile, if the initial and final values of the resultant shape filter function are zero,

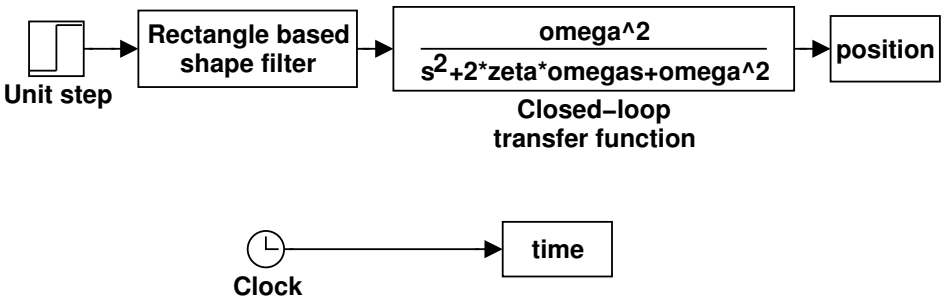

Figure 4.15: A simulation block of regular closed-loop control using rectangle based shape filter.

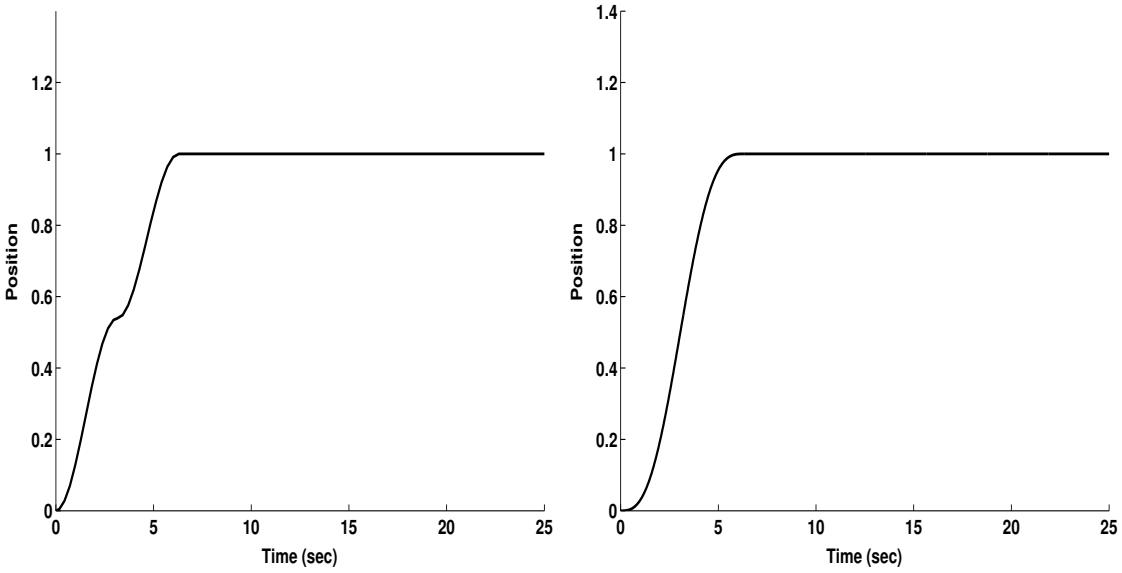

Figure 4.16: Position outputs with actual $\omega_i = 1$ rad/sec. Left: ZVD input shaper; Right: rectangle based shape filter $f_1[k]$.

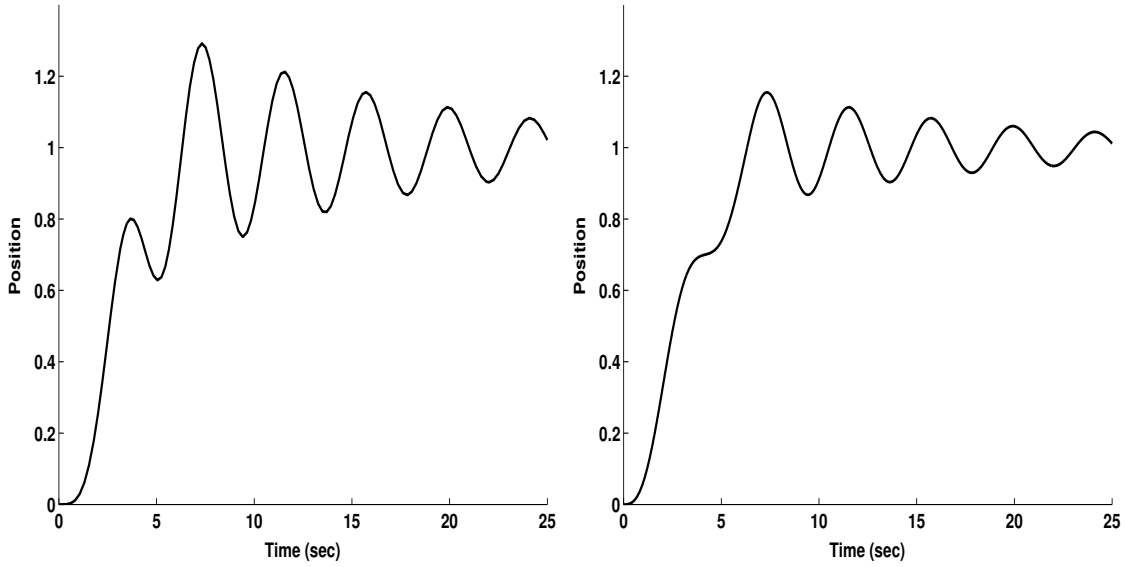

Figure 4.17: Position outputs with actual $\omega_i = 1.5$ rad/sec. Left: ZVD input shaper; Right: rectangle based shape filter $f_1[k]$.

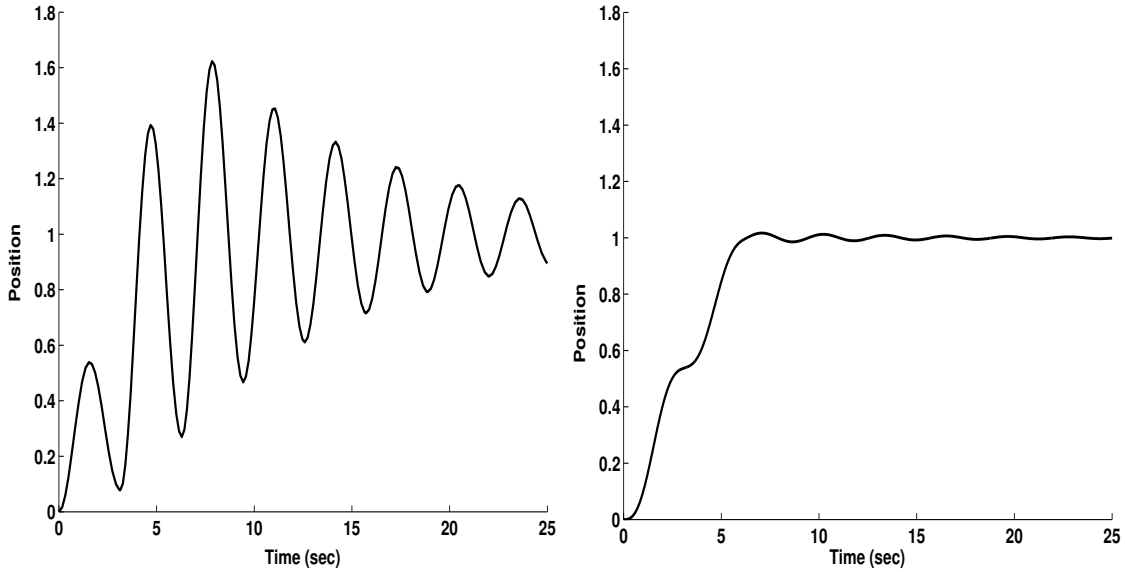

Figure 4.18: Position outputs with actual $\omega_i = 2$ rad/sec. Left: ZVD input shaper; Right: rectangle based shape filter $f_1[k]$.

it can be used as a robust velocity profile for the rigid mode. Figure 4.19 shows the robust rigid body acceleration, velocity, and position profiles generated from the rectangle based shape filter $f_2[k]$, with one resonant mode with parameters $\omega_i = 1$ rad/sec and $\zeta_i = 0.1$. Figure 4.20 shows the robust rigid body acceleration, velocity, and position profiles generated from the rectangle based shape filter $f_3[k]$, with one resonant mode with parameters $\omega_i = 1$ rad/sec and $\zeta_i = 0.1$. The price of more smoothness and robustness is the increase of the move time.

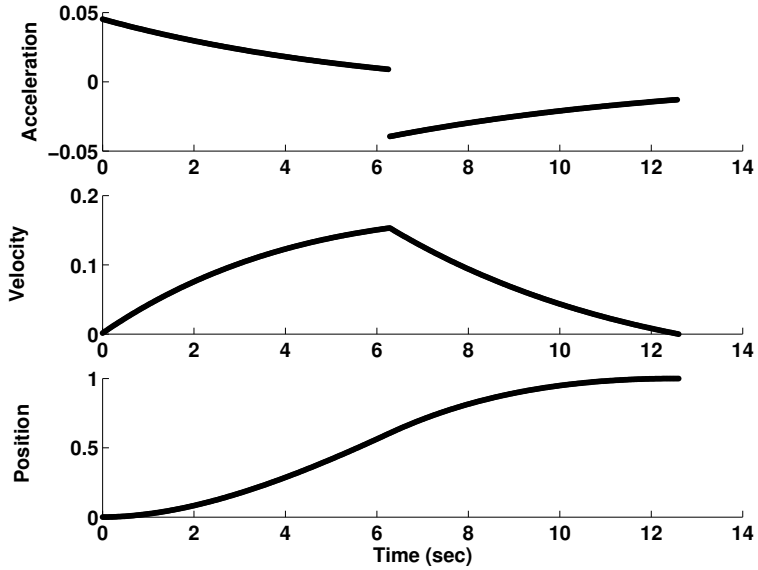

Figure 4.19: Robust acceleration, velocity and position profiles with rectangle based shape filter $f_2[k]$.

4.6.4 Discrete-Time Shape Filter Generation with an Arbitrary Sampling Period

The previous analysis assumes the discrete-time sequence has an exact integer number of impulses. In practice, the calculation result of $M = \frac{2\pi}{\omega_{di} T_s} - 1$ may not be an integer, but a floating point number. The strategy here is to slightly change the sampling period and make the new resultant M be an integer. So a new discrete-time sequence with a slightly

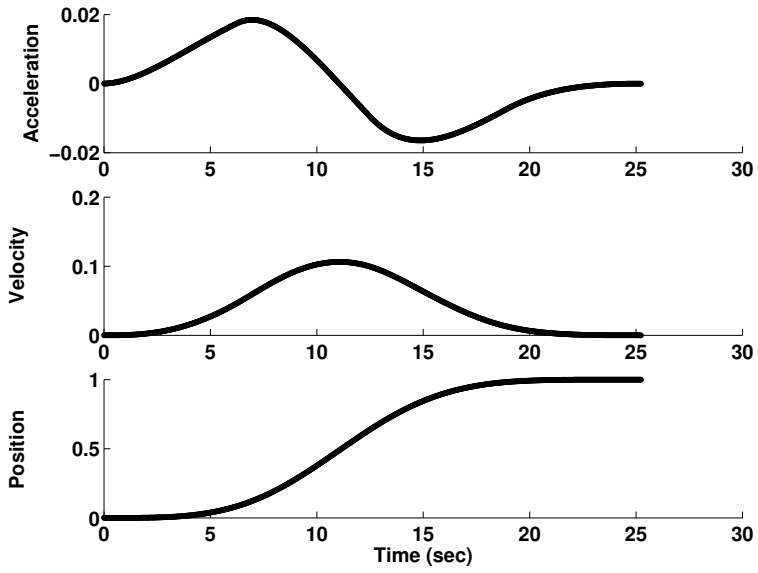

Figure 4.20: Robust acceleration, velocity and position profiles with rectangle based shape filter $f_3[k]$.

changed sampling period is generated. Then this new generated sequence will be replaced by a sequence having the sampling period T_s.

In the case of the rectangle base function, when $M = \frac{2\pi}{\omega_{di} T_s} - 1$ is not an integer but a floating point number, by choosing $M_1 = floor(M)$, and the resultant new sampling period is $T_{s1} = \frac{2\pi}{(M_1+1)\omega_{di}} > T_s$. So the new generated base function with the sampling period T_{s1} is

$$h_1[k] = \begin{cases} 1, & \text{if } 0 \le k \le M_1, \\ 0, & \text{otherwise.} \end{cases} \tag{4.105}$$

Here the operator $floor(x)$ rounds the elements of x to the nearest integer toward $-\infty$ and the operator $ceil(x)$ rounds the element of x to the nearest integer toward $+\infty$. If by choosing $M_2 = ceil(M)$ the resultant new sampling period is $T_{s2} = \frac{2\pi}{(M_2+1)\omega_{di}} < T_s$, the new generated base function with the sampling period T_{s2} is

$$h_2[k] = \begin{cases} 1, & \text{if } 0 \le k \le M_2, \\ 0, & \text{otherwise.} \end{cases} \tag{4.106}$$

To replace the base function $h_1[k]$ of the sampling period T_{s1} with a base function $h[k]$ of the sampling period T_s, two consecutive impulses (B_1 at nT_s and B_2 at $(n+1)T_s$) of $h[k]$ are calculated to replace the impulse B at kT_{s1} of $h_1[k]$. Here, n is an integer satisfying the relationship

$$nT_s \leq kT_{s1} < (n+1)T_s, \tag{4.107}$$

or

$$n \leq \frac{kT_{s1}}{T_s} = n + \alpha < n + 1, \tag{4.108}$$

where $\alpha = \frac{kT_{s1}}{T_s} - n$ and $0 \leq \alpha < 1$. The discrete-time Fourier transform of the original sequence should have the same value as the modified sequence, so

$$Be^{-j\omega(n+\alpha)} = B_1 e^{-j\omega n} + B_2 e^{-j\omega(n+1)}. \tag{4.109}$$

Solving the above equation and obtain

$$B_1 = \frac{\sin(\omega(1-\alpha))}{\sin\omega} B, \tag{4.110}$$

$$B_2 = \frac{\sin(\omega\alpha)}{\sin\omega} B. \tag{4.111}$$

Notice the unit of discrete-time Fourier transform variable ω is rad, then the impulses B_1 and B_2 in terms of ω_{di} rad/sec and sampling period T_s sec are

$$B_1 = \frac{\sin(\omega_{di}T_s(1-\alpha))}{\sin(\omega_{di}T_s)} B, \tag{4.112}$$

$$B_2 = \frac{\sin(\omega_{di}T_s\alpha)}{\sin(\omega_{di}T_s)} B. \tag{4.113}$$

The whole impulses of the modified base function $h[k]$ can be easily generated by the following program routine.

```
h[k] = 0, k = 0, 1, ... ceil(M_1 * T_s1 / T_s);
for k = 0; k = k + 1; k <= M1

  n = floor(k * T_s1 / T_s);
  alpha = k * T_s1 / T_s - n;

  //h1[k] is the modified sequence with sampling period Ts1
  B = h1[k];
  B1 = sin(omega_di * T_s * (1 - alpha)) / sin(omega_di * T_s) * B;
  B2 = sin(omega_di * T_s * (alpha)) / sin(omega_di * T_s) * B;

  if alpha == 0
     h[n] = h[n] + B1;
  else
     h[n] = h[n] + B1;
     h[n+1] = h[n+1] + B2;
  end
end
```

Notice the impulse at kT_{s1} may also be replaced by two non-consecutive impulses or more than two impulses, such as impulse at $(n-1)T_s$ and impulse at $(n+1)T_s$. Similarly, the modified base function of the sampling period T_s can also be generated from the base function $h_2[k]$ of the sampling period T_{s2}.

In the following sections, robust smooth shape filter generation based on other window functions is studied. Instead of analyzing the continuous-time case, the discrete-time case is directly generated. The algorithm described in this section applies to other base functions.

4.7 Robust Shape Filter Generation Using Hanning Window

If the sampling period is T_s sec and the total discrete-time sequence has $M+1$ impulses, the Hanning window function is

$$h[k] = \begin{cases} 0.5 - 0.5\cos\left(2\pi k/M\right), & \text{if } 0 \le k \le M, \\ 0, & \text{otherwise.} \end{cases} \tag{4.114}$$

By calculation, If $H(\omega_{di}T_s) = H(\sqrt{1-\zeta_i^2}\omega_i T_s) = 0$, then $\omega_{di}T_s = \frac{4\pi}{M}$ and $M = \frac{4\pi}{\omega_{di}T_s}$.

If M is a positive integer, a smooth shape filter can be generated as

$$f[k] = \frac{h[k]/e^{\zeta_i \omega_i k T_s}}{\sum_{m=0}^{M} h[m]/e^{\zeta_i \omega_i m T_s}}. \tag{4.115}$$

To improve robustness, the filter operation of Conclusion 4.3.2 is performed. Let $f_1[k] = f[k]$, then more robust shape filters $f_2[k], f_3[k], \ldots$ can be generated following the filter operation of Conclusion 4.3.2. Notice in (4.115), it is not necessary to derive the explicit form for $f[k]$. Since the sequence $h[k]$ is known, the sequence $f[k]$ can be generated through a simple numerical calculation.

The residual vibration level (4.68) can be plotted for the Hanning based shape filter $f_1[k]$ and rectangle based shape filter $f_1[k]$. In Figure 4.21, the left part shows the sensitivity curve of the rectangle based shape filter with $\omega_{model} = 1$ rad/sec and different damping $\zeta_i = 0, 0.05, 0.2$, and the right part shows the sensitivity curve of the Hanning based shape filter $f_1[k]$ with $\omega_{model} = 1$ rad/sec and different damping $\zeta_i = 0, 0.05, 0.2$. Clearly, the robustness of the Hanning based shape filter is increased both at the model natural frequency and the unmodeled high frequency.

The outputs of a step command through the ZVDDD input shaper and the Hanning based shape filter $f_1[k]$ are compared in Figure 4.22. The sudden change of the shaped command in the left plot is caused by the non-smoothness of the ZVDDD input shaper, however, in the right plot, the shaped command smoothly changes from the start set point to the end set point. Besides the potential disadvantages of inducing high frequency unmodeled dynamics, the other disadvantage of the non-smooth shaped command is that it is difficult to follow in the model reference closed-control scheme. The smoother command with more robustness of the Hanning based shape filter can be generated through the filter operation in Conclusion 4.3.2.

Since the Hanning function starts and ends at zero, the Hanning based shape filter $f_1[k]$ can be used as a robust velocity candidate. Figure 4.23 shows the robust rigid body acceleration, velocity, and position profiles generated from the Hanning based shape filter $f_1[k]$, with one resonant mode with parameters $\omega_i = 1$ rad/sec and different damping ratio (Left:

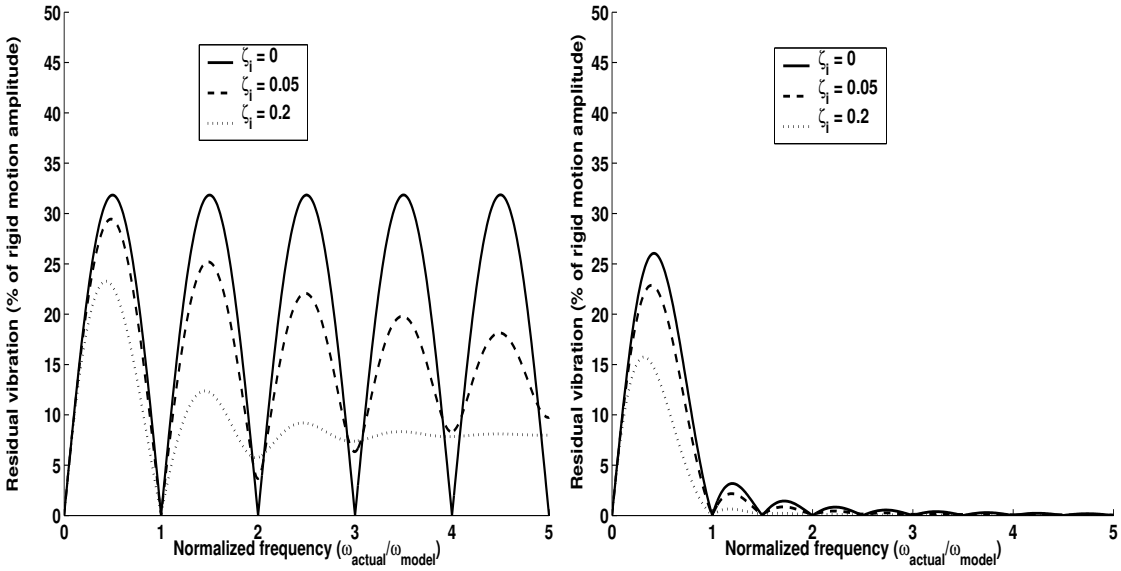

Figure 4.21: Left: Rectangle based shape filter $f_1[k]$ sensitivity plot versus actual natural frequency; Right: Hanning based shape filter $f_1[k]$ sensitivity plot versus actual natural frequency.

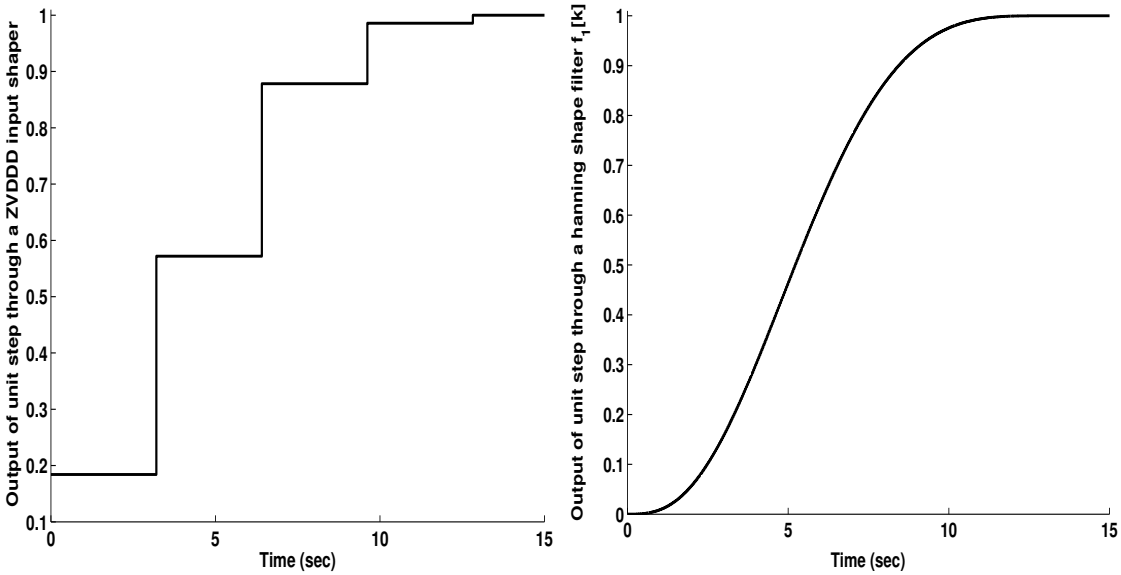

Figure 4.22: Left: Output of a unit step through a ZVDDD input shaping; Right: Output of a unit step through a Hanning based shape filter $f_1[k]$.

$\zeta_i = 0.2$; Right: $\zeta_i = 0.5$).

Hanning based shape filter generation for an arbitrary sampling period can be implemented following the procedure in Section 4.6.4.

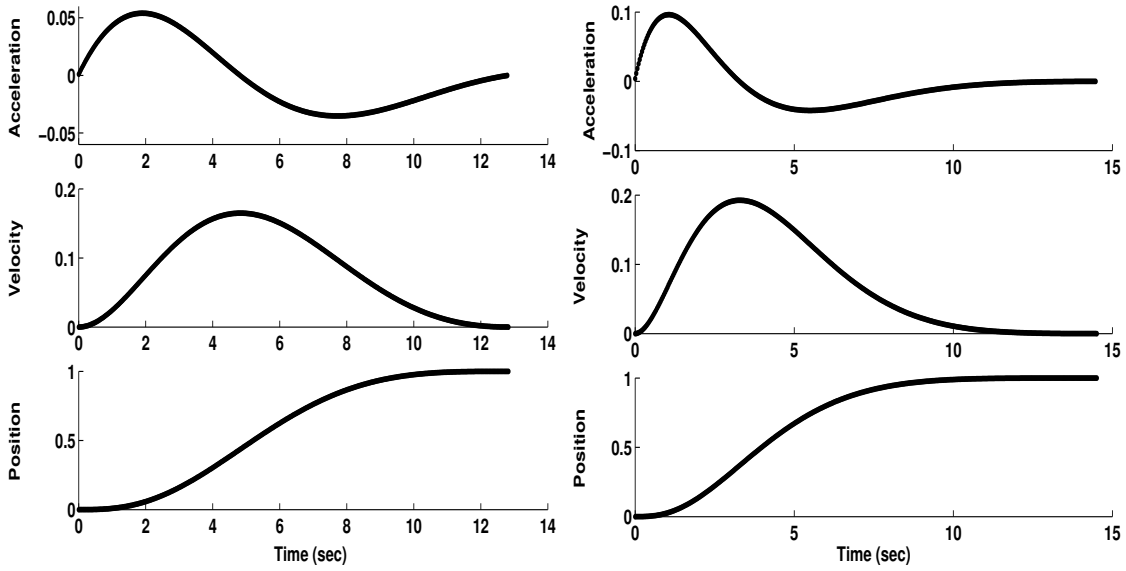

Figure 4.23: Robust acceleration, velocity and position profiles with the Hanning based shape filter $f_1[k]$ (Left: $\omega_i = 1$ rad/sec and $\zeta_i = 0.2$; Right: $\omega_i = 1$ rad/sec and $\zeta_i = 0.5$).

4.8 Robust Shape Filter Generation Using Blackman Window

If the sampling period is T_s sec and the total discrete-time sequence has $M + 1$ impulses, the Blackman window function is

$$h[k] = \begin{cases} 0.42 - 0.5\cos(2\pi n/M) + 0.08\cos(4\pi k/M), & \text{if } 0 \le k \le M, \\ 0, & \text{otherwise.} \end{cases} \tag{4.116}$$

By calculation, If $H(\omega_{di}T_s) = H(\sqrt{1-\zeta_i^2}\omega_i T_s) = 0$, then $\omega_{di}T_s = \frac{6\pi}{M}$ and $M = \frac{6\pi}{\omega_{di}T_s}$.

If M is a positive integer, a smooth shape filter can be generated as

$$f[k] = \frac{h[k]/e^{\zeta_i \omega_i k T_s}}{\sum_{m=0}^{M} h[m]/e^{\zeta_i \omega_i m T_s}}. \tag{4.117}$$

Again, it is not necessary to derive the explicit form for $f[k]$. Since sequence $h[k]$ is known, the sequence $f[k]$ can be generated through a simple numerical calculation. Let $f_1[k] = f[k]$, then more robust shape filters $f_2[k], f_3[k], \ldots$ can be generated following the filter operation of Conclusion 4.3.2.

Blackman window based shape filter generation for an arbitrary sampling period can be implemented following the procedure in Section 4.6.4.

4.9 Can Hamming Window be Used to Robust Shape Filter Generation?

If the sampling period is T_s sec and the total discrete-time sequence has $M + 1$ impulses, the Hamming window function is

$$h[k] = \begin{cases} \frac{25}{46} - \frac{21}{46}\cos\left(2\pi k/M\right), & \text{if } 0 \le k \le M, \\ 0, & \text{otherwise.} \end{cases} \tag{4.118}$$

The numerator of the real part of the discrete-time Fourier transform is calculated as

$$\begin{aligned} NR(\omega) = & -2 - 4\left(\cos\left(\frac{\pi}{M}\right)\right)^2 \cos\left(\omega M\right)\cos\left(\omega\right) + 25\left(\cos\left(\frac{\pi}{M}\right)\right)^2 \sin\left(\omega M\right)\sin\left(\omega\right) \\ & + 4\left(\cos\left(\frac{\pi}{M}\right)\right)^2 \cos\left(\omega M\right) - 23\sin\left(\omega M\right)\sin\left(\omega\right) - 2\sin\left(\omega\right)\sin\left(\omega M\right)\cos\left(\omega\right) \\ & + 2\cos\left(\omega M\right)\left(\cos\left(\omega\right)\right)^2 - 4\cos\left(\omega\right)\left(\cos\left(\frac{\pi}{M}\right)\right)^2 + 4\left(\cos\left(\frac{\pi}{M}\right)\right)^2 \\ & + 2\left(\cos\left(\omega\right)\right)^2 - 2\cos\left(\omega M\right). \end{aligned} \tag{4.119}$$

And the numerator of the imaginary part of the discrete-time Fourier transform is calculated

as

$$
\begin{aligned}
NI(\omega) = & -25 - 50\left(\cos\left(\frac{\pi}{M}\right)\right)^2\cos(\omega M)\cos(\omega) + 50\left(\cos\left(\frac{\pi}{M}\right)\right)^2\sin(\omega M)\sin(\omega) \\
& + 50\left(\cos\left(\frac{\pi}{M}\right)\right)^2\cos(\omega M) - 25\sin(\omega M)\sin(\omega) - 25\sin(\omega)\sin(\omega M)\cos(\omega) \\
& - 42\cos(\omega)\cos\left(\frac{\pi}{M}\right)\sin\left(\frac{\pi}{M}\right) + 25\cos(\omega M)(\cos(\omega))^2 \\
& - 50\cos(\omega)\left(\cos\left(\frac{\pi}{M}\right)\right)^2 + 50\left(\cos\left(\frac{\pi}{M}\right)\right)^2 + 42\sin\left(\frac{\pi}{M}\right)\cos\left(\frac{\pi}{M}\right) \\
& + 25(\cos(\omega))^2 - 42\sin\left(\frac{\pi}{M}\right)\cos\left(\frac{\pi}{M}\right)\cos(\omega M) \\
& - 25\cos(\omega M) + 42\sin\left(\frac{\pi}{M}\right)\cos\left(\frac{\pi}{M}\right)\cos(\omega M)\cos(\omega)
\end{aligned}
\tag{4.120}
$$

No ω exists such that $NR(\omega) = NI(\omega) = 0$. So $H(\omega) = 0$ has no solution and the shape filter cannot be generated from Hamming window in theory by following Conclusion 4.3.1. However, approximately when $\omega \approx \frac{4\pi}{M}$, $|H(\omega)|$ approaches an extremely small number [60]. If $M = \frac{4\pi}{\omega_{di}T_s}$ and M is a positive integer, a smooth shape filter can be generated as

$$
f[k] = \frac{h[k]/e^{\zeta_i\omega_i kT_s}}{\sum_{m=0}^{M} h[m]/e^{\zeta_i\omega_i mT_s}}. \tag{4.121}
$$

In this case, since $|H(\omega_{di}T_s)| \approx 0$, the residual vibration cannot be eliminated in theoretical sense. But an extremely small $|H(\omega_{di}T_s)|$ implies the residual vibration is sufficiently suppressed. Again, it is not necessary to derive the explicit form for $f[k]$. Since the sequence $h[k]$ is known, the sequence $f[k]$ can be generated through a simple numerical calculation. Let $f_1[k] = f[k]$, then more robust shape filters $f_2[k], f_3[k], \ldots$ can be generated following the filter operation of Conclusion 4.3.2.

Hamming based shape filter generation for an arbitrary sampling period can be implemented following the procedure in Section 4.6.4.

4.10 Robust Shape Filter Generation Using Other Continuous Functions

From Conclusion 4.3.1, a smooth robust shape filter can be generated from a finite support smooth function $h(t)$, such that $H(\omega_{di}) = 0$. Some simple window functions have been used as base functions to generate the robust shape filters in the previous sections. Numerous smooth functions $h(t)$ may have the property of $H(\omega_{di}) = 0$ or $H(\omega_{di}) \approx 0$. So all of them can be used as base functions to generate the robust shape filters. Here, some window functions that possess the property are listed. These window functions were originally used for harmonic analysis [31, 57, 29].

- $\cos^{\alpha}(X)$ window.
- Riesz window.
- Riemann window.
- de la Vallé-Poussin window.
- Tukey window.
- Bohman window.
- Poisson window.
- Hanning-Poisson window.
- Cauchy window.
- Gaussian window.
- Dolph-Chebeshev window.
- Kaiser-Bessel window.
- Barcilon-Temes window.
- Nuttall window.
- Modified Bartlett-Hanning window.
- Others.

4.11 Robust Shape Filter Generation Using Several Continuous Functions

A section of a base function $h[k]$ can be constructed from other smooth functions through products, sums, convolutions, integral, or other mathematical operations. If the constructed base function has the property of $H(\omega_{di}T_s) = 0$, then it can be used to generate the robust shape filters through Conclusion 4.3.1. Here, a simple example is given to show the basic idea.

Here, a base function $h[k]$ is generated from three Hanning window functions

$$h[k] = h_{s1}[k] + h_{s2}[k] + h_{s3}[k], \quad 0 \le k \le 2M, \tag{4.122}$$

where

$$h_{s1}[k] = \begin{cases} \frac{1}{2} - \frac{1}{2}\cos(\pi k/M), & \text{if } 0 \le k \le 2M, \\ 0, & \text{otherwise}, \end{cases} \tag{4.123}$$

$$h_{s2}[k] = \begin{cases} C\left[\frac{1}{2} - \frac{1}{2}\cos(2\pi k/M)\right], & \text{if } 0 \le k \le M, \\ 0, & \text{otherwise}, \end{cases} \tag{4.124}$$

$$h_{s3}[k] = \begin{cases} C\left[\frac{1}{2} - \frac{1}{2}\cos(2\pi k/M)\right], & \text{if } M \le k \le 2M, \\ 0, & \text{otherwise}, \end{cases} \tag{4.125}$$

where C is a constant number. Figure 4.24 shows a typical combination of functions $h_{s1}[k]$, $h_{s2}[k]$, $h_{s3}[k]$, and the resultant base function $h[k]$.

By calculation, If $H(\omega_{di}T_s) = H(\sqrt{1-\zeta_i^2}\omega_i T_s) = 0$, then

$$\omega_{di}T_s = \frac{2\left[\cos(\pi/M)\right]^2(C+1) + 2C\cos(\pi/M) - 1}{2C\cos(\pi/M) + 2C + 1}. \tag{4.126}$$

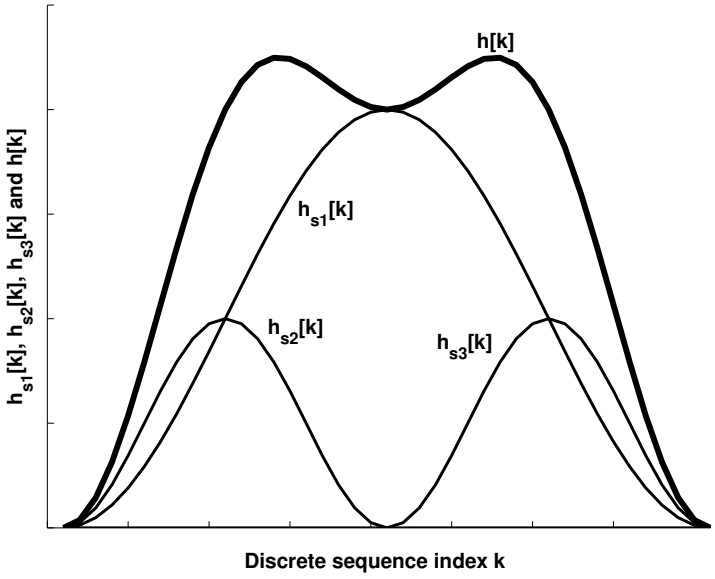

Figure 4.24: A typical combination of functions $h_{s1}[k]$, $h_{s2}[k]$, $h_{s3}[k]$, and the resultant base function $h[k]$.

So M can be derived to be

$$M = \frac{\pi}{\arccos \frac{C\cos(\omega_{di}T_s) - C + \sqrt{C^2[\cos(\omega_{di}T_s)]^2 + 2C^2\cos(\omega_{di}T_s) + C^2 + 2C + 6C\cos(\omega_{di}T_s) + 2 + 2\cos(\omega_{di}T_s)}}{2C+2}}. \tag{4.127}$$

If M is a positive integer, a smooth shape filter can be generated as

$$f[k] = \frac{h[k]/e^{\zeta_i\omega_i kT_s}}{\sum_{m=0}^{2M} h[m]/e^{\zeta_i\omega_i mT_s}} \quad 0 \le k \le 2M. \tag{4.128}$$

Normalized base functions $h[k]$ and shape filters are generated based on the same natural frequency $\omega_i = 1$ rad/sec and the damping ratio $\zeta_i = 0.2$ with different values of parameter C. Figure 4.25 shows the normalized base function $h[k]$ and the shape filter $f[k]$ with $C = 0.25$. Figure 4.26 shows the normalized base function $h[k]$ and the shape filter $f[k]$ with $C = 0.5$. Figure 4.27 shows the normalized base function $h[k]$ and the shape filter $f[k]$ with $C = 1$. Figure 4.28 shows the normalized base function $h[k]$ and the shape filter $f[k]$ with $C = 2$. It clearly shows that the time duration of the shape filter decreases with an increase in the parameter C.

The values of M from Figure 4.25 to Figure 4.28 are made to be positive integers by

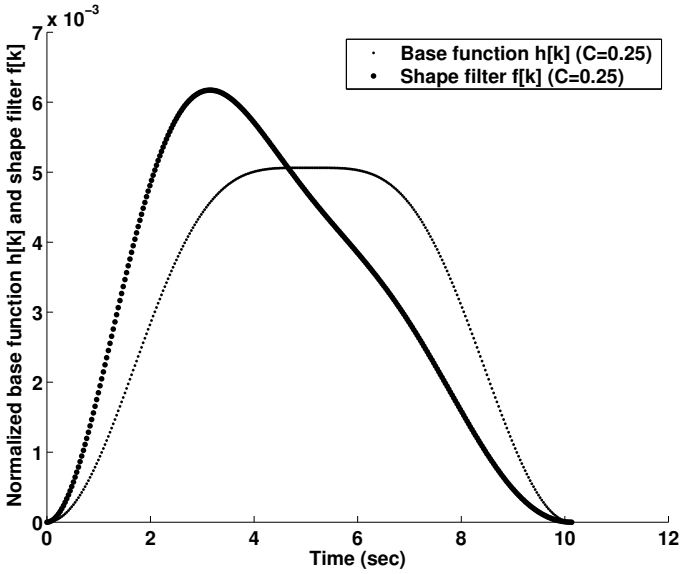

Figure 4.25: Normalized base function $h[k]$ and the shape filter $f[k]$ with $C = 0.25$.

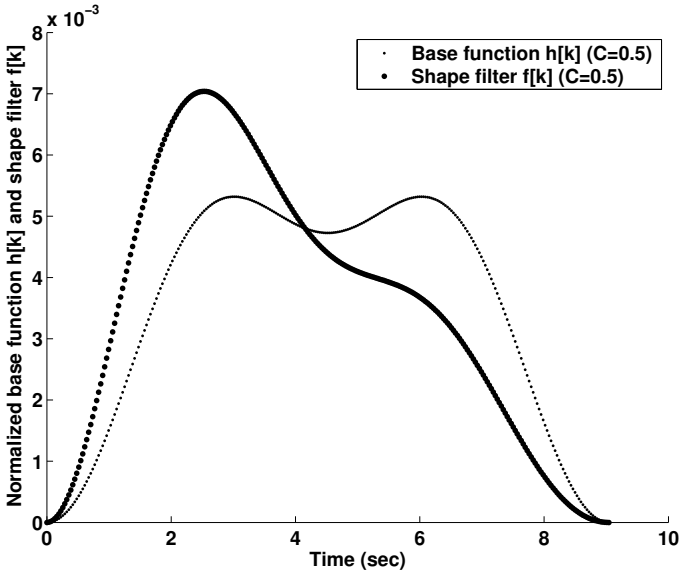

Figure 4.26: Normalized base function $h[k]$ and the shape filter $f[k]$ with $C = 0.5$.

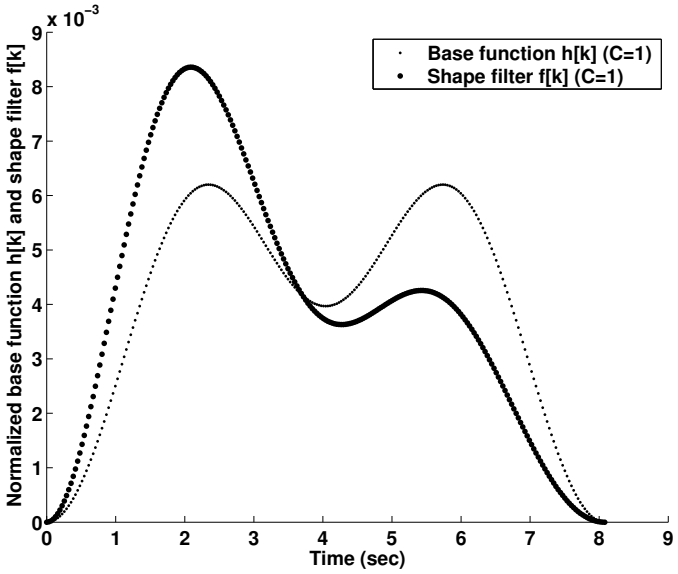

Figure 4.27: Normalized base function $h[k]$ and the shape filter $f[k]$ with $C = 1$.

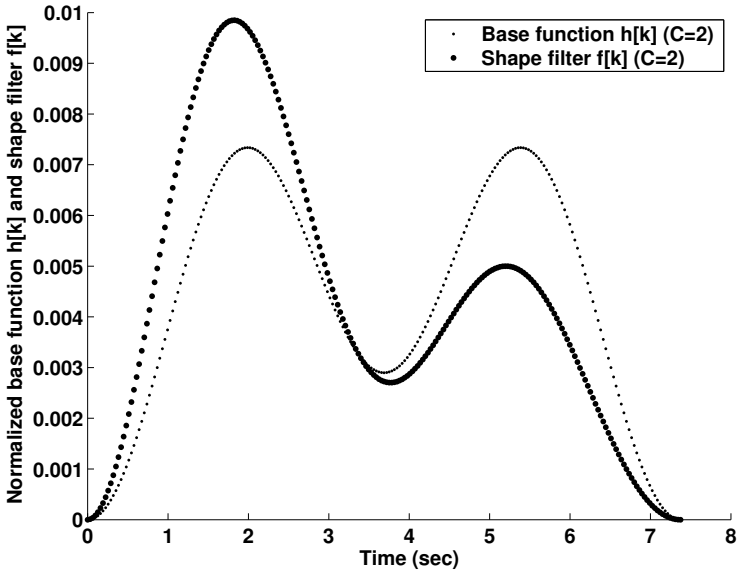

Figure 4.28: Normalized base function $h[k]$ and the shape filter $f[k]$ with $C = 2$.

choosing an appropriate sampling period. The modification of the original base function according to an arbitrary sampling period has already studied in the previous section. In the derivation, the total impulses of the base function $h[k]$ are assumed to be an odd number $2M + 1$, however, the total impulses of the base function can also be an even number $2M$.

4.12 Non-Symmetric Continuous Function Based Shape Filter Generation

Figure 4.29 shows the architecture of the vibration suppression shape filter. From the previous study, all the input shaping technique in Section 4.4 and OATF in Section 4.5 belong to the impulse function based shape filters.

In the previous robust vibration shape filter generation, all the base functions have a symmetric waveform. In this section, non-symmetric function based shape filter generation method is studied. Two methods to generate a non-symmetric base function are studied.

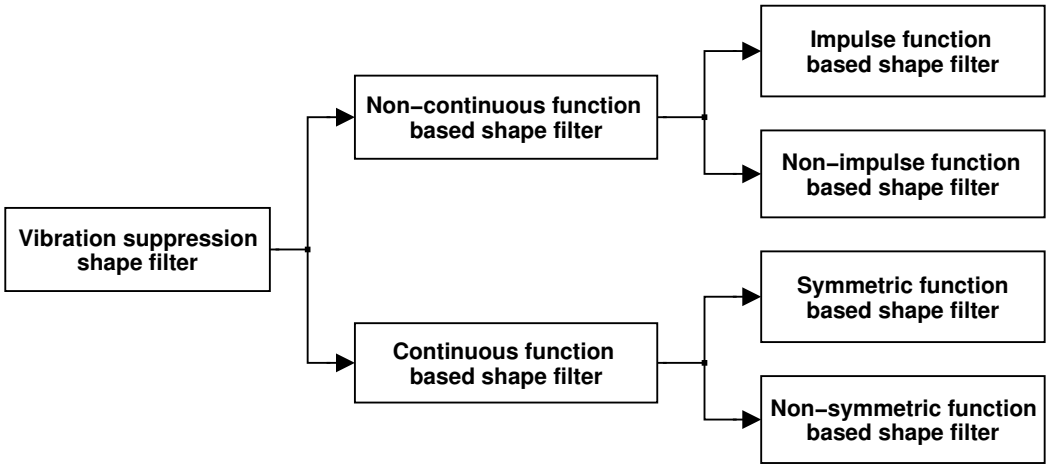

Figure 4.29: The architecture of the vibration suppression shape filter.

4.12.1 Non-Symmetric Base Function Generation from the Derivative of a Base Function

If $g(t)$ is a base function such that $G(\omega_{di}) = 0$, a non-symmetric base function can be generated by the linear combination of $g(t)$ and the derivative of $g(t)$, such that

$$h(t) = k_1 g(t) + k_2 \frac{d}{dt} g(t), \tag{4.129}$$

where k_1 and k_2 are two constants. The Fourier transform of $h(t)$ is given by

$$H(\omega) = \int_0^\infty h(t) e^{-j\omega t} dt, \tag{4.130}$$

$$= \int_0^\infty \left[k_1 g(t) + k_2 \frac{d}{dt} g(t) \right] e^{-j\omega t} dt, \tag{4.131}$$

$$= k_1 G(\omega) + k_2 j\omega G(\omega). \tag{4.132}$$

So the new function $h(t)$ can be used as a base function because the spectrum $H(\omega)$ at $\omega = \omega_{di}$ is exactly zero as given by

$$H(\omega_{di}) = k_1 G(\omega_{di}) + k_2 j\omega_{di} G(\omega_{di}), \tag{4.133}$$

$$= k_1 \cdot 0 + k_2 j\omega_{di} \cdot 0, \tag{4.134}$$

$$= 0. \tag{4.135}$$

The above derivation applies to discrete-time signals. If a discrete-time signal $g[k]$, $0 \leq k \leq M$, is a base function such that $G(\omega_{di} T_s) = 0$, here T_s is the sampling period in sec and ω_{di} is the damped natural frequency in rad/sec, the differencing in time of $g[k]$ is

$$dg[k] = \begin{cases} g[k] - g[k-1], & \text{if } 0 \leq k \leq M+1, \\ 0, & \text{otherwise.} \end{cases} \tag{4.136}$$

A non-symmetric base function $h[k]$ can be generated by the linear combination of $g[k]$ and the differencing signal $dg[k]$ by

$$h[k] = k_1 \cdot g[k] + k_2 \cdot dg[k] \quad 0 \leq k \leq M+1, \tag{4.137}$$

where k_1 and k_2 are two constants. The discrete-time Fourier transform of $h[k]$ is given by

$$H(\omega) = k_1 \cdot G(\omega) + k_2 \cdot (1 - e^{-j\omega})G(\omega). \tag{4.138}$$

So the new function $h[k]$ can be used as a base function because the spectrum $H(\omega)$ at $\omega = \omega_{di}T_s$ is exactly zero as given by

$$H(\omega_{di}T_s) = k_1 \cdot G(\omega_{di}T_s) + k_2 \cdot (1 - e^{-j\omega_{di}T_s})G(\omega_{di}T_s), \tag{4.139}$$

$$= k_1 \cdot 0 + k_2 \cdot (1 - e^{-j\omega_{di}T_s}) \cdot 0, \tag{4.140}$$

$$= 0. \tag{4.141}$$

A simple example generating a non-symmetric base function is demonstrated here. If $g[k]$ is a Hanning function

$$g[k] = \begin{cases} \frac{1}{2} - \frac{1}{2}\cos(2\pi k/M), & \text{if } 0 \le k \le M, \\ 0, & \text{otherwise}, \end{cases} \tag{4.142}$$

the new generated base function is $h[k] = k_1 \cdot g[k] + k_2 \cdot dg[k]$. If $H(\omega_{di}T_s) = H(\sqrt{1-\zeta_i^2}\omega_i T_s) = 0$, then $\omega_{di}T_s = \frac{4\pi}{M}$ and $M = \frac{4\pi}{\omega_{di}T_s}$. If M is a positive integer, a shape filter can be generated as

$$f[k] = \frac{h[k]/e^{\zeta_i\omega_i kT_s}}{\sum_{m=0}^{M} h[m]/e^{\zeta_i\omega_i mT_s}}. \tag{4.143}$$

Figure 4.30 shows a construction of a non-symmetric base function $h[k]$ with the undamped natural frequency $\omega_i = 1$ rad/sec and the damping ratio $\zeta_i = 0.1$. The constants k_1 and k_2 are chosen to be $k_1 = 1$ and $k_2 = -25$. Figure 4.31 shows the normalized base function $h[k]$ and the shape filter $f[k]$.

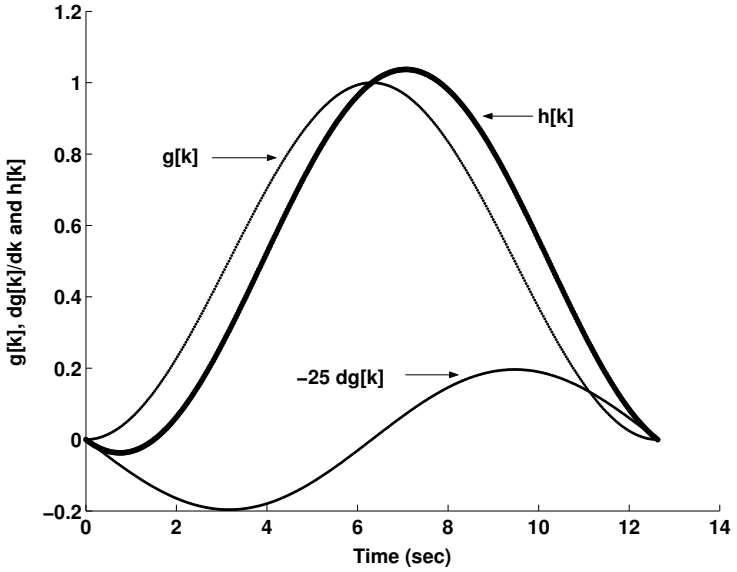

Figure 4.30: Construction of a non-symmetric base function h[k].

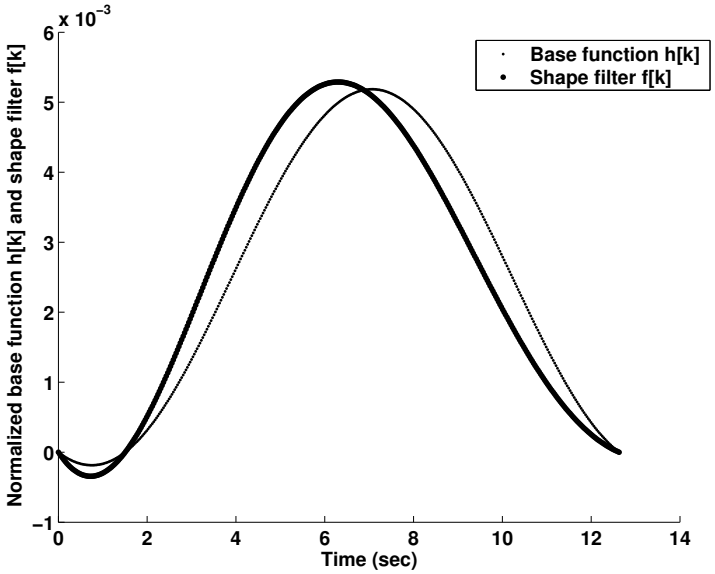

Figure 4.31: Normalized base function $h[k]$ and shape filter $f[k]$.

4.12.2 Non-Symmetric Base Function Generation from the Self Convolution of a Base Function

If $g(t)$ is a base function such that $G(\omega_{di}) = 0$, a non-symmetric base function can be generated by the linear combination of $g(t - t_1)$ and $g * g(t)$, such that

$$h(t) = k_1 g(t - t_1) + k_2 g * g(t), \tag{4.144}$$

where k_1 and k_2 are two constants and t_1 is a positive number. The Fourier transform of $h(t)$ is given by

$$H(\omega) = \int_0^\infty h(t) e^{-j\omega t} dt, \tag{4.145}$$

$$= \int_0^\infty \left[k_1 g(t - t1) + k_2 g * g(t)\right] e^{-j\omega t} dt, \tag{4.146}$$

$$= k_1 e^{-j\omega t_1} G(\omega) + k_2 G(\omega)^2. \tag{4.147}$$

So the new function $h(t)$ can be used as a base function because the spectrum $H(\omega)$ at $\omega = \omega_{di}$ is exactly zero as given by

$$H(\omega_{di}) = k_1 e^{-j\omega_{di} t_1} G(\omega_{di}) + k_2 G(\omega_{di})^2, \tag{4.148}$$

$$= k_1 e^{-j\omega_{di} t_1} \cdot 0 + k_2 \cdot 0^2, \tag{4.149}$$

$$= 0. \tag{4.150}$$

The above derivation applies to discrete-time signals. If a discrete-time signal $g[k]$, $0 \leq k \leq M$, is a base function such that $G(\omega_{di} T_s) = 0$, here T_s is the sampling period in sec and ω_{di} is the damped natural frequency in rad/sec, the self convolution of $g[k]$ is

$$g * g[k] = \begin{cases} \sum_{m=0}^{k} g[k - m] g[m], & \text{if } 0 \leq k \leq 2M, \\ 0, & \text{otherwise.} \end{cases} \tag{4.151}$$

A non-symmetric base function can be generated by the linear combination of $g[k]$ and the self convolution signal $g * g[k]$ by

$$h[k] = k_1 \cdot g[k - k_0] + k_2 \cdot g * g[k], \tag{4.152}$$

where k_0 is a non-negative integer. The discrete-time Fourier transform of $h[k]$ is given by

$$H(\omega) = k_1 \cdot e^{-j\omega k_0} G(\omega) + k_2 \cdot G(\omega)^2. \tag{4.153}$$

So the new function $h[k]$ can be used as a base function because the spectrum $H(\omega)$ at $\omega = \omega_{di} T_s$ is exactly zero as given by

$$\begin{aligned} H(\omega_{di}T_s) &= k_1 \cdot e^{-j\omega_{di}T_s k_0} G(\omega_{di}T_s) + k_2 \cdot G(\omega_{di}T_s)^2, && (4.154)\\ &= k_1 \cdot e^{-j\omega_{di}T_s k_0} \cdot 0 + k_2 \cdot 0, && (4.155)\\ &= 0. && (4.156) \end{aligned}$$

A simple example generating a non-symmetric base function is demonstrated here. If $g[k]$ is a Hanning function

$$g[k] = \begin{cases} \frac{1}{2} - \frac{1}{2}\cos(2\pi k/M), & \text{if } 0 \le k \le M, \\ 0, & \text{otherwise.} \end{cases} \tag{4.157}$$

and $k_0 = M$, the new generated base function is $h[k] = k_1 \cdot g[k - M] + k_2 \cdot g * g[k]$. If $H(\omega_{di}T_s) = H(\sqrt{1-\zeta_i^2}\omega_i T_s) = 0$, then $\omega_{di}T_s = \frac{4\pi}{M}$ and $M = \frac{4\pi}{\omega_{di}T_s}$. If M is a positive integer, a shape filter can be generated as

$$f[k] = \frac{h[k]/e^{\zeta_i \omega_i k T_s}}{\sum_{m=0}^{M} h[m]/e^{\zeta_i \omega_i m T_s}}. \tag{4.158}$$

Figure 4.32 shows a construction of a non-symmetric base function $h[k]$ with the undamped natural frequency $\omega_i = 1$ rad/sec and the damping ratio $\zeta_i = 0.1$. The constants k_1 and k_2 are chosen to be $k_1 = 1$ and $k_2 = 1/125$. Figure 4.33 shows the normalized base function $h[k]$ and the shape filter $f[k]$.

It must be noted that there are a number of methods to generate a non-symmetric base function. The methods described in this section are only possible methods and not exhaustive ones.

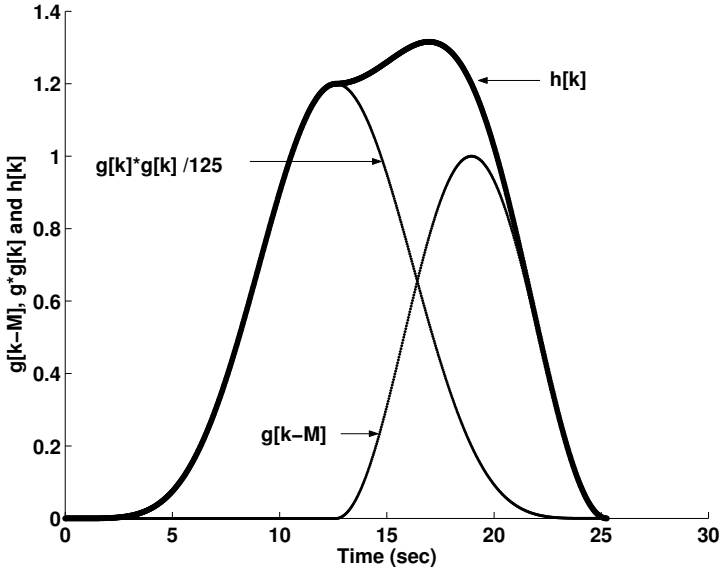

Figure 4.32: Construction of a non-symmetric base function $h[k]$.

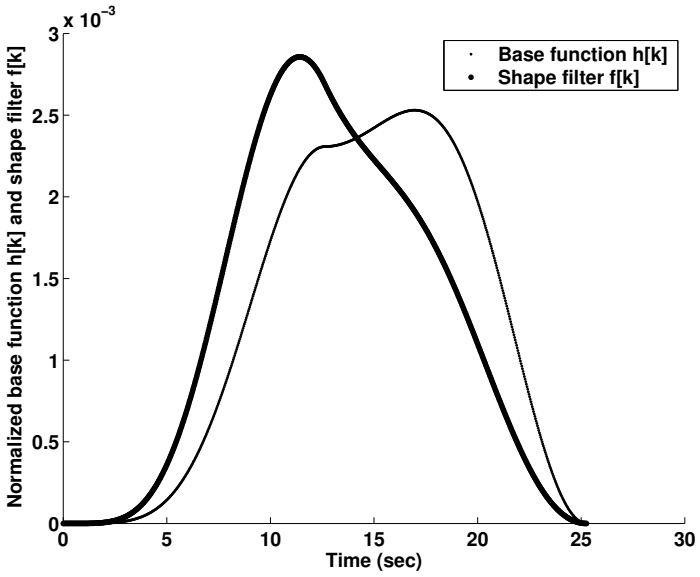

Figure 4.33: Normalized base function $h[k]$ and shape filter $f[k]$.

4.13 Simulation Results for Hard Disk Drive Seek Control

In this section, a robust vibration suppression shape filter is used to design a robust acceleration profile with the hard disk model in Chapter 3. In Chapter 3, the prolate spheroidal wave is used to design a robust acceleration profile with parameter settings $\Omega_0 = 9.68 \times 10^3$ rad/sec, a move time of 2.5×10^{-3} sec, and a sampling period of $T_s = 5 \times 10^{-5}$ sec. Figure 4.34 shows the position signal near the target track. It shows that all high frequency (≥ 9.68 rad/sec) resonant dynamics are suppressed by the prolate spheroidal wave based acceleration signal. However, a big vibration occurs immediately at the end of the move time. This resonant mode has a natural frequency $\omega_i = 6.12 \times 10^3$ rad/sec and damping ratio $\zeta_i = 0.7$.

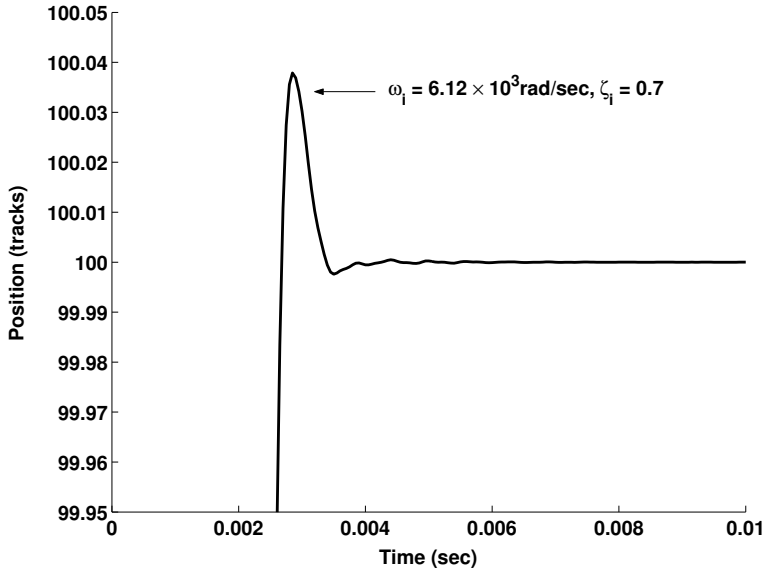

Figure 4.34: Position signal near the target track.

A rectangle based shape filter is designed based on the low frequency resonant mode with parameters $\omega_i = 6.12 \times 10^3$ rad/sec, $\zeta_i = 0.7$, and the sampling period $T_s = 5 \times 10^{-5}$ sec. Figure 4.35 shows the resultant rectangle based shape filter with the robustness order $n = 1$.

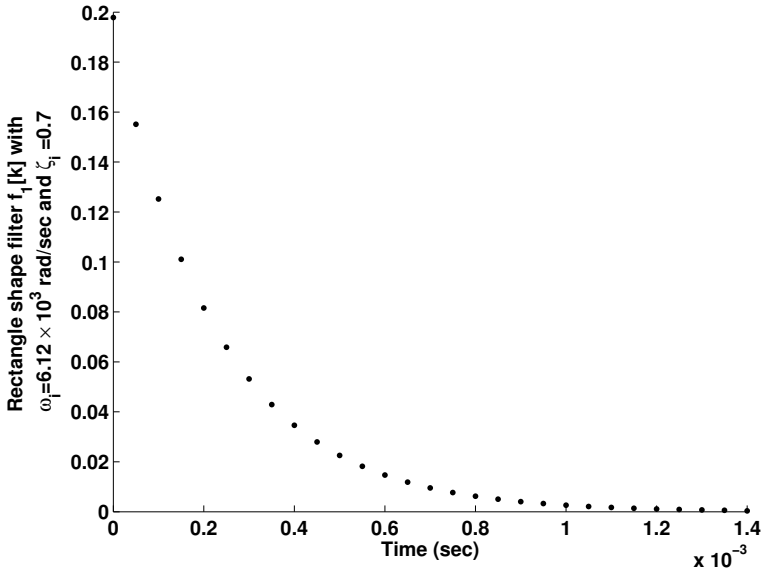

Figure 4.35: Rectangle based shape filter function $f_1[k]$ with resonance parameters $\omega_i = 6.12 \times 10^3$ rad/sec and $\zeta_i = 0.7$.

The robust velocity profile to suppress all the high frequency resonance modes is redesigned with a shorter move time of 2.0×10^{-3} sec by using the prolate spheroidal wave function. The final robust acceleration profile suppressing all the resonant modes is generated by a filter operation as shown in Figure 4.36. The acceleration profile suppressing all the high frequency resonant modes is an input of the shape filter suppressing all the low frequency resonant modes. The output of the shape filter is the robust acceleration profile suppressing all the resonant modes. In this disk drive seek simulation, there is only one low frequency resonant mode. In the case of several low frequency resonant modes, several shape filters can be generated and combined together to form one smooth shape filter. A smooth shape filter design which simultaneously suppresses several resonant modes is also possible.

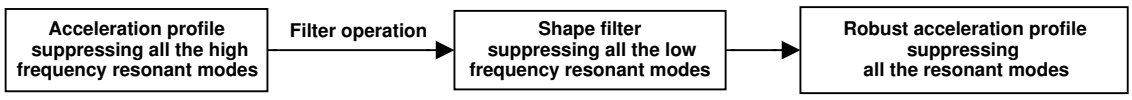

Figure 4.36: Robust acceleration profile generation.

Other control profiles can be generated from the robust acceleration profile. Figure 4.37 shows the current signal. Figure 4.38 shows the jerk signal, which is the derivative of the current signal. Figure 4.39 shows the position signal. Figure 4.40 shows the position signal near the target track. It shows that the position signal settles within $\pm\frac{1}{100}$ track before the move time of 3.4×10^{-3} sec. So the current signal suppresses the residual vibration induced by all the resonance modes. Figure 4.41 shows the reference velocity signal.

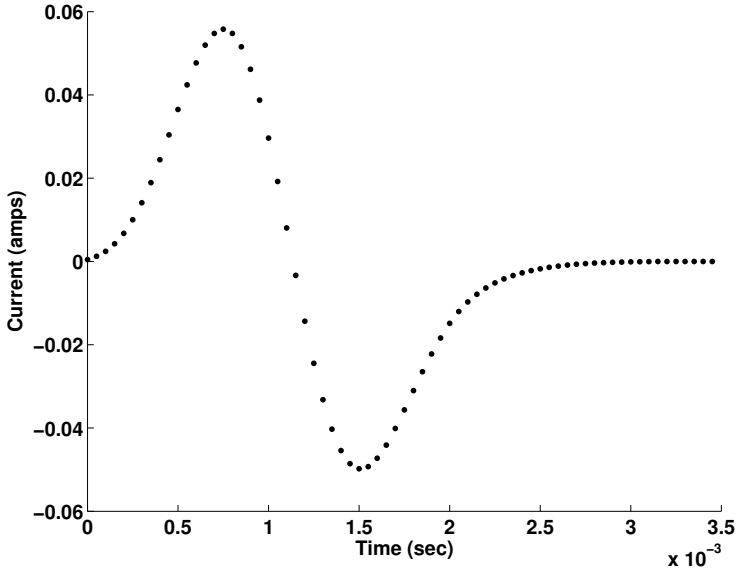

Figure 4.37: Current control input signal.

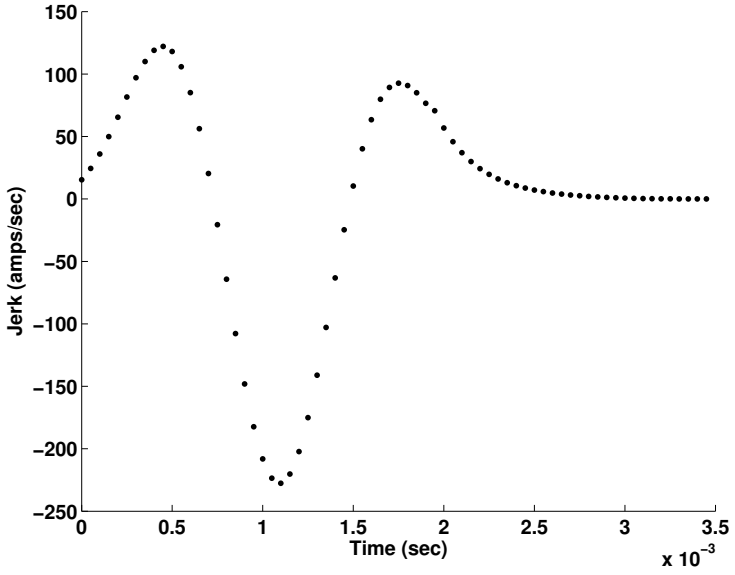

Figure 4.38: Jerk signal.

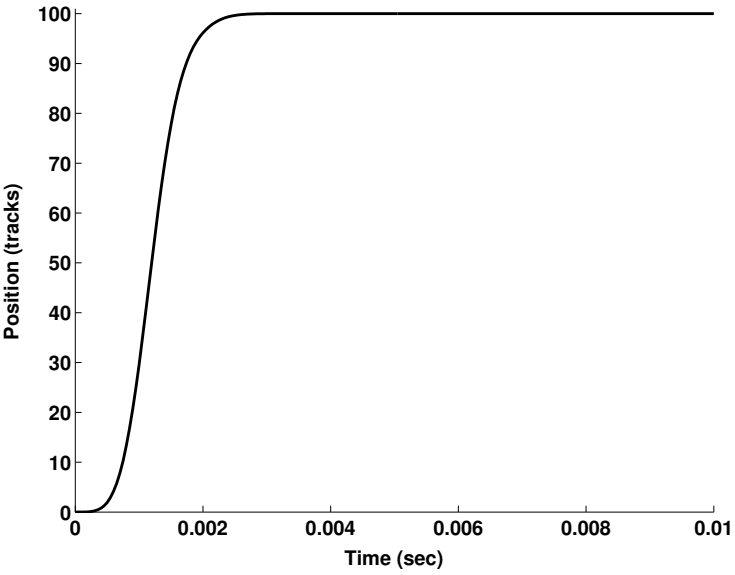

Figure 4.39: Position signal.

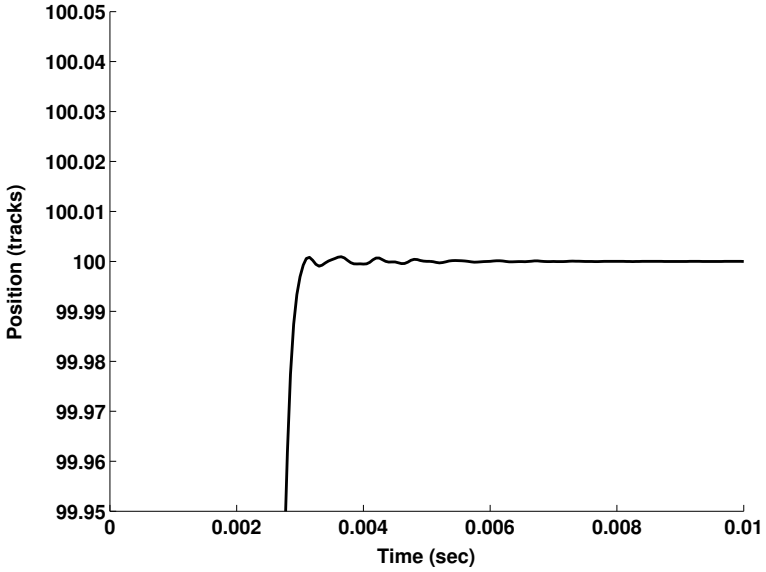

Figure 4.40: Position signal near the target track.

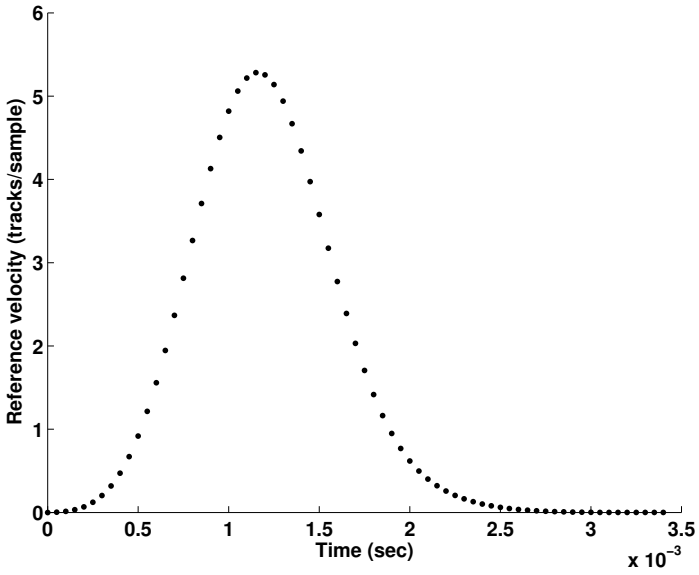

Figure 4.41: Reference velocity signal.

Chapter 5

Near Time-Optimal Robust Vibration Suppression Control Profile Generation with Multiple Constraints

5.1 Robust Vibration Suppression Control Profile Generation with Both Acceleration and Velocity Constraints

In this section, a robust vibration suppression control profile generation with both acceleration and velocity constraints for a flexible system is induced by using the robust vibration suppression shape filter technique.

5.1.1 Time-Optimal Control Profile with Velocity Constraint

The famous Bang-Bang Principle was explained by Hermes [32] as: "It had been an intuitive assumption for some time that if the control for a system is operating from a limited source of power and if it is desired to have the system change from one state to another in minimum time, then it is necessary at all times to utilize all the power available; that

is, to use bang-bang control." With the Bang-Bang Principle, the time-optimal commands must be piecewise constant functions of time and the constants are solely determined by the actuator maximum and minimum power limits. That means the time-optimal control must always saturate the actuators.

For a pure rigid body, it can be inferred that the time-optimal acceleration profile is composed by two parts. The first part is acceleration command which always reaches the maximum limit and the second part is deceleration command which always reaches the minimum limit. Figure 5.1 shows typical time-optimal control profiles with acceleration constraint. At the end of the positive acceleration command, the rigid body reaches its maximum velocity. Then the rigid body velocity decreases to zero with the minimum negative deceleration limit. If there is also a velocity limit for the rigid body movement, it can be inferred that the time-optimal acceleration profile is composed by three parts. The first part is acceleration command which always reaches the maximum limit. When the maximum velocity is reached, the acceleration command becomes zero. In this situation, the rigid body is cruising with a constant velocity. The third part is deceleration command which always reaches the minimum limit. Figure 5.2 shows typical time-optimal control profiles with both acceleration and velocity constraints. From the previous study, the time-optimal command has a poor energy concentration property so it is not suitable to suppress all the resonant dynamics in a flexible system.

5.1.2 Calculating the Number of the Time-Optimal Positive Acceleration Command Samples to Reach the Velocity Constraint

In this section, the number of the time-optimal positive acceleration command samples is calculated. The constraint of the acceleration $u[k]$ is assumed to be $|u[k]| \leq A_{max}$. The maximum velocity is assumed to be V_{max} and the sampling period is assumed to be T_s. The

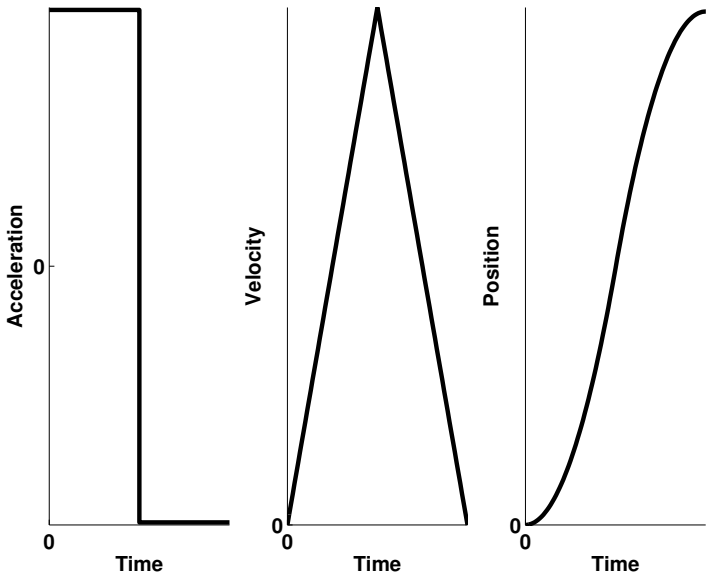

Figure 5.1: Time-Optimal control profiles with acceleration constraint.

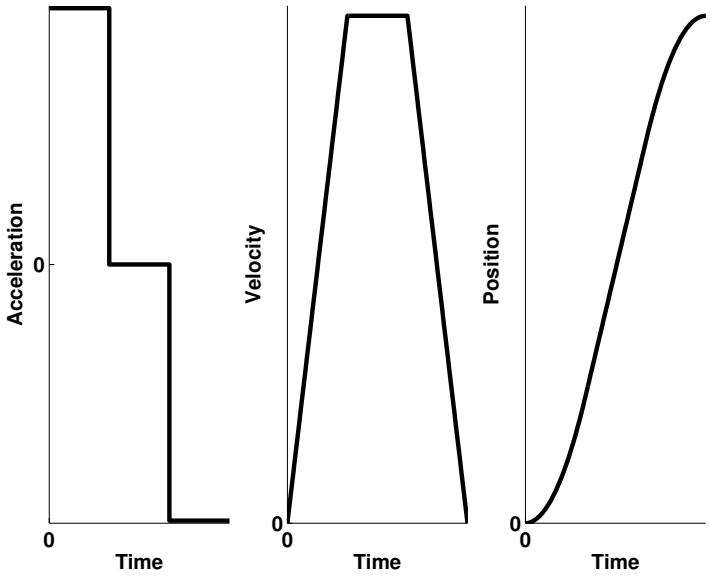

Figure 5.2: Time-Optimal control profiles with both acceleration and velocity constraints.

relationship between the acceleration command $u[k]$ and the velocity $v[k]$ is given as

$$\frac{V(z)}{U(z)} = K_a \frac{z^{-1}}{1 - z^{-1}}, \tag{5.1}$$

where K_a is a constant gain. The difference equation between acceleration $u[k]$ at the discrete-time instant kT_s and velocity $v[k]$ at the discrete-time instant kT_s is given as

$$v[k] = K_a u[k-1] + v[k-1]. \tag{5.2}$$

If the initial velocity $v[0]$ is zero, the velocity at the discrete-time instant kT_s can be computed as

$$v[0] = 0, \tag{5.3}$$

$$v[1] = K_a u[0] + 0, \tag{5.4}$$

$$v[2] = K_a u[1] + v[1] = K_a(u[1] + u[0]) = K_a \sum_{i=0}^{1} u[i], \tag{5.5}$$

$$\cdots = \cdots\cdots,$$

$$v[k] = K_a \sum_{i=0}^{k-1} u[i]. \tag{5.6}$$

Since the acceleration $u[k]$ always saturates before reaching the maximum velocity, the positive acceleration command $u[k]$ is described as

$$u[k] = A_{max},\ k = 0, \cdots, m-1. \tag{5.7}$$

So the following equation holds,

$$V_{max} = K_a \sum_{i=0}^{m-1} u[i] = K_a m A_{max}. \tag{5.8}$$

The number of the time-optimal positive acceleration command samples can be calculated as

$$m_1 = floor\left(\frac{V_{max}}{K_a A_{max}}\right) \tag{5.9}$$

and the maximum velocity V_{rmax} from (5.9) is

$$V_{rmax} = K_a m_1 A_{max} \leq V_{max}. \tag{5.10}$$

5.1.3 Calculating the Number of the Time-Optimal Zero Acceleration Command Samples

When the rigid body reaches the maximum velocity constraint described in (5.10), the rigid body is cruising at the constant velocity V_{rmax} as shown in Figure 5.2. If the position movement is assumed to be P_{max}, the number of the time-optimal zero acceleration command samples is calculated. The state-space model of the rigid body is described as

$$\begin{bmatrix} p[k+1] \\ v[k+1] \end{bmatrix} = G \begin{bmatrix} p[k] \\ v[k] \end{bmatrix} + K_b H u[k], \tag{5.11}$$

where $G = \begin{bmatrix} 1 & T_s \\ 0 & 1 \end{bmatrix}$ and $H = \begin{bmatrix} T_s^2/2 \\ T_s \end{bmatrix}$. $p[k]$ is the position at the discrete-time instant kT_s, $v[k]$ is the velocity at the discrete-time instant kT_s and K_b is a constant gain. The acceleration command u has the following format

$$u = [\underbrace{A_{max}, \cdots, A_{max}}_{m_1}, \underbrace{0,\ 0, \cdots, 0}_{n}, \underbrace{-A_{max}, \cdots, -A_{max}}_{m_1}]. \tag{5.12}$$

If the initial position $p[0]$ and velocity $v[0]$ are assumed to be zero, the position and velocity at the discrete-time instant kT_s can be computed as [58]

$$\begin{bmatrix} p[k] \\ v[k] \end{bmatrix} = G^k \begin{bmatrix} p[0] \\ v[0] \end{bmatrix} + \sum_{i=0}^{k-1} H^i K_b \begin{bmatrix} T_s^2/2 \\ T_s \end{bmatrix} u[k-i-1], \tag{5.13}$$

$$= \sum_{i=0}^{k-1} H^i K_b \begin{bmatrix} T_s^2/2 \\ T_s \end{bmatrix} u[k-i-1], \tag{5.14}$$

$$= \sum_{i=0}^{k-1} \begin{bmatrix} 1 & T_s \\ 0 & 1 \end{bmatrix}^i K_b \begin{bmatrix} T_s^2/2 \\ T_s \end{bmatrix} u[k-i-1]. \tag{5.15}$$

So at the discrete-time instant $(2m_1+n)T_s$,

$$\begin{bmatrix} p[2m_1+n] \\ v[2m_1+n] \end{bmatrix}$$

$$= \sum_{i=0}^{2m_1+n-1} \begin{bmatrix} 1 & T_s \\ 0 & 1 \end{bmatrix}^i K_b \begin{bmatrix} T_s^2/2 \\ T_s \end{bmatrix} u[2m_1+n-i-1], \tag{5.16}$$

$$= -A_{max} \sum_{i=0}^{m_1-1} \begin{bmatrix} 1 & T_s \\ 0 & 1 \end{bmatrix}^i K_b \begin{bmatrix} T_s^2/2 \\ T_s \end{bmatrix} + A_{max} \sum_{i=m_1+n}^{2m_1+n-1} \begin{bmatrix} 1 & T_s \\ 0 & 1 \end{bmatrix}^i K_b \begin{bmatrix} T_s^2/2 \\ T_s \end{bmatrix}, \tag{5.17}$$

$$= K_b A_{max} \left(\sum_{i=m_1+n}^{2m_1+n-1} \begin{bmatrix} T_s^2/2 + iT_s^2 \\ T_s \end{bmatrix} - \sum_{i=0}^{m_1-1} \begin{bmatrix} T_s^2/2 + iT_s^2 \\ T_s \end{bmatrix} \right), \tag{5.18}$$

$$= K_b A_{max} \begin{bmatrix} T_s^2((2m_1+n-1)(2m_1+n) - (m_1+n-1)(m_1+n) - (m_1-1)m_1) \\ 0 \end{bmatrix}, \tag{5.19}$$

$$= K_b A_{max} \begin{bmatrix} T_s^2 m_1(m_1+n) \\ 0 \end{bmatrix}. \tag{5.20}$$

If the position at the discrete-time instant $(2m_1+n)T_s$ is imposed to be P_{max},

$$K_b A_{max} T_s^2 m_1(m_1+n) = P_{max} \tag{5.21}$$

and

$$n = \frac{P_{max}}{K_b A_{max} T_s^2 m_1} - m_1. \tag{5.22}$$

Generally the above n is not an integer. Let $n = floor(n) + \alpha$, where $\alpha = n - floor(n)$ and $0 \leq \alpha < 1$. The number of zero acceleration command samples can be chosen to be

$$n_1 = floor(n) + 1. \tag{5.23}$$

In the above implementation, since the resultant number of zero acceleration command n_1 is generally greater than the required fractional number of samples n, the resultant position at the end of the acceleration command is greater than the required position constraint

which is P_{max}. Figure 5.3 shows the fractional number of the maximum velocity profile. The time interval between the final maximum velocity impulse V_{rmax} and the next velocity impulse b_0 is αT_s which is less than one sampling period T_s. Figure 5.4 shows the modification of the integer number of the maximum velocity profile from (5.23). Compared with Figure 5.3, the summation of velocity impulses in Figure 5.4 is increased by $(1-\alpha)V_{rmax}$ per sample. The additional velocity impulse summation can be compensated for by slightly modifying the velocity impulses. The acceleration command corresponding the velocity profile in Figure 5.4 is

$$u = [\underbrace{A_{max}, \cdots, A_{max}}_{m_1}, \underbrace{0,\ 0, \cdots, 0}_{n_1}, \underbrace{-A_{max}, \cdots, -A_{max}}_{m_1}]. \tag{5.24}$$

The velocity profile from (5.24) can be described as

$$\begin{aligned} v[0] &= 0, \\ v[1] &= K_a A_{max}, \\ v[k] &= K_a \sum_{i=0}^{k-1} u[i], \quad k = 2, \cdots, 2m_1 + n_1 - 2 \\ v[2m_1 + n_1 - 1] &= K_a A_{max}, \\ v[2m_1 + n_1] &= 0. \end{aligned}$$

The above velocity profile can be modified to

$$\begin{aligned} v_1[0] &= 0, \\ v_1[k] &= v[k] - \frac{(1-\alpha)V_{rmax}}{2m_1 + n_1 - 1}, \quad k = 1, \cdots, 2m_1 + n_1 - 1, \\ v_1[2m_1 + n_1] &= 0. \end{aligned}$$

The integral of the modified velocity impulses is exactly the same as the required integral of the velocity impulses in Figure 5.3. The resultant modified acceleration command

corresponding to (5.24) is

$$
\begin{aligned}
u_1[0] &= A_{max} - \frac{(1-\alpha)V_{rmax}}{K_a(2m_1+n_1-1)}, \\
u_1[k] &= u[k],\ k = 1, \cdots, 2m_1+n_1-1, \\
u_1[2m_1+n_1-1] &= -\left[A_{max} - \frac{(1-\alpha)V_{rmax}}{K_a(2m_1+n_1-1)}\right].
\end{aligned}
\tag{5.25}
$$

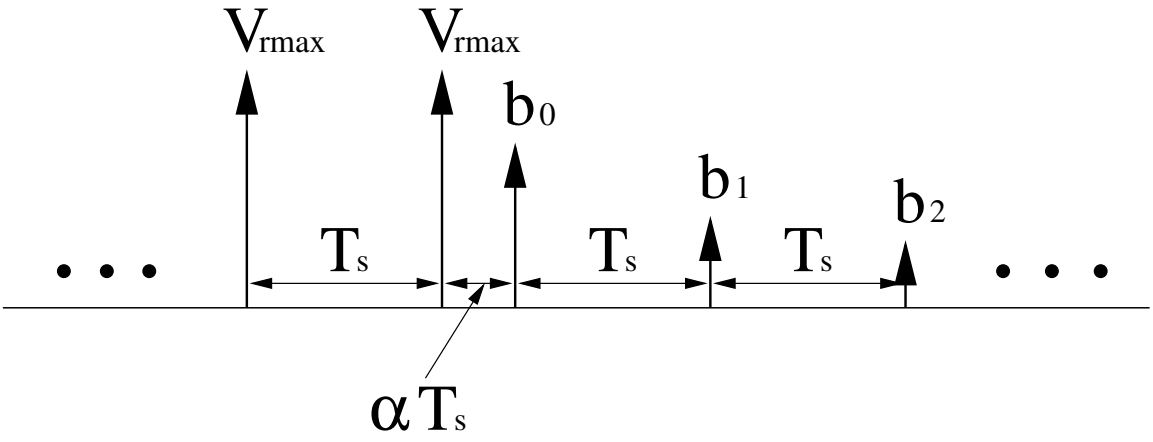

Figure 5.3: The calculated fractional number of the maximum velocity profile.

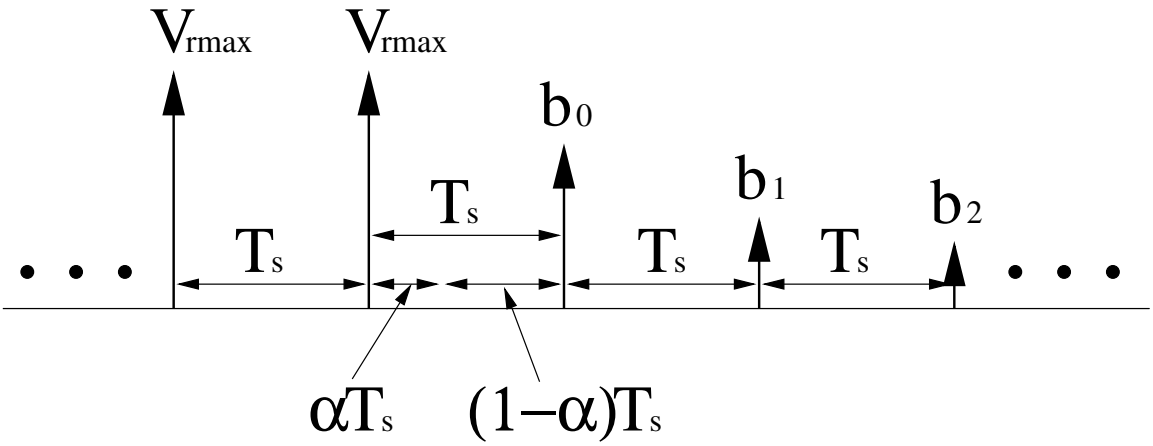

Figure 5.4: The modification of the integer number of the maximum velocity profile.

Remark 5.1 *In (5.23), if the resultant integer number n_1 of the zero acceleration command is less than 0, then the acceleration and the velocity limits are not required to achieve the position constraint. In this situation, to guarantee the position constraint, either a reduced*

acceleration limit or a reduced velocity limit may be implemented. It is easy to understand that the resultant maximum velocity from the modified acceleration command (5.25) is slightly less than V_{rmax} in (5.10).

5.1.4 Robust Vibration Suppression Control Profile Generation with Both Acceleration and Velocity Constraints

Since the time-optimal acceleration command is generated in the previous sections, a robust vibration suppression command can be generated as shown in Figure 5.5. The vibration suppression shape filter in Figure 5.5 is composed of low frequency vibration suppression shape filters as discussed in Chapter 2 and 3, and high frequency vibration suppression shape filter as discussed in Chapter 4.

Figure 5.5: Generation of a robust vibration suppression command.

5.1.5 Simulation Results for Hard Disk Drive Long Seek Control

Consider the following flexible system which is embedded in a hard disk assembly, where the input is the current signal in amps and the output is the position signal in tracks.

$$H(s) = K_c \cdot K_v \cdot K_p \cdot R(s)\frac{1}{s^2}, \tag{5.26}$$

here $K_c = 1.3\ \frac{\text{tracks/sample}^2}{\text{amp}}$ is a constant gain from current to acceleration, $K_v = 5 \times 10^4\ \frac{\text{samples}}{\text{sec}}$ is the velocity gain, $K_p = 5 \times 10^4\ \frac{\text{samples}}{\text{sec}}$ is the position gain, and $R(s)$ is a 28^{th} order resonance structure. The Bode magnitude plot of $R(s)$ is shown in Figure 1.2. The current limit is assumed to be 1 amp, the maximum velocity constraint is assumed to be 100 tracks/sample, and the long seek position movement is assumed to be 2×10^4 tracks.

The sampling period T_s is assumed to be 2×10^{-5} sec. Figure 5.6 shows the time-optimal current command with the velocity constraint. Figure 5.7 shows the resultant velocity signal. Figure 5.8 shows the resultant position signal. Figure 5.9 shows the position signal near the target track. The interval of Y axis in Figure 5.9 is scaled to exactly one track. It shows that the residual vibration exists for a long period of time after the end of the current command (5.6 msec).

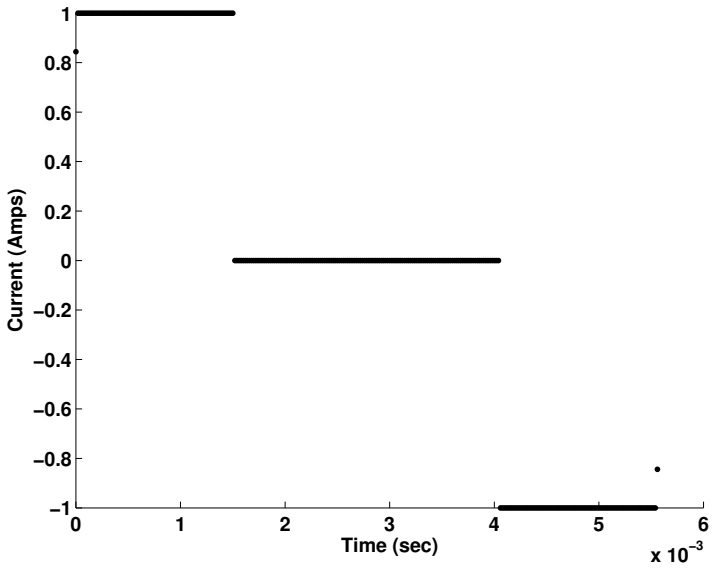

Figure 5.6: Time-Optimal current command with the velocity constraint.

To suppress the residual vibration, a rectangle based shaper filter is designed based on the first resonance mode in the flexible system. The first resonance mode has the parameter $\omega_1 = 6.12 \times 10^3$ rad/sec and $\zeta_1 = 0.7$. Figure 5.10 shows the resultant vibration suppression shape filter. Figure 5.11 shows the robust vibration suppression current command. Figure 5.12 shows the resultant velocity signal. Figure 5.13 shows the resultant position signal. Figure 5.14 shows the position signal near the target track. Although the residual vibration due to the first resonance mode has been canceled, there still a large vibration exists after the end of the current command. This residual vibration is caused by the second resonance mode in the flexible system.

To suppress the residual vibration of the second resonance mode, a rectangle based

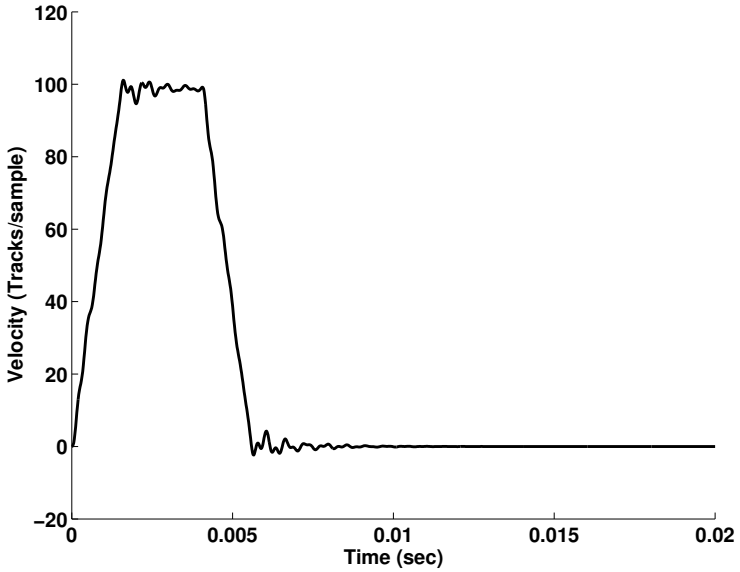

Figure 5.7: The velocity signal with the time-optimal current command.

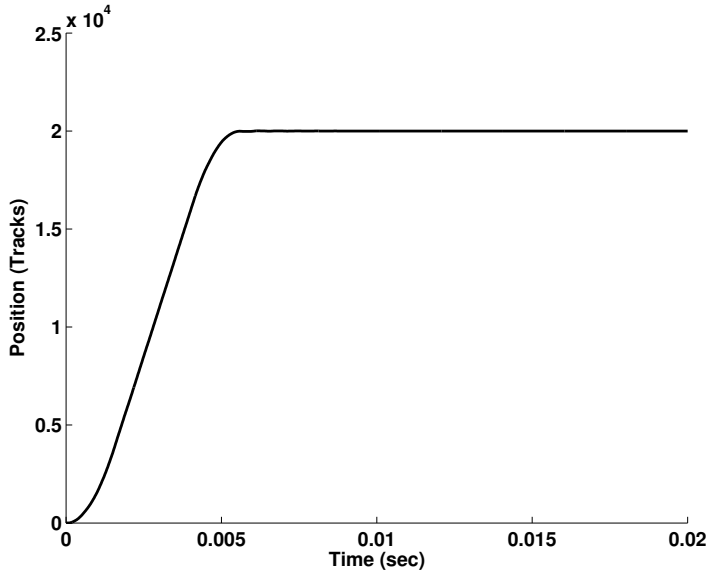

Figure 5.8: The position signal with the time-optimal current command.

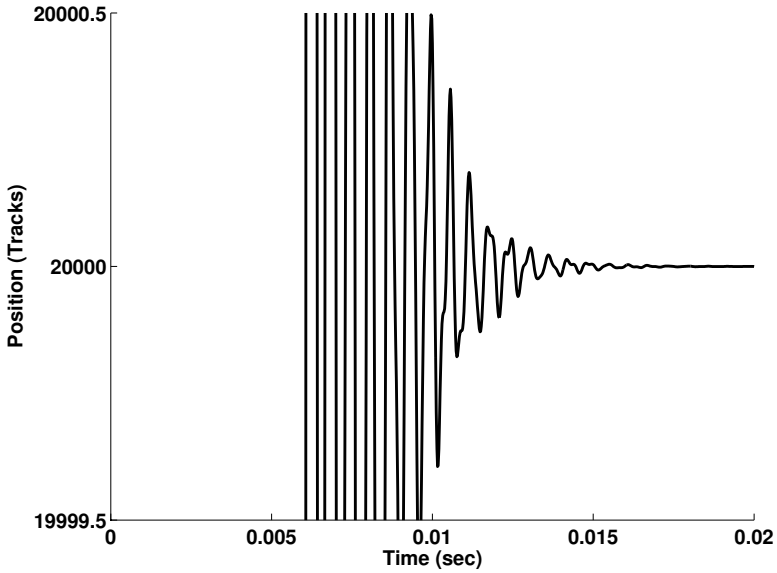

Figure 5.9: The position signal near the target track.

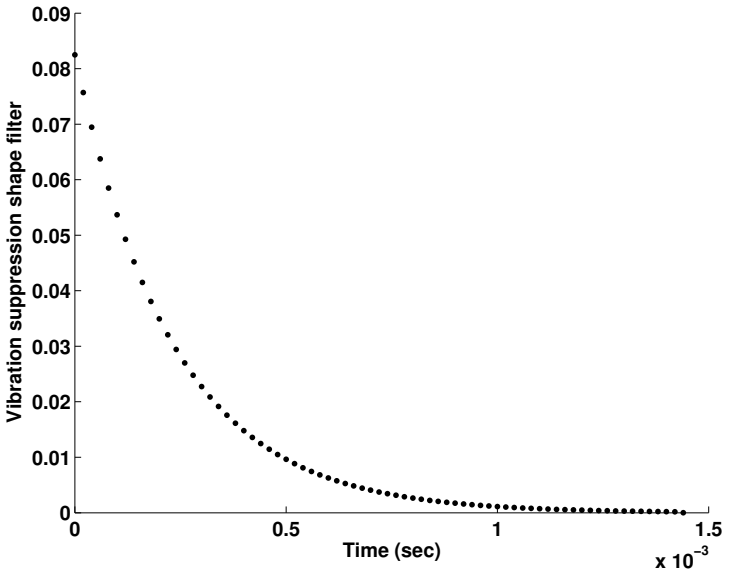

Figure 5.10: Rectangle based shape filter based on resonance parameter $\omega_1 = 6.12 \times 10^3$ rad/sec and $\zeta_1 = 0.7$.

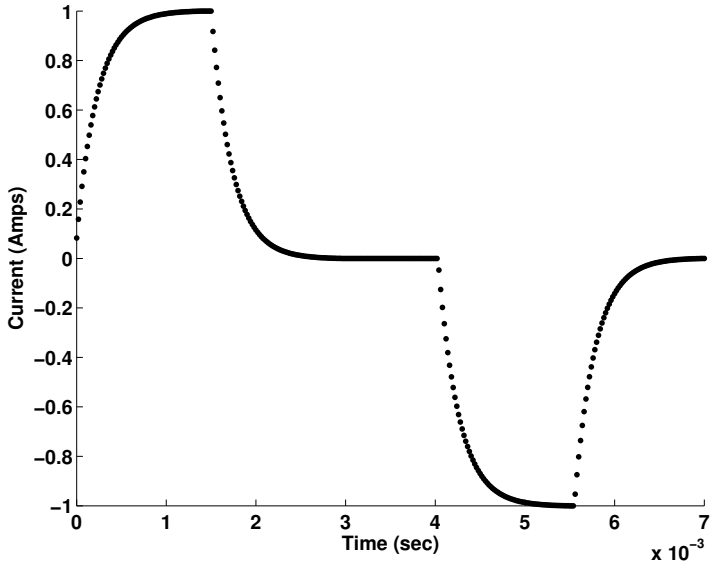

Figure 5.11: Robust vibration suppression current command.

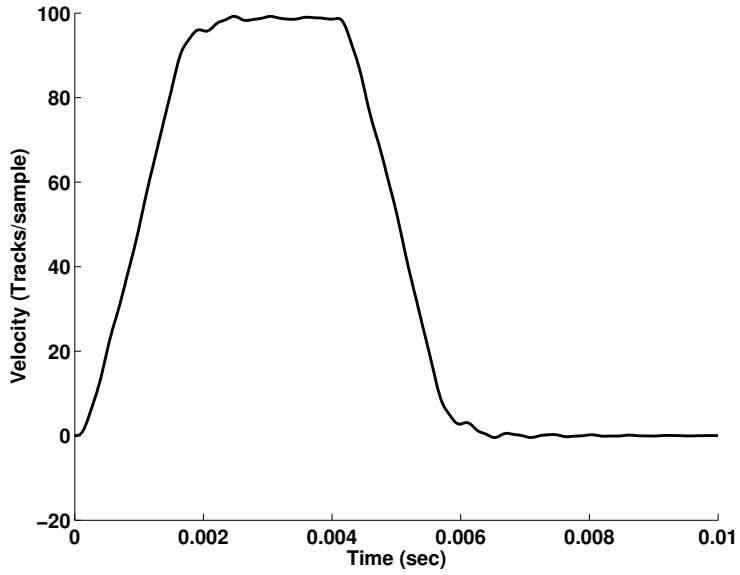

Figure 5.12: Velocity signal with the robust vibration suppression current command.

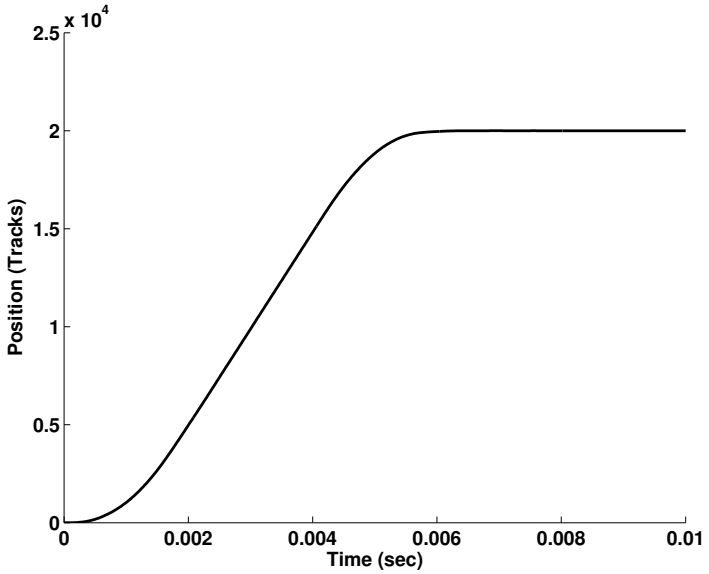

Figure 5.13: Position signal with the robust vibration suppression current command.

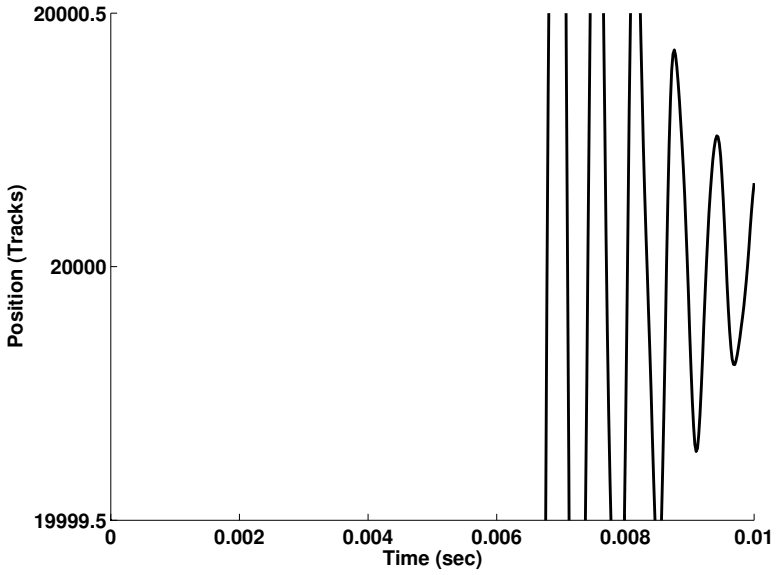

Figure 5.14: Position signal near the target track.

shaper filter is designed based on the second resonance mode in the flexible system. The second resonance mode has the parameter $\omega_1 = 1.02 \times 10^4$ rad/sec and $\zeta_1 = 0.08$. Figure 5.15 shows the resultant vibration suppression shape filter based on the second resonance mode. Combining the shape filter in Figure 5.10 and the shape filter in Figure 5.15 results a new shape filter as shown in Figure 5.16. The resultant new vibration suppression shape filter in Figure 5.16 cancels the residual vibration due to both the first resonance mode and the second resonance mode. Figure 5.17 shows the robust vibration suppression current command. Figure 5.18 shows the resultant velocity signal. Figure 5.19 shows the resultant position signal. Figure 5.20 shows the position signal near the target track. It shows that the residual vibration due to both the first resonance mode and the second resonance mode is canceled. Also the residual vibration due to the high frequency modes is also suppressed. In this case, it is not necessary to design a robust high frequency vibration suppression shape filter to suppress all the high frequency residual vibration because the high frequency vibration is sufficiently suppressed by the two rectangle based shape filters.

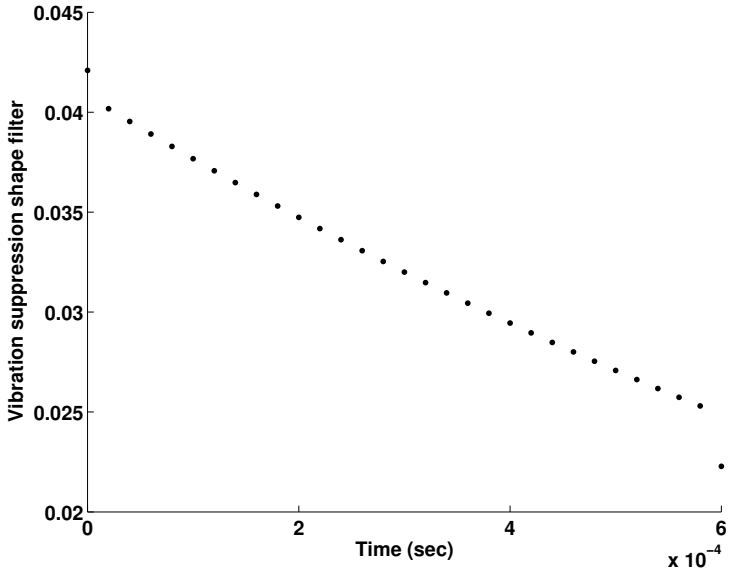

Figure 5.15: Rectangle based shape filter based on resonance parameter $\omega_2 = 1.02 \times 10^4$ rad/sec and $\zeta_1 = 0.08$.

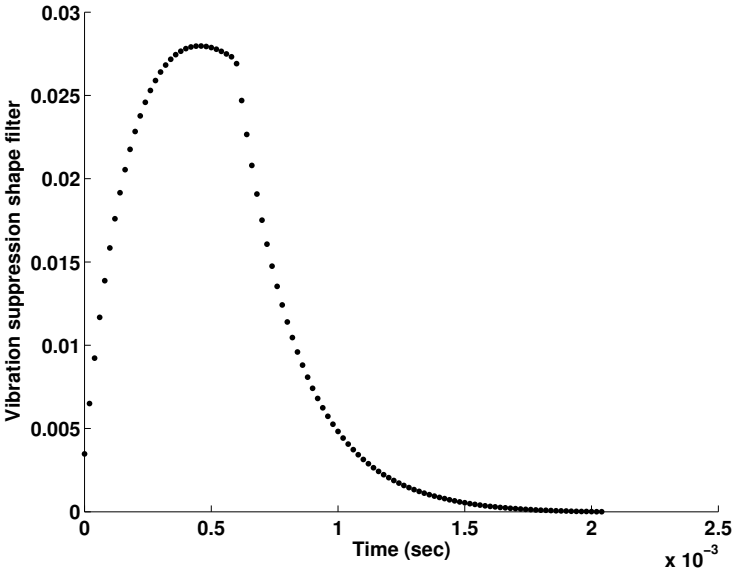

Figure 5.16: Robust vibration suppression shape filter to cancel both the first resonance mode and the second resonance mode.

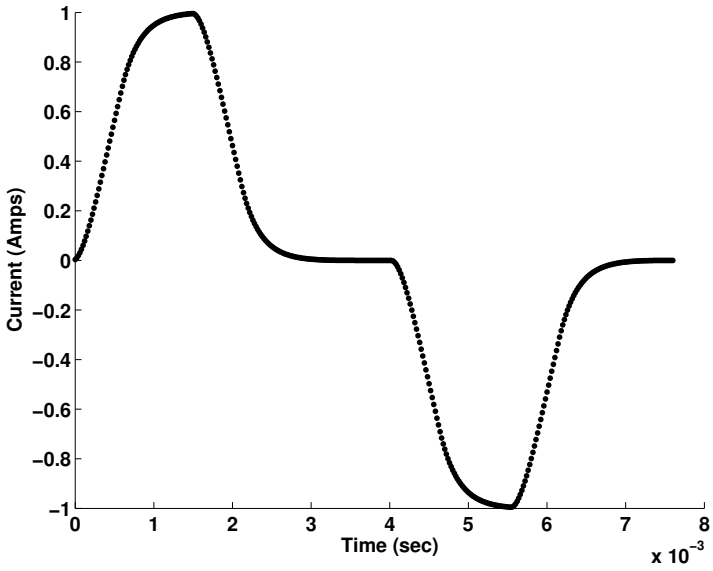

Figure 5.17: Robust vibration suppression current command.

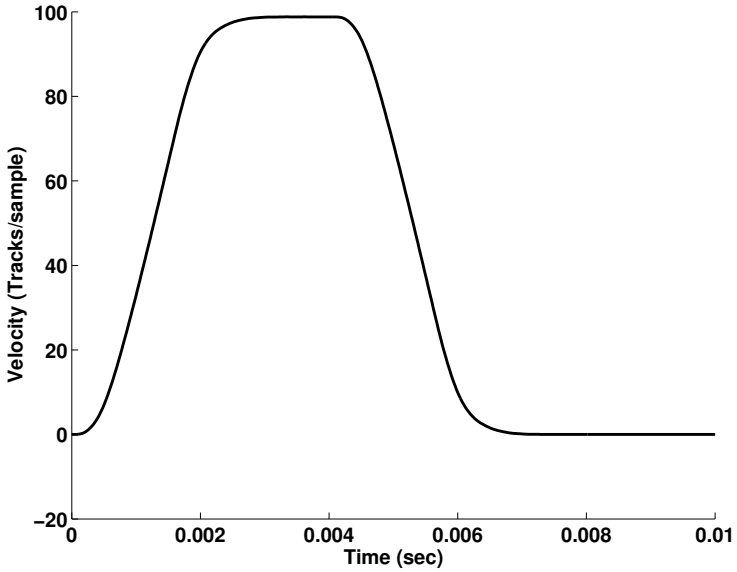

Figure 5.18: Velocity signal with the robust vibration suppression current command.

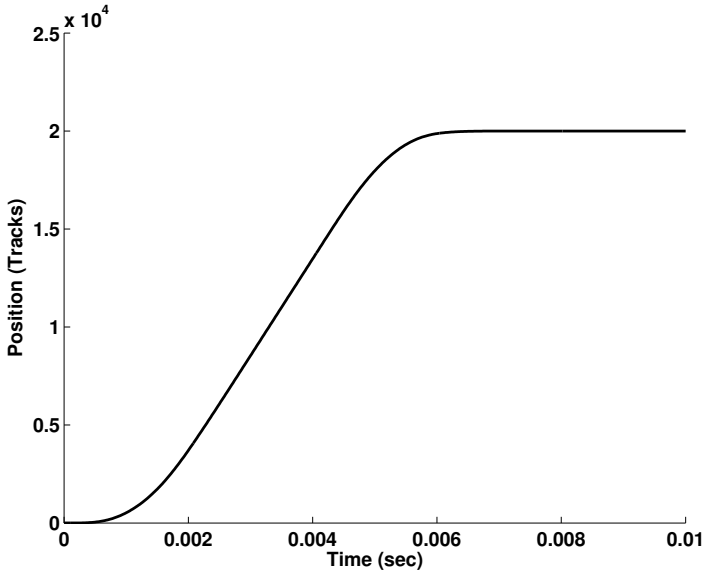

Figure 5.19: Position signal with the robust vibration suppression current command.

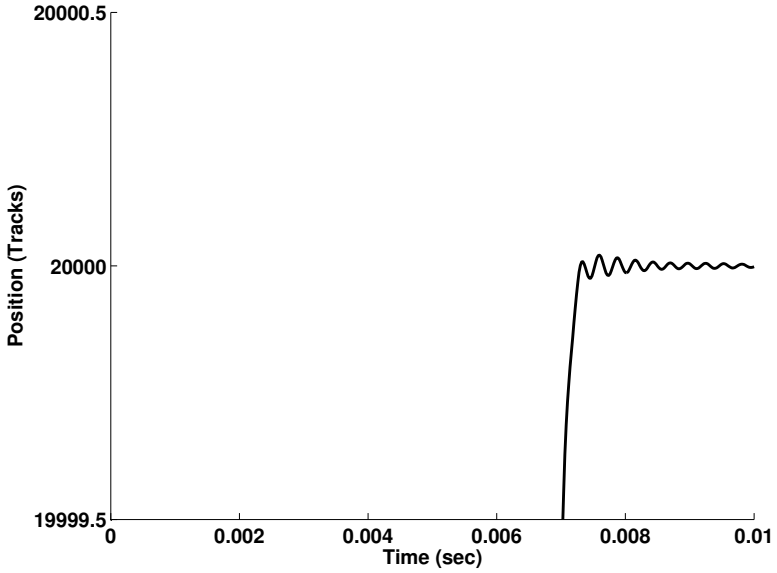

Figure 5.20: Position signal near the target track.

5.2 Long Seek Control Profile With Both Applied Voltage And Velocity Constraints

In the previous section, a robust vibration suppression control profile generation with both acceleration and velocity constraints is studied. The proposed method develops a robust vibration suppression control profile for hard disk drive long seek control. The control profile has both the drive current (or acceleration) and velocity constraints. In real application, the drive current does no saturate. It is the applied drive voltage that saturates. This section presents a robust vibration suppression control profile generation method with both the drive applied voltage and velocity constraints.

For a pure rigid body, it can be inferred that the time-optimal acceleration profile with velocity constraint is composed by three parts. The first part is acceleration command which always reaches the maximum limit. When the maximum velocity is reached, the acceleration command becomes zero. In this situation, the rigid body is cruising with a constant velocity. The third part is deceleration command which always reaches the minimum limit. Figure 5.21 shows typical time-optimal control profiles with both acceleration

and velocity constraints.

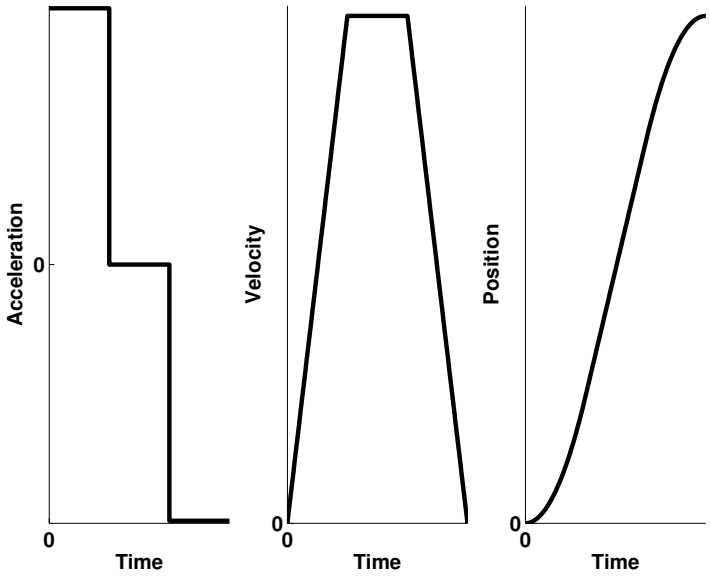

Figure 5.21: Time-Optimal control profiles with both acceleration and velocity constraints.

Figure 5.22 shows a simplified hard disk drive voice coil servo motor dynamics. The applied voltage V_a is the sum of the control voltage V_c and the back-emf voltage V_b. The control voltage in terms of motor current command i is $V_c = Ri + L\frac{di}{dt}$, where L is the armature inductance and R is the armature resistance. The back-emf voltage in terms of the arm velocity vel is $V_b = K_e vel$, where K_e is the back-emf constant. Since the back-emf voltage is proportional to the velocity, a sloped acceleration command can be designed to overcome the effect of the back-emf voltage as shown in Figure 5.23. The slope needs to be chosen such that the maximum allowable applied voltage is met for as long as possible but not saturated.

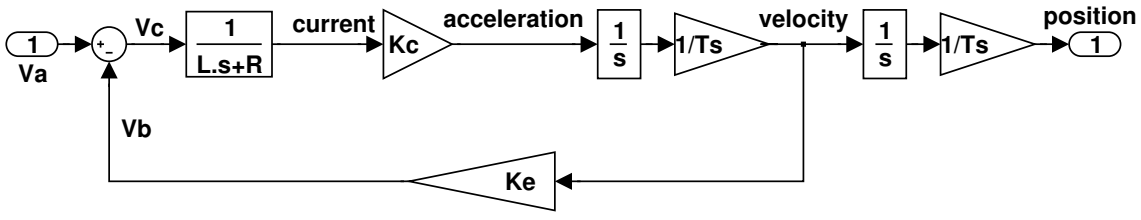

Figure 5.22: The voice coil servo motor dynamics.

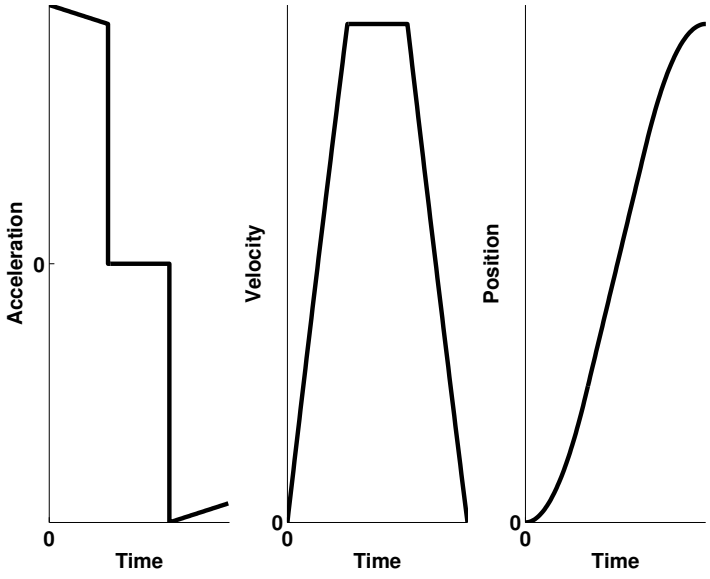

Figure 5.23: Sloped fast control profiles with both acceleration and velocity constraints.

A robust vibration suppression control profile generation with both applied voltage and velocity constraints for a flexible system is induced by using the robust vibration suppression shape filter technique.

5.2.1 Calculating the Number of the Sloped Positive Acceleration Command Samples to Reach the Velocity Constraint

In this section, the number of the sloped positive acceleration command samples is calculated. The constraint of the acceleration $u[k]$ is assumed to be $|u[k]| \leq A_{max}$. The maximum velocity is assumed to be V_{max} and the sampling period is assumed to be T_s. The relationship between the acceleration command $u[k]$ and the velocity $v[k]$ is given as $\frac{V(z)}{U(z)} = K_a \frac{z^{-1}}{1-z^{-1}}$, where K_a is a constant gain. The difference equation between acceleration $u[k]$ at the discrete-time instant kT_s and velocity $v[k]$ at the discrete-time instant kT_s is given as

$$v[k] = K_a u[k-1] + v[k-1]. \tag{5.27}$$

If the initial velocity $v[0]$ is assumed to be zero, the velocity at the discrete-time instant kT_s can be computed as

$$v[k] = K_a \sum_{i=0}^{k-1} u[i]. \tag{5.28}$$

The sloped positive acceleration command $u[k]$ is described as

$$u[k] = A_{max} - k \cdot S,\ k = 0, \cdots, m-1, \tag{5.29}$$

where S is the acceleration decrease per sample. So the following equation holds,

$$V_{max} = K_a \sum_{i=0}^{m-1} u[i] = K_a m \sum_{i=0}^{m-1} (A_{max} - i \cdot S), \tag{5.30}$$

$$= K_a (A_{max} + S/2)m - K_a S m^2/2. \tag{5.31}$$

Hence, m is the least positive solution of a second-order polynomial equation $K_a S m^2/2 - K_a(A_{max} + S/2)m + V_{max} = 0$. The number of the sloped positive acceleration command samples can be calculated as

$$m_1 = floor\,(m) \tag{5.32}$$

and the maximum velocity V_{rmax} from (5.32) is

$$V_{rmax} = K_a (A_{max} + S/2)m_1 - K_a S m_1^2/2 \leq V_{max}. \tag{5.33}$$

5.2.2 Calculating the Number of the Zero Acceleration Command Samples

When the rigid body reaches the maximum velocity constraint described in (5.33), the rigid body is cruising at the constant velocity V_{rmax} as shown in Figure 5.23. If the position movement is assumed to be P_{max}, the number of the zero acceleration command samples is calculated. The state-space model of the rigid body is described as

$$\begin{bmatrix} p[k+1] \\ v[k+1] \end{bmatrix} = G \begin{bmatrix} p[k] \\ v[k] \end{bmatrix} + K_b H u[k], \tag{5.34}$$

where $G = \begin{bmatrix} 1 & T_s \\ 0 & 1 \end{bmatrix}$ and $H = \begin{bmatrix} T_s^2/2 \\ T_s \end{bmatrix}$. $p[k]$ is the position at the discrete-time instant kT_s, $v[k]$ is the velocity at the discrete-time instant kT_s and K_b is a constant gain. The acceleration command u has the following format

$$\begin{aligned} u = [&\underbrace{A_{max}, A_{max} - S, \cdots, A_{max} - (m_1 - 1)S}_{m_1}, \\ &\underbrace{0,\ 0, \cdots, 0}_{n}, \\ &\underbrace{-A_{max}, -(A_{max} - S) \cdots, -(A_{max} - (m_1 - 1)S)}_{m_1}]. \end{aligned}$$

If the initial position $p[0]$ and velocity $v[0]$ are assumed to be zero, the position and velocity at the discrete-time instant kT_s can be computed as [58]

$$\begin{bmatrix} p[k] \\ v[k] \end{bmatrix} = G^k \begin{bmatrix} p[0] \\ v[0] \end{bmatrix} + \sum_{i=0}^{k-1} G^i K_b H u[k-i-1], \tag{5.35}$$

$$= \sum_{i=0}^{k-1} G^i K_b H u[k-i-1]. \tag{5.36}$$

So at the discrete-time instant $(2m_1 + n)T_s$,

$$\begin{bmatrix} p[2m_1+n] \\ v[2m_1+n] \end{bmatrix} = \sum_{i=0}^{2m_1+n-1} G^i K_b H u[2m_1+n-i-1],$$

$$= \begin{bmatrix} \frac{K_b m_1 T_s^2}{2}(2A_{max} + S - Sm_1)(m_1 + n) \\ 0 \end{bmatrix}.$$

If the position at the discrete-time instant $(2m_1 + n)T_s$ is imposed to be P_{max},

$$\frac{K_b m_1 T_s^2}{2}(2A_{max} + S - Sm_1)(m_1 + n) = P_{max} \tag{5.37}$$

and

$$n = \frac{2P_{max}}{K_b m_1 T_s^2 (2A_{max} + S - Sm_1)} - m_1. \tag{5.38}$$

Generally the above n is not an integer. Let $n = floor(n) + \alpha$, where $\alpha = n - floor(n)$ and $0 \leq \alpha < 1$. The number of zero acceleration command samples can be chosen to be

$$n_1 = floor(n) + 1. \tag{5.39}$$

In the above implementation, since the resultant number of zero acceleration command n_1 is generally greater than the required fractional number of samples n, the resultant position at the end of the acceleration command is greater than the required position constraint which is P_{max}. Figure 5.3 shows the calculated fractional number of the maximum velocity profile. The time interval between the final maximum velocity impulse V_{rmax} and the next velocity impulse b_0 is αT_s which is less than one sampling period T_s. Figure 5.4 shows the modification of the integer number of the maximum velocity profile from (5.39). Compared with Figure 5.3, the summation of velocity impulses in Figure 5.4 is increased by $(1-\alpha)V_{rmax}$ per sample. The additional velocity impulse summation can be compensated for by slightly modifying the velocity impulses. The acceleration command corresponding the velocity profile in Figure 5.4 is

$$\begin{aligned} u = [&\underbrace{A_{max}, A_{max} - S, \cdots, A_{max} - (m_1 - 1)S}_{m_1}, \\ &\underbrace{0,\ 0, \cdots, 0}_{n_1}, \\ &\underbrace{-A_{max}, -(A_{max} - S) \cdots, -(A_{max} - (m_1 - 1)S)}_{m_1}]. \end{aligned} \tag{5.40}$$

The velocity profile from (5.40) can be described as

$$\begin{aligned} v[0] &= 0, \\ v[k] &= K_a \sum_{i=0}^{k-1} u[i], k = 1, \cdots, 2m_1 + n_1 - 1, \\ v[2m_1 + n_1] &= 0. \end{aligned}$$

The above velocity profile can be modified to

$$\begin{aligned} v_1[0] &= 0, \\ v_1[k] &= v[k] - \frac{(1-\alpha)V_{rmax}}{2m_1+n_1-1}, \quad k = 1, \cdots, 2m_1+n_1-1, \\ v_1[2m_1+n_1] &= 0. \end{aligned}$$

The integral of the modified velocity impulses is exactly the same as the required integral of the velocity impulses in Figure 5.3. The resultant modified acceleration command corresponding to (5.40) is

$$\begin{aligned} u_1[0] &= A_{max} - \frac{(1-\alpha)V_{rmax}}{K_a(2m_1+n_1-1)}, \\ u_1[k] &= u[k], \ k = 1, \cdots, 2m_1+n_1-1, \\ u_1[2m_1+n_1-1] &= -[A_{max} - \frac{(1-\alpha)V_{rmax}}{K_a(2m_1+n_1-1)}]. \end{aligned} \tag{5.41}$$

In (5.39), if the resultant integer number n_1 of the zero acceleration command is less than 0, then the acceleration and the velocity limits are not required to achieve the position constraint. In this situation, to guarantee the position constraint, either a reduced acceleration limit or a reduced velocity limit may be implemented. It is easy to understand that the resultant maximum velocity from the modified acceleration command (5.41) is slightly less than V_{rmax} in (5.33).

5.2.3 Robust Vibration Suppression Control Profile Generation with Both Acceleration and Velocity Constraints

Since the sloped fast acceleration command is generated in the previous section, a robust vibration suppression command can be generated as shown in Figure 5.24. The vibration suppression shape filter in Figure 5.5 is composed of low frequency vibration suppression shape filters as discussed in Chapter 2 and 3, and high frequency vibration suppression shape filter as discussed in Chapter 4.

Figure 5.24: Generation of a robust vibration suppression command.

5.2.4 Simulation Results for Hard Disk Drive Long Seek Control

Consider the following flexible system which is embedded in a hard disk assembly, $H(s) = K_c \cdot K_v \cdot K_p \cdot R(s)\frac{1}{s^2}$, where the input is the current signal in amps and the output is the position signal in tracks. The variable $K_c = 1.3\ \frac{\text{tracks/sample}^2}{\text{amp}}$ is a constant gain from current to acceleration, $K_v = 1/T_s = 5 \times 10^4\ \frac{\text{samples}}{\text{sec}}$ is the velocity gain, $K_p = 1/T_s = 5 \times 10^4\ \frac{\text{samples}}{\text{sec}}$ is the position gain and $R(s)$ is a resonance structure. The Bode magnitude plot of a reduced order (28^{th}) $R(s)$ is shown in Figure 1.2. This resonance transfer function $R(s)$ was derived from the flexible arm of an open disk drive at the Oklahoma State University Advanced Controls Laboratory. The resonance modes change drastically due to variation of the mode parameters. On the Bode plot, the peaks of the frequency response may shift both in frequency and in amplitude.

The maximum current is $A_{amx} = 1.3$ amp, the maximum velocity constraint is $V_{max} = 130$ tracks/sample, the applied voltage constraint is $V_a = 12$ volts, and the long seek position movement is $P_{max} = 3 \times 10^4$ tracks. The sampling period is $T_s = 2 \times 10^{-5}$ sec. The slope value is $S = 0.0025\ \frac{\text{tracks/sample}^2}{\text{sample}}$ which is the acceleration decrease per sample. Figure 5.25 shows the sloped fast current command with the velocity constraint. Figure 5.26 shows the resultant velocity signal. Figure 5.27 shows the resultant position signal. Figure 5.28 shows the position signal near the target track. The interval of Y axis in Figure 5.28 is scaled to exactly 10 tracks. It shows that the residual vibration exists for a long period of time after the end of the current command (6.3 msec).

To suppress the residual vibration, a rectangle based shaper filter is designed based on the first resonance mode in the flexible system. The first resonance mode has the parameter

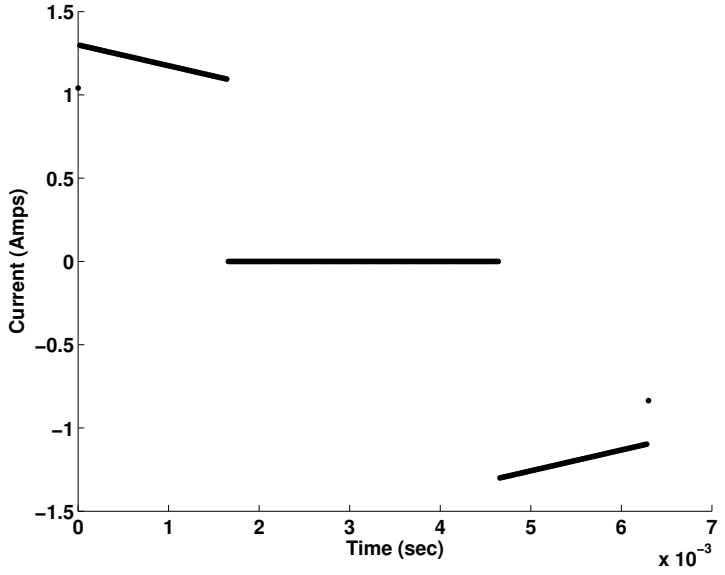

Figure 5.25: Sloped fast current command with the velocity constraint.

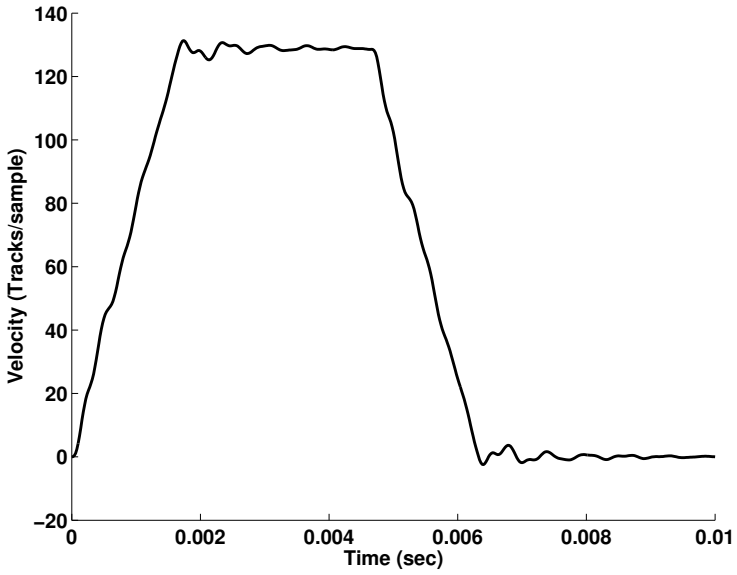

Figure 5.26: The velocity signal with the sloped fast current.

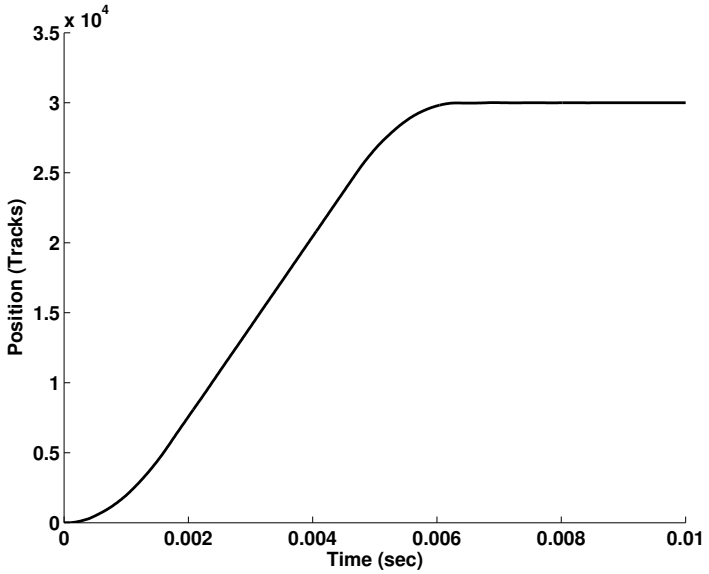

Figure 5.27: The position signal with the sloped fast current command.

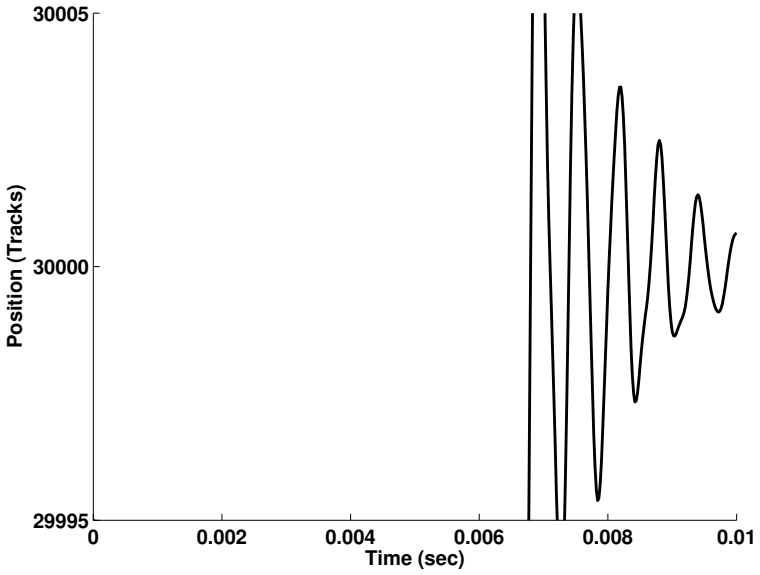

Figure 5.28: The position signal near the target track.

$\omega_1 = 6.12 \times 10^3$ rad/sec and $\zeta_1 = 0.7$. Figure 5.29 shows the resultant vibration suppression shape filter. Figure 5.30 shows the robust vibration suppression current command. Figure 5.31 shows the resultant velocity signal. Figure 5.32 shows the resultant position signal near the target track. The interval of Y axis in Figure 5.32 is scaled to exactly 10 tracks. Although the residual vibration due to both the first resonance mode has been canceled, there still a large vibration exists after the end of the current command. This residual vibration is caused by the second resonance mode in the flexible system.

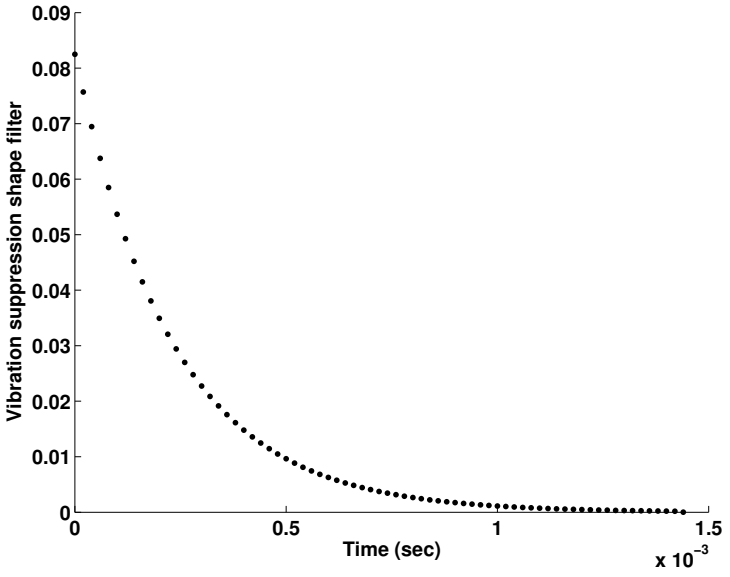

Figure 5.29: Rectangle based shape filter based on resonance parameter $\omega_1 = 6.12 \times 10^3$ rad/sec and $\zeta_1 = 0.7$.

To suppress the residual vibration of the second resonance mode, a rectangle based shaper filter is designed based on the second resonance mode in the flexible system. The second resonance mode has the parameter $\omega_1 = 1.02 \times 10^4$ rad/sec and $\zeta_1 = 0.08$. Figure 5.33 shows the resultant vibration suppression shape filter based on the second resonance mode. Combining the shape filter in Figure 5.29 and the shape filter in Figure 5.33 results a new shape filter as shown in Figure 5.34. The resultant new vibration suppression shape filter in Figure 5.34 cancels the residual vibration due to both the first resonance mode and the second resonance mode. Figure 5.35 shows the robust vibration suppression

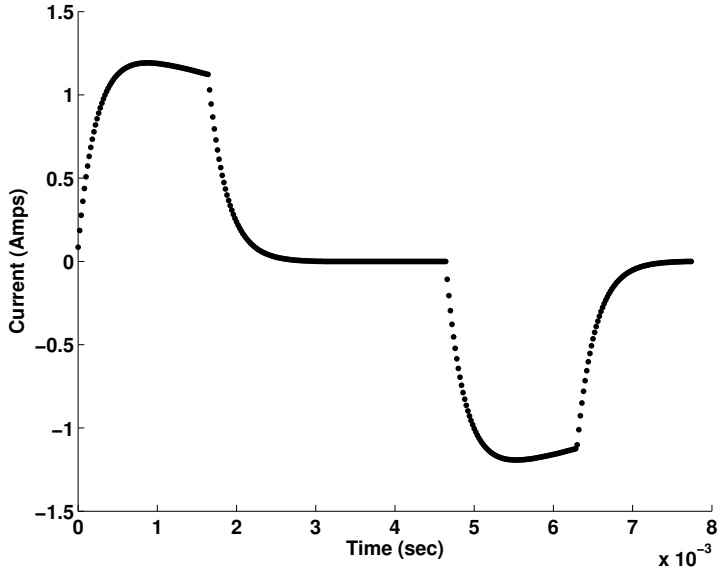

Figure 5.30: Robust vibration suppression current command.

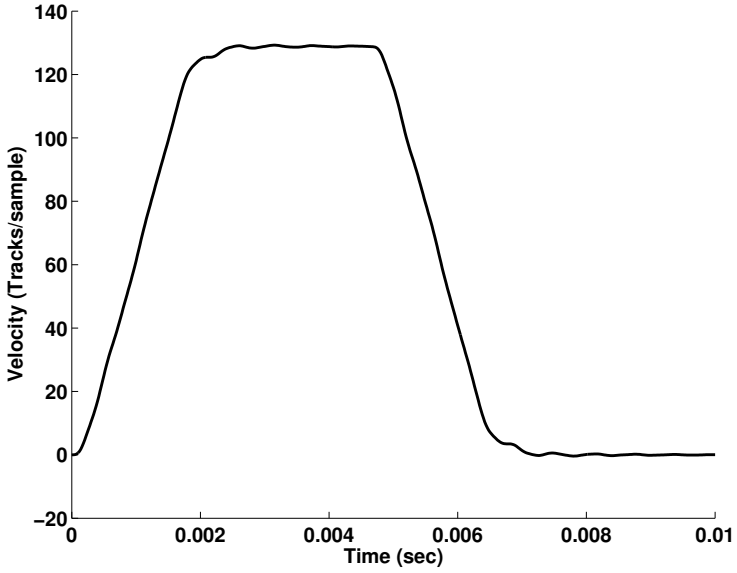

Figure 5.31: Velocity signal with the robust vibration suppression current command.

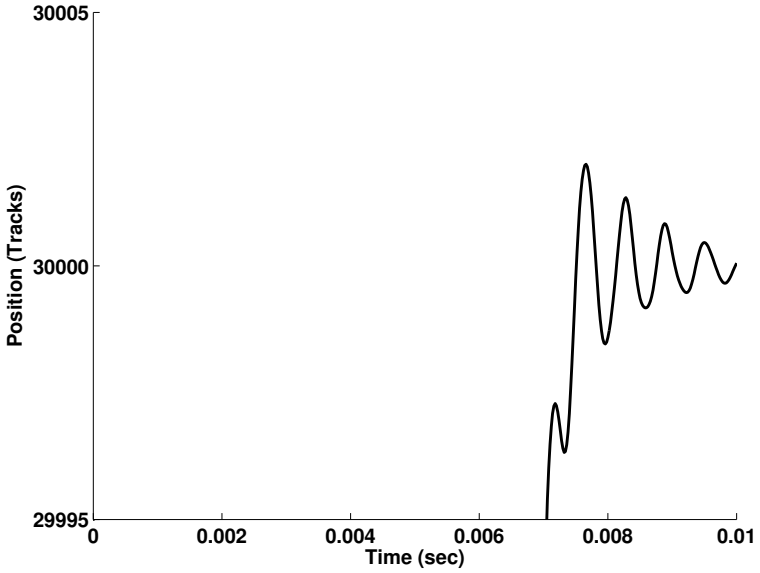

Figure 5.32: Position signal near the target track.

current command. Figure 5.36 shows the resultant velocity signal. Figure 5.37 shows the resultant position signal near the target track. The interval of Y axis in Figure 5.37 is scaled to exactly 1 track. It shows that the residual vibration due to both the first resonance mode and the second resonance mode is canceled. Also the residual vibration due to the high frequency modes is also suppressed. In this case, it is not necessary to design a robust high frequency suppression shape filter to suppress all the high frequency residual vibration because the high frequency vibration is sufficiently suppressed by the two rectangle based shape filters.

Based on the armature inductance $L = 0.6$ mH, the armature resistance $R = 10$ ohm, and the back-emf constant $K_e = \frac{5}{3} \times 10^{-6} \frac{\text{volts}}{\text{tracks/sample}}$ as shown in Figure 5.22, the drive applied voltage signal due to the drive current command can be derived. Figure 5.38 shows the drive applied voltage signal due to the drive current command. It shows that the maximum allowable applied voltage is met but not saturated.

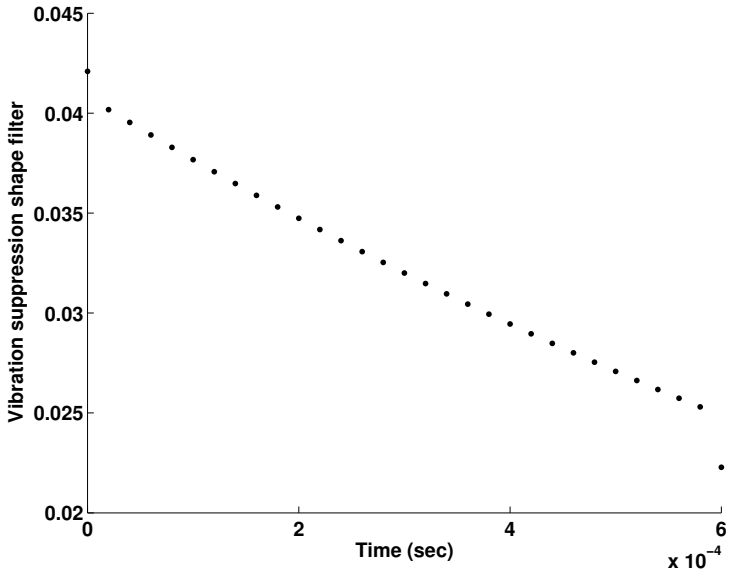

Figure 5.33: Rectangle based shape filter based on resonance parameter $\omega_2 = 1.02 \times 10^4$ rad/sec and $\zeta_1 = 0.08$.

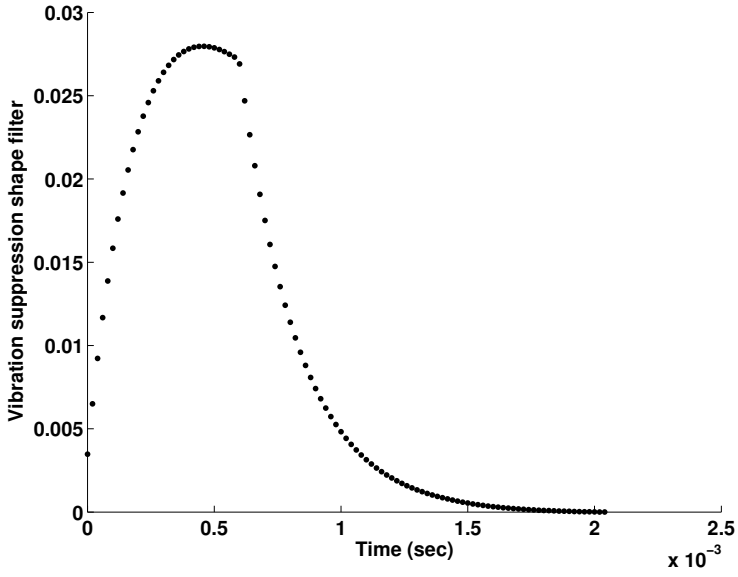

Figure 5.34: Robust vibration suppression shape filter to cancel both the first resonance mode and the second resonance mode.

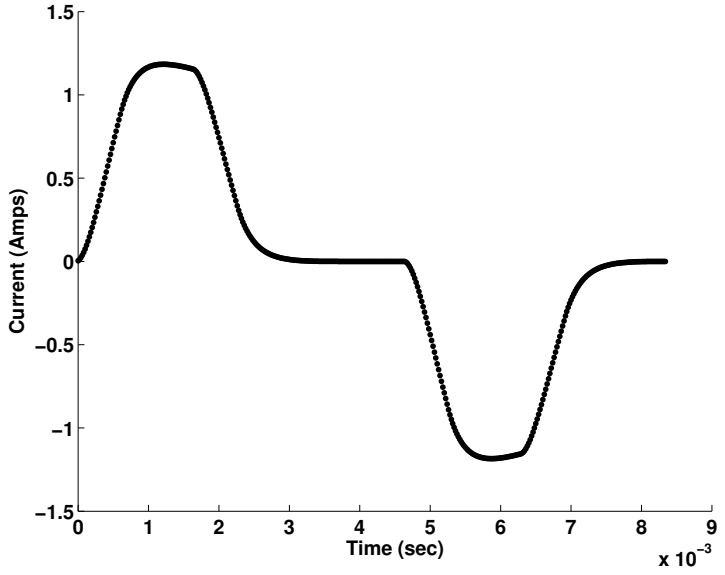

Figure 5.35: Robust vibration suppression current command.

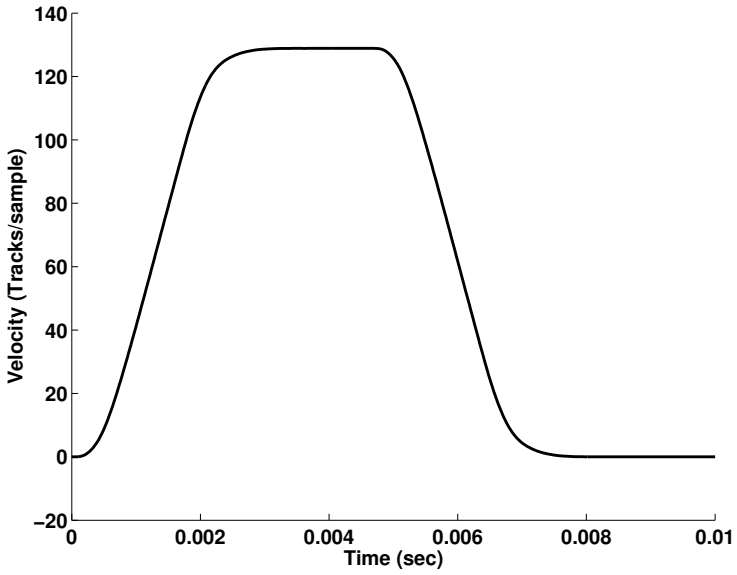

Figure 5.36: Velocity signal with the robust vibration suppression current.

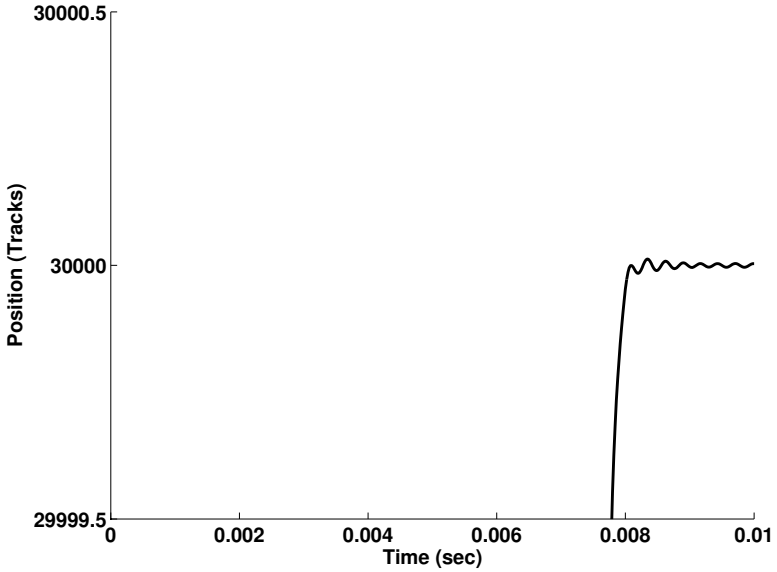

Figure 5.37: Position signal near the target track.

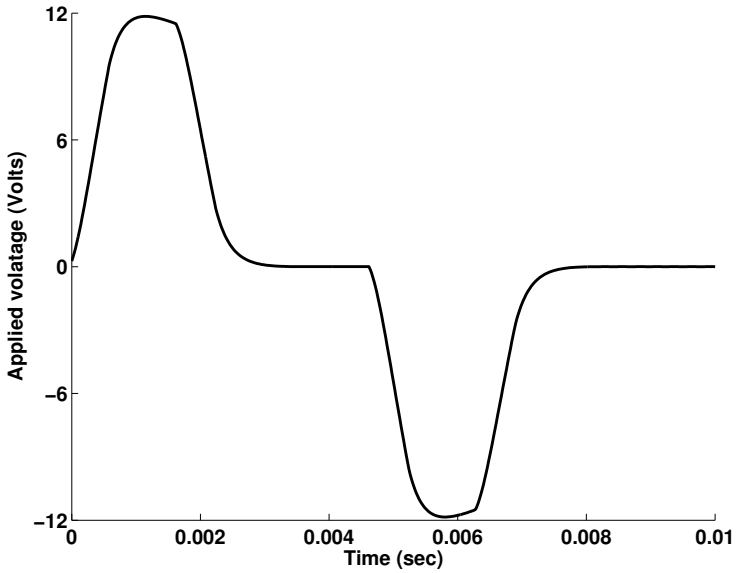

Figure 5.38: Applied drive voltage signal due to the drive current command.

Chapter 6

Hard Disk Drive Experimental Results

6.1 Hard Disk Drive Flexible Arm Control Experimental Setup - Hardware Components

This section gives a detailed description of the experimental setup on which the designed robust vibration suppression method was tested. Most part of this section is from Chee [17]. The equipment used to set up the experiment is shown in Table 6.1. The disc drive used for the setup was an old drive manufactured by Conner. The model is CP3000 and the series is E59JKA. Since the focus of this research was to control the actuator arm, the disc and the cover were removed for convenience. The Polytec laser Doppler vibrometer (LDV) consists of controller OFV-3001 and sensor head OFV-303. The main purpose of the LDV was to feedback the position and velocity signals of the actuator. A Kepco power amplifier with a maximum output of 2 Amps was used to supply current to drive the disc drive. DS1104 PPC controller board from dSPACE was used to interface between the real system and computer. This controller board has a frequency range of 100 KHz. A Lecroy 1 GHz digital oscilloscope was used to take measurements. The software used for the real-time control was MATLAB real-time workshop. The tests were performed on a Newport vibration isolation table to minimize external disturbances. The computer used for this experiment has a Pentium II 450 MHz processor.

Equipments For Disk Drive Research
An Open Disk Drive
Kepco Power Supply/ Amplifier
Polytec Laser Doppler Vibrometer (LDV)
DS1104 PPC Controller Board (dSPACE)
1GHz Lecroy Oscilloscope
MATLAB Real-Time Workshop
Newport Vibration Isolation Table
Pentium II 450 MHz computer

Table 6.1: Equipment for the Disk Drive Experiment.

Figure 6.1 shows the block diagram of the hardware architecture of the experimental setup. In standard operation, the servo feedback controller is designed in the host computer using MATLAB and SIMULINK Real-Time Workshop. The controller algorithm is compiled and downloaded to the DS1104 PPC controller board. The DS1104 controller board sends a signal to the Kepco power amplifier, which supplies the current to the voice coil motor (VCM). The VCM controls the position of the actuator. The Polytec laser Doppler vibrometer (LDV) measures the position and velocity of the actuator and provides feedback to the DS1104 PPC controller board. The Lecroy digital oscilloscope is used to measure the signals of interest.

6.1.1 Polytec Laser Doppler Vibrometer (LDV)

The Polytec vibrometer is an instrument for non-contact measurement of surface vibrations based on laser interferometry [67]. The vibrometer consists of the controller OFV-3001 and the sensor head OFV-512.

The beam of a helium neon laser is focused on the object under investigation, scattered

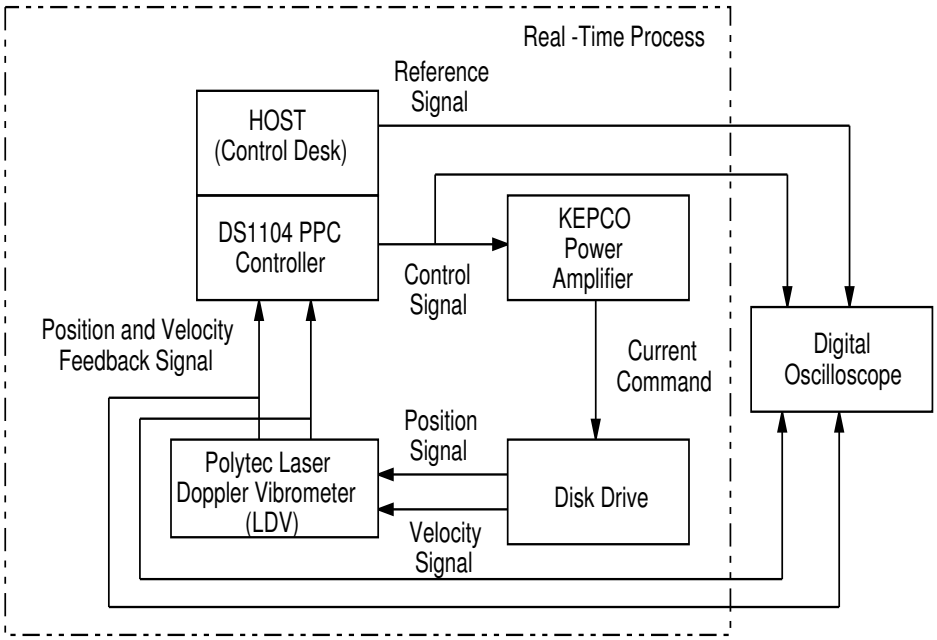

Figure 6.1: Hardware Architecture of the Experimental Setup.

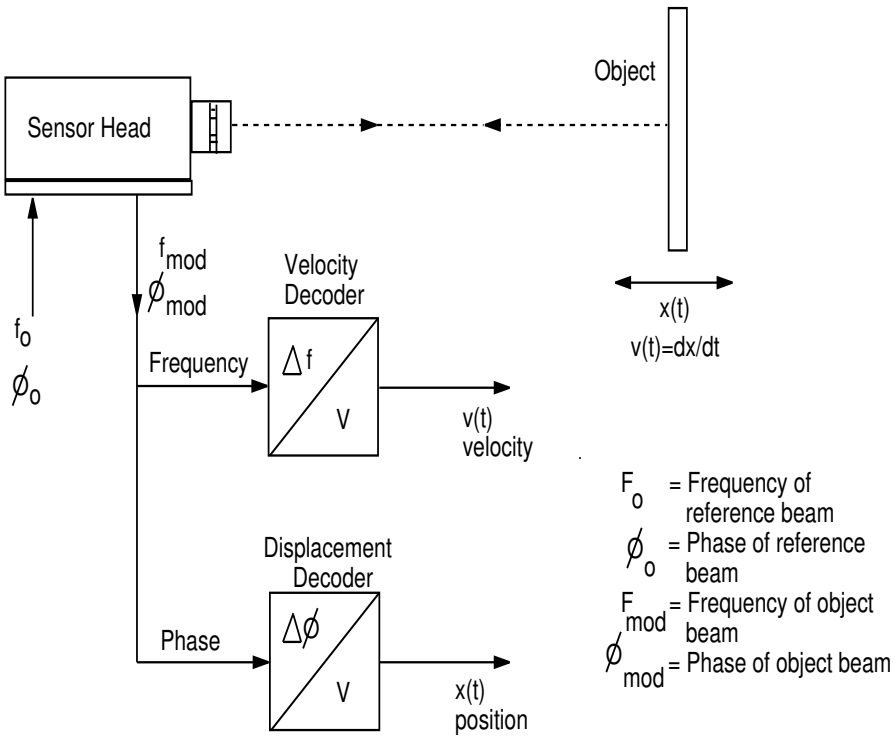

Figure 6.2: Vibrometer Signals.

back from there and coupled into the interferometer in the sensor head. The interferometer in Figure 6.2 compares the phase, ϕ_{mod}, and the frequency, f_{mod}, of the object beam and with those of the internal reference beam, ϕ_o and f_o. The frequency difference is proportional to the instantaneous velocity and the phase difference is proportional to the instantaneous position of the object.

The signal is decoded using the velocity decoder and the position decoder. Two voltage signals are generated which are proportional to the instantaneous velocity and to the instantaneous position (displacement) of the object, respectively. Both signals are externally available for measurement. Figure 6.3 shows the Polytec LDV equipment used in the experiment.

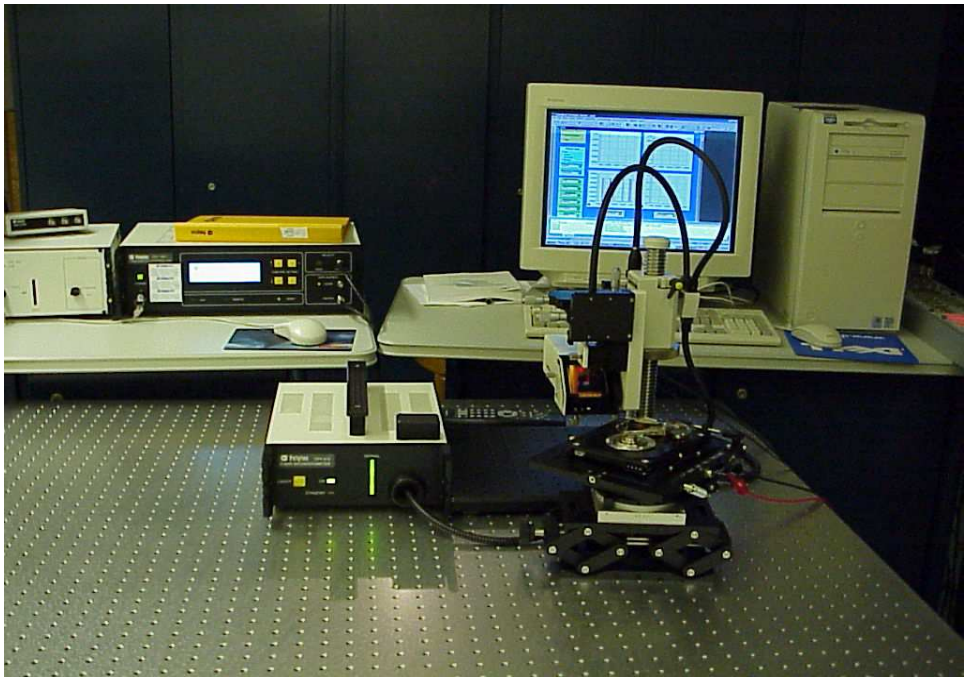

Figure 6.3: Polytec LDV in the Experimental Setup.

6.1.2 Kepco Power Amplifier

The Kepco power amplifier model BOP $50-2M$ amplifies the controller output to a level which is capable of driving the voice coil motor. The amplifier has direct current (dc) range

of $\pm 50V$ and $\pm 2A$. The Kepco power amplifier is a bipolar operational power (BOP) supply/amplifier, which can be used for in a great variety of applications. As a precision voltage or current source, the BOP output can be controlled locally through the front panel bipolar VOLTAGE or CURRENT controls or remotely by voltage and current signals. The amplifier has independently adjustable or remotely programmable limit circuits for both voltage and current output. The built-in preamplifiers for the voltage as well as the current channel of the BOP permit amplification of the control signal to the required amplitude and provide the interface with high and low impedance signal sources. A detailed description on the Kepco power amplifier can be found in [35].

6.1.3 DSP Controller Board

The DSP board model DS1104 PPC controller board is from dSPACE. This type of board is specifically designed for development of high-speed multivariable digital controllers and real-time applications in various fields. It is a complete real-time system based on a 603 PowerPC processor running at 250 MHz. For advanced I/O purposes, the board includes a slave-DSP subsystem based on the Texas Instruments TMS320F240 DSP micro-controller. A detailed description about the board is available in [21].

Information on the DS1104 PPC controller board:

- 603 PowerPC at 250MHz
- 2 MB local SRAM
- 32 MB global DRAM
- 1 16-bit ADC with four multiplexed input signals
- 4 12-bit parallel ADC with one one input signal each
- 8 14-bit parallel DAC

- Incremental encoder interface (2 inputs)
- 1 bit I/O unit with 20-bit I/O
- Serial interface

6.1.4 Vibration Isolation Table

The Newport vibration isolation table provides an ideal working platform for vibration sensitive devices such as interferometers. The table surface is isolated from floor motion using the Newport's rigid, laminated honeycomb panel technology and pneumatic suspension system. In the experimental setup, both the Polytec Laser Doppler Vibrometer and the hard disk drive are put on the vibration isolation table. More detail about the vibration isolation table can be found in [56].

6.1.5 Disc Drive

The disc drive used for the experiment is produced by Conner. The model of the disc drive is CP3000 and the series number is E59JKA. For the purpose of this experiment, an open disk drive with the disc and the cover removed is used. The object to be controlled is the actuator arm. The Polytec LDV shines the laser at the tip of the actuator arm where the read/write head is located. Figure 6.4 shows the open disc drive that is used for the experiment. The function of the voice coil motor is to control the position of the actuator arm. The read/write head which is located at the tip of the arm read and write information onto the magnetic disc. Figure 6.5 shows the flexible printed circuit. The flexible printed circuit creates a one directional force on the disc drive actuator. Figure 6.6 shows the whole setup of the experiment.

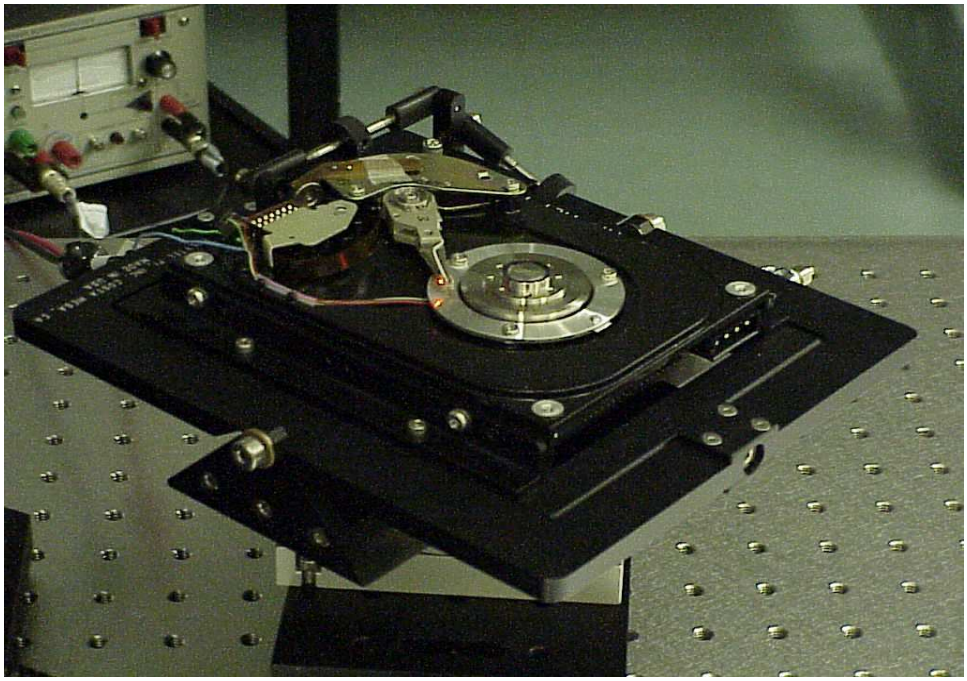

Figure 6.4: Open Disk Drive.

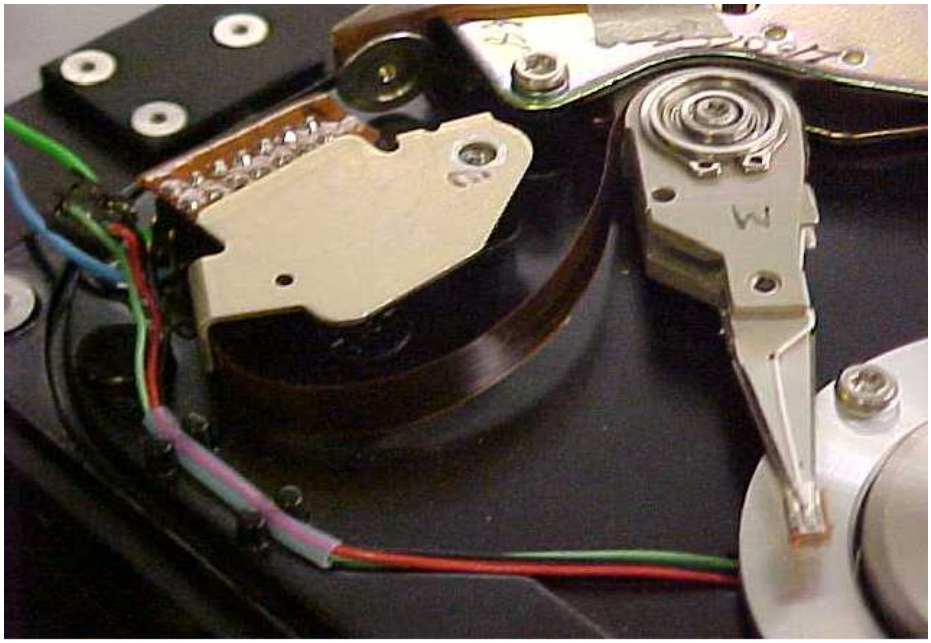

Figure 6.5: Flexible Printed Circuit.

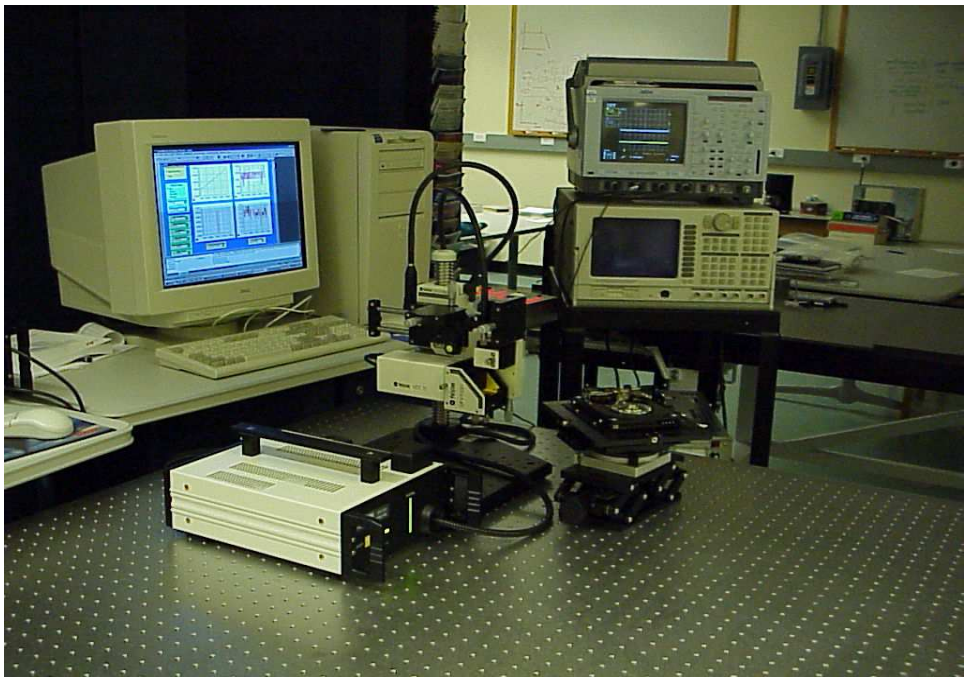

Figure 6.6: The Experimental Setup.

6.2 Hard Disk Drive Flexible Arm Control Experimental Setup - Software Components

6.2.1 MATLAB Real-Time Workshop

MATLAB real-time workshop provided by MathWorks is the final piece in the design process. MATLAB real-time workshop provides a real-time development environment. The real-time workshop is the direct path from system design to hardware implementation. The MATLAB real-time workshop supports the execution of dynamic system models on hardware by automatically converting models to code and providing model-based debugging support. It is well suited for accelerating the development of simulations and embedded real-time applications [51].

6.2.2 dSPACE Software

- Control Desk

  Control desk is a graphical user interface software for managing the dSPACE board. In addition, the control desk manages the registering of hardware and applications via the Platform Manager.

- Real-Time Interface (RTI and RTI-MP)

  The real-time Interface communicates between Simulink and the dSPACE board. The real-time interface, RTI, is used to build real-time code, download and execute this code on dSPACE real-time processor.

- Control Desk Standard

  Control desk standard offers a variety of virtual instruments to build and configure virtual instrument panels via instrumentation providing functions to perform parameter studies via the parameter editor and functions to automate control desk's via automation.

- MLIB/MTRACE

  This is the MATLAB-dSPACE interface libraries. The functions of these libraries allow direct access to dSPACE real-time hardware from the MATLAB workspace.

6.3 Open Disk Drive Mathematical Model Development

In this section, a mathematical model of the open disk drive is developed. The disk drive used in the experiment is manufactured by Conner. A Simulink model is generated to perform system identification of the disk drive actuator. The Simulink model is compiled and downloaded to the DSPACE 1104 board. Figure 6.7 shows the input current signal and the output velocity signal for the system identification.

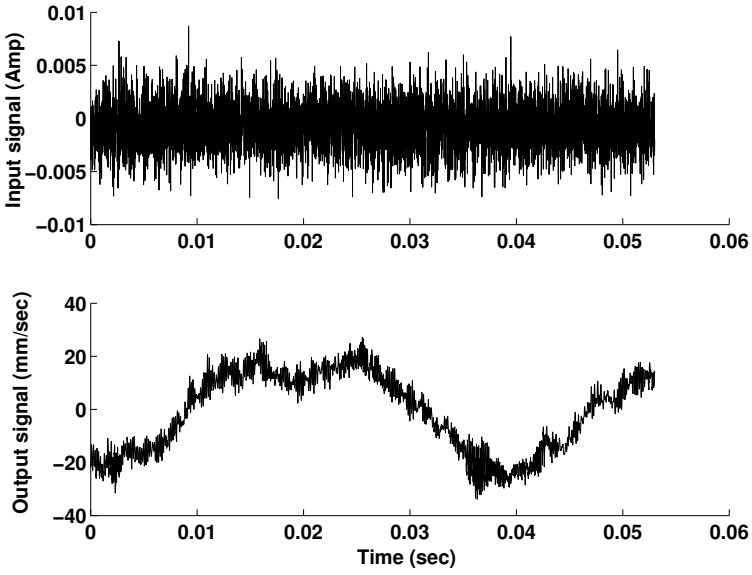

Figure 6.7: Input and output signals.

Figure 6.8 shows the empirical transfer function estimate [45, 44] from the current input to the velocity output.

Figure 6.9 shows a 15^{th} order mathematical model. Figure 6.10 is a reduced integrator model. The first order mathematical model matching the current input to the velocity output is

$$7.5 \times 10^6 \frac{1}{s}. \tag{6.1}$$

The reduced second order model from the current input in amp to position in μm is

$$7.5 \times 10^9 \frac{1}{s^2}. \tag{6.2}$$

6.4 Standard Closed-Loop Control with Step Reference Command

A position and velocity feedback control is used to control the position of the flexible arm. Figure 6.11 shows the Simulink diagram of the position and velocity feedback closed-loop

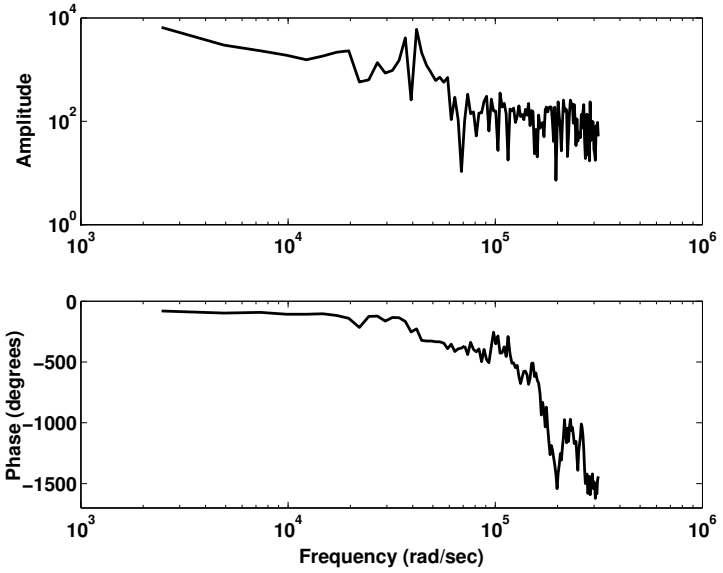

Figure 6.8: Empirical transfer function estimate from current input to velocity.

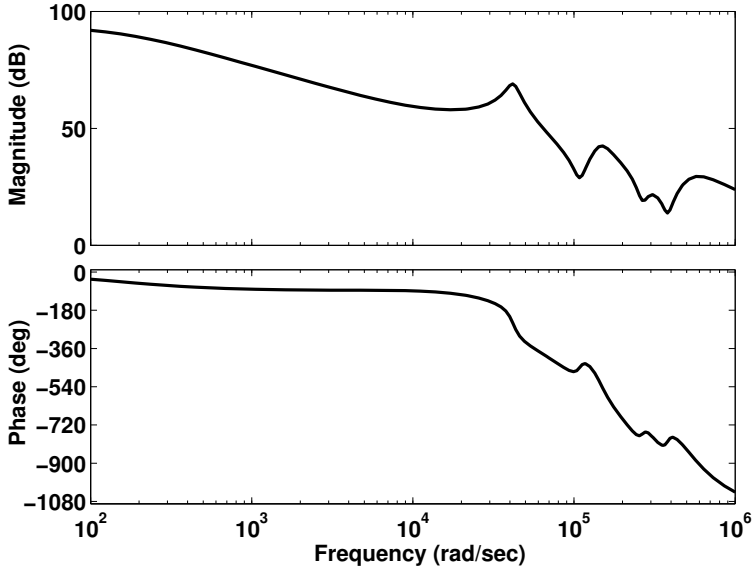

Figure 6.9: Bode plot of 15^{th} order transfer function from current input to velocity.

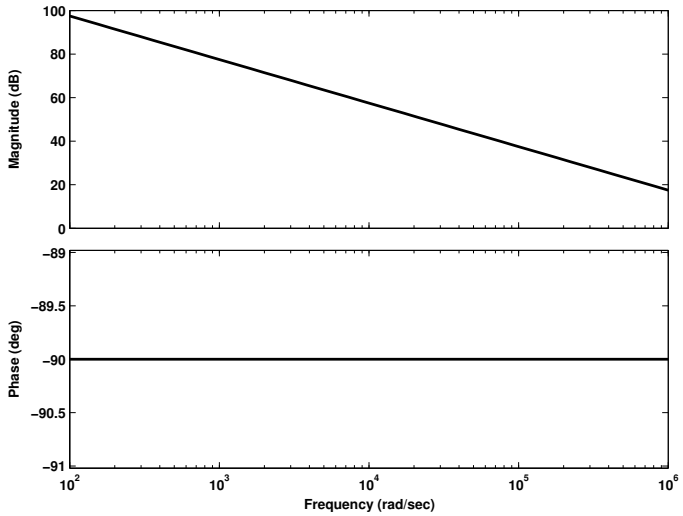

Figure 6.10: Bode plot of reduced order transfer function from current input to velocity.

control structure. The position gain is chosen to be 3.162278 Amp/mm and the velocity gain is chosen to be 0.000316 Amp/(mm/sec). The command reference is a step function with amplitude 10 μm and frequency 20 Hz. The resultant position and the control signal are shown in Figure 6.12. It shows that residual vibration exists after a long period of time.

6.5 Experimental Verification Between ZVD Input Shaping Technique and Rectangle Based Shape Filter

In section 4.6.3, comparison of simulation results between the ZVD input shaper and rectangle based shape filter is performed. The ZVD input shaper amplifies the high frequency vibrations, but the rectangle based shape filter reduces the high frequency vibrations. In this section, both ZVD input shaper and rectangle based shape filter are used to suppress the low frequency vibrations in the hard disk flexible arm control. The undamped natural frequency and the damping ratio of the low frequency mode are $\omega_1 = 3.64 \times 10^3$ rad/sec and $\zeta_1 = 0.425$. Figure 6.13 shows the discrete-time ZVD input shaper with the sam-

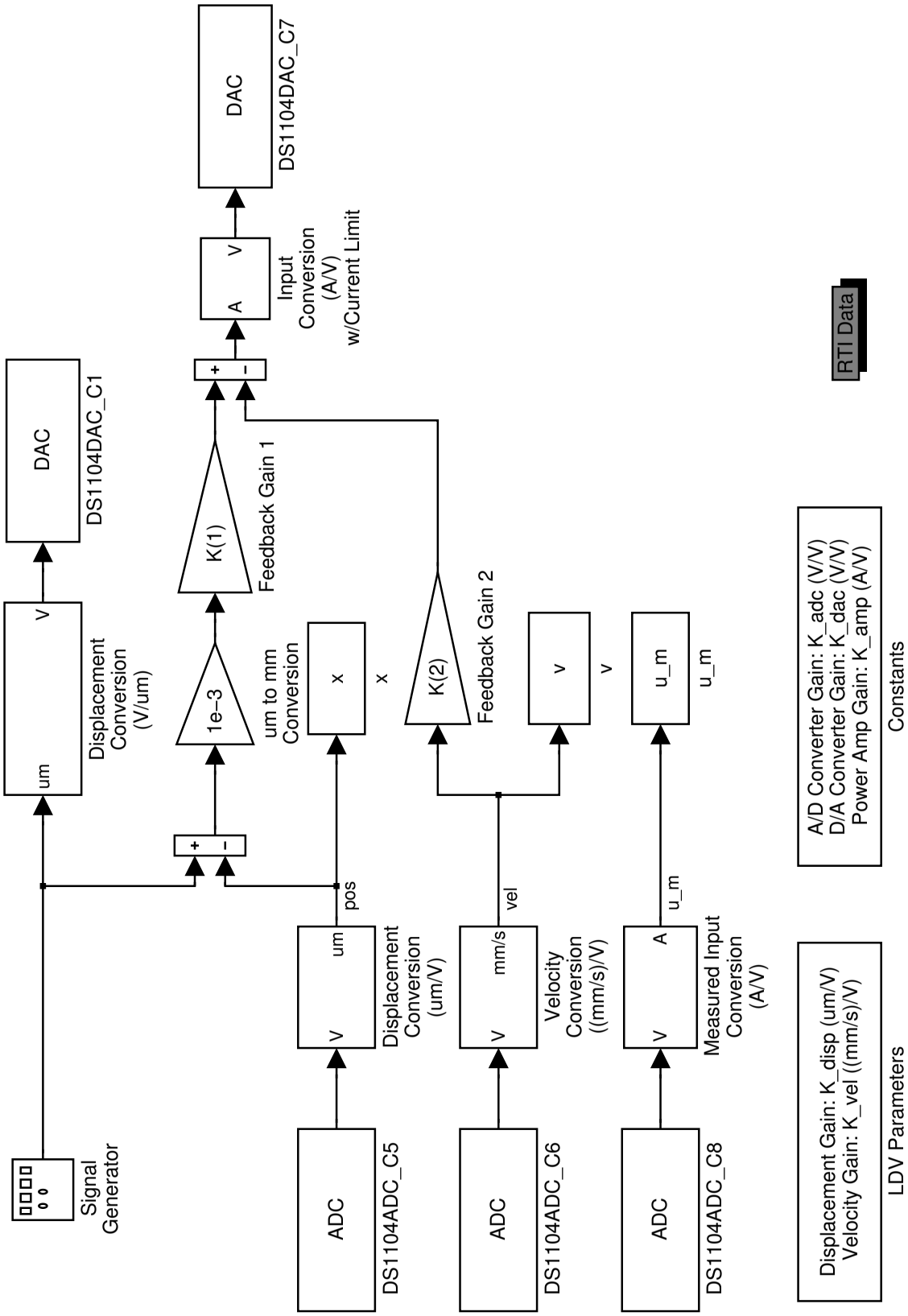

Figure 6.11: Simulink diagram for the position and velocity feedback control.

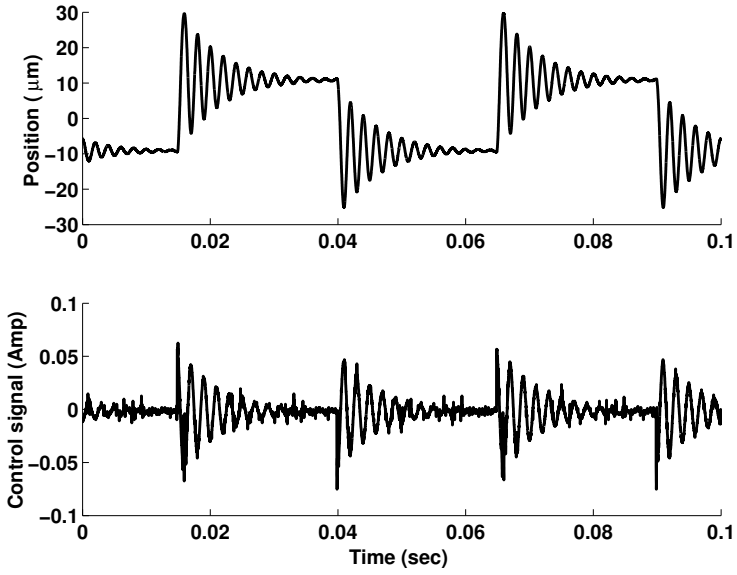

Figure 6.12: Experimental result for 20 μm move with the standard closed-loop control and step reference.

pling period $T_s = 10^{-5}$ sec. Figure 6.14 shows the discrete-time rectangle based shape filter with the sampling period $T_s = 10^{-5}$ sec. The step reference command is first sent to the the ZVD input shaper or rectangle based shape filter, then the shaped reference command is sent to the closed-loop control. Figure 6.15 shows the experimental results with the discrete-time ZVD input shaper. Figure 6.16 shows the experimental results with the discrete-time rectangle based shape filter. In both cases, the low frequency vibration is canceled. The position reference generated from step reference and discrete-time ZVD input shaper amplifies the high frequency vibrations as shown in Figure 6.15. However, the position reference generated from step reference and discrete-time rectangle based shape filter suppresses all the high frequency vibrations as shown in Figure 6.16. From comparison of the control signals in Figure 6.15 and Figure 6.16, it is also clear that the ZVD input shaper makes the control signal very aggressive since the high frequency vibrations are amplified. A robust vibration suppression shape filter that can suppress all the resonant dynamics will be generated and tested in the hard disk drive flexible arm control in the following sections.

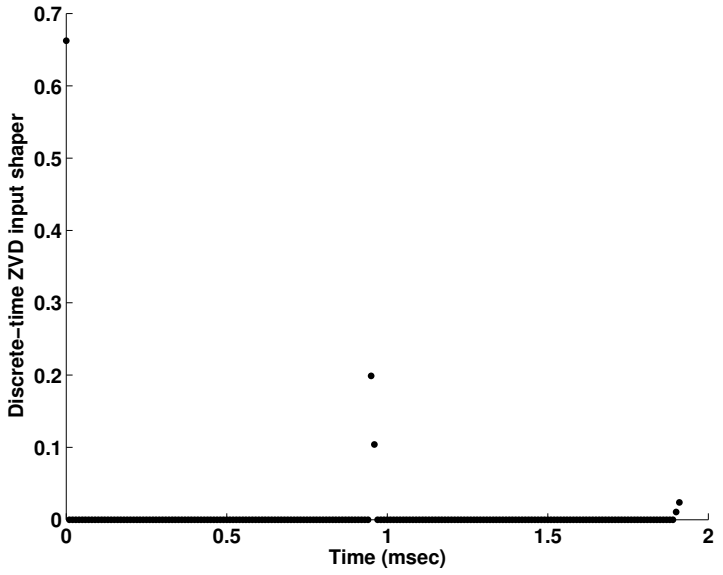

Figure 6.13: Discrete-time ZVD input shaper.

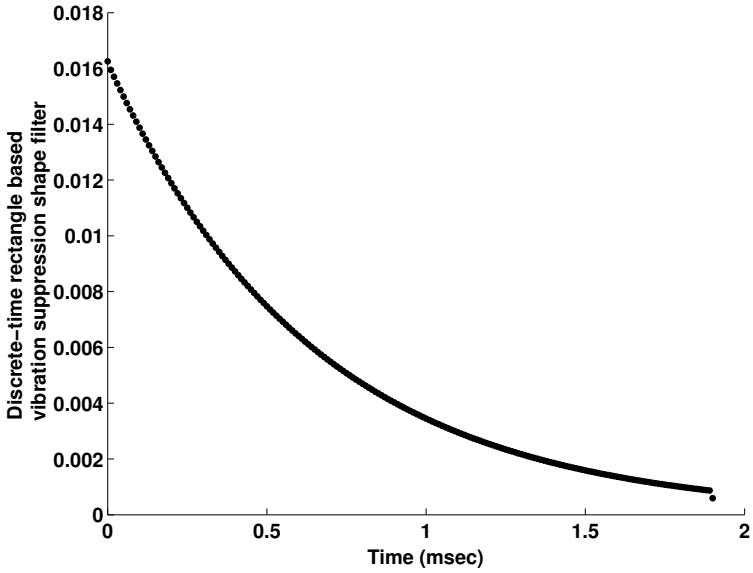

Figure 6.14: Discrete-time rectangle based shape filter.

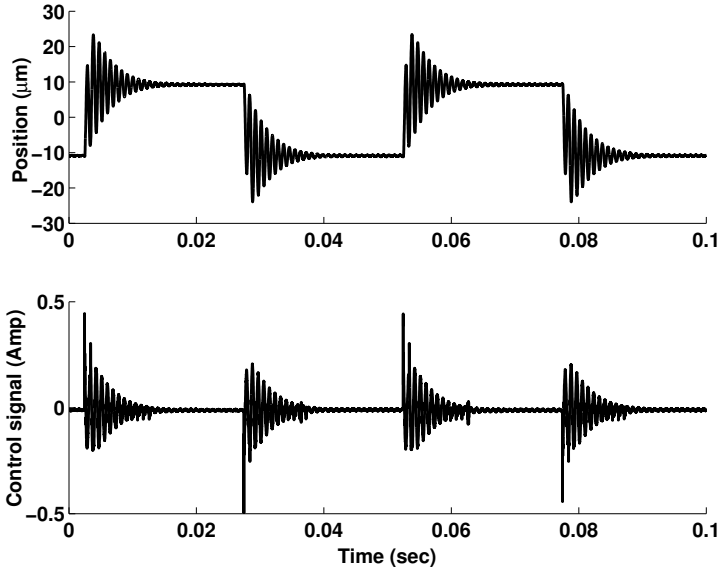

Figure 6.15: Experimental results for 20 μm move with step reference and discrete-time ZVD input shaper.

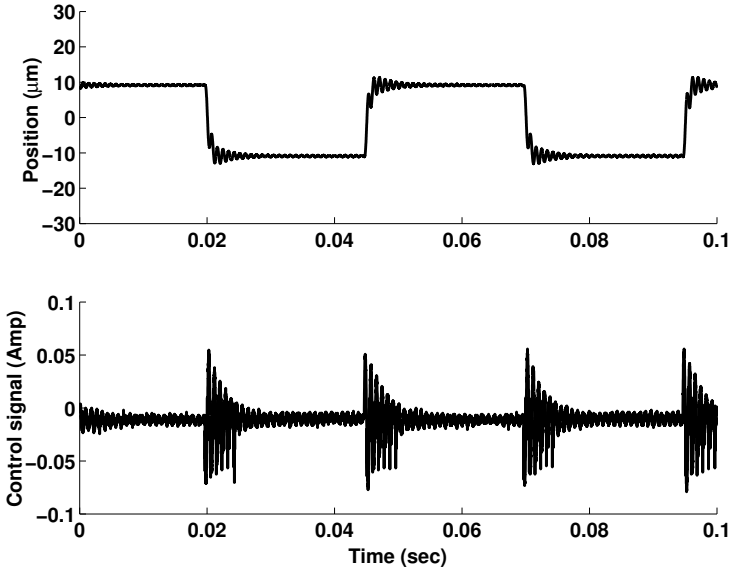

Figure 6.16: Experimental results for 20 μm move with step reference and discrete-time rectangle based shape filter.

6.6 Standard Closed-Loop Control with Robust Vibration Suppression Shape Filter

In this section, a robust vibration suppression shape filter is generated to shape the command reference. The high frequency resonant modes in the closed-loop control approximately occur beyond $\Omega_{h0} = 10^4$ rad/sec. The move time duration of the high frequency vibration suppression shape filter is chosen to be 1.5 msec. The prolate spheroidal wave function based high frequency vibration suppression shape filter is shown in Figure 6.17. Before the high frequency resonance modes, there is one low frequency resonance mode in the closed-loop transfer function. The undamped natural frequency and the damping ratio of this low frequency mode are $\omega_{l1} = 3.64 \times 10^3$ rad/sec and $\zeta_{l1} = 0.425$. The rectangle window based low frequency vibration suppression shape filter is shown in Figure 6.18 which is the same as Figure 6.14. The high frequency vibration suppression shape filter and low frequency vibration suppression shape filter can be combined together through the filtering operation. The filtering operation is mathematical convolution in the time domain and multiplication in the frequency domain. The resultant robust vibration suppression shape filter is shown in Figure 6.19.

The robust vibration suppression shape filter is implemented as in Figure 6.20. The reference command is first input to the robust vibration suppression shape filter, then the shaped reference command is sent to the closed-loop control. Figure 6.21 shows experimental results of the step reference command and the robust vibration suppression shape filter. It shows both the low frequency and high frequency residual vibrations are suppressed.

The movement of 20 μm is a representative of about 8 tracks in a 10000 tracks per inch (TPI) disk drive. The position signal in Figure 6.21 is zoomed in both horizontal axis and vertical axis. Figure 6.22 shows the position signal in the time interval from 0.026 sec to 0.036 sec. Figure 6.23 shows the position signal near the target track, where the

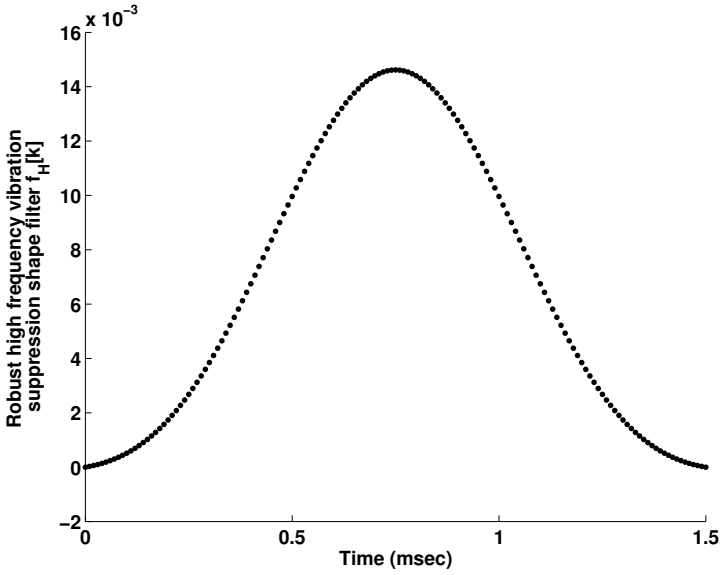

Figure 6.17: Robust high frequency vibration suppression shape filter.

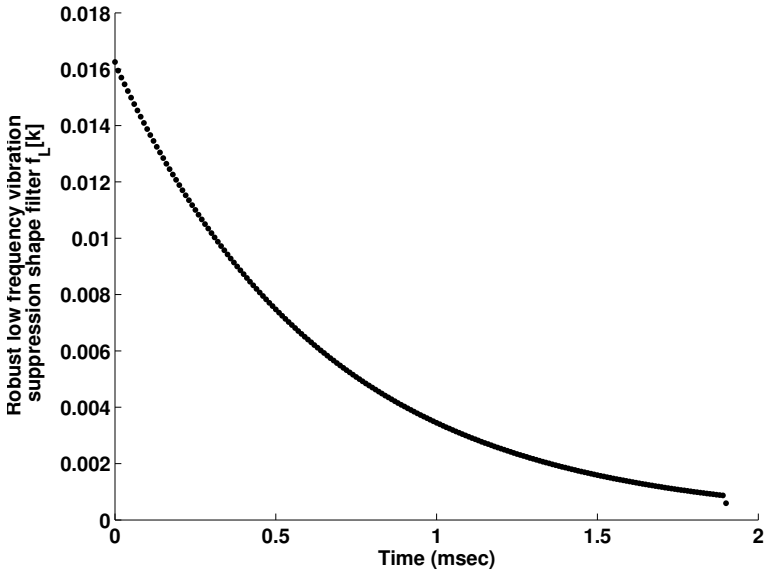

Figure 6.18: Robust low frequency vibration suppression shape filter.

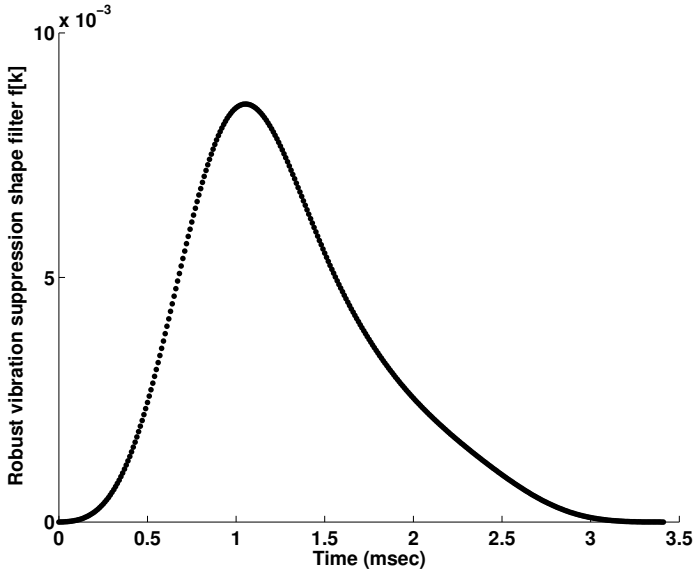

Figure 6.19: Robust vibration suppression shape filter.

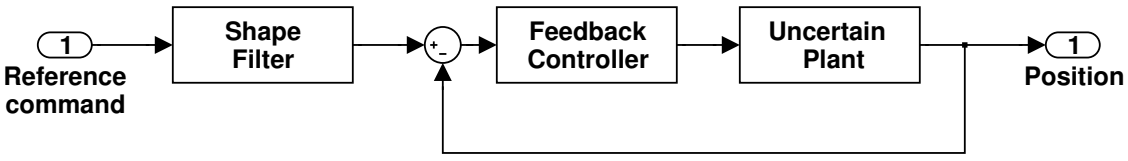

Figure 6.20: Implementation of a robust vibration suppression shape filter.

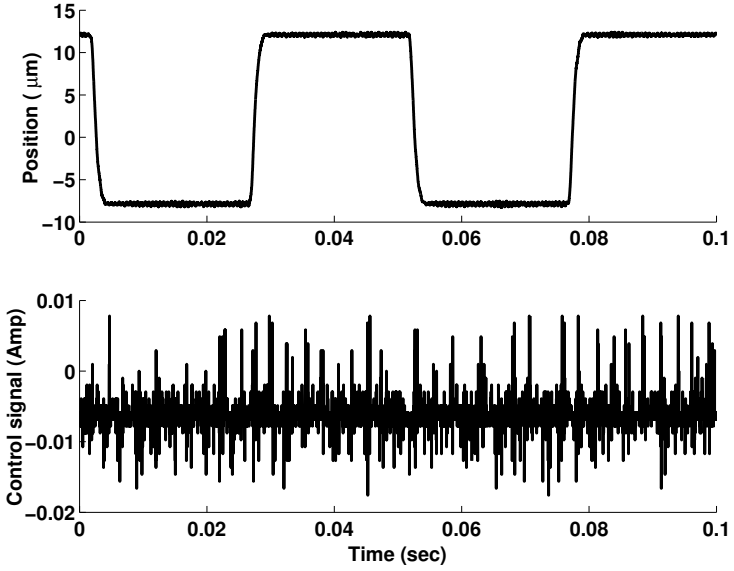

Figure 6.21: Experimental result for 20 μm move with the standard closed-loop control and shaped reference.

range of the vertical axis is exactly one track interval (2.54 μm). It shows that position signal immediately settles at the move time of 3.4 msec with $\pm 10\%$ track error criterion. In Figure 6.23, the distance between two dashed lines is 20% track.

6.7 Model Reference Closed-Loop Control with Robust Vibration Suppression Control Profile

In this section, model reference closed-loop control is implemented as shown in Figure 6.24. Both feed forward control profile and position reference profile can be generated from the robust velocity profile. The robust vibration suppression shape filter itself is a normalized velocity profile. The real velocity reference to realize a certain position movement can be generated by multiplying the velocity profile with a constant gain. Figure 6.25 shows the robust vibration suppression velocity profile for a 20 μm movement. From the robust velocity profile, position reference and feed forward control input can be generated.

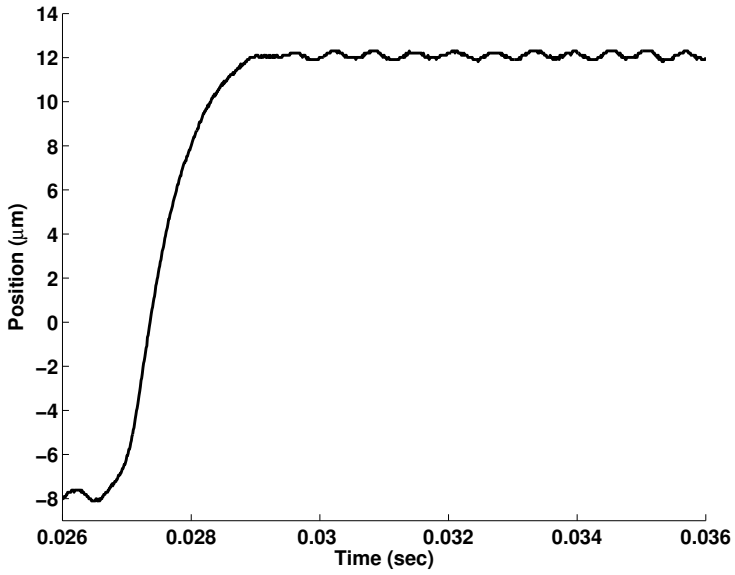

Figure 6.22: Position signal zoomed in horizontal axis.

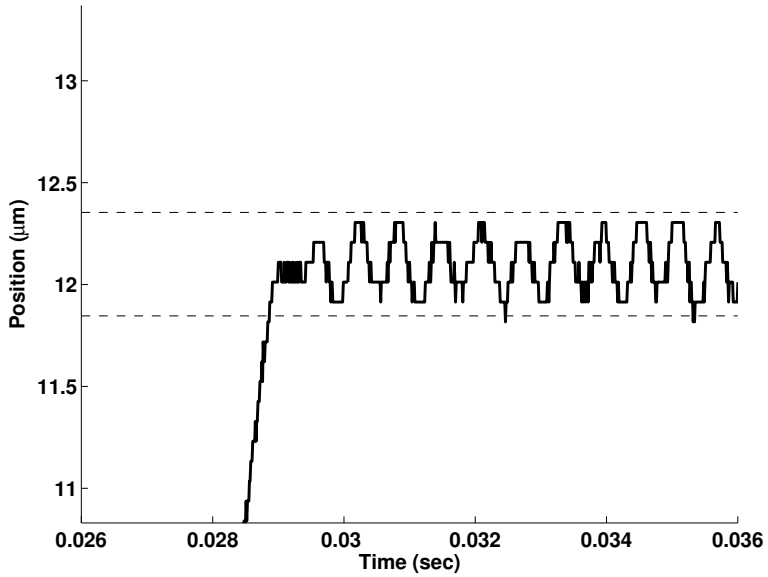

Figure 6.23: Position signal zoomed in vertical axis.

Figure 6.26 shows the resultant robust vibration suppression position profile for a 20 μm movement. Figure 6.27 shows the robust vibration suppression feed forward control input for a 20 μm movement.

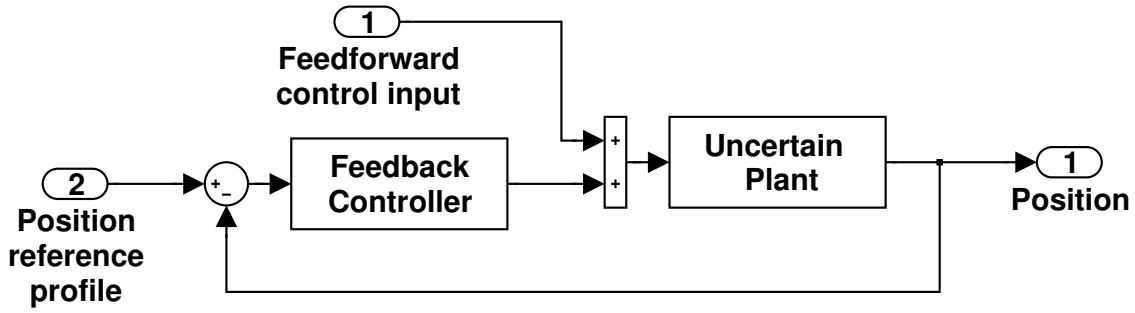

Figure 6.24: Implementation of model reference closed-loop control with robust vibration suppression control profiles.

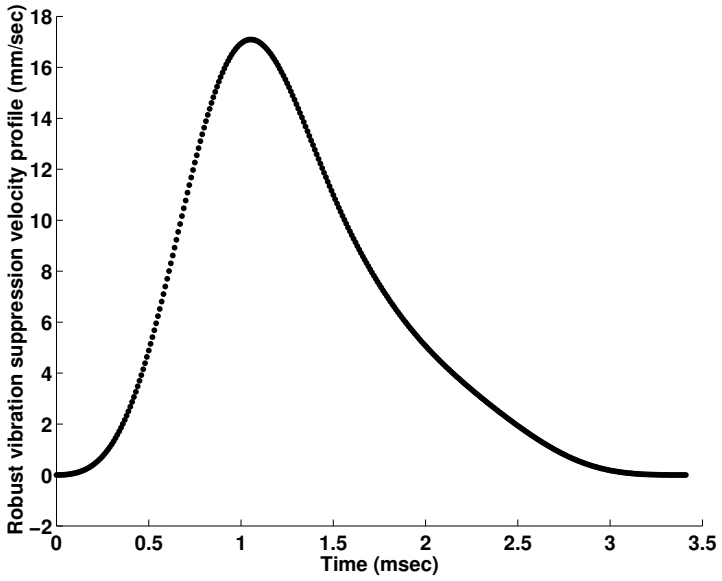

Figure 6.25: Robust vibration suppression velocity profile.

Figure 6.28 shows experimental results of the model reference closed-loop control with the robust vibration suppression control profiles. It shows both the low frequency and high frequency residual vibrations are suppressed.

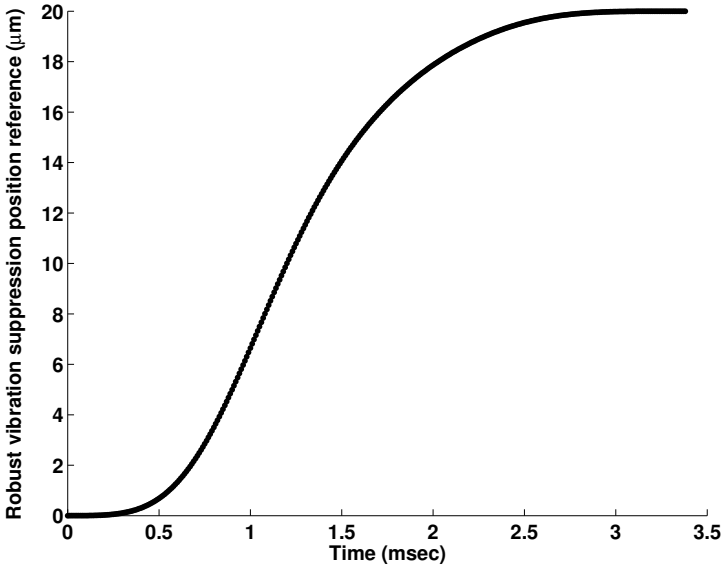

Figure 6.26: Robust vibration suppression position profile.

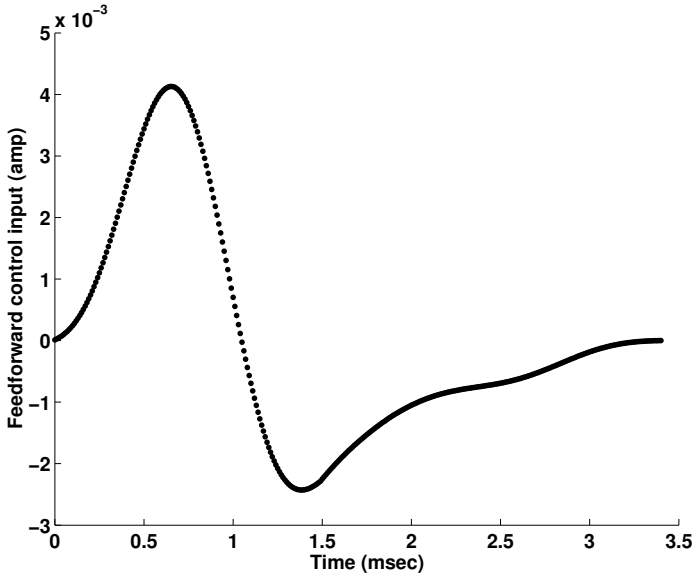

Figure 6.27: Robust vibration suppression feedforward control input.

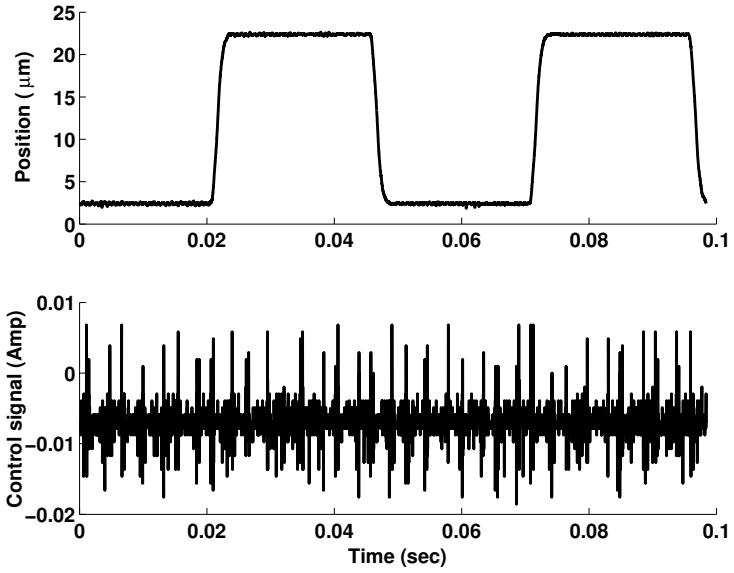

Figure 6.28: Experimental result for 20 μm move with the model reference closed-loop control and shaped reference.

The movement of 20 μm is a representative of about 8 tracks in a 10000 tracks per inch (TPI) disk drive. The position signal in Figure 6.28 is zoomed in both horizontal axis and vertical axis. Figure 6.29 shows the position signal in the time interval from 0.02 sec to 0.03 sec. Figure 6.30 shows the position signal near the target track, where the range of the vertical axis is exactly one track interval (2.54 μm). It shows that position signal immediately settles at the move time of 3.4 msec with $\pm 10\%$ track error criterion. In Figure 6.30, the distance between two dashed lines is 20% track.

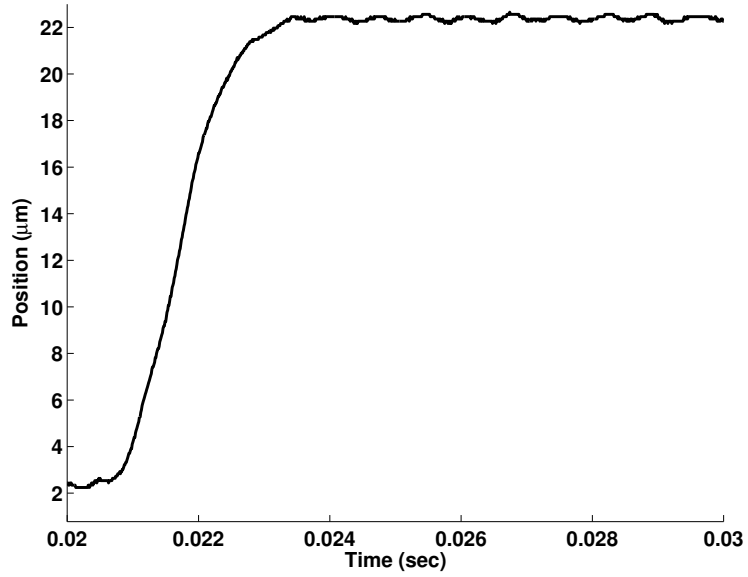

Figure 6.29: Position signal zoomed in horizontal axis.

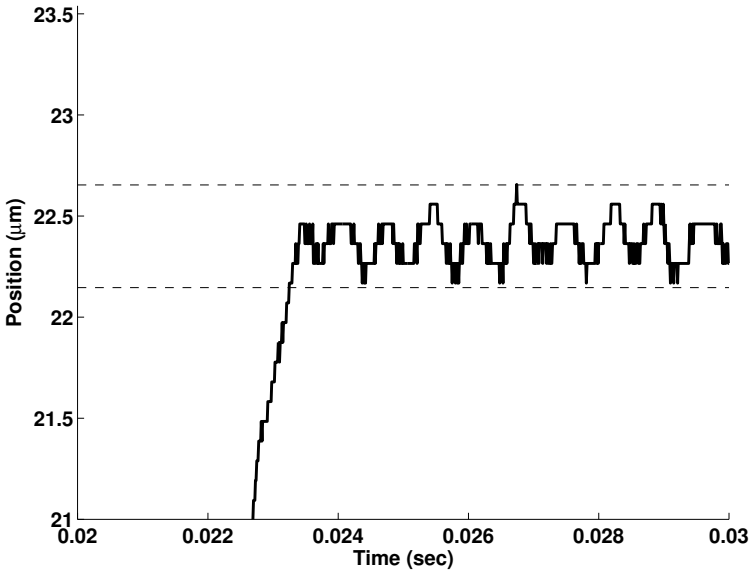

Figure 6.30: Position signal zoomed in vertical axis.

Chapter 7

Concluding Remarks

7.1 Conclusions

A robust vibration suppression control profile is generated which suppresses all the resonant modes in a flexible system. This robust control profile is based on a continuous function which can generate a robust velocity profile, or a robust shape filter to an arbitrary control command.

The robust vibration suppression forcing function can be directly used in open-loop control. For closed-loop control, two control schemes are studied. The first one is the standard closed-loop control. In this control scheme, the tracking reference command is generated from a step reference through a robust vibration suppression shape filter. The vibration suppression shape filter is designed by considering the resonance modes in the closed-loop system. The other closed-loop control scheme is the model reference control. In this control scheme, the open-loop forcing function is directly sent to the real plant and a reference model. The feedback controller compares and compensates for the output difference of the real plant and the reference model. This control scheme is suitable for the case that the real plant changes a lot at different working conditions. The feed forward forcing function and position reference are designed by considering the resonance modes in the closed-loop system.

Experimental results from the flexible link position control with strain gauge and hard disk drive position control verify the effectiveness of the methods.

7.2 Future Research

A number of directions are available for future research in both the theory and application of this new technology. The following categories highlight some promising ones. Theory:

1. Non-Continuous Function Based Shape Filter. From the architecture of the vibration suppression shape filter as shown in Figure 4.29, all shape filters from the input shaping technique [71, 73, 79, 85, 98] belong to the impulse function based shape filters. However, the non-impulse function based shape filters, for example, a piecewise continuous function based shape filters, are not studied in this report. There are a number of questions about the non-continuous function based shape filter, such as time duration of the shape filter, robustness, etc. A systematic comparison of those properties between non-continuous function based shape filters and continuous function based shape filters is greatly helpful to control engineers. The research done in this report obviously assists the fruition of this research direction.

2. Time-Optimal Control. The relationship between non-continuous impulse shape filters (for example, the input shaping technique) and time-optimal control, has been studied by a lot of researchers. Pao and Singhose [62, 63] investigated the equivalence of minimum time input shaping with traditional time-optimal control and they showed that several robust time-optimal shaper designs for flexible systems are equivalent to the time-optimal controls for different systems. Singhose and Pao [77] compared several types of input shapers and the time-optimal flexible body control in terms of a number of engineering factors. Lau and Pao [41, 42] proved that some input shapers are equivalent to traditional time-optimal control, possibly of different systems basing on the Karush-Kuhn-Tucker conditions. Baumgart and Pao [7]

showed that for MIMO systems, the input shaping problem for unknown inputs is equivalent to a set of SISO optimal control problems. All the above investigations generate bang-bang form forcing functions, which possibly potentially induces the higher order unmodeled dynamics in a flexible system. The relationship between continuous shape filters and time-optimal control (possibly sub-optimal control) is a prominent research topic.

3. Input and State Constraints. Without increasing move time, the robust vibration suppression control profiles in this report can be multiplied by an arbitrary constant if the resultant forcing functions do not saturate. In real applications, not only the forcing functions are limited, but also the state variables are constrained. For example, in hard disk drive industry, the read/write flexible arm movement must have a velocity constraint for safety reasons. Robust vibration suppression control profile generation with the input and state constraints is a useful study.

4. Compensation for Non-Zero Initial State Values. The open-loop robust vibration suppression control profiles in this report force a flexible system from one set point to another set point. Although the experiments show satisfying results even if the small initial state values are not considered, compensation for the non-zero initial state values will definitely improve the position precision.

5. Nonlinear System Controls. The robust vibration suppression control profile and robust vibration suppression shape filter developed in this report are based on the linear system theory. However, the research direction on this new technology to nonlinear systems is possible. As a special case of shape filter, input shaping technique has been studied and applied to some nonlinear systems. The initial study of those techniques may bring about a good start. Banerjee and Singhose [6] used input shaping for nonlinear control of a two-link flexible manipulator. Smith, Kozak, and Singhose [90] designed effective zero-vibration input shapers for a class of nonlinear systems.

Park and Schrader [64] proved that an input shaper with two impulses can eliminate the residual vibrations in a kind of nonlinear system completely if the impulses are chosen properly. All these available results suggest that the new technology developed in this report has a promising extension to nonlinear system controls.

The methods developed in this report applies to most mechanical and electronic systems to suppress unwanted residual vibration. It may also apply to chemical processes. Several applications are discussed below.

Application:

1. Hard Disk Drive Long Seek Problem. Due to the limitation of the laser Doppler vibrometer, hard disk drive long seek experiment cannot be tested in the experimental setup discussed in this thesis. In real hard disk drive product, the position error signal (PES) [1, 27] is used to feedback control. The techniques in this thesis can be directly implemented to the hard disk long seek control. Since at the long seek control, the maximum allowable control voltage are desired but not saturated. The current command should be designed as large as possible as long as the voltage saturation is avoided.

2. Manipulator Arm Motion Control in Robotics. "The technique for (space) manipulators was, and continuous to be, to move the joints slowly and wait for the tip of the arm to settle to equilibrium (Book [15])." With the requirement of light weight and fast response, flexibility becomes a formidable problem in manipulator arm motion control in robotics. Generally, the robotic systems are multi-input multi-output, nonlinear systems. The flexible modes suppression technique in this thesis could be an effective method to contribute to performance advances in future.

3. Human Operated Machines. Vibration in human operated machines is harmful to both human and machines. "Millions of (U.S.) workers are also exposed to whole-body vibrations through the operation of trucks, fork-lifts, buses, heavy equipment,

farm vehicles, helicopters, aircraft, railroad and subway trains, hovercraft boats, overhead cranes and other vibrating fixed plant equipment [25]." Since most human operated machines involve motion of physical flexible plants, the vibration suppression command generation methods in this thesis may provide a smooth motion trajectory for those kinds of machines to suppress unwanted vibrations.

4. Chemical Processes. It is hard to say now how this approach may be implemented to chemical processes. However, the command reference generation methods may be used to suppress oscillations in chemical processes.

Bibliography

[1] K. G. Ashar. *Magnetic Disk Drive Technology: Heads, Media, Channel, Interface*. Institute of Electrical and Electronics Engineers, Inc., 1997.

[2] D. M. Aspinwall. Acceleration profiles for minimizing residual response. *ASME, Journal of Dynamic Systems, Measurement, and Control*, 102(3):3–6, 1980.

[3] M. Athans and P. L. Falb. *Optimal Control: An Introduction and the Theory and Its Applications*. McGraw-Hill Book Company, 1966.

[4] H. B. C. Kuo and F. Golnaraghi. *Automatic control systems, 8th edition*. John Wiley & Sons, New York, 2003.

[5] M. J. Balas. Feedback control of flexible systems. *IEEE Transactions on Automatic Control*, AC-23:673–679, 1978.

[6] A. K. Banerjee and W. E. Singhose. Command shaping for nonlinear tracking control of a two-link flexible manipulator. *Advances in the Astronautical Sciences*, 97(2):1859–1876, 1997.

[7] M. D. Baumgart and L. Y. Pao. Discrete time-optimal command shapers and controls for multi-input multi-output systems. In *Proceedings of the American Control Conference*, volume 3, pages 2279–2284, 2002.

[8] E. Bayo. Computed torque for the position control of open-chain flexible robots. In *Proceedings of the 1988 IEEE International Conference on Robotics and Automation*, pages 316–321, 1988.

[9] E. Bayo and B. Paden. On trajectory generation for flexible robots. *Journal of Robotic Systems*, 4(2):229–235, 1987.

[10] S. P. Bhat. *Point-To-Point Control of Linear Time Invariant Dynamical Systems: Theory and Experiments*. PhD thesis, University of California, Los Angeles, CA, 1990.

[11] S. P. Bhat and D. K. Miu. Precise point-to-point positioning control of flexible structures. *ASME, Journal of Dynamic Systems, Measurement, and Control*, 112:667–674, 1990.

[12] S. P. Bhat and D. K. Miu. Solutions to point-to-point control problems using Laplace transform technique. *ASME, Journal of Dynamic Systems, Measurement, and Control*, 113(3):425–431, 1991.

[13] S. Bochner. *Lectures on Fourier Integrals, Annals of Mathematics Studies, No. 42*. Princeton University Press, Princeton, N. J., 1959.

[14] W. J. Book. *Modeling, Design and Control of Flexible Manipulator Arms*. PhD thesis, Massachusetts Institute of Technology, 1974.

[15] W. J. Book. Controlled motion in an elastic world. *ASME, Journal of Dynamic Systems, Measurement, and Control*, 115:252–261, 1993.

[16] W. J. Book, O. Maizza-Neto, and D. E. Whitney. Feedback control of two beam, two joint systems with distributed flexibility. *ASME, Journal of Dynamic Systems, Measurement, and Control*, 97:424–431, 1975.

[17] B. F. Chee. Optimization-based tuning of a discrete loop transfer recovery controller with hardware in-the-loop. Master's thesis, Oklahoma State University, 2002.

[18] C. K. Chui. *An Introduction to Wavelets*. Academic Press, New York, 1992.

[19] C. K. Chui. *Wavelets: A Mathematical Tool for Signal Analysis*. SIAM, Philadelphia, 1997.

[20] R. Courant and D. Hilbert. *Methods of Mathematical Physics, Vol. 1*. Interscience Publishers, New York, 1955.

[21] dSPACE. *DS1104 Instalation and Configuration Guide*, 2001.

[22] P. E. Falloon. Theory and computation of spheroidal harmonics with general arguments. Master's thesis, University of Western Australia, 2001.

[23] P. E. Falloon, P. C. Abbott, and J. B. Wang. Theory and computation of spheroidal wavefunctions. *Journal of Physics A: Mathematical and General*, 36:5477–5495, 2003.

[24] C. Flammer. *Spheroidal Wave Functions*. Standard Univ. Press, Stanford, CA, 1957.

[25] The Institute for the Study of Human Vibration at The University of Tennessee. http://www.engr.utk.edu/ishv/.

[26] G. E. Forsythe, M. A. Malcolm, and C. B. Moler. *Computer Methods for Mathematical Computations*. Prentice-Hall, Englewood Cliffs, N.J., 1977.

[27] G. F. Franklin, J. D. Powell, and M. L. Workman. *Digital Control of Dynamic Systems*. Addison-Wesley Publishing Company, 1990.

[28] D. Gorinevsky and G. Vukovich. Nonlinear input shaping control of flexible spacecraft reorientation maneuver. *Journal of Guidance, Control, and Dynamics*, 21(2):264–270, 1998.

[29] Y. H. Ha and A. Pearce. A new window and comparison to standard windows. *IEEE Transactions on Acoustics, Speech, and Signal Processing*, 37(2):298–301, 1989.

[30] C. M. Harris. *Shock and Vibration Handbook*. McGraw-Hill Book Company, New York, 1988.

[31] F. J. Harris. On the use of windows for harmonic analysis with the discrete Fourier transform. *Proceedings of the IEEE*, 66(1):51–83, 1978.

[32] H. Hermes and J. P. LaSalle. *Functional Analysis and Time Optimal Control*. Academic Press, New York, 1969.

[33] S. D. Jones and A. G. M. Ulsoy. Control input shaping for coordinate measuring machines. In *American Control Conference*, pages 2899–2903, Baltimore, MD, 1994.

[34] M. Kenison and W. Singhose. Input shaper design for double-pendulum planar gantry cranes. In *Proceedings of IEEE Conference on Control Applications*, volume 1, pages 539–544, 1999.

[35] Kepco. *BOP 50-2M Operational Power Supply Instruction Manual*, 2000.

[36] R. Kinceler and P. H. Meckl. Input shaping for nonlinear systems. In *Proceedings of the American Control Conference*, volume 1, pages 914–918, 1995.

[37] D. E. Kirk. *Optimal control theory: an introduction*. Prentice-Hall, Englewood Cliffs, N.J., 1970.

[38] K. C. Kozak. *Robust Command Generation For Nonlinear Systems*. PhD thesis, Georgia Institute of Technology, 2003.

[39] H. J. Landau and H. O. Pollak. Prolate spheroidal wave functions, Fourier analysis and uncertainty, II. *The Bell System Technical Journal*, 40(1):65–84, 1961.

[40] H. J. Landau and H. O. Pollak. Prolate spheroidal wave functions, Fourier analysis and uncertainty, III. *The Bell System Technical Journal*, 41(4):1295–1336, 1962.

[41] M. A. Lau and L. Y. Pao. Comparison of input shaping and time-optimal control of flexible structures. In *Proceedings of the American Control Conference*, volume 2, pages 1485–1490, 2001.

[42] M. A. Lau and L. Y. Pao. Input shaping and time-optimal control of flexible structures. *Automatica*, 39(5):893–900, 2003.

[43] E. B. Lee and L. Markus. *Foundations of Optimal Control Theory*. John Wiley & Sons, Inc., 1967.

[44] L. Ljung. *System Identification: Theory for the User*. Upper Saddle River, New Jersey: Prentice-Hall, Inc., 1999.

[45] L. Ljung and T. Glad. *Modeling of Dynamic Systems*. Englewood Cliffs, New Jersey: Prentice-Hall, Inc., 1994.

[46] D. P. Magee. *Optimal Arbitrary Time-Delay Filtering to Minimize Vibration in Elastic Manipulator Systems*. PhD thesis, Georgia Institute of Technology, 1996.

[47] D. P. Magee and W. J. Book. The application of input shaping to a system with varying parameters. In *Japan/USA Symposium on Flexible Automation*, pages 519–525, 1992.

[48] D. P. Magee and W. J. Book. Optimal filtering to minimize the elastic behavior in serial link manipulators. In *Proceedings of the American Control Conference*, volume 1, pages 2637–2641, 1998.

[49] D. P. Magee and W. J. Book. Optimal arbitrary time-delay (OAT) filter and method to minimize unwanted system dynamics. United States Patent, 6,078,844, June 2000.

[50] O. Maizza-Neto. *Modal Analysis and Control of Flexible Manipulator Arms*. PhD thesis, Massachusetts Institute of Technology, 1974.

[51] Mathworks. *Real-Time Workshop for Use with Simulink*, 2000.

[52] Mathworks. *Signal Processing Toolbox for Use with MATLAB*, 2002.

[53] P. H. Meckl and K. Roberto. Robust motion control of flexible systems using feedforward forcing functions. *IEEE Transactions on Control Systems Technology*, 2(3):245–253, 1994.

[54] Y. Mizoshita, S. Hasegawa, and K. Takaishi. Vibration minimized access control for disk drives. *IEEE Transactions on Magnetics*, 32(3):1793–1798, 1996.

[55] H. Moulin and E. Bayo. On the accuracy of end-point trajectory tracking for flexible arms by noncausal inverse dynamic solutions. *ASME, Journal of Dynamic Systems, Measurement, and Control*, 113(2):320–324, 1991.

[56] Newport. *Vibration Control System, Instruction Manual*, 1991.

[57] A. H. Nuttall. Some windows with very good sidelobe behavior. *IEEE Transactions on Acoustics, Speech, and Signal Processing*, 29(1):84–91, 1981.

[58] K. Ogata. *Discrete-Time Control Systems*. Prentice Hall, Inc., Englewood Cliffs, NJ, 1995.

[59] K. Ogata. *System Dynamics, Fourth Edition*. Prentice Hall, Inc., Upper Saddle River, NJ, 2004.

[60] A. V. Oppenheim. *Discrete-Time Signal Processing*. Prentice Hall, Inc., Englewood Cliffs, NJ, 1989.

[61] L. Y. Pao. *Proximate Time-Optimal Control of Higher-Order Servomechanisms*. PhD thesis, Stanford University, 1991.

[62] L. Y. Pao and W. E. Singhose. A comparison of constant and variable amplitude command shaping techniques for vibration reduction. In *IEEE Conference on Control Applications*, pages 875–881, 1995.

[63] L. Y. Pao and W. E. Singhose. On the equivalence of minimum time input shaping with traditional time-optimal control. In *IEEE Conference on Control Applications*, pages 1120–1125, 1995.

[64] J. Park and C. B. Schrader. Can an input shaper with two impulses suppress nonlinear residual vibrations? In *Proceedings of the American Control Conference*, volume 4, pages 3172–3177, 2003.

[65] D. B. Percival and A. T. Walden. *Spectral Analysis for Physical Applications - Multitaper and Conventional Univariate Techniques*. Cambridge University Press, 1993.

[66] A. Piazzi and A. Visioli. Minimum-time system-inversion-based motion planning for residual vibration reduction. *IEEE/ASME Transactions on Mechatronics*, 5(1):12–22, 2000.

[67] Polytec. *Laser Doppler Vibrometer, User's Manual*, 2000.

[68] Quanser Consulting, Inc. *WinCon 3.1: Real-Time Digital Signal Processing and Control Under Windows 95/98 and Windows NT Using SIMULINK and TCP/IP Technology*, 2001.

[69] B. W. Rappole, N. C. Singer, and W. P. Seering. Input shaping with negative sequences for reducing vibrations in flexible structures. In *Proceedings of the American Control Conference*, pages 2695–2699, San Francisco, CA, 1993.

[70] E. P. Ryan. *Optimal Relay and Saturating Control System Synthesis*. Peter Peregrinus Ltd., 1982.

[71] N. C. Singer. *Residual Vibration Reduction in Computer Controlled Machines*. PhD thesis, Massachusetts Institute of Technology, 1988.

[72] N. C. Singer and W. P. Seering. Preshaping command inputs to reduce system vibration. *ASME, Journal of Dynamic Systems, Measurement, and Control*, 112:76–82, 1990.

[73] N. C. Singer, W. P. Seering, and K. A. Pasch. Shaping command inputs to minimize unwanted dynamics. United States Patent, 4,916,635, April 1990.

[74] T. Singh and S. R. Vadali. Robust time-delay control. *ASME, Journal of Dynamic Systems, Measurement, and Control*, 115:303–306, 1993.

[75] T. Singh and S. R. Vadali. Robust time-delay control of multimode systems. *International Journal of Control*, 62:1319–1339, 1995.

[76] W. Singhose, A. Banerjee, and W. Seering. Slewing flexible spacecraft with deflection-limiting input shaping. *Journal of Guidance, Control, and Dynamics*, 20(2):291–298, 1997.

[77] W. Singhose and L. Pao. Comparison of input shaping and time-optimal flexible-body control. *Control Engineering Practice*, 5(4):459–467, 1997.

[78] W. Singhose and N. C. Singer. Initial investigations into the effects of input shaping on trajectory following. In *Proceedings of the American Control Conference*, pages 2526–2532, Baltimore, MD, 1994.

[79] W. E. Singhose. *Command Generation for Flexible Systems*. PhD thesis, Massachusetts Institute of Technology, 1997.

[80] W. E. Singhose, B. Mills, and W. Seering. Vibration reduction with specified-swing input shapers. In *Proceedings of the IEEE International Conference on Control Applications*, 1999.

[81] W. E. Singhose, L. J. Porter, T. D. Tuttle, and N. C. Singer. Vibration reduction using multi-hump input shapers. *ASME, Journal of Dynamic Systems, Measurement, and Control*, 119:320–326, 1997.

[82] W. E. Singhose, W. P. Seering, and N. C. Singer. Shaping inputs to reduce vibration: A vector diagram approach. In *IEEE International Conference on Robotics and Automation*, volume 2, pages 922–927, 1990.

[83] W. E. Singhose, W. P. Seering, and N. C. Singer. Residue vibration reduction using vector diagrams to generate shaped inputs. *ASME, Journal of Mechanical Design*, 1994.

[84] W. E. Singhose, W. P. Seering, and N. C. Singer. Time-optimal negative input shapers. *ASME, Journal of Dynamic Systems, Measurement, and Control*, 119:198–205, 1997.

[85] W. E. Singhose, N. C. Singer, S. J. Derezinski III, B. W. Rappole Jr., and K. Pasch. Method and apparatus for minimizing unwanted dynamics in a physical system. United States Patent, 5,638,267, June 1997.

[86] D. Slepian. Prolate spheroidal wave functions, Fourier analysis and uncertainty, IV. *The Bell System Technical Journal*, 43(6):3009–3058, 1964.

[87] D. Slepian. Prolate spheroidal wave functions, Fourier analysis and uncertainty, V: The discrete case. *The Bell System Technical Journal*, 57(5):1371–1430, 1978.

[88] D. Slepian. Some comments on Fourier analysis, uncertainty and modeling. *SIAM Review*, 25:379–393, 1983.

[89] D. Slepian and H. O. Pollak. Prolate spheroidal wave functions, Fourier analysis and uncertainty, I. *The Bell System Technical Journal*, 40(1):43–64, 1961.

[90] J. Y. Smith, K. Kozak, and W. E. Singhose. Input shaping for a simple nonlinear system. In *Proceedings of the American Control Conference*, volume 1, pages 821–826, 2002.

[91] O. J. M. Smith. Posicast control of damped oscillatory systems. *Proceedings of the IRE*, 45:1249–1255, 1957.

[92] O. J. M. Smith. *Feedback Control Systems*. McGraw-Hill, New York, 1958.

[93] J. A. Stratton, P. M. Morse, L. J. Chu, J. D. C. Little, and F. J. Corbató. *Spheroidal Wave Functions*. The Technology Press of M. I. T., Cambridge, MA, and John Wiley and Sons, New York, 1956.

[94] C. J. Swigert. Shaped torque techniques. *Journal of Guidance and Control*, 3(5):460–467, 1980.

[95] G. H. Tallman and O. J. M. Smith. Analog study of dead-beat posicast control. *IRE Transactions on Automatic Control*, pages 14–21, 1958.

[96] R. C. Thompson, J. L. Junkins, and S. R. Vadali. Near-minimum time open-loop slewing of flexible vehicles. *Journal of Guidance, Control, and Dynamics*, 12(1):82–88, 1989.

[97] Q. Tu, J. Rastegar, and F. Tangerman. Trajectory synthesis and inverse dynamics formulation for minimal vibrational excitation for flexible structures based on trajectory patterns. In *Proceedings of the 1993 American Control Conference, Part 3, June 1993, San Francisco, CA*, pages 2716–2720, 1993.

[98] T. D. Tuttle. *Creating Time-Optimal Commands for Linear Systems*. PhD thesis, Massachusetts Institute of Technology, Cambridge, MA, 1997.

[99] T. D. Tuttle and W. P. Seering. A zero-placement technique for designing shaped inputs to suppress multiple-mode vibration. In *Proceedings of the American Control Conference*, pages 2522–2537, Baltimore, MD, 1994.

[100] T. D. Tuttle and W. P. Seering. Creating time-optimal commands for systems with denominator dynamics. In *Proceedings of the 1996 IEEE International Conference on Control Applications*, pages 385–390, Dearborn, MI, 1996.

[101] T. D. Tuttle and W. P. Seering. Deriving and verifying time-optimal commands for linear systems. In *Proceedings of the American Control Conference*, pages 1325–1329, Albuquerque, New Mexico, 1997.

[102] T. D. Tuttle and W. P. Seering. Creating time-optimal commands with practical constraints. *Journal of Guidance, Control, and Dynamics*, 22(2):241–250, 1999.

[103] M. L. Workman. *Adaptive Proximate Time-Optimal Servomechanisms*. PhD thesis, Stanford University, 1987.

[104] H. Yamamura and K. Ono. Vibrationless access control of a positioning mechanism for high-order natural modes of vibration (2nd report, vibrationless velocity control) (in Japanese). *Nippon Kikai Gakkai Ronbunshu, C Hen/Transactions of the Japan Society of Mechanical Engineers, Part C*, 59(568):3710–3716, 1993.

[105] H. Yamamura and K. Ono. Vibrationless access control of a positioning mechanism for high-order natural modes of vibration (in Japanese). *Nippon Kikai Gakkai Ronbunshu, C Hen/Transactions of the Japan Society of Mechanical Engineers, Part C*, 59(559):727–732, 1993.

[106] H. Yamamura and K. Ono. Vibrationless access control of a positioning mechanism for high-order natural modes of vibration (3rd report, vibrationless acceleration control) (in Japanese). *Nippon Kikai Gakkai Ronbunshu, C Hen/Transactions of the Japan Society of Mechanical Engineers, Part C*, 61(585):1891–1898, 1995.

[107] H. Yamamura and K. Ono. Robust access control for a positioning mechanism with mechanical flexibility. In *Proceedings of the 1st International Conference on Motion and Vibration Control*, pages 437–442, Yokohama, Japan, September 1992.

Appendix A

Continuous-Time and Discrete-Time Fourier Transform

A.1 Continuous-Time Fourier Transform

Consider a measurable function $g(t) \in L^2(-\infty, \infty)$, the Fourier transform of $g(t)$ is defined as

$$G(\omega) := \int_{-\infty}^{\infty} g(t) e^{-j\omega t} dt, \tag{A.1}$$

and the inverse Fourier transform is defined as

$$g(t) = \frac{1}{2\pi} \int_{-\infty}^{\infty} G(\omega) e^{j\omega t} d\omega. \tag{A.2}$$

In this notation, Parseval's theorem is

$$\int_{-\infty}^{\infty} g(t)\overline{h(t)} dt = \frac{1}{2\pi} \int_{-\infty}^{\infty} G(\omega)\overline{H(\omega)} d\omega. \tag{A.3}$$

Equations (A.1) and (A.2) are referred to as the continuous-time Fourier transform pair. In engineering field, t is generally referred to as time in sec, ω as angular frequency in rad/sec, and $\frac{\omega}{2\pi}$ as frequency in Hz. Here lower case and upper case versions of a letter always denote a Fourier transform pair. If $\omega = 2\pi f$, where f has the unit of Hz, the following equations can be easily derived from the above definitions.

$$G(f) = \int_{-\infty}^{\infty} g(t) e^{-j2\pi ft} dt, \tag{A.4}$$

$$g(t) = \int_{-\infty}^{\infty} G(f) e^{j2\pi ft} df. \tag{A.5}$$

In this notation, Parseval's theorem is

$$\int_{-\infty}^{\infty} g(t)\overline{h(t)} dt = \int_{-\infty}^{\infty} G(f)\overline{H(f)} df. \tag{A.6}$$

A.2 Discrete-Time Fourier Transform

Suppose a continuous-time signal $g(t) \in L^2(-\infty, \infty)$ is sampled at equally spaced time intervals of duration T_s, a discrete-time sequence is generated as follows

$$g[k] := g(kT_s), \quad k = \cdots, -2, -1, 0, 1, 2, \cdots. \tag{A.7}$$

The discrete-time Fourier transform of $f[k]$ is defined as

$$G(\omega) := \sum_{k=-\infty}^{\infty} g[k] e^{-j\omega k}, \tag{A.8}$$

and the inverse discrete-time Fourier transform is defined as

$$g[k] = \frac{1}{2\pi} \int_{-\pi}^{\pi} G(\omega) e^{j\omega k} d\omega. \tag{A.9}$$

In this notation, Parseval's theorem is

$$\sum_{k=-\infty}^{\infty} g[k]\overline{h[k]} = \frac{1}{2\pi} \int_{-\pi}^{\pi} G(\omega)\overline{H(\omega)} d\omega. \tag{A.10}$$

Equations (A.8) and (A.9) are the discrete-time counterparts of (A.1) and (A.2). $G(\omega)$ in (A.8) is a periodic function in ω with period 2π. In engineering field, T_s is generally referred to as sampling period. The unit of ω in the discrete-time Fourier transform is rad. If the sampling period is T_s sec, $\frac{\omega}{T_s}$ is generally referred to as angular frequency in rad/sec, and $\frac{\omega}{2\pi T_s}$ as frequency in Hz. If T_s is assumed to be 1 and $\omega = 2\pi f$, where f has the unit of Hz, the following equations can be easily derived from the above definitions.

$$G(f) = \sum_{k=-\infty}^{\infty} g[k] e^{-j2\pi fk}, \tag{A.11}$$

$$g[k] = \int_{-1/2}^{1/2} G(f) e^{j2\pi fk} df. \tag{A.12}$$

In this notation, Parseval's theorem is

$$\sum_{k=-\infty}^{\infty} g[k]\overline{h[k]} = \int_{-1/2}^{1/2} G(f)\overline{H(f)} df. \tag{A.13}$$

Appendix B

Positive Definite Functions

This section gives a basic knowledge on positive definite functions in Analysis. Most part of this section is from Bochner [13].

B.1 The Function Class $\mathfrak{B}$

A distribution function $V(\alpha)$, is a function which is defined in $(-\infty, \infty)$, is bounded and monotonically increasing, and for which

$$V(\alpha) = \frac{1}{2}[V(\alpha + 0) + V(\alpha - 0)]$$

everywhere.

For each distribution function $V(\alpha)$, the integral [1]

$$f(x) := \int e^{jx\alpha} dV(\alpha) \tag{B.1}$$

exists for all x. The set of all the functions defined in (B.1) is denoted as function class $\mathfrak{B}$.

B.2 Positive Definite Functions

A function $f(x)$ is called positive definite if 1) it is continuous in the finite region, and is bounded in $(-\infty, \infty)$, 2) it is "hermitian", i.e.,

$$\overline{f(-x)} = f(x), \tag{B.2}$$

and it satisfies the following conditions: For any points $x_1, x_2, \ldots, x_m$, $(m = 1, 2, 3, \ldots)$, and any numbers $\rho_1, \rho_2, \ldots, \rho_m$

$$\sum_{\mu=1}^{m} \sum_{\nu=1}^{m} f(x_\mu - x_\nu) \rho_\mu \overline{\rho_\nu} \geq 0. \tag{B.3}$$

[1] Limits of integration will be omitted if there is no misunderstanding.

The relationship between positive definite functions and function class $\mathfrak{B}$ is given in the following theorem.

Theorem B.1 (Theorem 23 in Bochner [13]) *In order that a function belong to class $\mathfrak{B}$, it is necessary and sufficient that it is positive definite.*

From Theorem B.1, it can be shown that the function

$$\frac{\sin\left(W(t-s)\right)}{(t-s)}, \quad W > 0, \tag{B.4}$$

is a positive definite function. The conclusion can be deduced from that fact that function (B.4) belongs to the function class $\mathfrak{B}$. Let $\tau = t - s$, since

$$\frac{\sin\left(W\tau\right)}{\tau} = \frac{1}{2}\int_{-W}^{W} e^{j\omega\tau} d\omega, \tag{B.5}$$

function $\frac{\sin\left(W\tau\right)}{\tau}$ belongs to the function class $\mathfrak{B}$. So the conclusion is drawn.

Appendix C

The Relationship between Optimal Energy Concentration Functions in the Band-Limited Space and Prolate Spheroidal Wave Functions

This section discusses the relationship between the optimal energy concentration functions in the band-limited space and the prolate spheroidal wave functions. The relationship was attacked by Slepian and his colleagues at Bell Labs in 1961 when they studied the communication theory. Their results seemed to hinge on a "lucky accident" they referred to [88].

Instead of using concentration in the sense of Heisenberg uncertainty, Slepian et al. introduced a more meaningful measure of a signal for the communication engineer

$$\alpha^2(T) := \frac{\int_{-T/2}^{T/2} |f(t)|^2 dt}{\int_{-\infty}^{\infty} |f(t)|^2 dt}, \tag{C.1}$$

i.e., the fraction of the signal's energy that lies in the time interval $[-T/2, T/2]$. Similarly,

$$\beta^2(W) := \frac{\int_{-W}^{W} |F(\omega)|^2 d\omega}{\int_{-\infty}^{\infty} |F(\omega)|^2 d\omega} \tag{C.2}$$

is a measure of concentration of the amplitude spectrum of $f(t)$.

Slepian's original question was to determine how large $\alpha^2(T)$ can be for $f(t)$ in the space of band-limited signals. They reduced the problem to the solution of the following equation.

$$\int_{-1}^{1} \frac{\sin\left(c(x-y)\right)}{\pi(x-y)} \psi(y) dy = \lambda \psi(x), \quad |x| \leq 1. \tag{C.3}$$

From the Fredholm equation theory [20], (C.3) has solutions in $L^2(-1, 1)$ only for a set of discrete real positive values of λ, such as $\lambda_0 \geq \lambda_1 \geq \lambda_2 \geq \ldots$ and that $\lim_{n\to\infty} \lambda_n = 0$.

The corresponding solutions, $\psi_0(x), \psi_1(x), \psi_2(x), \ldots$ can be chosen to be real and orthogonal on $[-1, 1]$. They are complete in $L^2(-1, 1)$.

Slepian et al. found that the solutions of (C.3) are also solutions to the following second-order differential equation eigenvalue problem

$$\frac{d}{dx}(1-x^2)\frac{d\psi}{dx} + (\chi - c^2x^2)\psi = 0. \tag{C.4}$$

Equation (C.4) is known as the equation of prolate spheroidal wave functions. The detail of prolate spheroidal wave functions can be found in [93], [24]. It is known that (C.4) has solutions bounded everywhere only for discrete real positive values of χ, such as, $0 < \chi_0 < \chi_1 < \chi_2 < \ldots$. The corresponding solutions $\psi_0, \psi_1, \psi_2, \ldots$ are known as prolate spheroidal wave functions. Slepian pointed out that the solutions of (C.4) satisfy (C.3) because ψ's are complete in $L^2(-1, 1)$ and the differential operator

$$P_x := \frac{d}{dx}(1-x^2)\frac{d}{dx} - c^2x^2$$

commutes with the kernel of (C.3), i.e., for all signals $r(y)$ and real x,

$$P_x \int_{-1}^{1} \frac{\sin\left(c(x-y)\right)}{\pi(x-y)} r(y)dy = \int_{-1}^{1} \frac{\sin\left(c(x-y)\right)}{\pi(x-y)} P_y r(y)dy. \tag{C.5}$$

Equation (C.5) is the "lucky accident" referred to by Slepian [88].

The equation of (C.5) can be proved in the following way. The left hand side (LHS) of (C.5) can be reduced to the following form.

$$\begin{aligned}
LHS &= P_x \int_{-1}^{1} \frac{\sin\left(c(x-y)\right)}{\pi(x-y)} r(y)dy, \\
&= \frac{d}{dx}(1-x^2)\frac{d}{dx}\int_{-1}^{1} \frac{\sin\left(c(x-y)\right)}{\pi(x-y)} r(y)dy - c^2x^2 \int_{-1}^{1} \frac{\sin\left(c(x-y)\right)}{\pi(x-y)} r(y)dy, \\
&= \int_{-1}^{1} \frac{d}{dx}(1-x^2)\frac{d}{dx}\frac{\sin\left(c(x-y)\right)}{\pi(x-y)} r(y)dy - \int_{-1}^{1} c^2x^2 \frac{\sin\left(c(x-y)\right)}{\pi(x-y)} r(y)dy, \\
&= \int_{-1}^{1} \Bigg\{ -2\,x \left(\frac{\cos\left(c\left(x-y\right)\right)c}{\pi\ \left(x-y\right)} - \frac{\sin\left(c\left(x-y\right)\right)}{\pi\ \left(x-y\right)^2} \right) \\
&\quad + \left(1-x^2\right) \left(-\frac{\sin\left(c\left(x-y\right)\right)c^2}{\pi\ \left(x-y\right)} - 2\,\frac{\cos\left(c\left(x-y\right)\right)c}{\pi\ \left(x-y\right)^2} + 2\,\frac{\sin\left(c\left(x-y\right)\right)}{\pi\ \left(x-y\right)^3} \right) \Bigg\} r\left(y\right) dy \\
&\quad - \int_{-1}^{1} c^2x^2 \frac{\sin\left(c\left(x-y\right)\right) r\left(y\right)}{\pi\ \left(x-y\right)} dy, \\
&= \int_{-1}^{1} (A_1 + A_2 + A_3) r(y)dy,
\end{aligned} \tag{C.6}$$

where

$$A_1 = -\frac{c\left(2\,\cos\left(c\left(x-y\right)\right)x+\sin\left(c\left(x-y\right)\right)c\right)}{\pi\,\left(x-y\right)}, \tag{C.7}$$

$$A_2 = 2\,\frac{x\sin\left(c\left(x-y\right)\right)}{\pi\,\left(x-y\right)^2} - 2\,\frac{\left(1-x^2\right)\cos\left(c\left(x-y\right)\right)c}{\pi\,\left(x-y\right)^2}, \tag{C.8}$$

$$A_3 = 2\,\frac{\left(1-x^2\right)\sin\left(c\left(x-y\right)\right)}{\pi\,\left(x-y\right)^3}. \tag{C.9}$$

The right hand side (RHS) of (C.5) can be reduced to the following form.

$$\begin{aligned}
RHS &= \int_{-1}^{1}\frac{\sin\left(c(x-y)\right)}{\pi(x-y)}P_y r(y)dy,\\
&= \int_{-1}^{1}\frac{\sin\left(c(x-y)\right)}{\pi(x-y)}\left(\frac{d}{dy}(1-y^2)\frac{d}{dy}-c^2y^2\right)r(y)dy,\\
&= \int_{-1}^{1}-2\,\frac{\sin\left(c\left(x-y\right)\right)y}{\pi\,\left(x-y\right)}dr\left(y\right)+\int_{-1}^{1}\frac{\sin\left(c\left(x-y\right)\right)\left(1-y^2\right)}{\pi\,\left(x-y\right)}d\left(\frac{d}{dy}r\left(y\right)\right)\\
&\quad - c^2y^2\int_{-1}^{1}\frac{\sin\left(c\left(x-y\right)\right)r\left(y\right)}{\pi\,\left(x-y\right)}dy,\\
&= -\int_{-1}^{1}r\left(y\right)\frac{\partial}{\partial y}\left(-2\,\frac{\sin\left(c\left(x-y\right)\right)y}{\pi\,\left(x-y\right)}\right)dy\\
&\quad +\int_{-1}^{1}r\left(y\right)\frac{\partial}{\partial y}\left(-\frac{\cos\left(c\left(x-y\right)\right)c\left(1-y^2\right)}{\pi\,\left(x-y\right)}+\frac{\sin\left(c\left(x-y\right)\right)\left(1-y^2\right)}{\pi\,\left(x-y\right)^2}\right.\\
&\quad \left.-2\,\frac{\sin\left(c\left(x-y\right)\right)y}{\pi\,\left(x-y\right)}\right)dy-\int_{-1}^{1}\frac{\sin\left(c\left(x-y\right)\right)c^2y^2r\left(y\right)}{\pi\,\left(x-y\right)}dy,\\
&= \int_{-1}^{1}r\left(y\right)\frac{\partial}{\partial y}\left(-\frac{\cos\left(c\left(x-y\right)\right)c\left(1-y^2\right)}{\pi\,\left(x-y\right)}+\frac{\sin\left(c\left(x-y\right)\right)\left(1-y^2\right)}{\pi\,\left(x-y\right)^2}\right)dy\\
&\quad -\int_{-1}^{1}\frac{\sin\left(c\left(x-y\right)\right)c^2y^2r\left(y\right)}{\pi\,\left(x-y\right)}dy,\\
&= \int_{-1}^{1}r\left(y\right)\left\{-\frac{\sin\left(c\left(x-y\right)\right)c^2\left(1-y^2\right)}{\pi\,\left(x-y\right)}-2\,\frac{\cos\left(c\left(x-y\right)\right)c\left(1-y^2\right)}{\pi\,\left(x-y\right)^2}\right.\\
&\quad \left.+2\,\frac{\cos\left(c\left(x-y\right)\right)cy}{\pi\,\left(x-y\right)}+2\,\frac{\sin\left(c\left(x-y\right)\right)\left(1-y^2\right)}{\pi\,\left(x-y\right)^3}-2\,\frac{\sin\left(c\left(x-y\right)\right)y}{\pi\,\left(x-y\right)^2}\right\}dy\\
&\quad -\int_{-1}^{1}\frac{\sin\left(c\left(x-y\right)\right)c^2y^2r\left(y\right)}{\pi\,\left(x-y\right)}dy,\\
&= \int_{-1}^{1}(B_1+B_2+B_3)r(y)dy,
\end{aligned} \tag{C.10}$$

where

$$B_1 = -\frac{c\left(\sin\left(c\left(x-y\right)\right)c - 2\,\cos\left(c\left(x-y\right)\right)y\right)}{\pi\,\left(x-y\right)}, \tag{C.11}$$

$$B_2 = -2\,\frac{\cos\left(c\left(x-y\right)\right)c\left(1-y^2\right)}{\pi\,\left(x-y\right)^2} - 2\,\frac{\sin\left(c\left(x-y\right)\right)y}{\pi\,\left(x-y\right)^2}, \tag{C.12}$$

$$B_3 = 2\,\frac{\sin\left(c\left(x-y\right)\right)\left(1-y^2\right)}{\pi\,\left(x-y\right)^3}. \tag{C.13}$$

By calculation, the following equation holds

$$\left(A_1 - B_1\right) + \left(A_2 - B_2\right) + \left(A_3 - B_3\right) = 0. \tag{C.14}$$

So Equation (C.5) is proved to hold for all signals $r(y)$ and all real x.

Appendix D

Eigenvalues and Eigenfunctions of a Linear Integral Equation

This section gives a basic concept on the linear integral equations.

D.1 Kernels

Let $K(s,t)$ be a function of the two variables s and t defined and continuous in the region $a \leq s \leq b$, $a \leq t \leq b$, and let λ be a parameter. The functional equation

$$f(s) = \psi(s) - \lambda \int K(s,t)\psi(t)dt \tag{D.1}$$

is called a linear integral equation of the second kind with the kernel $K(s,t)$, where $f(s)$ and $\psi(s)$ are two functions of variable s continuous in the interval $a \leq s \leq b$. A kernel is called a degenerate kernel, if it can be written as a finite sum of products of functions of s and functions of t

$$K(s,t) = \sum_{i=1}^{p} \alpha_i(s)\beta_i(t). \tag{D.2}$$

It can be shown that kernel $\frac{\sin(\pi N(f-f'))}{\sin(\pi(f-f'))}$, where N is a positive integer, is a degenerate

kernel, since

$$\frac{\sin\left(\pi N(f-f')\right)}{\sin\left(\pi(f-f')\right)} = \frac{e^{-j\pi(f-f')N} - e^{j\pi(f-f')N}}{e^{-j\pi(f-f')} - e^{j\pi(f-f')}}, \tag{D.3}$$

$$= \frac{e^{-j\pi(f-f')N}}{e^{-j\pi(f-f')}} \frac{1 - e^{i2\pi(f-f')N}}{1 - e^{i2\pi(f-f')}}, \tag{D.4}$$

$$= e^{-j\pi(f-f')(N-1)} \frac{1 - e^{j2\pi(f-f')N}}{1 - e^{j2\pi(f-f')}}, \tag{D.5}$$

$$= e^{-j\pi(f-f')(N-1)} \sum_{k=0}^{N-1} e^{j2\pi(f-f')k}, \tag{D.6}$$

$$= \sum_{k=0}^{N-1} e^{i\pi f(2k-N+1)} e^{i\pi f'(-2k+N-1)}. \tag{D.7}$$

D.2 Eigenvalues and Eigenfunctions

If the function $f(s)$ in (D.1) vanishes identically, (D.1) reduces to a homogeneous integral equation. A value λ for which the homogeneous equation possesses non-vanishing solutions is called an eigenvalue of the kernel; the corresponding solutions $\psi_1, \psi_2, \ldots, \psi_h$ (assumed normalized and mutually orthogonal) are called the eigenfunctions of the kernel for the eigenvalue λ.

Appendix E

Matlab Scripts

E.1 Energy Concentration $1 - J$ of a Discrete-Time Acceleration Profile Based on Gaussian Function

```
function result = energy_fraction_acc_based_gaussian(n, M, T,
$omega_c) ENERGY_FRACTION_ACC_BASED_GAUSSIAN is to calculate
%the energy fraction of the acceleration profile based on
%derivative of Gaussian function.
%     int_0^omega |Acc(w)|^2 dw
%     ----------------------, where acc[k] is a discrete
%       int_0^pi |Acc(w)|^2 dw
%sequence of the derivative of Gaussian function.
%The result is only a approximate value. For a precise result,
%use ENERGYFRACTION_IN_FREQINTERVAL. However, for a long
%discrete sequence, ENERGYFRACTION_IN_FREQINTERVAL is slow.
%Out:
%fraction   - energy concentration after omega_c, i.e., 1-J
%Input:
%n          - scale parameter n
%M          - integer number, acc(0)...acc(M), move time is M*T
%T          - sampling period in second
%omega_c    - first resonant frequency in rad/sec,

%the unit of discrete-time Fourier transform variable omega
%is rad.
omega = omega_c*T;%[0 - pi]

%delta omega to calculate the energy of sequence.
```

```
%Reduce the value if more accuracy is required
delt_omega = 1e-3;

if rem(M, 2) == 0 %M is even
    k=[1:M/2];

    %the energy before omega (rad)
    result=0;

    for i=[0:delt_omega:omega];
        result = result + (2*T*sum(k.*exp(-2^(2*n-1)*k.^2*T^2)...
                 .*sin(i.*k)))^2;
    end
    num=result;

    %the total energy in frequency band 0 - pi
    omega=pi;
    result=0;

    for i=[0:delt_omega:omega];
        result = result + (2*T*sum(k.*exp(-2^(2*n-1)*k.^2*T^2)...
                 .*sin(i.*k)))^2;
    end

    fraction = (result-num) / result;
else %M is odd
    k=[1:(M+1)/2];

    %the energy before omega (rad)
    result=0;

    for i=[0:delt_omega:omega];
        result = result + (2*T*sum((k-.5).*exp(-2^(2*n-1)*...
                 (k-.5).^2*T^2).*sin(i.*(k-.5))))^2;
    end
    num=result;
```

```
    %the total energy in frequency band 0 - pi
    omega=pi;
    result=0;

    for i=[0:delt_omega:omega];
        result = result + (2*T*sum((k-.5).*exp(-2^(2*n-1)*...
                 (k-.5).^2*T^2).*sin(i.*(k-.5))))^2;
    end

    %fraction of the energy after omega
    fraction = (result-num) / result;
end
```

E.2 Energy Concentration $1-J$ of a Discrete-Time Gaussian Sequence

```
function fraction = energy_fraction_gaussian(n, M, T, omega_c)
%ENERGY_FRACTION_GAUSSIAN is to calculate the energy fraction
%of the Gaussian function profile
%     int_0^omega |G(w)|^2 dw
%     ----------------------,
%       int_0^pi |G(w)|^2 dw
% where g[k] is a discrete Gaussian sequence.
%The result is only a approximate value. For a precise result,
%use ENERGYFRACTION_IN_FREQINTERVAL. However, for a long
%discrete sequence, ENERGYFRACTION_IN_FREQINTERVAL is slow.
%Out:
%fraction   - energy concentration after omega_c, i.e., 1-J
%Input:
%n          - scale parameter n
%M          - integer number, g(0)...g(M)
%T          - sampling period in second
%omega_c    - first resonant frequency in rad/sec,

%the unit of discrete-time Fourier transform variable omega
%is rad.
```

```
omega=omega_c*T;%[0 - pi]

%delta omega to calculate the energy of sequence.
%Reduce the value if more accuracy is required
delt_omega=1e-3;

if rem(M, 2) == 0 %M is an even number
    k=[1:M/2];

    %the energy before omega (rad)
    result=0;

    for i = [0:delt_omega:omega];
        result = result + (1 + 2*sum(exp(-2^(2*n-1)*k.^2*T^2)...
                 .*cos(i.*k)))^2;
    end
    num=result;

    %the total energy in frequency band 0 - pi
    omega=pi;
    result=0;

    for i=[0:delt_omega:omega];
        result = result + (1 + 2*sum(exp(-2^(2*n-1)*k.^2*T^2)...
                 .*cos(i.*k)))^2;
    end

    %fraction of the energy after omega
    fraction = (result-num) / result;

else %M is an odd number
    k=[1:(M+1)/2];

    %the energy before omega (rad)
    result=0;

    for i=[0:delt_omega:omega];
```

```
        result = result + (2*sum(exp(-2^(2*n-1)*(k-.5).^2*T^2)...
                 .*cos(i.*(k-.5))))^2;
    end
    num=result;

    %the total energy in frequency band 0 - pi
    omega=pi;
    result=0;

    for i=[0:delt_omega:omega];
        result = result + (2*sum(exp(-2^(2*n-1)*(k-.5).^2*T^2)...
                 .*cos(i.*(k-.5))))^2;
    end

    %fraction of the energy after omega
    fraction = (result-num) / result;
end
```

E.3 Energy Concentration $\beta^2(W)$ of a Sequence

```
function beta2 = energyfraction_in_freqinterval(h, Ts, Omega)
%ENERGYFRACTION_IN_FREQINTERVAL is to compute the fraction of
%a signal's energy that lies in the frequency interval [-Omega,
% Omega]
%Out:
%beta2 - The fraction of signal's energy that lies in the
%frequency interval [-Omega, Omega]
%Input:
%h     - A finite sequence with sampling period Ts sec
%Ts    - Sampling period in sec
%Omega - Frequency bandwidth Omega in rad/sec

%Make h to be an N by 1 vector
if size(h, 1) == 1
    h = h';
end
```

```
%Normalized frequency
W = Omega/(2*pi/Ts);

if W >= 0.5
    W
    disp('Wrong parameter settings. Possibly Omega is too ...
    large!');
    return;
end

%h[k], k=0,1, ... M
M = length(h)-1;

%Symmetric matrix A
for t1 = 0 : M
    for t2 = 0 : M
        if t1 == t2
            A(t1+1,t2+1) = 2*W;
        else
            A(t1+1,t2+1) = sin(2*pi*W*(t1-t2))/(pi*(t1-t2));
        end
    end
end

%Compute the energy fraction
beta2 = h'*A*h/norm(h)^2;
```

E.4 Robust Vibration Suppression Velocity Profile Generation from the Discrete Prolate Spheroidal Sequence

```
function [vel] = robust_dpss_velocity_profile(MoveTime, ...
omega0, Ts)
%ROBUST_DPSS_VELOCITY_PROFILE is to generate a robust vibration
%suppression profile from the first discrete prolate spheroidal
```

```
%sequence v_0[k]. A velocity constant must be multiplied to
%realize certain position movement.
%Output:
%vel      - Robust velocity profile
%Input:
%movetime - Move time in sec of the velocity profile
%omega0   - The resonance frequency in rad/sec
%Ts       - Sampling period in sec

M = length([0:Ts:MoveTime])-1;%[0:M] total M+1 sequences
n = M + 1;%total data numbers of a sequence

%Normalized frequency bandwidth
W=omega0/(2*pi/Ts);

if W >= 0.5
    W
    disp('Wrong parameter settings. Possibly omega0 is too ...
    large!');
    return;
end


%Discrete prolate spheroidal sequence
[e,v]=dpss(n, n*W, [1]);

%Velocity profile with initial and final values zero from
%vertically shifted DPSS
vel = e(:,1) - e(1,1);
```

E.5 Generation of Rectangle Based Shape Filter with Robustness Order 1

```
function [f] = rectbased_shapefilter(omega, zeta, Ts)
%RECTBASED_SHAPEFILTER is to generate the rectangle based
%vibration suppression shape filter with robust order 1.
```

```
%Output:
%f     - Rectangle based shape filter sequence
%Input:
%omega - The undamped natural frequency in rad/sec
%zeta  - Damping ratio
%Ts    - Sampling period in sec

%Damped natural frequency in rad/sec
omega_d = omega * sqrt(1 - zeta^2);

%Sequence total floating number for given Ts
M=(2*pi/Ts/omega_d-1);

%A slightly changed sampling period
M1 = floor(M);
Ts1 = 2*pi/(M1+1)/omega_d;

%Initialization of the base function
h(1:ceil(M1*Ts1/Ts)+1)=0;

%The modified base function
for k=0:M1
    n = floor(k * Ts1 / Ts);
    beta = k * Ts1/Ts - n;

    B = 1;
    B1 = sin(omega_d * Ts * (1 - beta)) / sin(omega_d * Ts) * B;
    B2 = sin(omega_d * Ts * (beta)) / sin(omega_d * Ts) * B;

    if beta == 0
        h(n+1) = h(n+1) + B1;
    else
        h(n+1) = h(n+1) + B1;
        h(n+2) = h(n+2) + B2;
    end
end
```

```
%Shape filter
f = h./exp(zeta*omega*[0:length(h)-1]*Ts);

%Normalization
f = f/sum(f);
```

E.6 Generation of Hanning Based Shape Filter with Robustness Order 1

```
function [f] = hanningbased_shapefilter(omega, zeta, Ts)
%HANNINGBASED_SHAPEFILTER is to generate the hanning based
%vibration suppression shape filter with robust order 1.
%Output:
%f     - Hanning based shape filter sequence
%Input:
%omega - The undamped natural frequency in rad/sec
%zeta  - Damping ratio
%Ts    - Sampling period in sec

%Damped natural frequency in rad/sec
omega_d = omega * sqrt(1 - zeta^2);

%Sequence total floating number for given Ts
M=(4*pi/Ts/omega_d);

%A slightly changed sampling period
M1 = floor(M);
Ts1 = 4*pi/(M1)/omega_d;

%Initialization of the base function
h(1:ceil(M1*Ts1/Ts)+1)=0;

%The modified base function
for k=0:M1
    n = floor(k * Ts1 / Ts);
    beta = k * Ts1/Ts - n;
```

```
    %Hanning window function
    B = 0.5 * (1-cos(2*pi*k/M1));
    B1 = sin(omega_d * Ts * (1 - beta)) / sin(omega_d * Ts) * B;
    B2 = sin(omega_d * Ts * (beta)) / sin(omega_d * Ts) * B;

    if beta == 0
        h(n+1) = h(n+1) + B1;
    else
        h(n+1) = h(n+1) + B1;
        h(n+2) = h(n+2) + B2;
    end
end

%Shape filter
f = h./exp(zeta*omega*[0:length(h)-1]*Ts);

%Normalization
f = f/sum(f);
```

E.7 Generation of Blackman Based Shape Filter with Robustness Order 1

```
function [f] = blackmanbased_shapefilter(omega, zeta, Ts)
%BLACKMANBASED_SHAPEFILTER is to generate the blackman based
%vibration suppression shape filter with robust order 1.
%Output:
%f     - Blackman based shape filter sequence
%Input:
%omega - The undamped natural frequency in rad/sec
%zeta  - Damping ratio
%Ts    - Sampling period in sec

%Damped natural frequency in rad/sec
omega_d = omega * sqrt(1 - zeta^2);
```

```
%Sequence total floating number for given Ts
M=(6*pi/Ts/omega_d);

%A slightly changed sampling period
M1 = floor(M);
Ts1 = 6*pi/(M1)/omega_d;

%Initialization of the base function
h(1:ceil(M1*Ts1/Ts)+1)=0;

%The modified base function
for k=0:M1
    n = floor(k * Ts1 / Ts);
    beta = k * Ts1/Ts - n;

    %Blackman window function
    B = 0.42 - 0.5 * cos(2*pi*k/M1) + 0.08 * cos(4*pi*k/M1);
    B1 = sin(omega_d * Ts * (1 - beta)) / sin(omega_d * Ts) * B;
    B2 = sin(omega_d * Ts * (beta)) / sin(omega_d * Ts) * B;

    if beta == 0
        h(n+1) = h(n+1) + B1;
    else
        h(n+1) = h(n+1) + B1;
        h(n+2) = h(n+2) + B2;
    end
end

%Shape filter
f = h./exp(zeta*omega*[0:length(h)-1]*Ts);

%Normalization
f = f/sum(f);
```

E.8 Generation of Hamming Based Shape Filter with Robustness Order 1

```
function [f] = hammingbased_shapefilter(omega, zeta, Ts)
%HAMMINGBASED_SHAPEFILTER is to generate the hamming based
%vibration suppression shape filter with robust order 1.
%Output:
%f     - Hamming based shape filter sequence
%Input:
%omega - The undamped natural frequency in rad/sec
%zeta  - Damping ratio
%Ts    - Sampling period in sec

%Damped natural frequency in rad/sec
omega_d = omega * sqrt(1 - zeta^2);

%Sequence total floating number for given Ts
M=(4*pi/Ts/omega_d);

%A slightly changed sampling period
M1 = floor(M);
Ts1 = 4*pi/(M1)/omega_d;

%Initialization of the base function
h(1:ceil(M1*Ts1/Ts)+1)=0;

%The modified base function
for k=0:M1
    n = floor(k * Ts1 / Ts);
    beta = k * Ts1/Ts - n;

    %Hamming window function
    B = 25/46-21/46*cos(2*pi*k/M1);
    B1 = sin(omega_d * Ts * (1 - beta)) / sin(omega_d * Ts) * B;
    B2 = sin(omega_d * Ts * (beta)) / sin(omega_d * Ts) * B;

    if beta == 0
```

```
        h(n+1) = h(n+1) + B1;
    else
        h(n+1) = h(n+1) + B1;
        h(n+2) = h(n+2) + B2;
    end
end

%Shape filter
f = h./exp(zeta*omega*[0:length(h)-1]*Ts);

%Normalization
f = f/sum(f);
```

E.9 Shape Filter Operation of Two Shape Filters

```
function [f] = shapefilter_operation(f1, f2)
%SHAPEFILTER_OPERATION is to generate a shape filter from two
%shape filters f1 and f2. f1 and f2 could be the same or
%different. f1 and f2 must have the same sampling period.
%Output:
%f   - The shape filter sequence with sampling period Ts from a
%      shape filter operation of two shape filters f1 and f2.
%Input:
%f1  - The first discrete shape filter sequence with sampling
%      period Ts.
%f2  - The second discrete shape filter sequence with sampling
%      period Ts.

%total number
num_f = length(f1)+length(f2)-1;

%Filter operation
f = filter(f1, 1, [f2 zeros(1,length(f1)-1)]);

%Normalization to make sum f[k] = 1
f = f / sum(f);
```

Appendix F

Maple Scripts

F.1 Find the Minimum ω such that the Discrete-Time Fourier Transform of a Hanning Window $H(\omega) = 0$

```
> restart:
> M:='M':omega:='omega':assume(M>0,omega>0);

#Inert form discrete-time Fourier transform of Hanning window
> Sum('(1/2-1/2*cos(2*Pi*n/M))*exp(-I*omega*n)','n'=0..M);

            M~
          -----
           \
            )   //1   1    /2 Pi n\\                \
           /    ||- - - cos|------|| exp(-I omega n)|
          ----- \\2   2    \  M   //                /
          n = 0

#Real and imaginary part of the discrete-time Fourier transform
of Hanning window
> WC:=simplify(sum('(1/2-1/2*cos(2*Pi*n/M))*cos(omega*n)',
'n'=0..M)):
> WS:=simplify(sum('(1/2-1/2*cos(2*Pi*n/M))*sin(omega*n)',
'n'=0..M)):

#Simplified numerators of the real and imaginary parts
> NC:=simplify(expand(numer(WC),'trig'));
> NS:=simplify(expand(numer(WS),'trig'));
```

```
                                          /            2\
                                          |        /Pi\ |
        NC := sin(omega~ M~) sin(omega~) |-1 + cos|--| |
                                          \        \M~/ /

                    /                         2          2
                    |                    /Pi\       /Pi\
NS := -sin(omega~) |-cos(omega~ M~) - cos|--|  + cos|--|
                    \                    \M~/       \M~/

                                          \
                                          |
                          cos(omega~ M~) + 1|
                                          /
```

```
> DC:=simplify(expand(denom(WC),'trig'));
> DS:=simplify(expand(denom(WS),'trig'));
```

```
                                  2                        2
                    2        /Pi\                     /Pi\
 DC := 2 cos(omega~)  + 4 cos|--|  - 4 cos(omega~) cos|--|  - 2
                             \M~/                     \M~/

                                  2                        2
                    2        /Pi\                     /Pi\
 DS := 2 cos(omega~)  + 4 cos|--|  - 4 cos(omega~) cos|--|  - 2
                             \M~/                     \M~/
```

```
#Factorization of NC and NS
> factor(NC);factor(NS);
```

```
                                /   /Pi\    \ /   /Pi\    \
    sin(omega~ M~) sin(omega~) |cos|--| - 1| |cos|--| + 1|
                                \   \M~/    / \   \M~/    /

             /   /Pi\    \ /   /Pi\    \
 -sin(omega~) |cos|--| - 1| |cos|--| + 1| (-1 + cos(omega~ M~))
```

```
             \   \M~/    / \   \M~/    /
#Factorization of DC and DS
> factor(DC);factor(DS);

                          /                      2    \
                          |                   /Pi\     |
       2 (cos(omega~) - 1) |cos(omega~) - 2 cos|--|  + 1|
                          \                   \M~/     /

                          /                      2    \
                          |                   /Pi\     |
       2 (cos(omega~) - 1) |cos(omega~) - 2 cos|--|  + 1|
                          \                   \M~/     /
> combine(subs(omega=2*Pi/M,NS));combine(subs(omega=2*Pi/M,DS));

                              0

                              0
#Obviously, omega=2*Pi*k/M, k=1,2,... are pssible solutions.
For k=1, omega=2*Pi/M, both NC and DC are zero. So minimum
solution omega = 4*Pi/M.
```

VITA

Li Zhou

Candidate for the Degree of

Doctor of Philosophy

Thesis: ROBUST VIBRATION SUPPRESSION CONTROL PROFILE GENERATION

Major Field: Mechanical Engineering

Biographical:

Personal Data: Born in Jilin, P. R. China, on December 15, 1971, the son of Dianfu Zhou and Lianting Liu.

Education: Graduated from Changbai Shiyan High School, Changbai County, Jilin Province, P. R. China, in July 1989; received Bachelor of Science degree in Mechanical Engineering from Jilin University of Technology, Changchun, P. R. China, in July 1993; received Master of Science degree in Mechanical Engineering from Dalian University of Technology, Dalian, P. R. China, in July 1996; Completed the requirements for the Doctor of Philosophy degree with a major in Mechanical Engineering at Oklahoma State University in May, 2005.

Professional Experience: Worked as a research assistant, Institute of Vibration Engineering, Dalian University of Technology, P. R. China, September 1993 - July 1996; employed as a software development engineer, H & B System Company, Tokyo, Japan, October 1996 - July 2000; worked as an intern at Servo Dynamic Group, Seagate Technology LLC, Oklahoma City, Oklahoma, May 2003 - October 2003; employed as a research assistant, Oklahoma State University, School of Mechanical & Aerospace Engineering, Advanced Controls Laboratory, August 2000 - present; employed as a teaching assistant, Oklahoma State University, School of Mechanical & Aerospace Engineering, August 2002 - present; employed as a system administrator, Oklahoma State University, School of Mechanical & Aerospace Engineering, Advanced Controls Laboratory, December 2003 - present.

Professional Memberships: American Society of Mechanical Engineers.

Name: Li Zhou Date of Degree: May, 2005

Institution: Oklahoma State University Location: Stillwater, Oklahoma

Title of Study: ROBUST VIBRATION SUPPRESSION CONTROL PROFILE GENERATION

Pages in Study: 260 Candidate for the Degree of Doctor of Philosophy

Major Field: Mechanical Engineering

Scope and Method of Study:

The control of flexible structures has been extensively studied in recent years. Flexible structures such as high-speed disk drive actuators require extremely precise positioning under very tight time constraints. Whenever a fast motion is commanded, residual vibration in the flexible structure is induced, which increases the settling time. One solution is to design a closed-loop control to damp out vibrations caused by the command inputs and disturbances to the plant. However, the resulting closed-loop response may still be too slow to provide an acceptable settling time. Also, the closed-loop control is not able to compensate for high frequency residual vibration which occurs beyond the closed-loop bandwidth. An alternative approach is to develop an appropriate reference trajectory that is able to minimize the excitation energy imparted to the system at its natural frequencies.

Findings and Conclusions:

A robust vibration suppression control profile is generated which suppresses all the high frequency vibrations in a flexible dynamic system. This robust control profile is the shifted time-limited version of the functions that optimally achieve the energy concentration property. The robust control profile is designed by considering the first resonance frequency. In practical system, a lower resonance frequency mode may exist which is located far from the high frequency resonance modes. In this case, a robust control profile is generated which suppresses one specific resonant mode in a flexible dynamic system. This robust control profile is a smooth function which can be used as a robust velocity profile, or as a robust shape filter to an arbitrary control command. The robustness can be arbitrarily improved, which brings about a smoother profile. Combination of high frequency vibration suppression control profile and low frequency vibration suppression control profile generates a robust vibration suppression control profile that is able to suppress all the resonant dynamics in a flexible dynamic system. The technique can be applied to both open-loop and closed-loop systems.

ADVISOR'S APPROVAL: _____